INVESTIGATION OF ADVANCED BUTLER MATRICES WITH INTEGRATED FILTER FUNCTIONS

by

Vittorio Tornielli di Crestvolant

A thesis submitted to the University of Birmingham for the degree of

Doctor of Philosophy

School of Electronic, Electrical and Systems Engineering
College of Engineering and Physical Sciences
University of Birmingham
July 2015

Vittorio Tornielli di Crestvolant (ID 1188203): *Investigation of advanced Butler matrices with integrated filter functions,* School of Electronic, Electrical and Systems Engineering, University of Birmingham, July 2015.

Plagiarism checked on 14th July 2015, Turnitin ID 46086594. Submitted on 15th July 2015. Viva Voce examination held on 17th September 2015 in Birmingham, UK; panel composed by Dr P. Tricoli (chairperson), Dr R. Cameron (external examiner) and Dr F. Huang (internal examiner). Revised on 6th October 2015; date of current version 24th October 2015.

Printed using LaTeX 2_ε with ClassicThesis and ArsClassica, mathematical fonts standard of the $\mathcal{AMS}$.

COPYRIGHT

ABSTRACT

This study presents a novel synthesis technique for Butler matrices that include filter transfer functions through a circuit based only on resonators. The Butler matrix is the fundamental building block to split and recombine the signals in Multi-port Power Amplifiers, where multiple inputs are delivered to a bank of amplifiers sharing them, and later recombined through an output network. However, to suppress spurious frequencies generated by the amplifiers or to provide near-band rejection in order not to interfere with other transmission/receiving bands, separate filtering is often required. Here, the traditional properties of the Butler matrix are included together with filtering selectivity into one single device based only on coupled resonators. An analytical synthesis procedure of the coupling matrix is presented here for the first time. The proposed solution has shown significant advantages in terms of size reduction compared to the traditional baseline consisting of a Butler matrix plus a bank of band-pass filters. Based on the technique proposed, three prototypes are designed and manufactured: a 180° hybrid coupler based on resonators and two versions of a 4×4 Butler matrix with filtering, built with additive manufacturing and with milling. Experimental measurements are in good agreement with simulations and theoretical expectations.

«il bel paese
ch'Appennin parte, e 'l mar circonda et l'Alpe.»

Petrarca, Canzoniere, CXLVI, vv. 13-14

ACKNOWLEDGEMENTS

This work is the outcome of a 3 years PhD programme in partnership between the University of Birmingham, the European Space Agency (ESA) and Airbus Defence and Space under the Networking Partnering Initiative No. 4000107492/13/NL/GLC/fe. In this context, the work has been carried out at the University of Birmingham, UK, at the European Space research and Technology Centre (ESTEC) in Noordwijk, The Netherlands, and at the Airbus Defence and Space facilities of Stevenage, UK. The Author wishes to thank Prof. Michael Lancaster for the continuous support over the whole period of the study. A special and grateful thank is for Mr. Petronilo Martin Iglesias who firmly and tirelessly gave support during the period spent at ESTEC, for his availability and openness in discussing problems, other than for always finding opportunities to make this work visible and acknowledged among colleagues. A thank goes to Mr. Paul Booth, who was the referee during the intern-ship at Airbus Defence and Space, for his comments and suggestions. The Author also thanks Dr. Piero Angeletti, head of the ESA RF Equipment and Technology section, for his feedbacks and interest in this work, to Hanno Ertel and Andre Zandvliet of the ESTEC workshop for planning, designing, and producing the physical devices with milling. Also, a thank goes to the friends and people met during all these years: in particular to the YGT community of ESTEC and to all other friends with whom was a pleasure to work with and to share time and experiences together.

A special thought and thank also goes to my family for the continuous support and to those people who always have been close, providing invaluable help and support throughout all this experience.

Birmingham, UK, July 2015

CONTENTS

LIST OF FIGURES

LIST OF TABLES

ACRONYMS

AM	Additive Manufacturing
BFN	Beam Forming Network
BM	Butler Matrix
BPF	Band-Pass Filter
BPP	Band-Pass Prototype
BGC	Branch-Guide Coupler
CAD	Computer Aided Design
CNC	Computerized Numerical Control
CST	Computer Simulation Technology
CW	Common Wave
DC	Direct Current
ECSS	European Cooperation for Space Standardisation
EIRP	Equivalent Isotropic Radiated Power
EM	Electromagnetic
ESA	European Space Agency
ESTEC	European Space research and Technology Centre
FBW	Fractional Bandwidth
FIR	Frequency Invariant Reactance
FSS	Fixed Satellite Service
GD	Group Delay
HPA	High Power Amplifier
HTS	High Throughput Satellite

IL	Insertion Loss
INET	Input network
LPF	Low-Pass Filter
LPP	Low-Pass Prototype
MPA	Multi-port Power Amplifier
ONET	Output network
PA	Power Amplifier
PIM	Passive Inter-Modulation
RF	Radio Frequency
RL	Return Loss
RX	Receiver
RZ	Reflection Zero
SEE	Secondary Electron Emission
SEY	Secondary Emission Yield
SSPA	Solid State Power Amplifiers
TWTA	Travelling Wave Tube Amplifier
TX	Transmitter
TZ	Transmission Zero
VNA	Vector Network Analyser
VSWR	Voltage Standing Wave Ratio

1 INTRODUCTION

Space technologies find extensive applications in areas such as global navigation satellite systems, communications, earth observation, weather forecasting, radio, TV, phone links, military and governmental services or surveillance. Among them, the communication satellites are a consistent part of any complex telecommunication system and the overall space industry. They perform radio links with users on ground or directly communicate between satellites. Typically, the link of data from satellite to earth is called *down link* while when the communication is performed from earth to in orbit satellite is called *up link*. Usually they incorporate complex Radio Frequency (RF) payload systems as the signal coming from earth arrives attenuated by the atmosphere and needs to be reconstructed, amplified and then sent back.

Among the communication satellites are the Fixed Satellite Service (FSS), which provide radio links with fixed points at specified areas on earth, as well as providing inter-satellite communications. They are typically placed in *geostationary orbit*, meaning that their angular speed and revolutionary period is the same as the earth, hence making it possible to broadcast to specific geographical areas [1]. The most common examples of services provided are television and radio broadcasting delivered to wide area of users [2]. With a geostationary satellite, different services can be distributed to areas on earth that are variable in size, using different directivity antennas to create variable beams. A beam can cover a large area with low antenna gain, or a smaller zone such as a continent. Recent satellite technologies are challenged by the higher demand and increasing data rates, mobile access and use of relatively cheap terminals by the users. This required the industry to move towards High Throughput Satellite (HTS), which are characterised by higher number of radiating elements covering

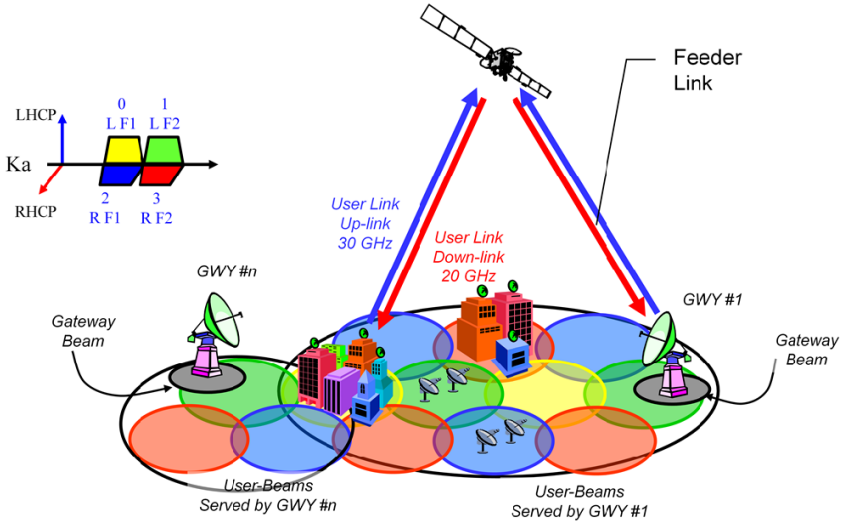

Figure 1.1: Example of Ka-band multi-beam satellite system. Courtesy of ESA

limited areas (about 26 000 km^2); they are also called *spot beams* [3]. In this kind of system there are only few reflectors which are used by plenty of radiating elements. The throughput provided by the HTS architecture is greater by several orders with respect the previous conventional FSS. Frequency reuse is possible through the different beams in order to enhance the data rate to the users. Fig. 1.1 is an example of HTS with reuse of frequencies. The frequencies are identified with the different colours on the geographical area. Adjacent beams use different frequencies in order to avoid interference. Moreover, orthogonal polarisations could be used in some systems in order to further increase the capacity.

It is possible to consider every beam of Fig. 1.1 as an independent sub-system of the satellite, each requiring a partially dedicated payload. This puts a major challenge on the complexity, number of components and the consequent accommodation problems of the on board equipment. Also, power distribution, cooling and temperature control, disposal of the equipment are important. Conventional payload system architectures tend to hundreds of beams operating in frequency reuse. In order to minimise the number of amplifiers, a single High Power Amplifier (HPA) is often used in multi-carrier mode to amplify the downlink signals on different spot beams. Fig. 1.2 is a schematic of such architecture. Depending on the required Equivalent Isotropic

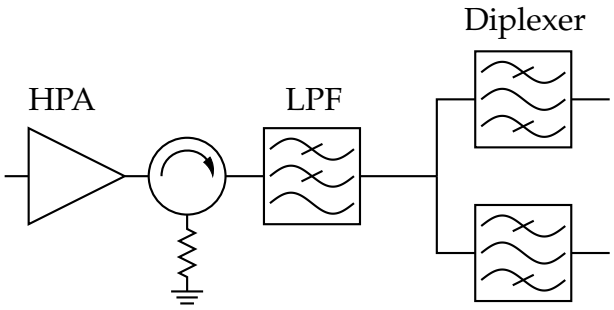

Figure 1.2: Conventional payload amplification architecture

Radiated Power (EIRP) and frequency plan, the HPA can be shared among 2 or 4 beams. The amplifier of Fig. 1.2 is sharing 2 signals on different frequencies, which are separated and delivered to the radiating elements through a diplexer. The Low-Pass Filter (LPF) is to clean spectrum by intermodulation products, while the isolator prevents that reflected power goes back into the amplifier.

In a multi-beam environment the distribution of traffic is a variable and uniform division of bandwidth and power is not an optimal solution. Some spot beams might temporarily have to serve high volume of traffic (hot spot) while others covering an area with reduced number of users (cold spot) in a specified time. If there is no flexibility in place, capacity might get unused among the cold spots while reduced for the users served by the hot spots. The conventional system of Fig. 1.2 does not provide any kind of flexibility for power nor bandwidth allocation. This is because the signals are statically shared by the HPA and the frequencies are delivered to the diplexer. Additionally, an adequate redundancy strategy is to be applied in order to ensure the service. The amplifiers need to be dimensioned in order to allow the maximum level of input power possible, leading to larger equipment with more power consumption than necessary when the traffic load is not at maximum level. This concept is expressed in Fig. 1.3a, here are the cases of uniform and non uniform distribution of users among the beams. To overcome this limitation, a Multi-port Power Amplifier (MPA) is adopted in place of having a single HPA as it was for the example of Fig. 1.2. All the amplifiers are working in the available bandwidth. The description of uniform traffic allocation on the left part of Fig. 1.3a can also lead to

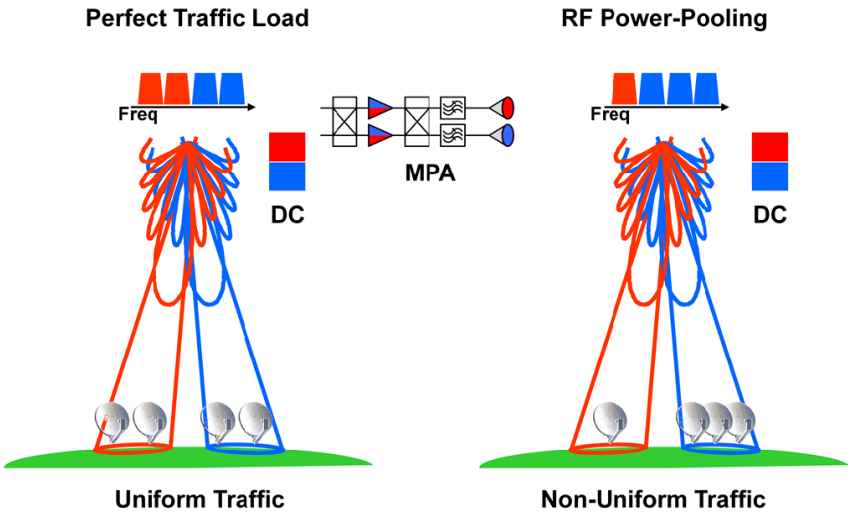

(a) Flexible allocation of power

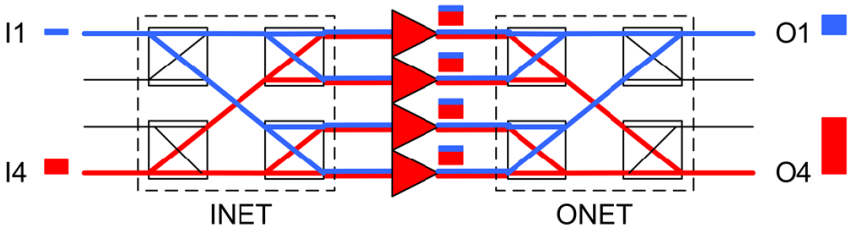

(b) MPA power sharing

Figure 1.3: Non uniform allocation of users and power. Courtesy of ESA

flexibility of power levels: with the MPA it is possible to allocate different power levels to the two beams, however narrow-band filters are necessary in order to avoid interference among the them (ie. red and blue), as shown in the schematic of Fig. 1.3a. On the right part of Fig. 1.3a, there is the case where both power and frequency are variable through the use of the MPA of Fig. 1.3b. The dynamic allocation of the frequency is done by a processor before the stage of the MPA, and it is made possible by the absence of the narrow-band filters. The main difference between the systems of Fig. 1.3a, is that for the one on the left part a fixed frequency multiplexing is provided by the output filters with flexibility on the power levels, whilst on the right part the broadband behaviour of the MPA allows a flexibility of allocation of the frequency, meaning that theoretically the entire bandwidth can be allocated to a single signal.

In order to design efficient MPAs, before and after the amplifiers of Fig. 1.3b there are distribution networks, known as *Butler matrices* that are responsible for the deliv-

ering of the input power to the Power Amplifier (PA) and to recombine the signals. With reference of Fig. 1.3b, the Butler matrix on the left side of the amplifiers is also called Input network (INET), while the one on the right-hand side is named Output network (ONET). Such a structure, that will be described in detail in the following of this work, is a solution to the problem of power flexibility because all the amplifiers work on the same power level, regardless the traffic distribution. With this solution it is possible to reduce the size of the PAs because they are operating always at the same level of power and eventual peaks of traffic in some of the beams will balance the ones with less power.

The constant growing demand for more bandwidth and capacity of communication satellites, requires to have multiple services operating on adjacent bands. These services should not interfere with the other bands so requiring additional filtering. Hence, at the output stage of the MPA of Fig. 1.3b it might be necessary to include a Band-Pass Filter (BPF) for each RF path to protect from spurious signals in other bands. The additional filtering is meant to be wider in bandwidth with respect the case of the left part of Fig. 1.3a, thus allowing efficient frequency and power allocation. Clearly, this is going to add more complexity, space, number of interfaces, etc., to the existing RF payload system. The aim of this work is to create a Butler matrix (ie. the circuit right-hand cascaded to the amplifiers of Fig. 1.3b) with all the filtering transfer functions included in one single device.

This work is organised in the following chapters:

CHAPTER 2 describes the basic knowledge and background that is necessary to the complete understanding of the following chapters.

CHAPTER 3 introduces the 90° hybrid couplers based on transmission lines and then shows further development of equivalent circuits based only on resonators that include filter transfer functions. This chapter also addresses the problems and limitations of the quadrature hybrids with resonators and a method to predict the electrical response of such networks.

CHAPTER 4 is the chapter in which is presented a novel technique for the synthesis of the coupling matrix of $N \times N$ Butler matrices with filter transfer functions included.

CHAPTER 5 describes the design, manufacturing and measurements of some prototypes in order to provide experimental verification of the results presented in chapter 4.

APPENDIX A shows in detail the synthesis technique of the conventional quadrature hybrid couplers based on transmission lines.

APPENDIX B gives the theory of multi-port networks based on electromagnetically coupled resonators, other than a general form of coupling matrix used in the work to describe all the electrical properties of the circuits proposed.

APPENDIX C is the list of publications.

2 BACKGROUND

Some basic knowledge and background information that is useful for the rest of the work is summarised in this chapter. It is essential to point out that some details are not mentioned here for brevity and are referred to the appendix or to the bibliography, where appropriate.

2.1 THE BUTLER MATRIX AND ITS DEVELOPMENTS

The Butler matrix is a multi port microwave passive component with the purpose of providing input to output signal power splitting with prescribed phase relationship. This network is formed by the arrangement of several 4-port hybrid couplers and phase shifters like the example of 4×4 configuration of Fig. 2.1. The aim is to shape the beam pattern in an antenna arrays [4, 5]. The Butler Matrix (BM) is to control beam pattern by means of the phase shifters [6]. A key role is played by the adoption of the hybrid coupler as it can guarantee equal output power distribution of the input signals

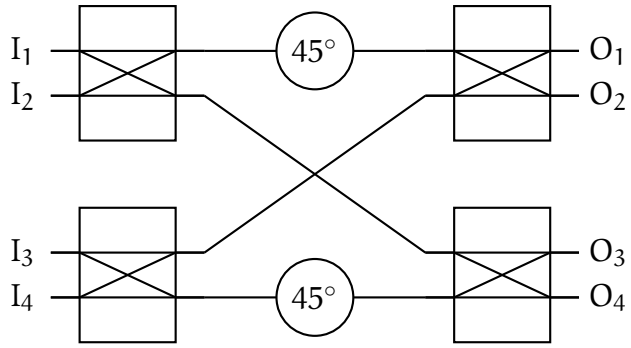

Figure 2.1: Schematic of 4×4 Butler matrix

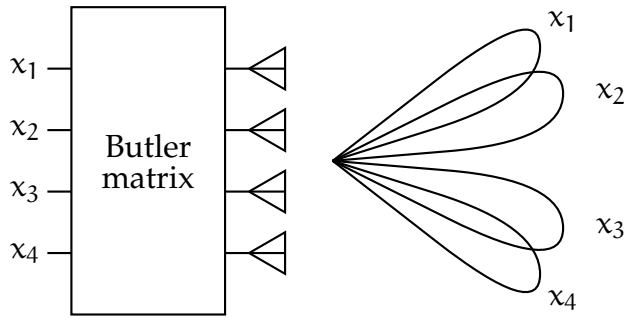

Figure 2.2: Butler matrix used to shape signal beams

as well as having good isolation. In the general case this network accommodates N input signals, each of them is delivered with equal amplitude to all the N outputs with a constant phase shift. The BM represents a very widely used device in many microwave telecommunications systems, both terrestrial and for space, where several signals need to cover each an angular spatial area [7]. A simple high-level schematic of Beam Forming Network (BFN) realised with a Butler matrix feeding an array of antennas is shown in Fig. 2.2.

The BM of Fig. 2.1 is formed by 90° hybrids couplers (rectangular boxes) and fixed phase shifters (circles with the indication of phase). The input signals are applied to ports $I_1, \ldots, I_4$ and the radiating antenna elements to ports $O_1, \ldots, O_4$. All other lines here are transmission lines of matched characteristic impedance. The network in Fig. 2.1 is the simplest example of BM for the purpose of BFN and it can be easily scaled to more general $N \times N$ configurations [8]. The equal power distribution and the phase of the input signals is responsible for the different shape of beams in the open space. The 3 dB power splitter limits the design to accept only 2^k inputs/outputs, if a different number is required, a larger matrix is needed with the spare ports loaded on matched terminations. The hybrids are fixed, previously designed elements, hence the synthesis involves the calculation of the phases of each phase shifter of the network through systematic techniques [9–11]. It is also found how the design is not limited to the use of 90° hybrids but it can also be obtained through a different arrangement of only 180° couplers and phase shifters [12].

2.2 MULTI-PORT POWER AMPLIFIER

The Butler matrix is the fundamental building block of a MPA because of its properties of combination and recombination of the signals. The concept of using an INET to split N input signals to a bank of PA and then cascading a second network, the ONET, to recombine them was introduced in [13]. This configuration is also called *hybrid transponder*. In Fig. 2.3 are shown the schematics of a 2×2 and of a more general $N \times N$ MPA. With this configuration each amplifier shares all input signals x_i at the same time because of the equal power distribution property of the INET. In Fig. 2.3a is shown the phase and amplitude relations of each path of the hybrids as well as the gain G of the amplifiers (all identical). The BM is found as the ideal candidate at this stage as it divides equally the input power with a prescribed phase relationship. This property is exploited in the ONET as an identical Butler matrix recombines signals avoiding interferences. Also, the phase shifters included in the INET and ONET of the original version of the study by Sandrin are no longer necessary [14, 15]. The basic configuration of 2-input, 2-output, MPA of Fig. 2.3a can be extended to the more general case of $N \times N$ (Fig. 2.3b) as shown in [14].

The circuit of Fig. 2.3a can be decomposed as a cascade of the transfer function matrix of the INET, T_I, the one of PA, T_{PA} and for the ONET, T_O. For this simple case it follows that:

$$\mathbf{T}_I = \mathbf{T}_O = \frac{1}{\sqrt{2}} \begin{bmatrix} 1 & j \\ j & 1 \end{bmatrix} \tag{2.1}$$

while the amplification stage is:

$$\mathbf{T}_{PA} = G\mathbf{I}_2 \tag{2.2}$$

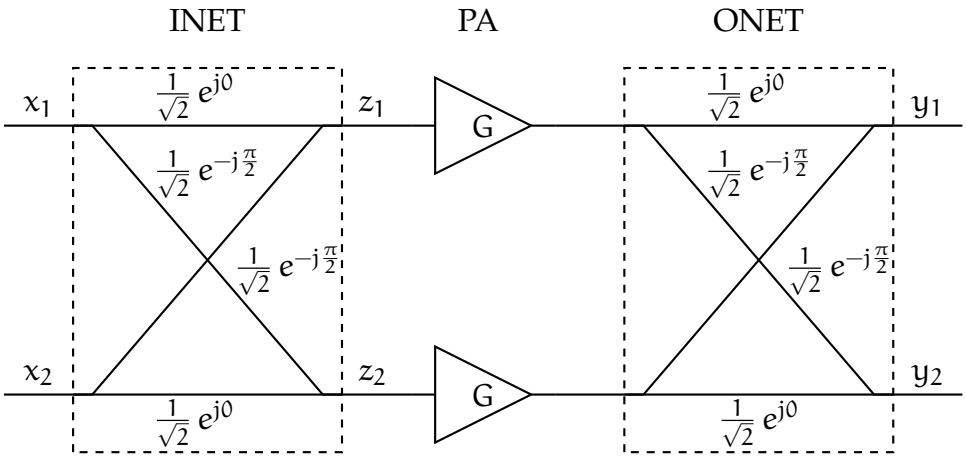

(a) Schematic of 2×2 MPA based on 90° hybrid couplers

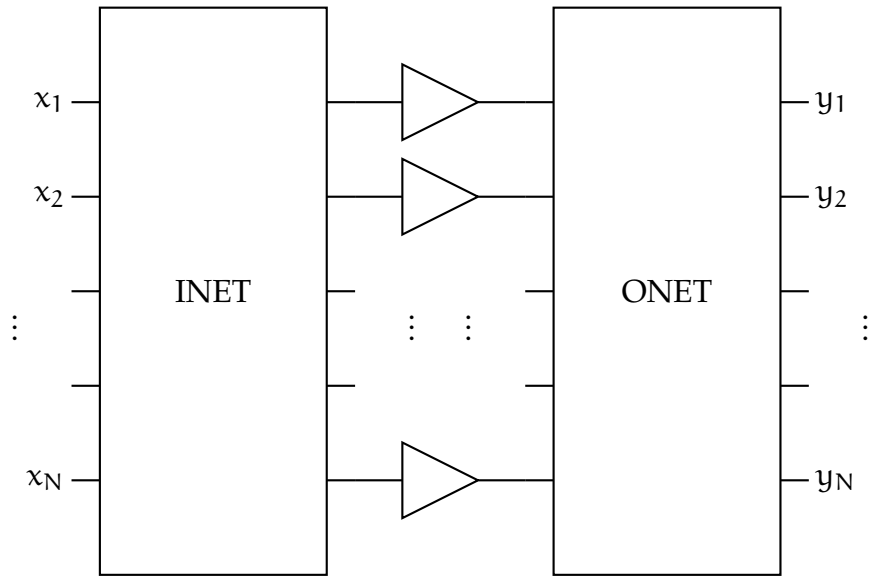

(b) General configuration of MPA

Figure 2.3: Multi-port Power Amplifier

where $\mathbf{I}_2$ is the 2×2 unitary matrix. The resulting transfer function matrix of the MPA of Fig. 2.3a is then found to be

$$\mathbf{T}_{\mathrm{MPA}} = \mathbf{T}_{\mathrm{I}} \cdot \mathbf{T}_{\mathrm{PA}} \cdot \mathbf{T}_{\mathrm{O}} = \begin{bmatrix} 0 & -G \\ -G & 0 \end{bmatrix} \tag{2.3}$$

These three equations can be directly extended to the general $N \times N$ MPA. The result of eq. (2.3) outlines that outputs are in reverse order, with gain G and 180° phase shift with respect to the inputs. For the scope of this study there is no need for the outputs to have a particular phase relation as long as it is constant. Also, the anti-diagonal characteristic of transfer function matrix of eq. (2.3) just shows how the output interfaces should be referenced. This means that the only condition over the splitting and recombination network is that the resulting transfer matrix is, apart for a constant complex scaling factor, an orthogonal matrix or any its transpositions. The constant complex scaling factor refers to the gain and phase relation of the outputs while the orthogonality condition is essential for the correct separation and reconstruction of the signals. Finally, a transposition of the transfer function matrix just indicates the relation between the sequence of the output interfaces to the input signals. In general it is possible to say that the eq. (2.3) should be a permutation matrix, apart for a constant value. The power delivered to the amplifiers is governed by transmission matrix of eq. (2.1) through signals z_1 and z_2. If input signals are

$$x_1 = A_1 \cos(2\pi f_0 t + \phi) \tag{2.4a}$$

$$x_2 = A_2 \cos(2\pi f_0 t + \phi) \tag{2.4b}$$

with amplitudes $A_1 \neq A_2$, it results that each PA will receive a power of

$$E\{|z_1^2|\} = \frac{1}{2}(|A_1|^2 + |A_2|^2) \tag{2.5a}$$

$$E\{|z_2^2|\} = \frac{1}{2}(|A_2|^2 + |A_1|^2) \tag{2.5b}$$

Among the advantages are the recovery of a signal if one of the PA fails and of greater flexibility in term of power allocation at input level [16]. This power amplifier architecture is widely used in many telecommunication satellites where multiple beams are covering a geographical area by means of spots. It is important to stress that for this application the pair of Butler matrices is used not to shape a set of beams but just to split signals to deliver to a bank of amplifiers and to recombine them. This operation should be transparent to the system. With the classical approach of one single HPA per beam, the input power is function of the number of terminals for the specific area. Thus, the power levels at the input of each amplifier is generally not equal. This generates two main problems [17]:

1. many HPA are under utilised,

2. despite of a lower traffic, each amplifier (typically Solid State Power Amplifiers (SSPA) or Travelling Wave Tube Amplifier (TWTA)) should be configured to operate with the maximum number of terminals.

These two points have a major impact over the dimensions of the equipment and the available power to be supplied. On the contrary, an MPA architecture, through eq. (2.5), shows how signals with unequal input power are combined equally to all amplifiers. This is a major advantage with respect the classical configuration of one single HPA per arm. A direct consequence of the adoption of the MPA is that dimensions of the single amplifiers can be reduced thus saving mass and size of the overall payload or, alternatively, to support up to twice the traffic with controllable inter-beam isolation [18].

2.3 COUPLED RESONATORS BASED NETWORKS

In this work a Butler matrix that includes filter transfer functions will be investigated, hence a preliminary introduction of networks based on resonators is introduced here.

2.3.1 Main-line band-pass filters

Filters are the most common example of two ports resonant circuits [19]. More specifically, BPF are made by several resonators mutually coupled by electromagnetic couplings in order to provide frequency selectivity in one or more bands. The classical synthesis process of such devices starts from the calculation of the parameters g and r of the prototype in Fig. 2.4 in order to provide the prescribed Return Loss (RL) and selectivity in the Low-Pass Prototype (LPP) [20]. The filter prototype of Fig. 2.4 has a variable source generator V_s with the correspondent impedance R_s and the normalised load resistance r as termination. Normally the input impedance is normalized to 1 to ease the calculation. The last element of the filter is either a series inductor if n is even, or a shunt capacitor if odd. In the literature elements R_s and r are often indicated, respectively with g_0 and g_{n+1}. The first step of the synthesis is to define a suitable transfer function through a set of characteristic polynomials. Then the elements of the LPP are calculated to synthesise the response [21]. Two examples of filtering characteristics are the *Butterworth* maximally-flat or the *Tchebycheff* equal-ripple responses, shown in Fig. 2.5. The attenuation A of the input-to-output amplitude as function

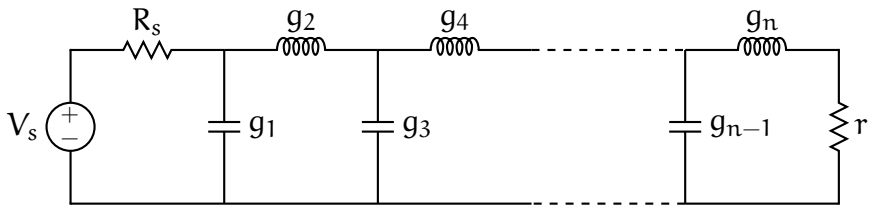

Figure 2.4: Low-pass filter prototype

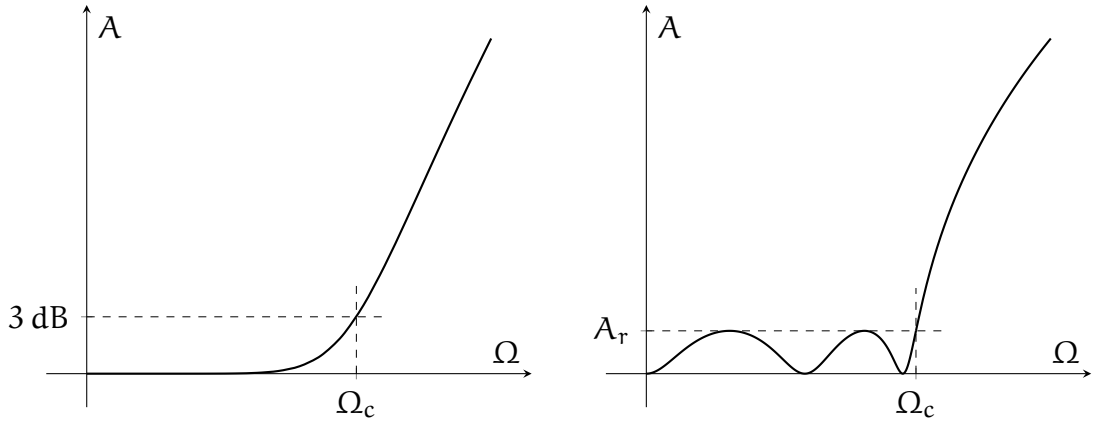

(a) Butterworth **(b)** Tchebycheff

Figure 2.5: Fifth order prototype low-pass filter attenuation characteristics

of the normalized low-pass variable Ω is shown in these graphs. The band edge or low-pass cut off frequency is indicated with Ω_c, it is usually normalised to 1. For the maximally flat response of Fig. 2.5a the band edge corresponds to 3 dB attenuation while the Tchebycheff characteristic introduces flat ripples of maximum amplitude A_r in the whole band. The polynomials of the Butterworth transfer function have all the poles coincident and located in $\Omega = 0$, producing a maximally-flat response. The normalised parameters for the maximally flat response are calculated as follows [20]:

$$g_0 = 1 \tag{2.6a}$$

$$g_k = 2\sin\left[\frac{(2k-1)\pi}{2n}\right], \qquad k = 1, 2, \ldots, n \tag{2.6b}$$

$$g_{n+1} = 1 \tag{2.6c}$$

The response shown in Fig. 2.5a is also expressed by the following formula valid for $\Omega_c = 1$:

$$A = 10\log_{10}\left(1 + \Omega^{2n}\right)$$

The Tchebycheff has a sharper rejection with the same number of resonators at the price of introducing a ripple. Hence, amplitude of the ripples can be controlled by variable A_r here expressed in dB through the following mathematical expressions [20]:

$$g_0 = 1 \tag{2.7a}$$

$$\beta = \ln\left[\coth\left(\frac{A_r}{17.37}\right)\right] \tag{2.7b}$$

$$\gamma = \sinh\left(\frac{\beta}{2n}\right) \tag{2.7c}$$

$$a_k = \sin\left[\frac{(2k-1)\pi}{2n}\right], \qquad k = 1, 2, \ldots, n \tag{2.7d}$$

$$b_k = \gamma^2 + \sin^2\left(\frac{k\pi}{n}\right), \qquad k = 1, 2, \ldots, n \tag{2.7e}$$

$$g_1 = \frac{2a_1}{\gamma} \tag{2.7f}$$

$$g_k = \frac{4a_{k-1}a_k}{b_{k-1}g_{k-1}} \qquad k = 2, 3, \ldots, n \tag{2.7g}$$

$$g_{n+1} = \begin{cases} 1 & \text{for } n \text{ odd}, \\ \coth^2\left(\frac{\beta}{4}\right) & \text{for } n \text{ even}. \end{cases} \tag{2.7h}$$

These are not the only two possible prototypes. The attenuation characteristic as shown in Fig. 2.5b is only for the case of unitary low-pass cut off frequency:

$$A = \begin{cases} 10\log_{10}\left[1 + \left(10^{A_r/10} - 1\right)\cos^2\left(n \arccos \Omega\right)\right] & \text{for } \Omega \leqslant 1 \\ 10\log_{10}\left[1 + \left(10^{A_r/10} - 1\right)\cosh^2\left(n \operatorname{arccosh} \Omega\right)\right] & \text{for } \Omega > 1 \end{cases}$$

It is important to remember that other types of LPP can be obtained with modification of the configuration of the filter of Fig. 2.4. An example are *elliptic filters* (also known as Cauer filters) where a capacitor is added in parallel to each inductor in Fig. 2.4 providing a minimum rejection in the out-band [22]. The values of the reactances for the elliptic filter are usually tabulated although they can be obtained explicitly [23, 24]. Another interesting family of transfer functions is given by the Zolotarev

polynomials: they are similar to Tchebycheff LPF except for a first ripple of attenuation close to the Direct Current (DC) [25]. The Zolotarev LPP is of the same type of the one proposed in Fig. 2.4 and it is able to provide a lobe of attenuation in the frequency range $x_1 < \Omega < \lambda$ with $\lambda < 1$ with a prescribed maximum attenuation at x_s [26]. These transfer functions are normally used to generate two narrower band-pass with sharper out-band rejection with regard the conventional Tchebycheff filter [27, 28].

The following step is to map the frequency response from the LPP Ω to band-pass in variable $\omega = 2\pi f$, band edges $\omega_1 = 2\pi f_1$ and $\omega_2 = 2\pi f_2$ as:

$$\Omega \rightarrow \frac{1}{w}\left(\frac{\omega}{\omega_0} - \frac{\omega_0}{\omega}\right) \tag{2.8}$$

where $\omega_0 = 2\pi f_0$ is the central frequency and w is the Fractional Bandwidth (FBW) [29]. The transformation is made in order to map the low-pass band edges $\Omega = \pm 1$ into, ω_1 and ω_2:

$$\begin{aligned} -1 &= \frac{1}{w}\left(\frac{\omega_1}{\omega_0} - \frac{\omega_0}{\omega_1}\right) \\ 1 &= \frac{1}{w}\left(\frac{\omega_2}{\omega_0} - \frac{\omega_0}{\omega_2}\right) \end{aligned}$$

Solving the last two equations results that central frequency and FBW are:

$$\omega_0 = \sqrt{\omega_1 \cdot \omega_2} \tag{2.9}$$

$$w = \frac{\omega_2 - \omega_1}{\omega_0} \tag{2.10}$$

The frequency transformation of eq. (2.8) is applied to the elements of the LPP of Fig. 2.4. It is easy to show that any shunt capacitor is transformed into a resonator formed with a parallel of a capacitor and inductor, while all the series inductor are

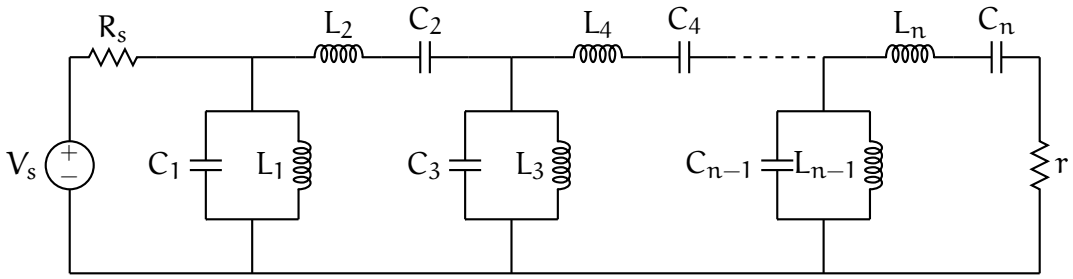

Figure 2.6: Lumped elements band-pass filter

transformed into a resonator with a series of inductor and capacitor. The series elements are transformed:

$$\begin{aligned} Z = j\Omega L \Rightarrow jL\frac{1}{w}\left(\frac{\omega}{\omega_0} - \frac{\omega_0}{\omega}\right) = \\ = j\left(\frac{L}{w\omega_0}\right)\omega - \frac{j}{\omega\frac{w}{L\omega_0}} \\ = j\omega\bar{L} - \frac{j}{\omega\bar{C}} \end{aligned} \tag{2.11}$$

with the new transformed elements $\bar{L} = \frac{L}{w\omega_0}$ and $\bar{C} = \frac{w}{L\omega_0}$. The low-pass to band-pass transformation of the impedance elements creates a resonator formed by a series of a inductor $\bar{L}$ and $\bar{C}$. The same transformation is applied to the shunt capacitors:

$$\begin{aligned} Y = j\Omega C \Rightarrow jC\frac{1}{w}\left(\frac{\omega}{\omega_0} - \frac{\omega_0}{\omega}\right) = \\ = j\left(\frac{C}{w\omega_0}\right)\omega - \frac{j}{\omega\frac{w}{C\omega_0}} \\ = j\omega\hat{C} - \frac{j}{\omega\hat{L}} \end{aligned} \tag{2.12}$$

The admittances instead are transformed into a parallel resonator of $\hat{C} = \frac{C}{w\omega_0}$ and $\hat{L} = \frac{w}{C\omega_0}$. The frequency mapping expressed with eq.s (2.11) and (2.12) is performed to all the elements of the LPP of Fig. 2.4. The result is a band-pass filter where series and parallel resonators are cascaded as shown in Fig. 2.6. In this figure the elements are numbered progressively, with odd numbers for the shunt resonators and even for the series ones. In Fig. 2.6 the last series resonator is only present if the order n is

even, otherwise the last resonator is shunt. The lumped elements of the band-pass filter are related to the g constants with the following:

$$L_{k,odd} = \frac{w}{\omega_0 \Omega_c g_k} \tag{2.13a}$$

$$C_{k,odd} = \frac{\Omega_c g_k}{w \omega_0} \tag{2.13b}$$

$$L_{k,even} = \frac{\Omega_c g_k}{w \omega_0} \tag{2.13c}$$

$$C_{k,even} = \frac{w}{\omega_0 \Omega_c g_k} \tag{2.13d}$$

where has been introduced the low-pass cut-off frequency Ω_c for greater generality of the final solution [20]. All the resonators are tuned at central frequency ω_0 as it is possible to demonstrate by multiplication of any odd or even pair of L-C elements in eq. (2.13):

$$L_k C_k = \frac{1}{\omega_0^2} \tag{2.14}$$

The BPF of Fig. 2.6 is formed by cascading several parallel and series resonators as it is a direct derivation of the frequency transformation from low-pass to band-pass. Such a solution is not practical because it is more convenient to manage a filter with just either type of resonators. Thus, the impedance inverters are introduced in order to overcome this limitation. Fig. 2.7 shows the theoretical model of both impedance and admittance inverters. Their behaviour is dual and they are represented by a box with expressed the inversion parameter. The ideal impedance inverter of Fig. 2.7a acts as a quarter-wavelength transmission line of characteristic impedance K at all frequencies. Hence the relation between the load impedance Z_L and the input is given as:

$$Z_{in} = \frac{K^2}{Z_L} \tag{2.15}$$

As a consequence the phase shift introduced by the inverter is of $\varphi = \pm 90°$. This is an ideal component, this means that the inversion parameter remains unchanged

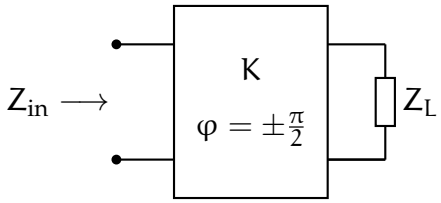

(a) Impedance inverter

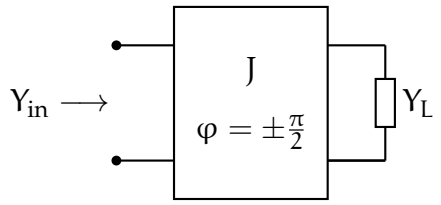

(b) Admittance inverter

Figure 2.7: Ideal immittance inverters.

regardless the frequency variation. Very useful in many calculations is the description in term of $ABCD$ matrix [30]:

$$\begin{bmatrix} A & B \\ C & D \end{bmatrix}_{imp} = \begin{bmatrix} 0 & jK \\ \frac{j}{K} & 0 \end{bmatrix} \tag{2.16}$$

The admittance inverter is the dual case of the impedance one and is often used with a parallel representation the circuit. It is shown in Fig. 2.7b with a load admittance Y_L. The input admittance is defined as:

$$Y_{in} = \frac{J^2}{Y_L} \tag{2.17}$$

while it can be demonstrated that the $ABCD$ matrix is:

$$\begin{bmatrix} A & B \\ C & D \end{bmatrix}_{adm} = \begin{bmatrix} 0 & \frac{j}{J} \\ jJ & 0 \end{bmatrix} \tag{2.18}$$

In literature it is common to refer to either the impedance or admittance inverters with the more general *immittance inverters*. The inverters can be realised by mean of a quarter-wavelength transmission line of impedance K. Alternatively, in Fig. 2.8 are

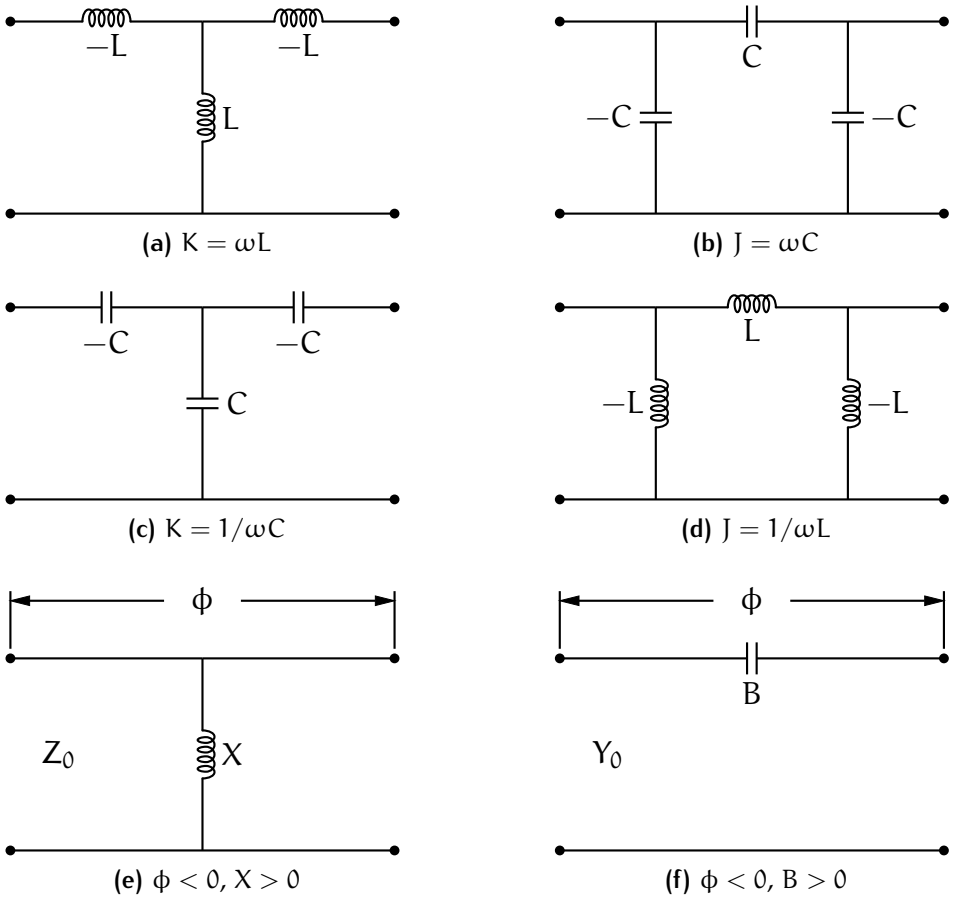

Figure 2.8: Practical realisation of inverters

shown some useful broadband networks that are implementing the same response [29]. On left column are typical impedance inverters while on the right side are the admittance inverters. Usually it is convenient to adopt a T of impedances for K inverters (Fig. 2.8a) while the π of admittances of Fig. 2.8b is often used for admittance inverters. These circuits can be analysed with the even/odd mode technique due to their symmetry. The impedance for the even mode Z_e is obtained with a magnetic wall at the plane of symmetry of the network. This breaks the two halves with an open circuit. Consequently, the odd mode impedance Z_o is calculated when the network is divided by an electric wall, hence with a shorted circuit. In Fig. 2.8a and 2.8b the shunt impedance $j\omega L$ and series admittance $j\omega C$ are divided in two parallel inductor or series capacitor of double inductance/capacitance. The shunt admittance and series

conductance of Fig. 2.8a and 2.8d are divided in two element, respectively parallel and series, of half value. The value of inversion K and phase shift φ are given as [20]:

$$K = \sqrt{Z_e Z_o} \tag{2.19a}$$

$$\varphi = 2 \arctan\left(\pm\sqrt{\frac{-Z_o}{Z_e}}\right) \tag{2.19b}$$

The inversion parameters indicated in below the circuits of Fig. 2.8 are obtained with the last two equations. It is possible to verify that either the T or π lumped circuits are giving a phase shift of $\varphi = \pm 90°$ that is constant with respect the frequency. Finally, the distributed circuits of Fig. 2.8e and 2.8f the electrical length ϕ of the transmission line and reactance X and B are functions of the inversion coefficients with the constraint of $\varphi = \pm 90°$ in order to keep the proper phase shift [29]. For the impedance inverter of Fig. 2.8e is:

$$\left|\frac{X}{Z_0}\right| = \frac{\frac{K}{Z_0}}{1 - \left(\frac{K}{Z_0}\right)^2} \tag{2.20a}$$

$$\phi = -\arctan\frac{2X}{Z_0} \tag{2.20b}$$

while for the admittance of Fig. 2.8f is:

$$\left|\frac{B}{Y_0}\right| = \frac{\frac{J}{Y_0}}{1 - \left(\frac{J}{Y_0}\right)^2} \tag{2.21a}$$

$$\phi = -\arctan\frac{2B}{Y_0} \tag{2.21b}$$

The inverter is able to transform an impedance into an admittance and vice versa, as well as a series circuit into a parallel one. Hence, it is possible to insert the inverters between each resonators of the BPF of Fig. 2.6 in order to get the same type of resonance for all the elements. If series resonators are to be designed, then the K

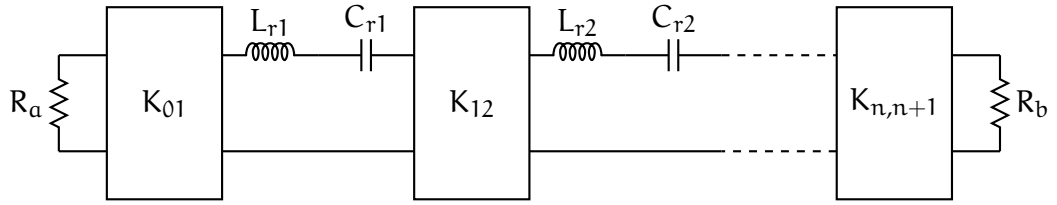

(a) Series resonators and K inverters

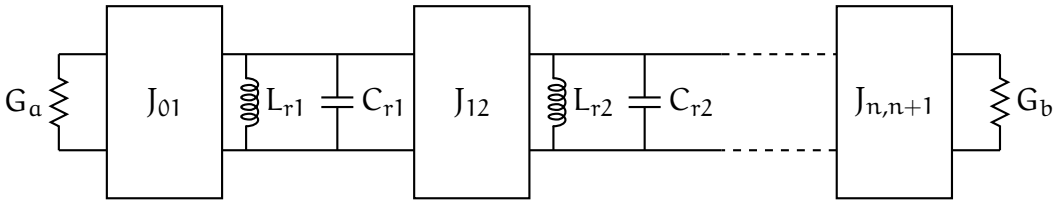

(b) Parallel resonators and J inverters

Figure 2.9: Filter transformation with ideal immittance inverters

inverter is able to produce the desired result as shown in Fig. 2.9a. Otherwise, the J inverter makes an all parallel filter as shown in Fig. 2.9b. In order to have the same type of resonance, inverters are to be included at both sides of each resonators. It derives that in a filter with n resonators there are $n+1$ inverters. In both diagrams of Fig. 2.9 the circuits are terminated with input and output impedances or admittances, respectively indicated with R_a and R_b for the series model, and G_a and G_b for the parallel one. It should be noted that the elements of the BPF with inverters are not exactly the same of the elements of Fig. 2.6. This is because the inclusion of the inverters in the model that changes the response of the filter. In order to have the same frequency response of the Band-Pass Prototype (BPP) filter, the elements of the K/J inverters need to be calculated and corrected accordingly. For this reason the inductors and capacitor in Fig. 2.9 have all a subscript r to differentiate them from the ones of Fig. 2.6. The correction is made imposing the same impedance seen in a section of the filter immediately after the second resonator, looking towards the source as shown in Fig. 2.10. In this way it will be calculated the value of the first inverter (or external inverter) and the second one (internal inverter between a pair of resonators).

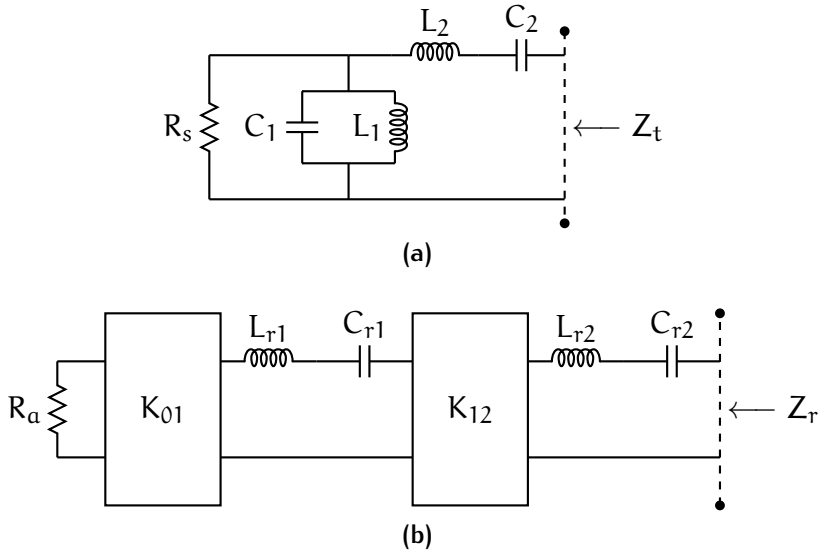

Figure 2.10: Equivalence with filters with inverters included

The circuits have been cut with a dashed line and the impedance calculated from this point. For the first filter of Fig. 2.10a the impedance is obtained as:

$$\begin{aligned} Z_t &= j\omega L_2 + \frac{1}{j\omega C_2} + \frac{1}{j\omega C_1 + \frac{1}{j\omega L_1} + \frac{1}{R_s}} \\ &= \sqrt{\frac{L_2}{C_2}} \left[j\left(\frac{\omega}{\omega_0} - \frac{\omega_0}{\omega}\right) + \frac{\sqrt{\frac{C_2 L_1}{L_2 C_1}}}{j\left(\frac{\omega}{\omega_0} - \frac{\omega_0}{\omega}\right) + \frac{1}{R_s}\sqrt{\frac{L_1}{C_1}}} \right] \end{aligned} \tag{2.22}$$

Note that eq. (2.14) has been used here. The same calculation is performed for the filter with inverters of Fig. 2.10b:

$$\begin{aligned} Z_r &= j\omega L_{r2} + \frac{1}{j\omega C_{r2}} + \frac{K_{12}^2}{j\omega L_{r1} + \frac{1}{j\omega C_{r1}} + \frac{K_{01}^2}{R_a}} \\ &= \sqrt{\frac{L_{r2}}{C_{r2}}} \left[j\left(\frac{\omega}{\omega_0} - \frac{\omega_0}{\omega}\right) + \frac{K_{12}^2\sqrt{\frac{C_{r1} C_{r2}}{L_{r1} L_{r2}}}}{j\left(\frac{\omega}{\omega_0} - \frac{\omega_0}{\omega}\right) + \frac{K_{01}^2}{R_a}\sqrt{\frac{C_{r1}}{L_{r1}}}} \right] \end{aligned} \tag{2.23}$$

The equality between the eq.s (2.22) and (2.23) is imposed:

$$Z_r = Z_t \tag{2.24}$$

It is possible to note that there is still a difference of a term $\sqrt{L_2/C_2}$ and $\sqrt{L_{r2}/C_{r2}}$ of the two relations and this is explained by the phase shift introduced by the inverters in the circuit. Apart for this, the numerator and denominator of the fraction between brackets of eq.s (2.22) and (2.23) are equated in order to get the formulation of the inverters:

$$K_{12}^2 \sqrt{\frac{C_{r1}C_{r2}}{L_{r1}L_{r2}}} = \sqrt{\frac{C_2 L_1}{L_2 C_1}} \tag{2.25}$$

$$\frac{K_{01}^2}{R_a} \sqrt{\frac{C_{r1}}{L_{r1}}} = \frac{1}{R_s} \sqrt{\frac{L_1}{C_1}} \tag{2.26}$$

Last relations are further transformed operating algebraic calculations and also the eq. (2.14), the following are obtained:

$$K_{01} = \sqrt{\frac{L_{r1}R_a}{C_1 R_s}}$$

$$K_{12} = \sqrt{\frac{L_{r1}L_{r2}}{L_1 C_2}}$$

At this point are recalled the eq.s (2.13) and that $R_s = g_0$ as it is the first element of the band-pass filter. Hence the formulation of all the K inverters are generalised for the arbitrary element k of the filter:

$$K_{0,1} = \sqrt{\frac{\omega_0 w}{\Omega_c} \cdot \frac{L_{r1}R_a}{g_0 g_1}} \tag{2.27a}$$

$$K_{k,k+1} = \frac{\omega_0 w}{\Omega_c} \sqrt{\frac{L_{rk}L_{r,k+1}}{g_k g_{k+1}}} \tag{2.27b}$$

$$K_{n,n+1} = \sqrt{\frac{\omega_0 w}{\Omega_c} \cdot \frac{L_{rn}R_b}{g_n g_{n+1}}} \tag{2.27c}$$

where the load impedance in filter of Fig. 2.6 is $r = g_{n+1}$. The values for the admittance inverters are calculated in the same way. Note that the frequency transformation of eq. (2.8) does not take into account of the dispersion of practical inverters. This is a phenomenon that affects the central frequency ω_0, the band edges ω_1 and ω_2 but also the ripples characteristic of the band-pass. The degradation of the response becomes worse with the increase of the bandwidth, hence it needs to be correct solving the following non linear equation [31]:

$$\frac{\omega_0}{\omega_1}\sin\left(\pi\frac{\omega_1}{\omega_0}\right) = -\frac{\omega_0}{\omega_2}\sin\left(\pi\frac{\omega_2}{\omega_0}\right) \tag{2.28}$$

Lumped elements circuit are difficult and not practical to build at microwave frequencies and distributed solutions are to be preferred. The impedance seen at the input of a circuit (lumped or distributed) is frequency dependent and can be expressed in terms of its resistance, the real part, and reactance, the imaginary one in this way:

$$X(\omega) = R(\omega) + jX(\omega)$$

Equivalently, it can be expressed with the input admittance also depending by the conductance and susceptance:

$$Y(\omega) = G(\omega) + jB(\omega)$$

The resonance of an arbitrary resonator i can be conveniently expressed by its central frequency ω_0 and the *slope* defined as the variation of the reactance (or susceptance) over the frequency:

$$\chi = \frac{\omega_0}{2}\left.\frac{\partial X_i(\omega)}{\partial\omega}\right|_{\omega=\omega_0} \tag{2.29}$$

$$b = \frac{\omega_0}{2}\left.\frac{\partial B_i(\omega)}{\partial\omega}\right|_{\omega=\omega_0} \tag{2.30}$$

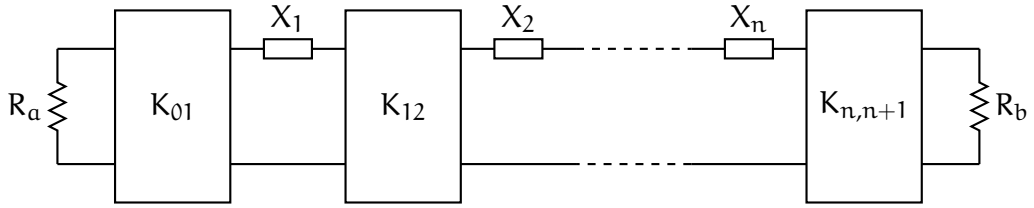

Figure 2.11: Band-pass filter with distributed resonators

The circuit of Fig. 2.9 is still interesting because the same type of resonances, however it is possible to describe it with distributed resonators in place of the lumped elements. Fig. 2.11 is the same filter with the resonators identified by their frequency responses $X_1(\omega), X_2(\omega), \cdots, X_n(\omega)$. The slope of the generic lumped elements k are calculated through the eq.s (2.29) and (2.30) and then applying the eq.s (2.13) relating them with the g constants:

$$\chi_k = \omega_0 L = \frac{1}{\omega_0 C} = \frac{\Omega_c g_k}{w} \tag{2.31a}$$

$$b_k = \omega_0 C = \frac{1}{\omega_0 L} = \frac{\Omega_c g_k}{w} \tag{2.31b}$$

The eq.s (2.31) are substituted in eq.s (2.27) in order to obtain the final expressions of the impedance inverters of a BPF:

$$K_{0,1} = \sqrt{\frac{R_a \chi_1 w}{g_0 g_1 \Omega_c}} \tag{2.32a}$$

$$K_{k,k+1} = \frac{w}{\Omega_c} \sqrt{\frac{\chi_k \chi_{k+1}}{g_k g_{k+1}}} \tag{2.32b}$$

$$K_{n,n+1} = \sqrt{\frac{R_b \chi_n w}{g_n g_{n+1} \Omega_c}} \tag{2.32c}$$

2.3.2 Coupling matrix of 2-port circuits

The distributed circuit of Fig. 2.11 can be eventually described in terms of its coupling matrix [32]. This is a convenient way to characterise a microwave device as many useful operations can be performed directly onto the coupling matrix such as inver-

sions or similarities. The synthesis can be carried out directly on the coupling matrix with normal algebraic operations and then mapped directly in the final microwave circuit. The procedure described above for in-line filters is rigorous and general for different types of characteristic prototypes. However, the physical dimensions, like the length of resonators coupling's aperture are obtained from the K inverters of eq.s (2.32) through approximated formulas that are specific for the particular technology used. These can be rectangular waveguide cavities, microstrip resonators, comb-line etc... They have a dedicated set of equations relating the inversion parameters to the physical dimensions of the cavities. Naturally, an overall optimisation of the final filter is often required to meet the specifications (bandwidth, RL, Insertion Loss (IL) and out-band rejection). There are two way to describe a 2-port circuit based on coupled resonators: one is to use the $n \times n$ coupling matrix [33], or the $n+2$ coupling matrix as shown in [34]. In this section are only summarised some aspects of coupling matrices for 2-port resonant circuits because a more general solution is deeply described in appendix B on page 241.

Fig. 2.12a shows a 2-port microwave circuit with n resonators, $n+1$ ideal inverters and the couplings between pairs of resonators. This is a LPP and the shunt resonators are represented with a unitary capacitor with a Frequency Invariant Reactance (FIR) in order to include non symmetric responses [34]. The rectangular blocks are admittance inverters between pairs of adjacent resonators, while the lines represent the eventual couplings between pairs of non adjacent resonators. Note that there is a close relation between an immittance inverter and its coupling coefficient. The coupling coefficient can be also expressed for the internal impedance (or admittance) inverters of prototype of Fig. 2.11 as [20]:

$$k_{j,j+1} = \frac{K_{j,j+1}}{\sqrt{\chi_j \chi_{j+1}}} = \frac{w}{\Omega_c \sqrt{g_j g_{j+1}}}, \qquad j = 1, \cdots, n-1 \tag{2.33}$$

The values $k_{j,j+1}$ refers also to the inner elements of matrix of Fig. 2.12b. In the distributed model of Fig. 2.11 it is also convenient to express the couplings between

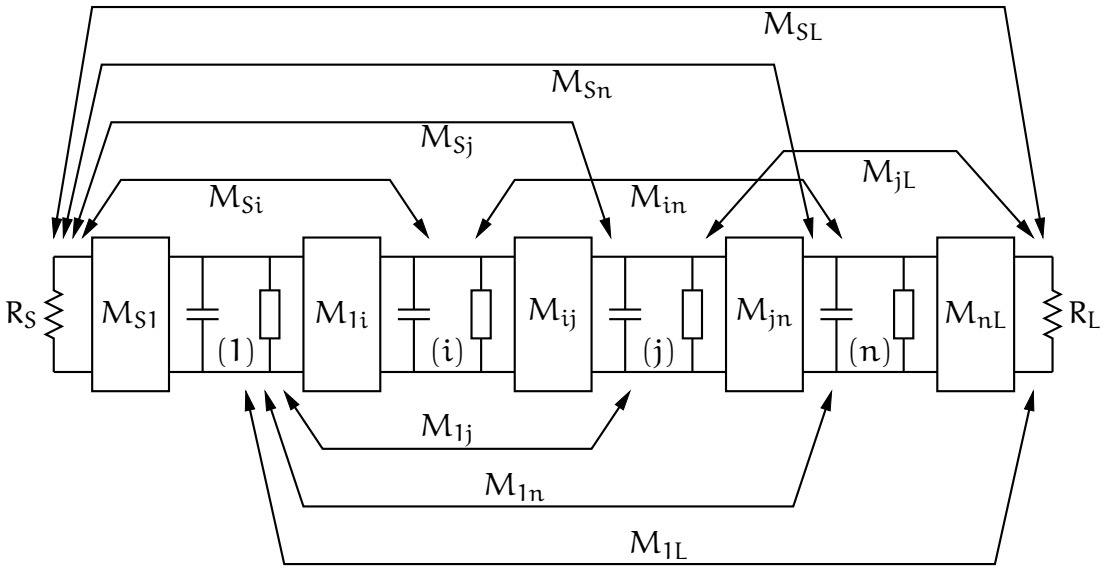

(a) Mutually coupled 2-port circuit

	S	1	i	j	⋯	n	L
S	$M_{S,S}$	$M_{S,1}$	$M_{S,i}$	$M_{S,j}$	⋯	$M_{S,n}$	$M_{S,L}$
1	$M_{1,S}$	$M_{1,1}$	$M_{1,i}$	$M_{1,j}$	⋯	$M_{1,n}$	$M_{1,L}$
i	$M_{i,S}$	$M_{i,1}$	$M_{i,i}$	$M_{i,j}$	⋯	$M_{i,n}$	$M_{i,L}$
j	$M_{j,S}$	$M_{j,1}$	$M_{j,i}$	$M_{j,j}$	⋯	$M_{j,n}$	$M_{j,L}$
⋮	⋮	⋮	⋮	⋮	⋱	⋮	⋮
n	$M_{n,S}$	$M_{n,1}$	$M_{n,i}$	$M_{n,j}$	⋯	$M_{n,n}$	$M_{n,L}$
L	$M_{L,S}$	$M_{L,1}$	$M_{L,i}$	$M_{L,j}$	⋯	$M_{L,n}$	$M_{L,L}$

(b) Coupling matrix $n+2$

Figure 2.12: Two ports inter-coupled resonant circuit

the external ports (in the case of the figure just the first and the last resonator) in terms of external quality factors (input *a* and output *b*):

$$Q_{e,a} = \frac{\chi_1}{K_{01}^2/R_a} = \frac{\Omega_c g_0 g_1}{w} \tag{2.34a}$$

$$Q_{e,b} = \frac{\chi_n}{K_{n,n+1}^2/R_b} = \frac{\Omega_c g_n g_{n+1}}{w} \tag{2.34b}$$

The relations (2.33) and (2.34) do not include any slope parameter χ_j which is the information of the particular type of resonator used. This is an important point as it is possible to separate the synthesis of the response of the filter from the particular technology used to implement it. Moreover, with the introduction of the coupling matrix it is possible to make the synthesis of a general microwave circuit where there exist couplings between any pair of resonators. With reference of Fig. 2.12a, the rectangular boxes represents the couplings between adjacent resonators, while the arrowed lines the generic couplings $M_{p,q}$ between the pairs of resonators p and q. For the internal resonators is necessary to build an $n \times n$ coupling matrix where the generic element on row p and column q represents the coupling $M_{p,q}$ of Fig. 2.12a. However, in order to have a complete characterisation of a 2-port resonant circuit, the coupling matrix should include also the information related to the couplings between internal resonators and external ports. In the main-line circuit of Fig. 2.11 only the first and last resonators are coupled with the external ports via the $Q_{e,a}$ and $Q_{e,b}$. In the general network of Fig. 2.12a are also included the couplings of source and loads with the internal resonators and between input-output. Thus a new coupling matrix having $n+2$ columns and rows can accommodate also this information as shown in Fig. 2.12b. Naturally, these additional couplings are always represented by inverters, but it is possible to create a new synthesis methodology for more complex transfer functions with respect to the one used for main-line filters. These techniques are based on the definition of characteristic polynomials that define the frequency response, and the calculation of the coupling coefficients in order to get the same

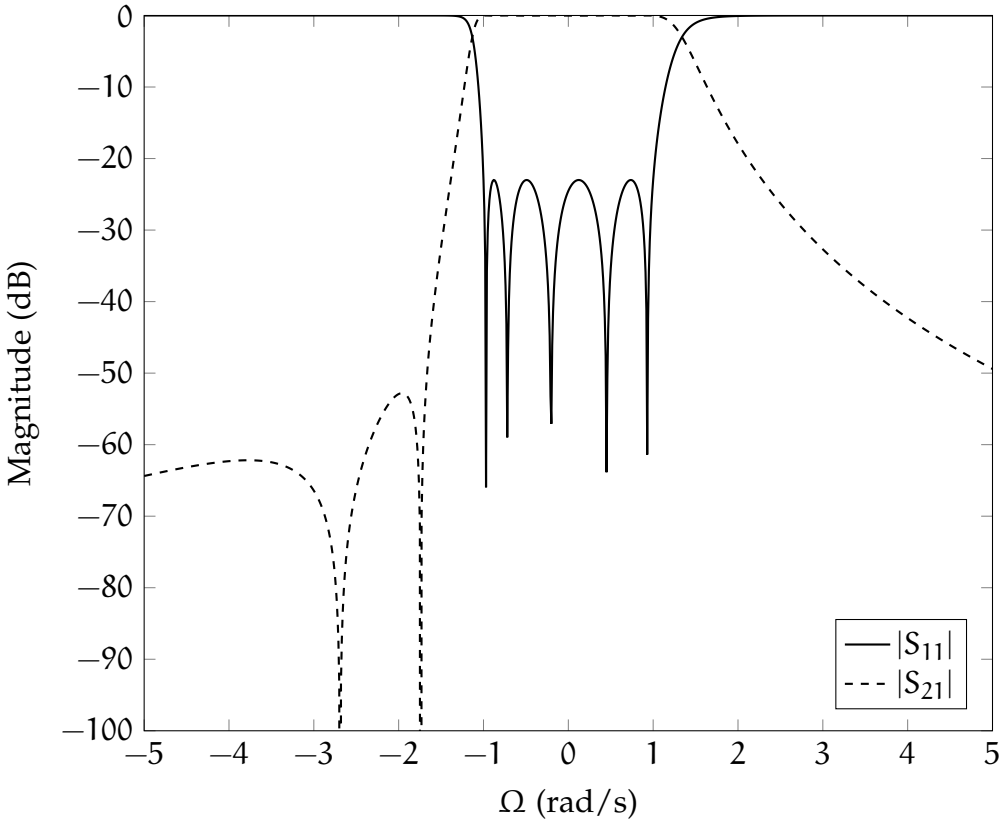

Figure 2.13: Example of generalised Tchebycheff filter. Order of the filter is $n = 5$, RL is 23 dB and 2 transmission zeros at $-j2.69$ and $-j1.74$.

response with an equivalent microwave circuit. The advantage of operating on the coupling coefficients is that the synthesis is operated mathematically on a matrix instead of on circuital components, hence keeping it independent from the technology used [35, 36]. This becomes more important in new communication systems where demands are for more stringent requirements in terms of sharper selectivity and reduced size. A convenient way is to introduce one or more TZ in order to increase the selectivity without altering the number of resonators. This is possible through the procedure introduced in the previous section at the price of a more complex model to manage because of the need of additional couplings (also known as cross-couplings) to be introduced in the prototype filter [36–38]. An example of transfer function of order 5 with a pair TZs [38] is shown in Fig. 2.13. This response is also called *generalised Tchebycheff* response.

The synthesis of coupling matrix for singly and double terminated networks based on all identical (synchronously tuned) cavities was first introduced in [39]. An iterative synthesis procedure of the polynomials and coupling matrix of generalised Tchebycheff filters has been presented in [40]. A more general synthesis technique was developed to create an $n+2$ coupling matrix with significant advantages with respect the previous matrices (typically $n \times n$) as it is able to [36, 41]:

- include multiple couplings between any internal resonator and input/output ports. Previously the input port was coupled directly to the first resonator while the output with the last one;
- implement a *fully canonical prototype* where a filter has n-th order characteristic and n TZs;
- provide more flexibility in complex matrix rotations where some couplings can be moved temporarily to the external rows/columns to operate more conveniently on the other internal elements of the matrix.

The coefficients on the main diagonal are indicating the resonators self-couplings, or their detuning. They usually affect the symmetry of the filtering response and they are modelled in the normalised LPP through the use of FIR added to the resonators [34].

The synthesis of the $n+2$ coupling matrix starts from the definition of the scattering parameters expressed as rational form of numerators and common denominator:

$$S_{11}(s) = \frac{F(s)}{\epsilon_R E(s)} \tag{2.35}$$

$$S_{21}(s) = \frac{P(s)}{\epsilon E(s)} \tag{2.36}$$

Table 2.1: Coefficients of polynomias of the generalised Tchebycheff filter of Fig. 2.13.

Degree of s	E(s)	F(s)	P(s)
5	1	1	
4	$2.3300 + j0.5088$	$+j0.5088$	
3	$3.8693 + j1.2957$	$+1.1548$	
2	$3.7665 + j2.1388$	$+j0.5011$	1
1	$2.1924 + j1.9879$	$+0.2413$	$+j4.4300$
0	$0.4849 + j0.8819$	$+j0.0597$	-4.6806

where ϵ is the Tchebycheff constant ripple factor providing the prescribed RL in dB is defined as:

$$\epsilon = \frac{1}{\sqrt{10^{RL/10} - 1}} \cdot \left.\frac{P(s)}{F(s)}\right|_{s=\pm j} \tag{2.37}$$

All the polynomials are expressed with respect to the complex low-pass variable:

$$s = \sigma + j\Omega \tag{2.38}$$

that in a lossless condition is simplified as $\sigma = 0$. Polynomials $E(s)$ and $F(s)$ are of degree n while $P(s)$ contains the finite-position zeros of the transfer function. Naturally the number of TZs n_z must not exceed the order of degree of polynomial $E(s)$ for a convergent characteristic. In the case of fully canonical network $n_z = n$, than the denominator of S_{11} is to be scaled:

$$\epsilon_R = \begin{cases} \dfrac{\epsilon}{\sqrt{\epsilon^2 - 1}} & \text{for } n_z = n \\ 1 & \text{for } n_z < n \end{cases} \tag{2.39}$$

For example, the response of Fig. 2.13 is obtained through the procedure of [40] that gives the set of polynomials listed in Tab. 2.1 with ripple coefficients $\epsilon = 4.6592$ and $\epsilon_r = 1$. For any 2-port lossless circuit, the unitary condition on power balance must

be verified:

$$|S_{11}(s)|^2 + |S_{21}(s)|^2 = 1 \tag{2.40}$$

This simplifies the space of physical solutions for the polynomials as they are directly related to each other. Depending on the specification, more advanced manipulations of the polynomials may be required for example to minimise the Group Delay (GD) leading to numerical optimisations of the characteristic polynomials both for their phase and amplitude [42].

Once the polynomials have been calculated to meet the specifications, they are transformed into their equivalent admittance matrix form. This transformation is found to be convenient in terms of elements calculation. Direct formulas are used to relate polynomials in admittance form to the equivalent *transversal matrix* of the circuit. A transversal network is one formed only of couplings between ports and between resonators and ports. No coupling between resonant cavities are in place in this initial configuration. This is a mathematical transformation used to easily relate the admittance polynomials to the elements of the matrix. Later, several matrix rotations are applied to the transversal matrix in order to get the coefficients for the final network configuration, or topology, of the circuit. Moreover, modern Computer Aided Design (CAD) techniques can be used on the coupling matrix to improve the frequency response of the device [33]. Any operation is performed mathematically on the elements of the matrix, hence it is possible to define a *goal transfer function* that is the target response to reach and the CAD design performs changes to the coupling coefficients in order to minimise a *cost function* to get the prescribe response. However, the large space of solution available and the complexity of global optimisation cannot totally replace the more analytical approach presented here.

A more detailed explanation of this procedure, with step-by-step examples included, is also presented in the appendix B.

2.3.3 Multi-port circuits

The $n+2$ coupling matrix is a powerful tool to describe any 2-port circuit based on resonators and it is particularly useful in the synthesis of advanced filters because of its great flexibility. However, a more general approach should be adopted for an arbitrary number of ports and resonators. Thus, the following coupling matrix extends the $n+2$ one: it is defined by blocks and can describe any circuit based on n resonators and p ports [43–48]:

$$\mathbf{M} = \begin{bmatrix} \mathbf{M_p} & \mathbf{M_{pn}} \\ \mathbf{M_{np}} & \mathbf{M_n} \end{bmatrix} \tag{2.41}$$

with $\mathbf{M}$ being a square matrix of dimension $p+n$. An example of matrix defined by blocks of a circuit of $p = 4$ ports and $n = 6$ resonators is shown in Fig. 2.14. The

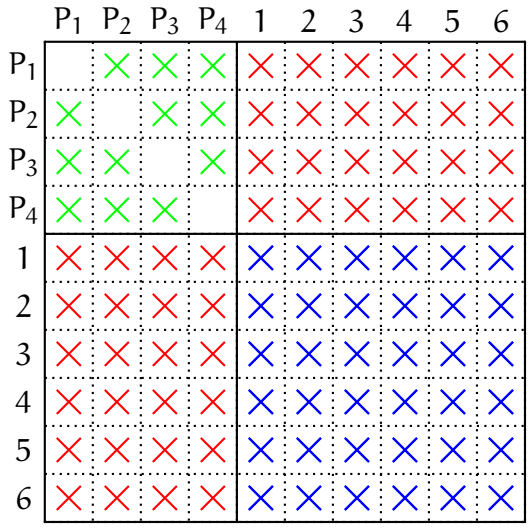

Figure 2.14: Coupling matrix defined by blocks

sub-matrices of the eq. (2.41) are:

$\mathbf{M_p} \in \mathbb{R}^{p\times p}$ matrix of the couplings between pairs of external ports. These are shown with the green colour of Fig. 2.14. Ports are here indicated with labels $P_1, P_2, \cdots, P_p$;

$\mathbf{M_{pn}} \in \mathbb{R}^{p \times n}$ are the coefficients between an external port and an internal cavity. These are indicated with the red colour on top right of Fig. 2.14. The $\mathbf{M_{np}}$ is just the transpose matrix of $\mathbf{M_{pn}}$ and its coefficients are marked with the red crosses on bottom left of the figure. The resonators are referred with numbers in the rows and columns of the matrix.

$\mathbf{M_n} \in \mathbb{R}^{n \times n}$ is the matrix of the coupling coefficients between pairs of internal resonators and are indicated in blue in Fig. 2.14.

In the notation of coupling matrix of Fig. 2.14, a cross symbolises a coefficient other than zero, hence the presence of a coupling. This picture is just an example to easily identify the position of the sub-matrices into the $\mathbf{M}$ block matrix and all the couplings are here marked. The only zero elements are the ones on the main diagonal of matrix of external ports $\mathbf{M_p}$ as it is not physically possible to have self-couplings between the external ports. The scattering parameters are directly calculated from the eq. (2.41) with the procedure described in appendix B. An alternative is the $n \times n$ matrix which is also capable to describe the electrical properties of a circuit with multiple ports [33]. It is possible to show that the $n \times n$ does not allow the matrix similarities as it does not include the information of couplings between internal cavities and external ports.

2.4 LIMITATIONS OF GENERAL SYNTHESIS TECHNIQUES

A general synthesis technique for any multi-port circuit can be performed independently for the sub-matrices $\mathbf{M_p}$, $\mathbf{M_{pn}}$ and $\mathbf{M_n}$ with an extension of the procedure shown in [40] and explained in detail in appendix B. Without discussing the methodology in all its aspects, here it is possible to summarise some important points:

1. The scattering polynomials are defined in order to set the response of the circuit as function of the complex low-pass variable s. They have the highest power's coefficient normalised to 1 and are all expressed in rational form of numerator and common denominator.

2. The scattering parameters are transformed into the equivalent admittance matrix. In order to easily identify the poles of the function also the admittance polynomials are expressed as rational form of numerators $n_{ij}(s)$ with a common denominator $y_d(s)$. In some cases there exist closed formulas to get the coefficients of the polynomials of the admittance matrix starting from the scattering polynomials [49]. Otherwise the curves of the $\mathbf{Y}$ with respect the frequency s can be calculated with the well known formula

$$\mathbf{Y} = (\mathbf{I} - \mathbf{S})(\mathbf{I} + \mathbf{S})^{-1} \tag{2.42}$$

where $\mathbf{S}$ is the scattering matrix and $\mathbf{I}$ the identity. Later the numerators and common denominators are obtained from eq. (2.42) with numerical techniques [50–53].

3. Rational parameters are expressed in terms of *partial fractional expansion*:

$$[\mathbf{Y}]_{ij}(s) = [\mathbf{Y}^{(\infty)}]_{ij} + \sum_{k=1}^{n} \frac{r_{ij,k}}{s - j\lambda_k} \tag{2.43}$$

where $[\mathbf{Y}^{(\infty)}]_{ij}$ is a constant term and $r_{ij,k}$ is the residue of element $[\mathbf{Y}]_{ij}(s)$ associated to pole λ_k.

4. From the eq. (2.43) the elements of the equivalent transversal network are calculated with direct formulas [44]. An example of transversal matrix is shown in Fig. 2.15 for a circuit with $p = 3$ ports and $n = 4$ resonators. The layout of the coupling matrix with all possible couplings is shown in Fig. 2.15a while the correspondent circuit in Fig. 2.15b. All possible couplings are included in

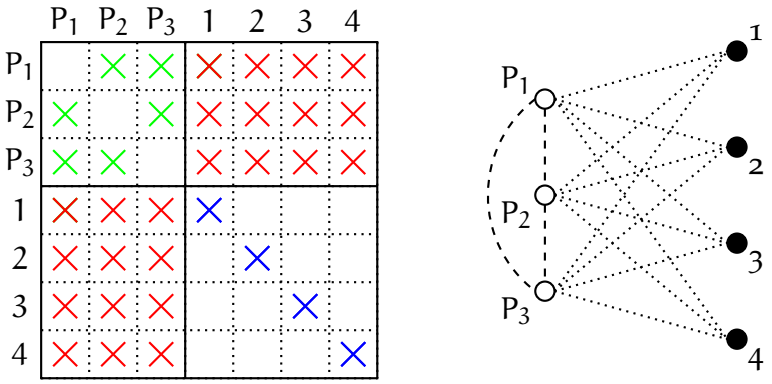

(a) Coupling matrix layout **(b)** Network topology

Figure 2.15: Example of transversal network of a 3-port circuit with 4 resonators

this transversal form between pairs of ports (white circles) and to resonators (black circles). Here the matrix of the internal couplings $\mathbf{M_n}$ is diagonal, meaning resonators are only coupled with themselves or, eventually, with external ports. This representation includes the magnitude information of the response of eq. (2.43) through the following set of equations (see appendix B or [44]):

$$\mathbf{M_n} = -\operatorname{diag}(\lambda_k), \qquad k = 1, \cdots, n \tag{2.44}$$

$$\mathbf{M_{pn}} = \frac{r_{ij,k}}{\sqrt{r_{ij,k}}}, \qquad i, j = 1, \cdots, p \tag{2.45}$$

$$\mathbf{M_p} = -j\mathbf{Y}^{(\infty)} \tag{2.46}$$

5. A set of matrix rotations are applied to the transversal matrix in order to get the coupling values of the final topology of the circuit [54]. With this procedure the unwanted matrix elements are annihilated in favour to the ones of the desired network. At each rotation the eigenvalues of the matrix are kept unchanged, hence not altering the response of the circuit.

The concept of a multi-port network made by p ports and by n resonators arbitrarily coupled puts a major challenge by the point of view of the synthesis technique. This is a different approach compared with the use of several 2-port filters connected together by means of junctions or manifolds, as for example many diplexers and multiplexers

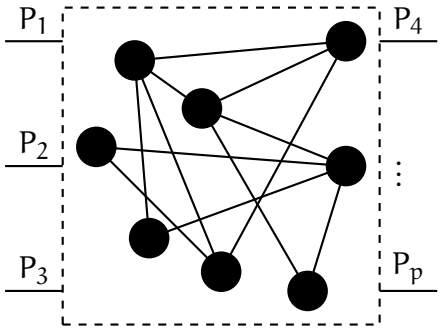

Figure 2.16: General multi-port all resonators network

[55–57]. For this case the synthesis was based on the already known techniques for filters without considering the structure in a whole. In recent years growing interest is observed in all-resonator networks with complex filtering response, new topologies have been investigated and the synthesis of the coupling matrix obtained through optimisation techniques [58–60]. The direct optimisation of the coupling matrix might hide some important details of the response to the designer as well as the general understanding of the network. Moreover, the cost function needs to be adapted to each application in order to adapt to the type of the circuit as well as a mix of different algorithms (ie. global genetic, gradient, etc...) should be applied in order to reach the final solution.

Despite the well known advantages of analytical techniques, for multi-port networks, there are some limitations of the general procedure explained above. The preliminary step is the definition of the polynomials of the scattering low-pass response. These characteristics, for lossless networks, must comply with the law of power balance generally expressed as:

$$\mathbf{S} \cdot \mathbf{S}^* = \mathbf{I} \tag{2.47}$$

where $\mathbf{S}^*$ is the complex conjugate of $\mathbf{S}$. This for the simple case of two port filters reduces to eq. (2.40). The response of the very general schematic of Fig. 2.16 of a multi-port network circuit formed by p ports and resonators arbitrarily coupled, can be described by the block matrix of eq. (2.41) with scattering polynomials satisfying

the eq. (2.47). The synthesis of such networks is well known when $p = 2$ (ie. filters), it is very complex for some circuits with $p = 3$ and does not exist for $p > 3$ as described in [61]. When increasing the number of ports, the condition of eq. (2.47) is satisfied through the following system of equations:

$$\begin{cases} \sum_{k=1}^{p} |S_{1k}|^2 = 1 \\ \sum_{k=1}^{p} |S_{2k}|^2 = 1 \\ \vdots \\ \sum_{k=1}^{p} |S_{pk}|^2 = 1 \end{cases} \tag{2.48}$$

While the condition on the two ports was directly relating the S_{21} to the S_{11}, with several ports additional variable terms are added, hence increasing the space of possible solutions. In such scenario having too many degrees of freedom on the polynomials might lead to an undefined synthesis a priori of the scattering responses. In [61] a solution is proposed by using several 2-port circuits, each providing a set of matching and rejecting frequencies. All these sub-circuit are matched through an electrical junction with the problem reducing to a match of several arbitrary loads also known as extended Nevanlinna-Pick interpolation problem [62].

The work presented in [61] is not totally concluded and mainly covers the problems associated to the synthesis of triplexers or multiplexers. However, the difficulties and limitations of the scattering polynomials synthesis are outlined clearly. Also, the maximum number of couplings each resonator can accommodate is limited by the practical realisation. If the final topology is not known a priori, the step of matrix rotations could bring to a non physically realisable structure. This is generally true with the increase of number of ports [61].

Another limitation is that the transfer function must have single poles [49]. This happens when the roots of the polynomial $y_d(s)$ are all distinct. If this is not the case, it means that some of the roots of $y_d(s)$ are coincident and thus that there are

repeated values on the matrix $\mathbf{M_n}$ of the transversal prototype. One reason to have multiple poles is when the same transfer function (in module) is associated with more outputs simultaneously. Also, in this case also some rows/columns of matrix $\mathbf{M_{pn}}$ are the same, so that the whole matrix $\mathbf{M}$ is singular. If singular, the repeated rows and columns are removed with the result of producing the same frequency response in magnitude with a reduced number of ports and resonators. If this occurs, an alternative synthesis technique needs to be investigated.

2.5 RESONATOR BASED BUTLER MATRIX

The behaviour of the MPA is broadband with normally no particular interest paid for the out-band response. This is not a selective sub-system and spurious frequencies are usually generated by the amplifiers. The Butler matrices proposed in the literature for MPAs are mainly implemented with several hybrid couplers based on transmission lines, producing a broadband response [63–70]. However, an additional stage of BPFs could be necessary and cascaded to the MPA if the near-band is to be cleared from interferences. A possible example is when the satellite is operating the Receiver (RX) and Transmitter (TX) in contiguous bands and the spurious frequencies could enter at the receiving stage of the system. Also, there could be a reserved band contiguous to the operational bandwidth to be protected and requiring additional filtering before the transmitting antenna. Fig. 2.17a is a schematic of the MPA with a bank of BPFs cascaded after the ONET. A practical example of a satellite where this architecture with filtering has been adopted is shown in [71], where 8 BPFs have been cascaded after an 8×8 Butler matrix. Clearly, the requirement of additional selectivity of the near-band spectrum at the output of the payload is met through the cascade of additional interfaces, increasing the size and mass of the equipment as well as the

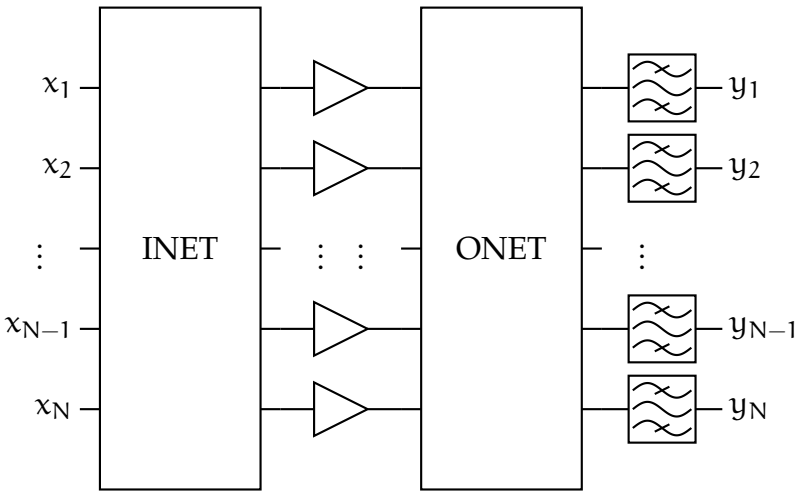

(a) MPA with bank of band-pass filters

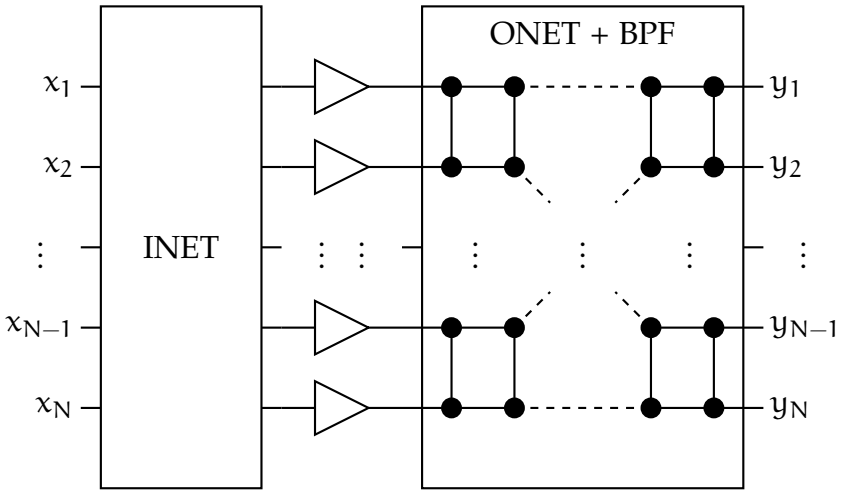

(b) MPA with filtering functions incorporated in the ONET

Figure 2.17: Proposed solution of MPA with filter functions included in the ONET.

risk of Passive Inter-Modulation (PIM) due to the additional connectors and flanges (see section 2.7 on page 57 for more details on high power handling).

The solution proposed in this work is to incorporate the filtering functions of the bank of identical BPFs and the ONET Butler matrix into a single device based on coupled resonators. A qualitative representation of the proposed architecture is shown in Fig. 2.17b: the INET and the amplifiers are not altered, while the pair of ONET and bank of BPFs is replaced by a new circuit made only by mutually coupled resonators. With the inclusion of the filters is also introduced an operational bandwidth inside which the system of Fig. 2.17b should work with the same properties of the traditional MPA. The advantages of a solution proposed reside in the lower number of components required to obtained the same response and in reduced size and mass. The last characteristics are particularly critical in a satellite where the on-board equipment can be limited by the available space. The main properties of the new Butler matrix that includes filter functions are:

- multi-port, multi-resonator circuit;
- provide equal output power splitting of the input signals;
- all the signals have same central frequency and bandwidth;
- same filtering response for all transmissions parameters;
- perfect isolations between pairs of input (or output) ports;
- output phase distribution to guarantee signals combination.

The new Butler matrix including filtering can be conveniently represented by the coupling matrix defined by blocks of Fig. 2.14. However, the previous points show how the traditional synthesis methods are affected by the limitations presented in section 2.4 as the high number of ports (theoretically 2N) put a major challenge on the definition of the scattering polynomials, as well as the same filtering characteristic for each transmission parameters leads to polynomials with non single poles.

2.6 PHYSICAL REALISATION OF COUPLED RESONATOR NETWORKS

The coupling matrix is an efficient an convenient tool as all the main synthesis can be carried out mathematically, with eventually one or more optimisations of the coefficients, before to obtain the physical dimensions of the components by use of Electromagnetic (EM) software. The computational power required to optimise a physical structure is much higher both for time consumption and for resources such as the memory. Also, for complex circuits a general optimisation might not even possible. When possible it is highly recommended to avoid any optimisation that involves any operation on the physical (or 3D) model. Thus, in the following of this work the synthesis will be carried out with the definition of the set of polynomials to produce the transfer function and later with the definition of the elements of the coupling matrix. The final stage will obtain the dimensions of the resonators and couplings in order to produce the same electrical properties of the ones of represented by the coupling matrix. The complexity of the EM model is reduced by iteratively performing optimisations of every coupling/resonator of the device, and only at the end a final optimisation on the entire circuit to refine the response. It can be seen that the information included in the coupling matrix can be translated in initial physical dimensions that produce a frequency response of the final circuit quite close to the specifications, reducing the time of the general optimisation.

2.6.1 Lumped element synthesis

In order to establish a direct relation between the physical elements of the circuit and the coupling matrix, first the synthesis is carried out on lumped elements and, later, the equation will be applied to the 3D structure. The lumped elements rep-

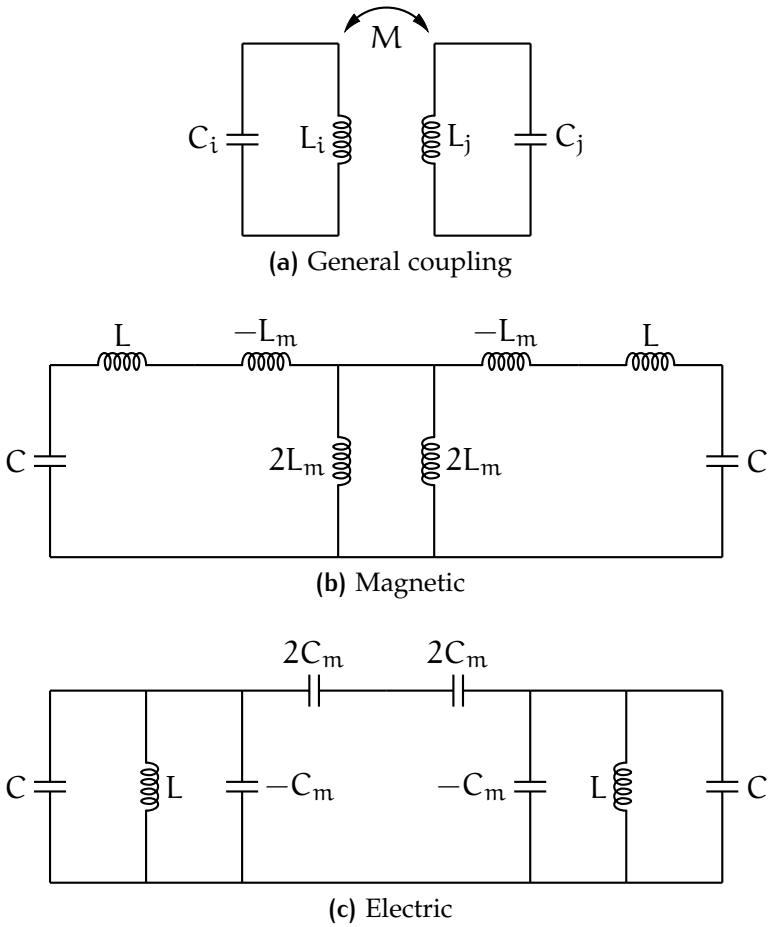

(a) General coupling

(b) Magnetic

(c) Electric

Figure 2.18: Electric and magnetic couplings

resentation of a generic coupling between 2 lossless resonators is shown in Fig. 2.18a. Note that in the figure there are no assumption regardless the central frequency of the 2 resonators except for the fact the elements must satisfy the resonance condition of eq. (2.18). With M is represented the coupling coefficient between the generic lumped elements resonators i and j. Instead of studying the coupling between the two resonators, symmetries are introduced in order to reduce the problem to one single resonator through the even/odd mode method [34]. Basically, with the even mode a magnetic wall is placed in the middle of the circuit while with the odd mode is used an electric wall [72]. The effect of putting a magnetic wall is to create an infinite impedance, hence an open circuit should be included between the two halves of the circuit. On the contrary, with the odd mode, the electric wall is responsible for closing the two halves with shorted circuit.

There are three type of couplings possible: the magnetic, electric and mixed coupling [33]. Starting with the magnetic one a series configuration is considered in Fig. 2.18b. The two resonators i and j are here considered equal, thus $L_i = L_j$ and $C_i = C_j$. The magnetic coupling can be represented in terms of an impedance inverter due to the series representation, and consequently with the T network of inductances of Fig. 2.8a. The shunt inductance is the element at the centre of symmetry and it will be divided in two parts. As it is a shunt impedance, the two halves of the original mutual inductance L_m have double value of shown in Fig. 2.18b. At this moment a magnetic wall is introduced and the circuit reduced to the series of a capacitor and three inductances L, $-L_m$ and $2L_m$. With an electric wall, for the odd mode, a short circuit is introduced thus eliminating the inductor of inductance $2L_m$. The resonance frequencies are calculated separated for the even and odd mode:

$$f_e = \frac{1}{2\pi\sqrt{(L + L_m)C}} \tag{2.49a}$$

$$f_o = \frac{1}{2\pi\sqrt{(L - L_m)C}} \tag{2.49b}$$

The magnetic coupling coefficient between 2 synchronous resonators is defined as:

$$K_M = \frac{L_m}{L} \tag{2.50}$$

The coupling coefficient is obtained solving the eq.s 2.49 with respect variables L and L_m and then substituted into eq. (2.50). Note that the even and odd resonant frequencies are determined from elements of the band-pass domain, hence a de-normalisation is required in order to get the value of coupling coefficient in the low-pass domain:

$$M = \frac{1}{w}\frac{f_o^2 - f_e^2}{f_o^2 + f_e^2} \tag{2.51}$$

The electric coupling is calculated in a similar fashion. In this case it is more convenient to express the circuit with a parallel notation with the two resonators coupled

with an admittance inverter as the π of capacitors of Fig. 2.8b. At the centre of the circuit is a series capacitor, hence divided into two elements of capacitance $2C_m$ as shown in Fig. 2.18c. Again, the resonance frequency of the even and odd modes are calculated. When a magnetic wall is placed at the symmetry plane an open circuit is seen at each half. In this case the capacitor of value $2C_m$ is useless as no current is flowing on it and the equivalent admittance is given as the parallel of capacitor C, inductor L and capacitor $-C_m$. With the electric wall the element of capacitance of $2C_m$ is also parallel to the rest of the circuit. The two resonance frequencies are:

$$f_e = \frac{1}{2\pi\sqrt{(C - C_m)L}} \tag{2.52a}$$

$$f_o = \frac{1}{2\pi\sqrt{(C + C_m)L}} \tag{2.52b}$$

The coupling coefficient of the electric type is defined as:

$$K_e = \frac{C_m}{C} \tag{2.53}$$

Thus the normalised coupling element M is obtained solving the eq. (2.52) into eq. (2.53) and divided for the FBW:

$$M = \frac{1}{w}\frac{f_e^2 - f_o^2}{f_e^2 + f_o^2} \tag{2.54}$$

It is immediate to observe that eq.s (2.51) and (2.54) are identical except for a minus at the numerator. In general it is possible to conclude that when $f_o > f_e$ the coupling is magnetic while it is electric otherwise. The general expression independent from the type of coupling (magnetic, electric of mixed) and valid for synchronous or asynchronous couplings is the following [73]:

$$M = \frac{1}{2w}\left(\frac{f_2}{f_1} + \frac{f_1}{f_2}\right)\sqrt{\left(\frac{f_b^2 - f_a^2}{f_b^2 + f_a^2}\right)^2 - \left(\frac{f_2^2 - f_1^2}{f_2^2 + f_1^2}\right)^2} \tag{2.55}$$

where f_1 and f_2 are the frequencies of the two resonators while f_a and f_b are the resonances of the even/odd modes with $f_b > f_a$. The eq. (2.55) reduces to eq. (2.51) or (2.54) in case of synchronous resonators ($f_1 = f_2$).

2.6.2 Extraction of the coupling coefficient

The lumped elements model of a pair of mutually coupled resonators is useful to relate the coupling coefficient to its even and odd mode resonances. The design process consists of dimensioning the elements of the resonators in order to obtain the prescribed coupling coefficients. This can be done either analytically or by optimisation with the LC circuit perfectly matching the electrical response of the associated coupling matrix. However, the lumped elements model is not practical to manage for most cases of microwave applications. Hence an alternative solution is to use a full-wave simulator where the resonance frequencies are numerically calculated and the physical dimensions are optimised in order to produce the desired coupling. With the simulator a pair of coupled resonators are drawn in 3D and the resonances calculated through an *eigenmode* solver. Unfortunately, not all the EM simulators provide this feature so a method based on optimisation of the scattering parameters is to be preferred. For example, a commercial tool which provides the eigenmode solver is Computer Simulation Technology (CST) [74]. If this tool or solver license are not available, the f_e and f_o are calculated numerically through the S_{21}. In the following, the simulation are performed with Fest3D [75] or Mician [76] because of their faster solver, then with CST for results confirmation.

The process of extracting the coupling coefficient evaluating the scattering response is independent by the type of coupling (magnetic, electric or mixed) and by the type of resonator used. Basically, the structure of 2 symmetric resonators is constructed inside the *modeller* of the simulator, having a variable element of coupling between them and weak couplings with the external ports. A general schematic of the resonators

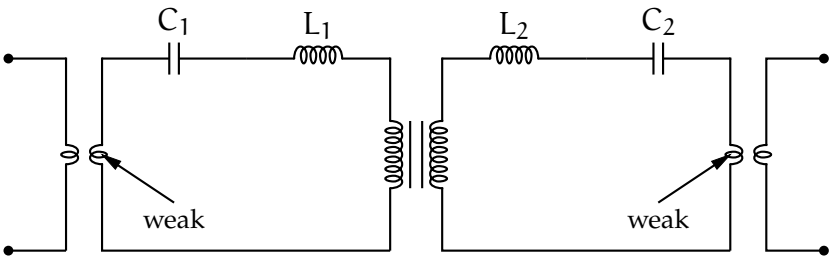

(a) Lumped elements model

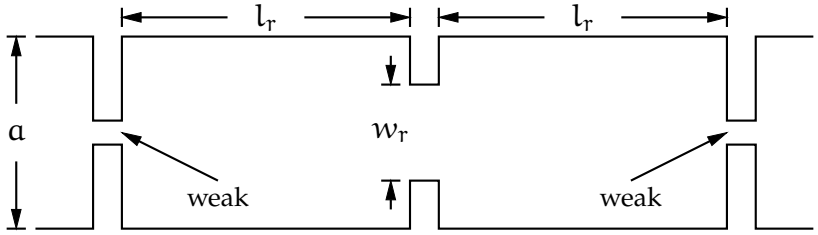

(b) Implementation in rectangular waveguide (top view)

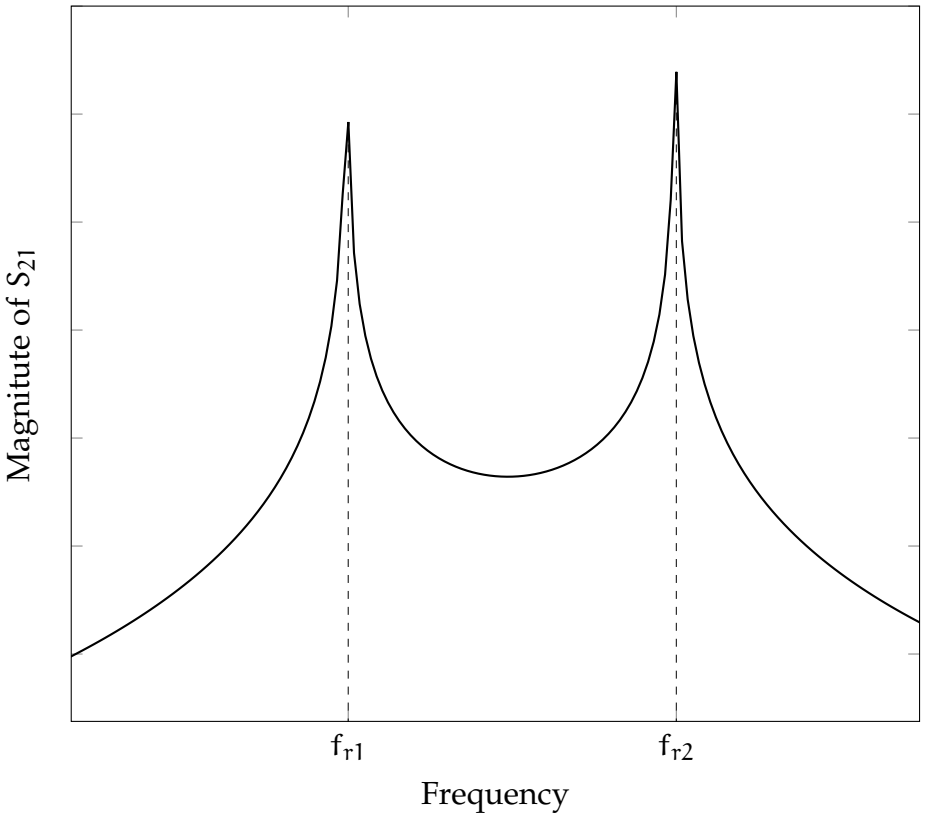

(c) Even and odd resonance frequencies

Figure 2.19: Extraction of internal coupling from physical structure

is shown in Fig. 2.19a: in this figure the couplings are represented with transformers and the resonators with the typical LC network. For the case of synchronously tuned resonators it derives that $L_1 = L_2$ and $C_1 = C_2$. The couplings with the external ports need to be weaker with respect the coupling between the 2 resonators in order to reduce the impact of the other interfaces on the resonances. An example of physical implementation of the circuit of Fig. 2.19a in rectangular waveguide with inductive irises and squared corners is shown in Fig. 2.19b. This is a top view of 2 coupled resonators having cross-section dimensions of a and b (not visible in the figure). The longitudinal length of resonators is indicated with l_r while the amplitude of the coupling iris dimension is w_r. The resonators in this case are synchronous so they have same length. The weak couplings are chosen to be less than 10% of the waveguide aperture a. For given dimensions of l_r and w_r the full-wave simulator is capable to calculate the scattering parameters of the structure of Fig. 2.19b. The result is shown for the S_{21} in Fig. 2.19c with the two resonance frequencies f_{r1} and f_{r2} (it must be $f_{r1} < f_{r2}$). The coupling coefficient and central frequency f_0 are [33, 34]:

$$M = \frac{1}{w}\frac{f_{r2}^2 - f_{r1}^2}{f_{r2}^2 + f_{r1}^2} \tag{2.56}$$

$$f_0 = \sqrt{f_{r1} \cdot f_{r2}} \tag{2.57}$$

It should be noted that, theoretically, a series half-wavelength resonator should be loaded with shorted circuits at both ends (the same as for a parallel one which requires open circuits as loads). Note that in transmission lines where the fundamental propagating modes are TE or TM, the expression of guided wavelength is:

$$\lambda_g = \frac{\lambda}{\sqrt{1 - \left(\frac{\lambda}{\lambda_c}\right)^2}} \tag{2.58}$$

where λ_c is the cut-off wavelength of the fundamental mode. Naturally both the apertures left and right of each resonator in Fig. 2.19b clearly show that it is physically very

difficult to create the theoretical required load. Also, the apertures are responsible of discontinuities that alter the resonance frequency. Thus, the length of the resonators l_r is to be adjusted in order to take into account this. The main contribution to this distortion is caused by the variable iris, becoming more relevant for higher values of w_r. Hence the calculation of the coupling coefficient is made by the following steps:

1. initially $l_r = \lambda_g/2$ using the eq. (2.58) and the w_r is arbitrarily,
2. calculation of f_{r1} and f_{r2} for a given dimension of w_r,
3. length l_r is adjusted in order to tune the resonator to central frequency f_0 with eq. (2.57) and
4. the coupling coefficient is obtained with eq. (2.56).

where the λ_g is the wavelength in the guide. This procedure is repeated for several values of w_r in order to create a set of curves relating the coupling coefficient to the dimension of coupling element (the inductive iris in this example).

From the computational point of view it is more efficient to get the dimensions of the single couplings separately rather than performing long optimisations of the entire structure. However, the method shown here is not exact because does not correct the dimensions of the resonators based on the loads that will substitute the weak couplings in the final circuit. Thus, at the end of this process a stage of optimisation is still required, but with the difference that in this case the response is expected to be closer to the final one, hence reducing the number of iterations to perform.

2.6.3 Extraction of the external quality factor

The external quality factor can be extracted from a physical structure (typically from a 3D full-wave simulator) in many different ways. Depending on the type of resonator and configuration one method might be easier than the others, so here will be shown

how to calculate the Q_e with a singly loaded resonator, with the group delay method and, finally, through a doubly loaded resonator.

Singly loaded resonator

The diagram of a resonator loaded on an external port is shown in Fig. 2.20. In

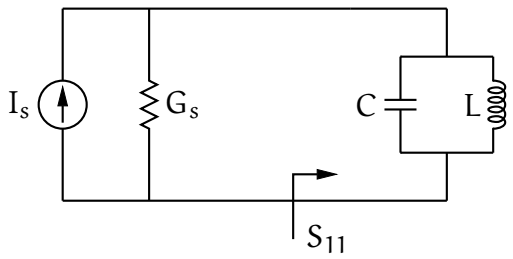

Figure 2.20: Singly loaded external resonator

a resonant circuit it is convenient to express the coupling between an external port and an internal resonator through the external quality factor Q_e. By definition, the external quality factor is the ratio between the energy stored in the resonator and the energy dissipated in the external loads as follows:

$$Q_e = \omega_0 \frac{C}{G_s} \tag{2.59}$$

This definition is consistent with the one of a resonator directly connected to the external port providing a source current I_s and a conductance of the generator of G_s as stated by the Norton theorem [30]. The reflection coefficient (S_{11}) seen after the generator towards the resonator is defined as:

$$S_{11} = \frac{G_s - Y_r}{G_s + Y_r} = \frac{1 - \frac{Y_r}{G_s}}{1 + \frac{Y_r}{G_s}} \tag{2.60}$$

where the admittance of a parallel resonator is given as:

$$Y_r = j\omega C + \frac{1}{j\omega L} = j\omega_0 C \left(\frac{\omega}{\omega_0} - \frac{\omega_0}{\omega} \right) \tag{2.61}$$

where in eq. (2.61) has been substituted the eq. (2.14). For a narrow variation of the frequency $\Delta\omega$ with respect the resonance ω_0 it is possible to introduce the following simplification [34]:

$$2\Delta\omega \approx \frac{\omega^2 - \omega_0^2}{\omega} \tag{2.62}$$

so as to reformulate the eq. (2.61) in a narrow interval around the central frequency:

$$Y_r = j\omega_0 C \frac{2\Delta\omega}{\omega_0} \tag{2.63}$$

Now the eq. (2.63) is substituted into the definition of S_{11} of eq. (2.60) with the inclusion of the external quality factor notation of eq. (2.59). Thus the formula of the S_{11} is re-written as function of the Q_e valid for a narrow frequency interval around the resonance:

$$S_{11} = \frac{1 - jQ_e(2\Delta\omega/\omega_0)}{1 + jQ_e(2\Delta\omega/\omega_0)} \tag{2.64}$$

It should be noted that at ω_0 the parallel resonator acts as an open circuit and consequently the $S_{11} = \pm 1$. Also, at the centre frequency the parallel resonator is exactly an open circuit and the phase is 0. Considering an interval $\Delta\omega_{\mp}$ around ω_0 where the phase is $\pm 90°$, it follows that $S_{11} = \pm j$, hence the eq. (2.64) can be rewritten as

$$2Q_e \frac{\Delta\omega_{\mp}}{\omega_0} = \mp 1 \tag{2.65}$$

The eq. (2.65) should be rewritten in function of term $\Delta\omega_{\mp}$ remembering that it defines the bandwidth in between S_{11} assumes a phase value of $\pm 90°$. Thus it is that:

$$\Delta\omega_{\pm 90°} = \Delta\omega_+ - \Delta\omega_- = \frac{\omega_0}{2Q_e} + \frac{\omega_0}{2Q_e} \tag{2.66}$$

Finally the value of the Q_e is given combining eq.s (2.66) and (2.65):

$$Q_e = \frac{\omega_0}{\Delta\omega_{\pm 90^\circ}} \tag{2.67}$$

where the term $\Delta\omega_{\pm 90^\circ}$ is the one calculated through the full wave simulation or measurements.

Method of the group delay

An alternative method for one resonator that is singly loaded to extract the Q_e is to exploit the group delay at the resonance. The equations describing the circuit of Fig. 2.20 are obviously the same, hence the relation of the S_{11} of eq. (2.64) can be rewritten in the form of magnitude and phase φ:

$$S_{11} = \left|\frac{1 - jQ_e(2\Delta\omega/\omega_0)}{1 + jQ_e(2\Delta\omega/\omega_0)}\right| \angle\varphi \tag{2.68}$$

where the phase is defined as [34]:

$$\varphi = -2\arctan\left(4Q_e\frac{\omega - \omega_0}{\omega_0}\right) \tag{2.69}$$

The group delay is defined as the derivative of the phase with respect to the frequency:

$$\tau(\omega) = -\frac{\partial\varphi}{\partial\omega} \tag{2.70}$$

The group delay of the $S_{11} = e^{-j2\varphi}$ evaluated at central frequency is calculating deriving the eq. (2.69):

$$\tau_{11}(\omega_0) = \frac{4Q_e}{\omega_0} \cdot \frac{1}{[1 + 2Q_e(\omega - \omega_0)/\omega_0]^2}\bigg|_{\omega=\omega_0} = \frac{4Q_e}{\omega_0} \tag{2.71}$$

where in eq. (2.71) has been used the derivative of arctan defined as:

$$\frac{\partial}{\partial\omega}\arctan(\omega) = \frac{1}{1+\omega^2}$$

The relation of the external quality factor is finally obtained from eq. (2.71) as:

$$Q_e = \omega_0 \frac{\tau_{11}(\omega_0)}{4} \tag{2.72}$$

The parameter to be measured from the simulator is the group delay calculated at central frequency $\tau_{11}(\omega_0)$ of the first resonator .

Doubly loaded resonator

A derivation of the previous two methods to extract the external quality factor, can be found with a resonator that is loaded on an input and output port. The following method is particularly useful with technologies like waveguides as it is easy to model and very fast to simulate. The equivalent circuit is shown in Fig. 2.21a. The source conductance G_s and the load conductance G are supposed to be identical in order to confer symmetry to the circuit with respect to plane T. The LC circuit of the resonator is hence split in two halves with the values indicated in the figure. At this point the S_{11} observed after the source toward the resonator is calculated through the even/odd mode. For the even mode a magnetic wall is obtain inserting an open circuit at the symmetry plane. In this case the second part of the circuit of Fig. 2.21a is removed hence degenerating to the one of Fig. 2.20. The even admittance of the resonator Y_{re} and the S_{11e} result to be:

$$Y_{re} = j\omega_0 C \frac{\Delta\omega}{\omega_0} \tag{2.73a}$$

$$S_{11e} = \frac{1 - jQ_e(\Delta\omega/\omega_0)}{1 + jQ_e(\Delta\omega/\omega_0)} \tag{2.73b}$$

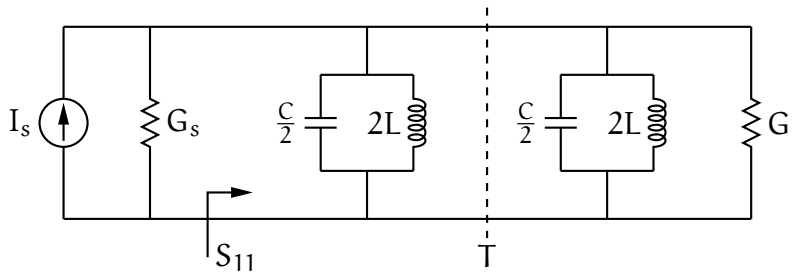

(a) Doubly loaded, symmetric resonator

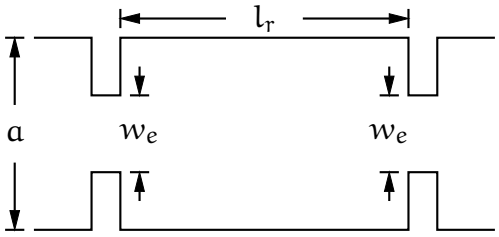

(b) Physical implementation (top view)

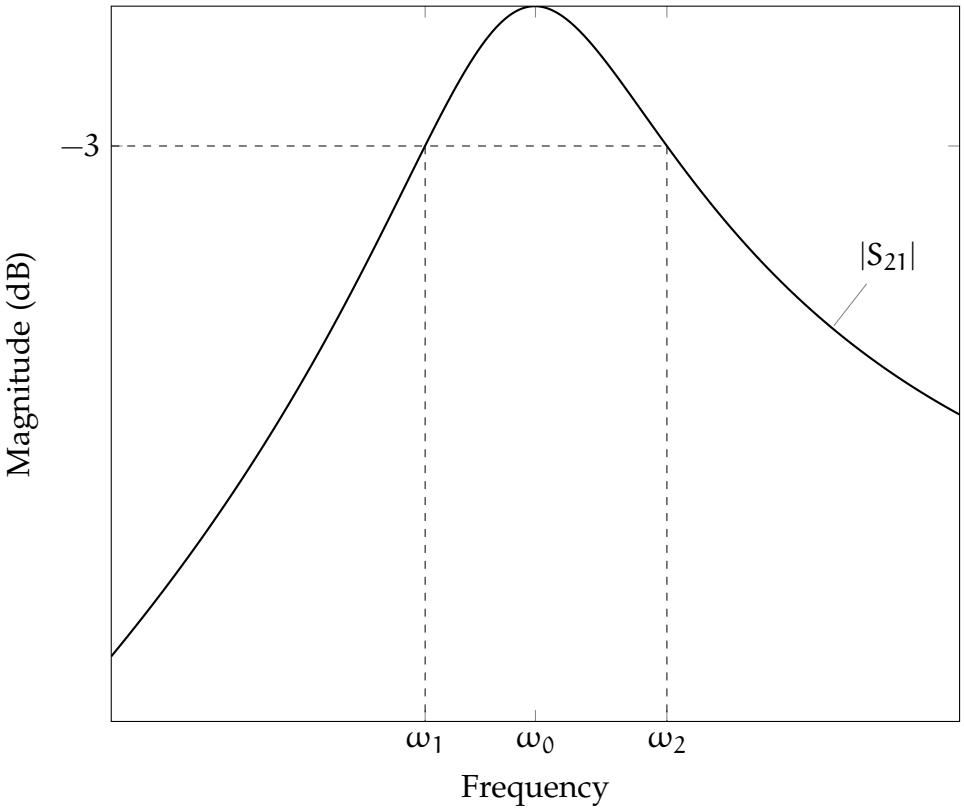

(c) Response of doubly loaded resonator

Figure 2.21: Equivalent circuit for external loaded resonator

The odd mode is obtained through an electric wall that implies a shorted circuit at the plane of symmetry. In this case the half of the resonator is excluded by the short circuit and the admittance and reflection are obtained straightforward:

$$Y_{ro} = \infty \tag{2.74a}$$

$$S_{11o} = -1 \tag{2.74b}$$

The S_{21} can be also calculated as combination of the even/odd part of the S_{11} as [33]:

$$S_{21} = \frac{1}{2}(S_{11e} - S_{11o}) = \frac{1}{1 + jQ_e(\Delta\omega/\omega_0)} \tag{2.75}$$

that in magnitude results to be:

$$|S_{21}| = \frac{1}{\sqrt{1 + (Q_e(\Delta\omega/\omega_0))^2}} \tag{2.76}$$

An example of such resonator is shown in Fig. 2.21b implemented in rectangular waveguide of cross-section dimensions a and b (not shown in the figure). The length of the resonator is indicated with l_r while the aperture of the external iris with w_e terms. The response is shown in Fig. 2.21c. When the deviation from the central frequency is $\Delta\omega = 0$ there is maximum transmission because the eq. (2.76) leads to $|S_{21}| = 1$. Now consider the band edges ω_1 and ω_2 where the eq. (2.76) becomes $|S_{21}| = 1/\sqrt{2}$, the denominator of the eq. (2.76) is of the form:

$$Q_e \frac{\Delta\omega_\pm}{\omega_0} = \pm 1 \tag{2.77}$$

By the introduction of the 3 dB bandwidth having edges ω_1 and ω_2 as shown in Fig. 2.21c, it can be also expressed as function of the definition of eq. (2.77) as:

$$\Delta\omega_{3\,dB} = \Delta\omega_+ - \Delta\omega_- = 2\frac{\omega_0}{Q_e} \tag{2.78}$$

The derivation carried out for the doubly loaded resonator has been conducted following a procedure that is very similar to the one for a singly loaded resonator. Thus it is necessary to correct eq. (2.78) in order to take into account also the port on the other end of the resonator. The expression of the external quality factor is given as:

$$Q'_e = \frac{Q_e}{2} = \frac{\omega_0}{\Delta\omega_{3\,dB}} \tag{2.79}$$

As it was for the extraction of the coupling between a pair of internal resonator, eq. (2.79) can be used to create curves of the Q_e for several values of external coupling dimensions. Again, it is important to stress that a variation of the dimensions of the external coupling causes a deviation of the central frequency of the resonator. Hence also the parameter l_r is also to be adjusted in order to tune the cavity on the correct centre frequency.

2.7 POWER HANDLING CAPABILITY

In this study the main application for the Butler matrix with filtering is after the bank of PAs to replace the baseline of ONET plus bank of BPFs for satellite RF payloads. Although this is not the only application possible for this kind of network, the attention here will be devoted to the study of the structure of Fig. 2.17b. From this it is clear that the network that will be developed in the next chapters will operate in *high power* condition because it will be cascaded to the amplifiers. Also, an application for space means that the device may work very close to a perfect vacuum condition. There are 3 main phenomena to consider for these kind of applications [77]:

- Multipactor[1],
- Corona discharge and

1 In some publications, many written in American-English, it is also referred as multipaction

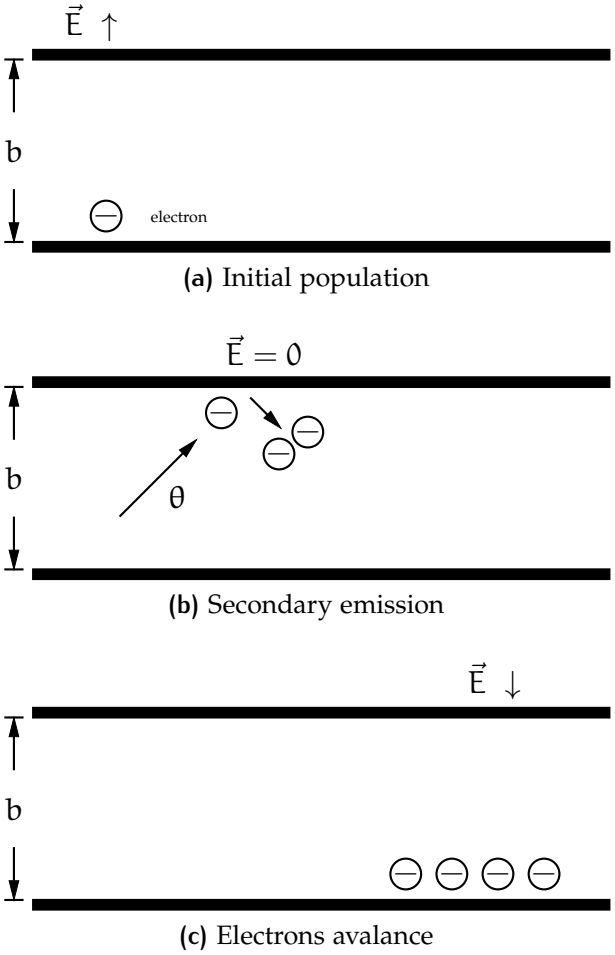

(a) Initial population

(b) Secondary emission

(c) Electrons avalance

Figure 2.22: Parallel plate multipactor model

- PIM.

Although in this work only the multipactor effect will be considered for some of the structures proposed, here are also briefly mentioned corona and PIM

Multipactor has been seen for the first time in the 1934 by Farnsworth during the early investigations on television to produce an image on the screen [78, 79]. In satellite communication it is a disruptive phenomena as it can cause a distortion of the signal, damage to the components or even to a fatal breakdown [80, 81]. It happens when a population of electrons is accelerated between two (conductive) walls of a resonant cavity in vacuum condition. The multipactor hence refers to the condition in which the avalanche of electrons is self sustained [82]. Fig. 2.22a is a schematic of the initial population of electrons (in the figure is shown one single electron for

instance) in a cavity with two parallel conductive plates at resonance. The accelerated electrons impact the other material with a certain speed V, energy e and angle θ. Depending on the combination of these parameters, the properties of the material, the resonance frequency f_0 and the gap distance d, a Secondary Electron Emission (SEE) can result in more free electrons introduced in the structure. The incident electrons are also called *primary* electrons, while the one caused by the SEE are *secondary* electrons. Fig. 2.22b shows an electron at the impact with the surface of the wall that is causing a secondary emission of 2 new electrons. The SEE can be responsible of an avalanche effect of electrons with the result of multiplication causing a discharge between the two walls. The effects of the SEE are shown in Fig. 2.22c where the population is higher with respect to the initial moment. It is a stochastic phenomena that can be predicted using numerical techniques. For each incident angle θ it is possible to measure the average ratio of secondary over primary electrons as function of the energy and the material: this is called Secondary Emission Yield (SEY) and it is a fundamental parameter when choosing the material for a specific application. An example of SEY for Aluminium is shown in Fig. 2.23. Note that to have a complete view of the SEY property of a material it is necessary to vary the incident angle θ, hence creating a set of functions. In Fig. 2.23 is the representation when $\theta = 0°$ only. Recently, have been presented techniques to deposit particular coatings over the internal material with the aim to introduce a microscopic surface roughness to reduce the avalanche of electrons, leading to an SEY < 1 for all incident angles [84, 85]. However these methods are still experimental, but the preliminary results are promising.

There are several ways to predict multipactor on an RF components. One is to calculate the voltage in the critical parts and then using the multipactor tool provided by ESA [86]. This tool works on comparison between measured data/background/ and numerical techniques with electrons accelerated between two parallel plates and a Common Wave (CW) input signal. It can be shown that this is a worst case as

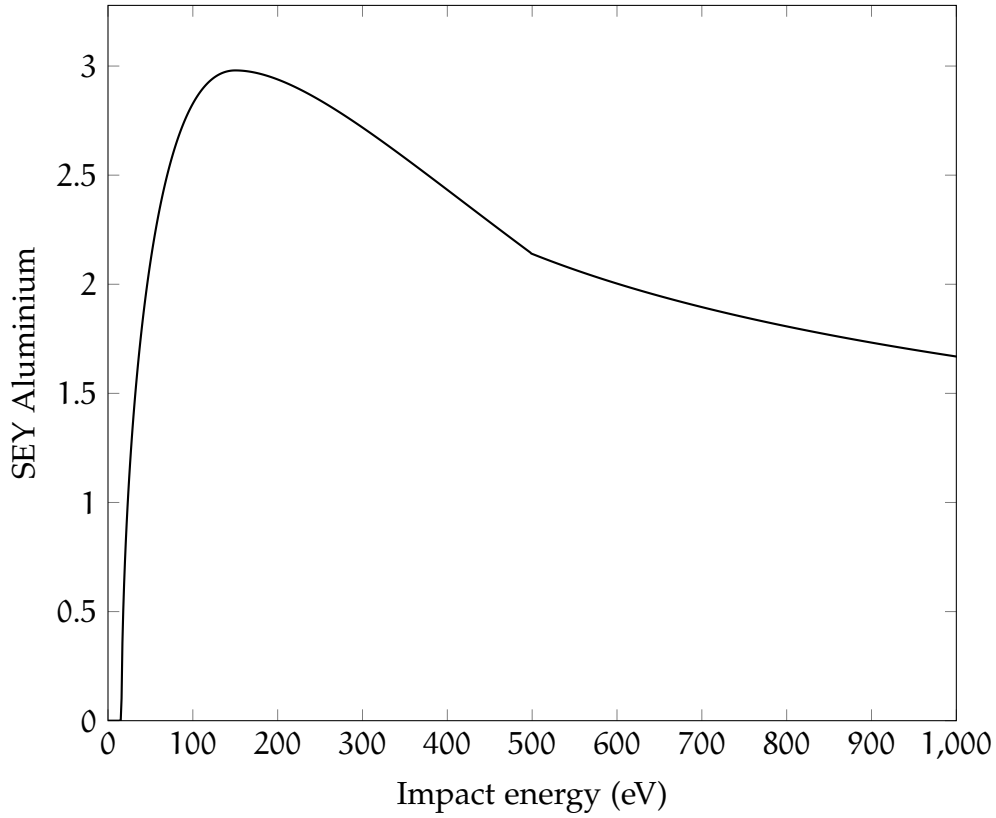

Figure 2.23: SEY of Aluminium for $\theta = 0°$ [83]

the population of electrons is not supposed to move to other non-resonating areas or with wider gaps. Due to the stringent and demanding requirements of modern telecommunication satellite, the need for more available signal power might clash with a too conservative multipactor prediction, leading to time consuming and expensive re-design of the devices which do not meet the power level requirements. Thus it is essential to double check the multipactor breakdown levels with more advanced software like Spark3D [83] and CST Particle Studio [74]. It is also essential to report that the properties of the material change over time and margins are to be applied over the multipactor threshold calculated with the simulators [86]. Hence governmental institutions such as ESA have defined the European Cooperation for Space Standardisation (ECSS) standard that introduces a margin of 9 dB over the multipactor discharge required by components operating at high power. This might put an additional challenge over the design of the devices. To reproduce and test mul-

tipactor in the laboratory it is necessary to include a radioactive or ionised source of electrons into a vacuum chamber as normally there are not free electrons on earth.

The Corona discharge occurs at higher pressure with respect multipactor and it is responsible for ionisation of the gas around a charged surface. The phenomena of Corona is when there exists an avalanche of electrons that transforms the isolating gas into conducting plasma, thus generating a discharge [77, 87]. The breakdown may happen to terrestrial RF devices as well as for space components those that are active during the launch, hence operating at higher pressures with respect the nominal, nearly vacuum, condition in space. Also for corona, there exists commercial software capable to simulate the discharge occurrence through numerical methods [83].

PIM is a phenomena that cannot be predicted in advance and mainly depends on the mechanical structure of the components and material. The name stands to remind that the result in the frequency domain is similar to those of intermodulation products typically generated by amplifiers. However, it can be observed that also passive components might produce lower level of intermodulation, thus it is referred to *passive* intermodulation, or PIM. The causes for this may be several, for example thin layers of oxide on the conducting surfaces, micro-cracks of the metal structure or by the presence of external dirty and particles [80]. These are responsible for micro-voltages that concur to localised currents, that all summed produce visible levels of PIM. It is useful to mention that for some specific cases there are techniques that can be adopted in order to reduce or minimise the level of PIM, as shown in [88].

3 QUADRATURE HYBRIDS BASED ON RESONATORS

Conventional Butler matrices, used as combining and splitting stages in MPAs, are mainly based on several 90° hybrid couplers. These conventional components are all based on transmission lines, hence, in this chapter the synthesis and properties of quadrature hybrids based on coupled resonators is investigated. Initially an introduction to hybrid couplers based on transmission lines is presented. The hybrids couplers are discussed initially for the basic 2-branch case and later extended to multiple branches. Then a technique to obtain an equivalent circuit based on resonators called *equivalence technique* is introduced. The study is focused then on the definition on polynomials for a generic quadrature hybrid based on resonators in order to demonstrate the possibilities and limitations of this configuration. At the end, the 2-branch quadrature hybrid coupler is implemented in a 3D structure to create a 4×4 Butler matrix with filtering included.

3.1 BASIC CONCEPTS OF THE 90° HYBRIDS

The basics concepts of a 2×2 quadrature coupler based on transmission lines is introduced in this section.

The schematic of the basic 2×2 quadrature hybrid coupler is shown in Fig. 3.1. It is formed by two pairs of parallel transmission lines of same length and given impedance. The impedances for the straight through lines are indicated in Fig. 3.1 with letter b_1 while a_1 and a_2 are the ones for shunt lines. The impedance of the

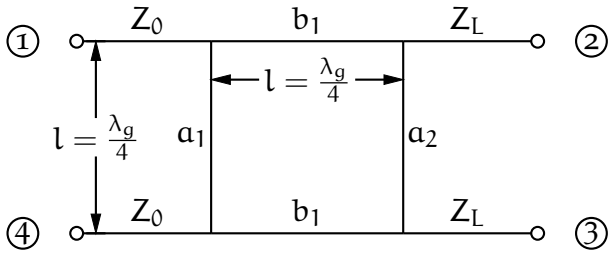

Figure 3.1: Schematic of 90° hybrid coupler

input line is indicated with Z_0 while the load is Z_L. In the figure the input ports are 1 and 4 while the outputs are 2 and 3. Also, when dealing with directional couplers it is common to identify ports with some special name: port 1 can also be called *input*, port 2 the *through*, port 3 the *coupled* and port 4 the *isolated* [30]. The following 3 quantities are usually used to characterise the coupler performance

$$\text{Coupling} = -20\log_{10}|S_{31}| \tag{3.1}$$

$$\text{Directivity} = 20\log_{10}\frac{|S_{31}|}{|S_{41}|} \tag{3.2}$$

$$\text{Isolation} = -20\log_{10}|S_{41}| \tag{3.3}$$

In addition to the above, the Voltage Standing Wave Ratio (VSWR) is an important figure used in many technical documents:

$$\text{VSWR} = \frac{1+|S_{11}|}{1-|S_{11}|} \tag{3.4}$$

In its usual form this circuit equally splits the input power among the outputs while provides a phase shift of the output signals of 90°. For this basic example the synthesis

will be carried out for a symmetric device, hence $a_1 = a_2$ and $Z_0 = Z_L = 1$. The scattering matrix takes this form

$$\mathbf{S} = \frac{-1}{\sqrt{2}} \begin{bmatrix} 0 & j & 1 & 0 \\ j & 0 & 0 & 1 \\ 1 & 0 & 0 & j \\ 0 & 1 & j & 0 \end{bmatrix} \tag{3.5}$$

This result is obtained at centre frequency when the normalised impedances of the hybrid of Fig. 3.1 are $b_1 = 1/\sqrt{2}$ and $a_1 = a_2 = 1$ [30]. The electrical length of the transmission lines is 90° for all of them, hence the physical length is $l = \lambda_g/4$ as shown in Fig. 3.1. Due to the symmetries of the hybrid it is possible to analyse it with the even/odd mode method [30, 72, 89–91]. With this approach a magnetic and electric walls split the shunt transmission lines in two, thus resulting in stubs of length of $\lambda_g/8$ with an open or short circuit at the end depending if evaluating, respectively, the even or odd mode. The stubs can be seen as a shunt admittance Y while the straight through lines as normal quarter-wavelength transmission lines. The ABCD matrix of a shunt admittance Y is defined as:

$$\begin{bmatrix} A & B \\ C & D \end{bmatrix}_{\text{shunt}Y} = \begin{bmatrix} 1 & 0 \\ Y & 1 \end{bmatrix} \tag{3.6}$$

In this case is $Y = jY_0 \tan(\beta l)$ where β is the propagation constant defined as:

$$\beta = \frac{2\pi}{\lambda_g} \tag{3.7}$$

and Y_0 is the characteristic admittance of the line. On the other hand, the ABCD matrix of just a piece of transmission line is

$$\begin{bmatrix} A & B \\ C & D \end{bmatrix}_{\text{line}} = \begin{bmatrix} \cos(\beta l) & jZ_0 \sin(\beta l) \\ jY_0 \sin(\beta l) & \cos(\beta l) \end{bmatrix} \tag{3.8}$$

The ABCD matrices have been introduced here because it is very convenient to model the single elements of the hybrid in this way and it is also possible to build one half of the circuit of Fig. 3.1 by cascading the matrices of eq. (3.6) and (3.8). Two separate ABCD matrices are obtained for the even and odd mode respectively. For the even mode the ABCD is

$$\begin{bmatrix} A_e & B_e \\ C_e & D_e \end{bmatrix} = \begin{bmatrix} 1 & 0 \\ ja_1 \tan\theta_s & 1 \end{bmatrix} \begin{bmatrix} \cos 2\theta_s & jb_1 \sin 2\theta_s \\ \dfrac{j}{b_1} \sin 2\theta_s & \cos 2\theta_s \end{bmatrix} \begin{bmatrix} 1 & 0 \\ ja_2 \tan\theta_s & 1 \end{bmatrix} \tag{3.9}$$

while for the odd mode the stubs are loaded with a short circuit:

$$\begin{bmatrix} A_o & B_o \\ C_o & D_o \end{bmatrix} = \begin{bmatrix} 1 & 0 \\ \dfrac{a_1}{j} \cot\theta_s & 1 \end{bmatrix} \begin{bmatrix} \cos 2\theta_s & jb_1 \sin 2\theta_s \\ \dfrac{j}{b_1} \sin 2\theta_s & \cos 2\theta_s \end{bmatrix} \begin{bmatrix} 1 & 0 \\ \dfrac{a_2}{j} \cot\theta_s & 1 \end{bmatrix} \tag{3.10}$$

Note that in eq.s (3.9) and (3.10) the argument of the trigonometric function has been substituted with the electrical length θ_s of the shunt stubs [92]. In this way it is possible to calculate all the parameters with respect to an independent frequency variable. Clearly it must be that

$$0 \leqslant 2\theta_s \leqslant \frac{\pi}{2} \tag{3.11}$$

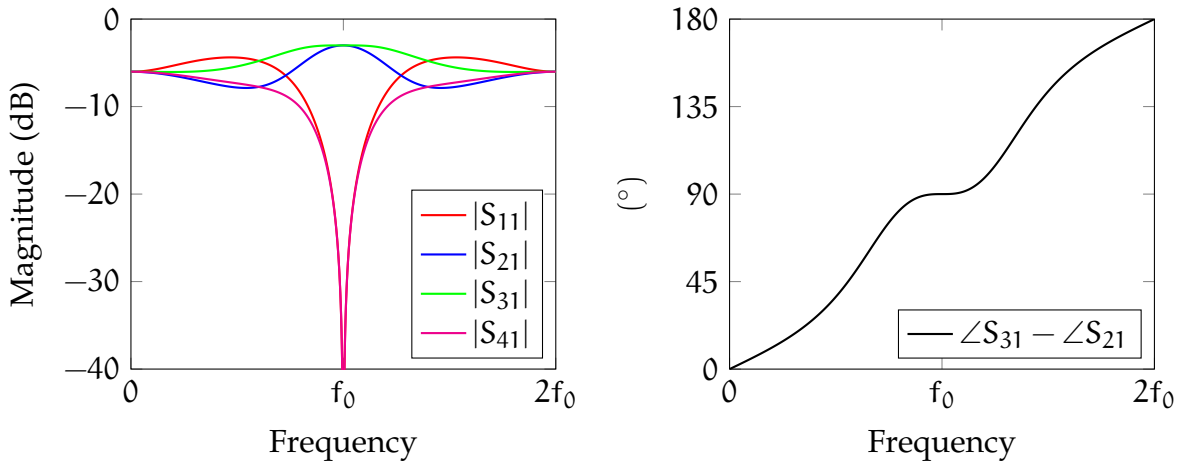

(a) Magnitude response

(b) Output phase shift

Figure 3.2: Frequency response of the conventional 2×2 quadrature hybrid

in order to avoid repetition of the response. S_{11} and S_{21} of the even/odd modes are obtained from the $ABCD$ matrix with the following relations [30]

$$S_{11}^{e,o} = \frac{A_{e,o} + B_{e,o} - C_{e,o} - D_{e,o}}{A_{e,o} + B_{e,o} + C_{e,o} + D_{e,o}} \tag{3.12}$$

$$S_{21}^{e,o} = \frac{2}{A_{e,o} + B_{e,o} + C_{e,o} + D_{e,o}} \tag{3.13}$$

Finally the scattering parameters are given as:

$$S_{11} = \frac{S_{11}^{e} + S_{11}^{o}}{2} \tag{3.14a}$$

$$S_{21} = \frac{S_{21}^{e} + S_{21}^{o}}{2} \tag{3.14b}$$

$$S_{31} = \frac{S_{21}^{e} - S_{21}^{o}}{2} \tag{3.14c}$$

$$S_{41} = \frac{S_{11}^{e} - S_{11}^{o}}{2} \tag{3.14d}$$

The result of this analysis is the magnitude of the transfer function shown in Fig. 3.2a. At f_0 there exists perfect isolation and input match while the output power is equally divided between ports 2 and 3. The x-axis of both graphs of Fig. 3.2 is the frequency, although the equivalent notation in terms of θ_s can be used as in appendix A. In this practical case it is possible to note how the quarter-wavelength transmission line

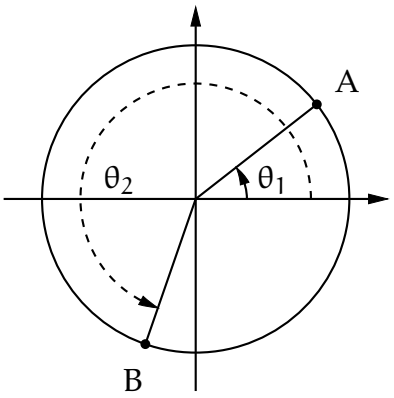

Figure 3.3: The phase difference between two signals A and B is the angular aperture of the minimum arc between them on the circumference.

guarantees a usable bandwidth of around 10% and usually limited to a maximum of 20% as shown in Fig. 3.2a [30]. All the characteristics also converge to $-6\,\mathrm{dB}$ at 0 and $2f_0$. fig. 3.2b shows the difference in phase between output ports 2 and 3. Note that here and in the following of this work the phase difference is defined as the angle of the minimum arc between two points on a circumference shown in Fig. 3.3. If θ_1 is the phase of the first signal (ie. A in Fig. 3.3) and θ_2 is of the second one (ie. B in Fig. 3.3), assuming that $\theta_1, \theta_2 \in [0, 2\pi]$, then the phase difference is defined as

$$\Delta\theta = \begin{cases} |\theta_2 - \theta_1| & \text{if } |\theta_2 - \theta_1| \leqslant \pi, \\ 2\pi - |\theta_2 - \theta_1| & \text{if } |\theta_2 - \theta_1| > \pi \end{cases} \tag{3.15}$$

As consequence of this definition the phase difference may vary between 0° and 180°. In Fig. 3.2b it is possible to see that in the range of a 20% FBW the drift of the phase with respect the nominal 90° is about $\pm 1.5°$.

In order to overcome the limitation of bandwidth more branches are included in the design of the quadrature hybrid coupler [92]. A schematic with n branches and $n-1$ straight lines is shown in Fig. 3.4. This structure is also called Branch-Guide Coupler (BGC). Again, all the transmission lines here are quarter-wavelength, although the several shunt and straight through elements permit a more complex synthesis of the response capable to produce a given transfer function. The synthesis

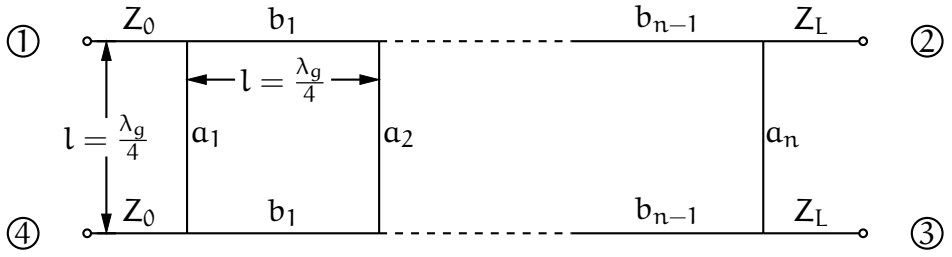

Figure 3.4: Schematic of a multi-branch 90° hybrid coupler

of BGC providing Butterworth or Tchebycheff response was introduced in [92] for symmetric networks and in [93] for an arbitrary load. In appendix A on page 197 the detailed synthesis technique as well as some examples are presented. Also, the synthesis of a BGC giving a Zolotarev transfer function was presented in [94]. Note that regardless the number of branches, the synthesis is based on calculating the characteristic impedance of each transmission line, both shunt and straight. There are 4 key parameters involved in the synthesis of any BGC:

n is the number of branches. It must be $n > 2$ for Butterworth response and $n > 3$ for Tchebycheff/Zolotarev transfer functions;

K is a parameter that controls the output coupling value;

θ_c is the cut-off of the Tchebycheff coupler;

R is the output impedance normalized with respect the input one. For symmetric couplers it is $R = 1$.

All these parameters are related to each other and influence the electrical response. If only one of these parameters is changed, then it is necessary to modify the others in order to meet the specifications. The analysis of the response once the impedances a_i and b_i are calculated, is performed in a similar way to the hybrid of Fig. 3.1. To generalise the procedure of extraction of the electrical parameters, it is convenient to define the transmission matrices for the shunt stub and straight line. The stubs are

influenced either by the magnetic or electric wall are placed at the symmetry plane of the circuit, hence there are two sets of equations:

$$\begin{bmatrix} A_e & B_e \\ C_e & D_e \end{bmatrix}_{\text{stub}} = \begin{bmatrix} 1 & 0 \\ ja_i \tan\theta_s & 1 \end{bmatrix} = \mathbf{T}_s^e(a_i) \tag{3.16a}$$

$$\begin{bmatrix} A_o & B_o \\ C_o & D_o \end{bmatrix}_{\text{stub}} = \begin{bmatrix} 1 & 0 \\ -ja_i \cot\theta_s & 1 \end{bmatrix} = \mathbf{T}_s^o(a_i) \tag{3.16b}$$

The straight through line is not affected and can conveniently be defined as the following:

$$\begin{bmatrix} A & B \\ C & D \end{bmatrix}_{\text{line}} = \begin{bmatrix} \cos 2\theta_s & jb_i \sin 2\theta_s \\ \frac{j}{b_i}\sin 2\theta_s & \cos 2\theta_s \end{bmatrix} = \mathbf{T}_l(b_i) \tag{3.17}$$

The even/odd transfer matrices are calculated recursively following the structure of multi-branch coupler shown in Fig. 3.4 by combination of the eq.s (3.16) and (3.17) as:

$$\begin{bmatrix} A_{e,o} & B_{e,o} \\ C_{e,o} & D_{e,o} \end{bmatrix}_{\text{BGC}} = \left[\prod_{i=1}^{n-1} (\mathbf{T}_s^{e,o}(a_i) \times \mathbf{T}_l(b_i))\right] \times \mathbf{T}_s^{e,o}(a_n) \tag{3.18}$$

The scattering parameters are calculated combining eq. (3.18) into eq.s (3.12) and (3.13), and finally into set of eq.s (3.14). Clearly the eq. (3.18) may also be applied to the simple 2-branch coupler. Following the synthesis procedure shown in appendix A, an example of a symmetric 7-branch Tchebycheff coupler with $K = 50$, cut-off $\theta_c = 35°$ is shown. The values of impedances a_i and b_i are shown in Tab. 3.1. For consistency with previous technical documents, where usually the values of the transmission lines are expressed as normalised admittances, the table shows both representations. The scattering parameters are then calculated with eq. 3.18 and final results are shown in Fig. 3.5. The schematic of the circuit with indication of the immittances is shown in

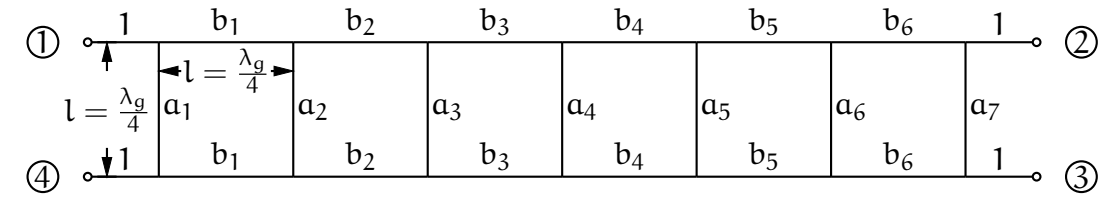

(a) Schematic

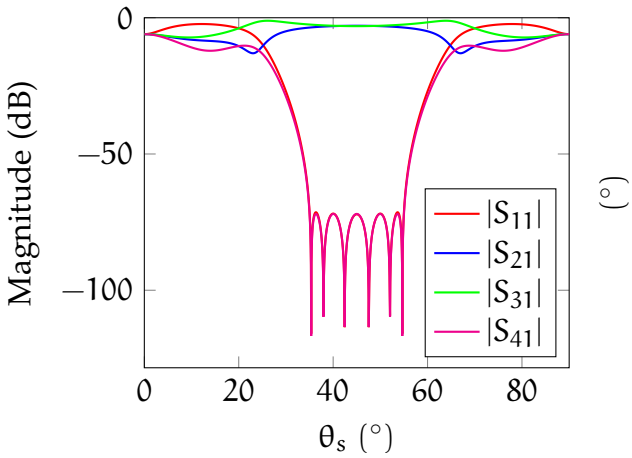

(b) Magnitude response

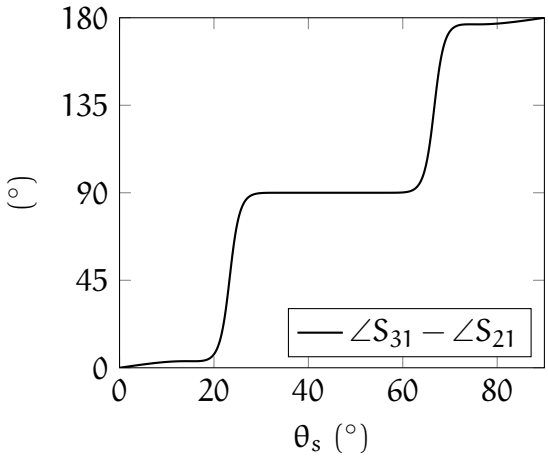

(c) Output phase shift

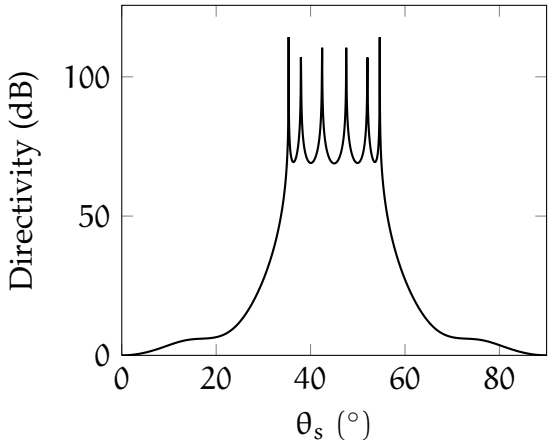

(d) Directivity response

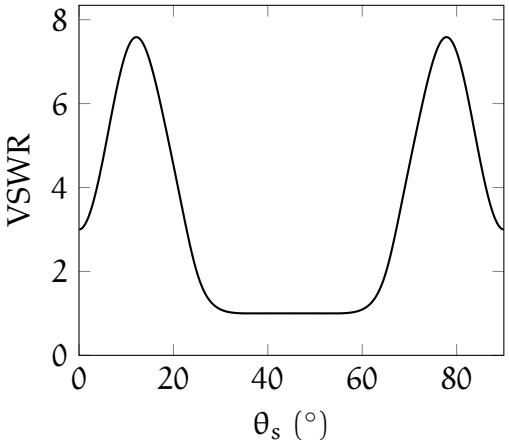

(e) VSWR response

Figure 3.5: Branch-guide coupler equal-ripple Tchebycheff transfer function with $n = 7$, $K = 50$, $\theta_c = 35°$ and $R = 1$

Table 3.1: Normalised characteristic immittances for 7-branch Tchebycheff hybrid coupler $n = 7$, $K = 50$, $R = 1$ and $\theta_c = 35°$.

Element (i)	Shunt line a_i (Ω)	(S)	Straight line b_i (Ω)	(S)
1	28.8474	0.0347	0.9361	1.0683
2	5.6115	0.1782	0.7241	1.3811
3	1.6896	0.5918	0.5209	1.9199
4	0.9973	1.0027	0.5209	1.9199
5	1.6896	0.5918	0.7241	1.3811
6	5.6115	0.1782	0.9361	1.0683
7	28.8474	0.0347		

Fig. 3.5a. Fig. 3.5b is the magnitude response of the 3 dB hybrid coupler with $n - 1$ poles of the Tchebycheff transfer function. Note that in this figure the characteristics are shown with the equivalent representation in term of electrical length θ_s instead of the frequency. This is for better clarity, although the two notations are related by

$$f = f_0 \frac{\theta_s}{45°} \tag{3.19}$$

It is possible to show that the degree of the polynomial for an n-branch hybrid is always $n - 1$ [92]. The FBW for this example is more than 45% due to the greater number of branches and because of the value of cut-off θ_c. The difference of output phase of Fig. 3.5c also confirms the greater bandwidth. Finally the value of the directivity in Fig. 3.5d and of the VSWR in Fig. 3.5e are shown. Note that in the interval $\theta_s = 45° \pm 10°$ the VSWR is almost flat and constant close to 1. It is important to stress that the cut-off variable θ_c defines the interval of frequencies in which the return loss is equal-ripple: the inferior and superior band edges are, respectively, θ_c and $90° - \theta_c$, hence the bandwidth is:

$$B_{BGC} = 90° - 2\theta_c \tag{3.20}$$

The impedances shown in Tab. 3.1, are made in practice by the connection of two main lines of several transversal coupling elements. The dimensions of all the lines,

that theoretically are all quarter-wavelength, should be optimised with a full-wave simulator in order to take into account the discontinuity of the straight and shunt lines [95–97]. Alternatively, the 3D physical implementation of the BGC is possible through a rigorous characterisation of the EM fields as shown in [98].

3.2 THE EQUIVALENCE METHOD

The *equivalence method* is used to relate the hybrid based on transmission lines to an equivalent circuit based on resonators in order to include a filtering transfer function. The theory of the BGC, both for the synthesis and design is well established and it provides broad-band or at least very wide-band responses (as seen, always more than 10%). Also, the behaviour out of band is not selective because of the intrinsic repetition of the magnitude of the electrical characteristic and the convergence of all parameters (RL, coupling and isolation) to the value of $-6\,\mathrm{dB}$ [30]. If any sort of frequency selectivity is required, it has to be added by including separate filters, hence leading to large bulky equipment. Here a solution to include the filter transfer function into an hybrid is explained. It should be noted that the method presented here is to synthesise a 2×2 network based on coupled resonators capable of providing filtering as well as the traditional power splitting and phase distribution of the hybrid. However in literature there are available different techniques that use transmission line hybrid couplers to incorporate filtering [99, 100]. These methods are not applicable to the problem of interest as they address 2 ports devices or 1-input to multiple output power network distributions. In the following, all the methods proposed will address the synthesis of the coupling matrix of multi-port, multi-resonator networks.

The synthesis of the coupling matrix of a 2-branch, 90° hybrid coupler with filtering was first presented in [101] and later in [102–104]. This method is called *equivalence technique* here because of the direct relation between the values of the coupling matrix

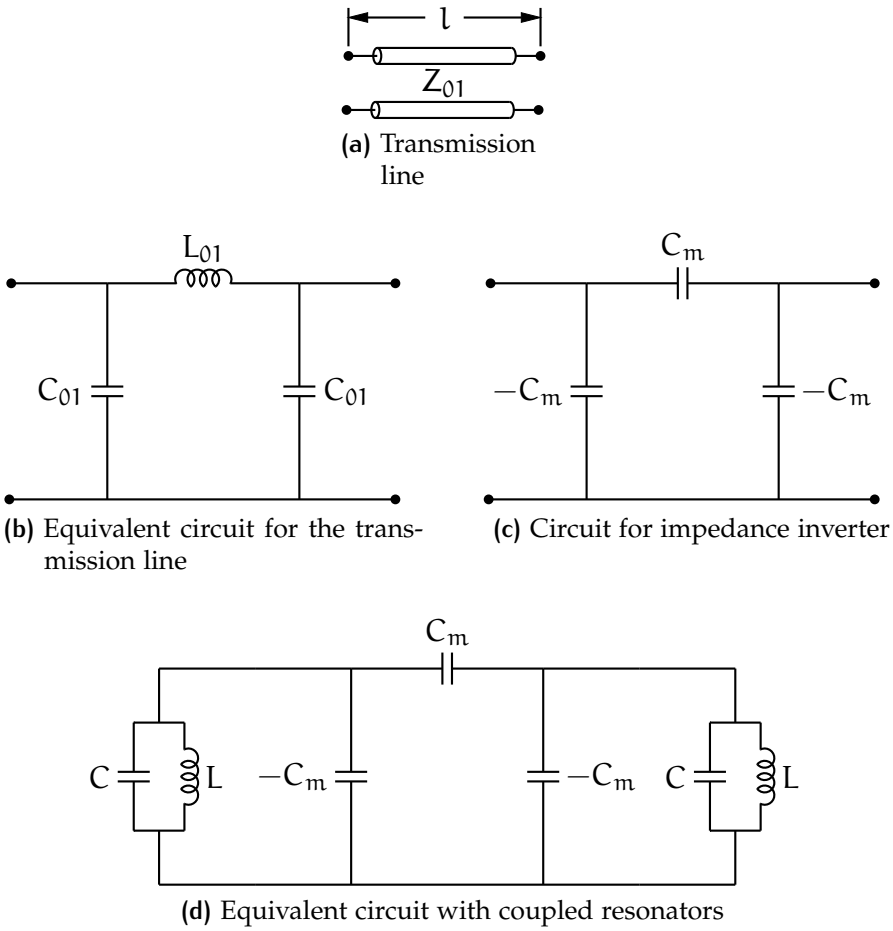

(a) Transmission line

(b) Equivalent circuit for the transmission line

(c) Circuit for impedance inverter

(d) Equivalent circuit with coupled resonators

Figure 3.6: Equivalent circuits for a transmission line

and the characteristic impedances of the BGC at the central frequency. An equivalent way to describe the through transmission line of Fig. 3.6a is through its $ABCD$ matrix:

$$\begin{bmatrix} A & B \\ C & D \end{bmatrix}_{\text{line}} = \begin{bmatrix} \cos \beta l & jZ_{01} \sin \beta l \\ (j/Z_{01}) \sin \beta l & \cos \beta l \end{bmatrix} \tag{3.21}$$

where l is the length of the line and Z_{01} is the characteristic impedance. The wave signal is supposed in propagation hence that Z_{01} is real. It is well known [30], that any line can be modelled by the π network of lumped elements as in Fig. 3.6b. In this

case the ABCD matrix of Fig. 3.6b is derived as the multiplication of the matrices of the single capacitors and inductors:

$$\begin{aligned}\begin{bmatrix} A & B \\ C & D \end{bmatrix}_{\text{line,lumped}} &= \begin{bmatrix} 1 & 0 \\ j\omega C_{01} & 1 \end{bmatrix} \times \begin{bmatrix} 1 & j\omega L_{01} \\ 0 & 1 \end{bmatrix} \times \begin{bmatrix} 1 & 0 \\ j\omega C_{01} & 1 \end{bmatrix} \\ &= \begin{bmatrix} 1-\omega^2 L_{01} C_{01} & j\omega L_{01} \\ 2j\omega C_{01} - j\omega^3 L_{01} C_{01}^2 & 1-\omega^2 L_{01} C_{01} \end{bmatrix} \end{aligned} \tag{3.22}$$

where $\omega = 2\pi f$. The values of the lumped elements L_{01} and C_{01} are calculated comparing the matrices of eq.s (3.21) and (3.22). The following important relations are obtained:

$$L_{01} = \frac{Z_{01} \sin \beta l}{\omega} \tag{3.23a}$$

$$C_{01} = \frac{1}{\omega Z_{01}} \sqrt{\frac{1-\cos \beta l}{1+\cos \beta l}} \tag{3.23b}$$

The present study is focused on BGC and it is known that they are composed by quarter-wavelength transmission lines. It derives that $\beta l = 90°$ and, consequently, the above relations reduce to

$$L_{01} = \frac{Z_{01}}{\omega} \tag{3.24a}$$

$$C_{01} = \frac{1}{\omega Z_{01}} \tag{3.24b}$$

Considering now a circuit based on synchronously tuned, mutually coupled resonators, each coupling can be conveniently expressed with a K or J inverter. Fig. 3.6c is the π network of capacitors that implements the inverter $J = j\omega C_m$ as shown in Fig. 2.7b and Fig. 2.8b. Here the equivalence has to be made between the transmission line and the model of coupling loaded by parallel resonators of Fig. 3.6d. At centre frequency the behaviour of the two parallel resonators is of an open circuits, thus the comparison is made directly between the π network of capacitors of Fig. 3.6c and the transmission

line of Fig. 3.6b. The comparison is made in terms of transfer matrices. The ABCD matrix of a transmission line of eq. (3.22) at $\omega = \omega_0$ reduces to the following

$$\begin{bmatrix} A & B \\ C & D \end{bmatrix}_{\text{line,lumped};\omega=\omega_0} = \begin{bmatrix} 0 & j\omega_0 L_{01} \\ j\omega_0 C_{01} & 0 \end{bmatrix} \tag{3.25}$$

This is then equate with the transmission matrix of the J inverter

$$\begin{bmatrix} A & B \\ C & D \end{bmatrix}_{J;\omega=\omega_0} = \begin{bmatrix} 0 & \pm\dfrac{j}{\omega_0 C_m} \\ \pm j\omega_0 C_m & 0 \end{bmatrix} \tag{3.26}$$

Finally it is possible to establish a direct relation between the element of the inverter C_m and the characteristic parameter C_{01}. Equating the eq. (3.26) with the eq. (3.25) and then with the definition of eq. (3.23), the following relation is derived

$$C_m = C_{01} = \frac{1}{\omega_0 Z_{01}} \tag{3.27}$$

Right now it as been found the relation between the value of the capacitor of the π lumped elements of the inverters with a quarter-wavelength transmission line of characteristic impedance Z_{01}. This circuit is exactly representative of the one loaded with resonators only at ω_0. From this point it is convenient to recall the definition of electric coupling of eq. (2.53) as it describe well the coupling structure of Fig. 3.6c

$$k_e = \frac{C_m}{C} = \frac{1}{\omega_0 C Z_{01}} \tag{3.28}$$

the relation of the C_m found in eq. (3.27).

The equivalence between a generic quarter-wavelength transmission line of arbitrary characteristic impedance and the coupling coefficient between two resonators has been obtained through eq. (3.28). The same procedure is applied to all the transmission lines of Fig. 3.1. Finally the 90° hybrid coupler can be equivalently represented

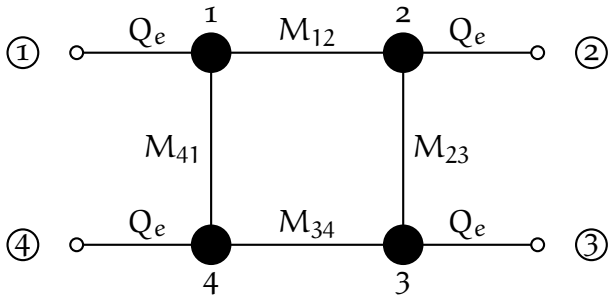

Figure 3.7: Hybrid based on coupled resonators

with the circuit based on resonators of Fig. 3.7: in this figure the black filled circles are the resonators while the solid lines are the coupling between them. The output ports are indicated with numbers inside circles. Each resonator is numbered, and above each coupling line is the corresponding element in the coupling matrix. In this figure the external couplings are also indicated by means of their external quality factor Q_e. This is a convenient way to express the elements of the circuits because the definition of external quality factor of eq. (2.59)

$$Q_e = \omega_0 C Z_0 \tag{3.29}$$

The characteristic impedance of the straight though lines is $Z_{01} = b_1 Z_0$ hence the coupling between resonators 1 and 2 and the one between resonators 1 and 4 are

$$M_{01} = M_{34} = \frac{1}{Q_e b_1} = \frac{\sqrt{2}}{Q_e} \tag{3.30a}$$

$$M_{41} = M_{32} = \frac{1}{Q_e a_1} = \frac{1}{Q_e} \tag{3.30b}$$

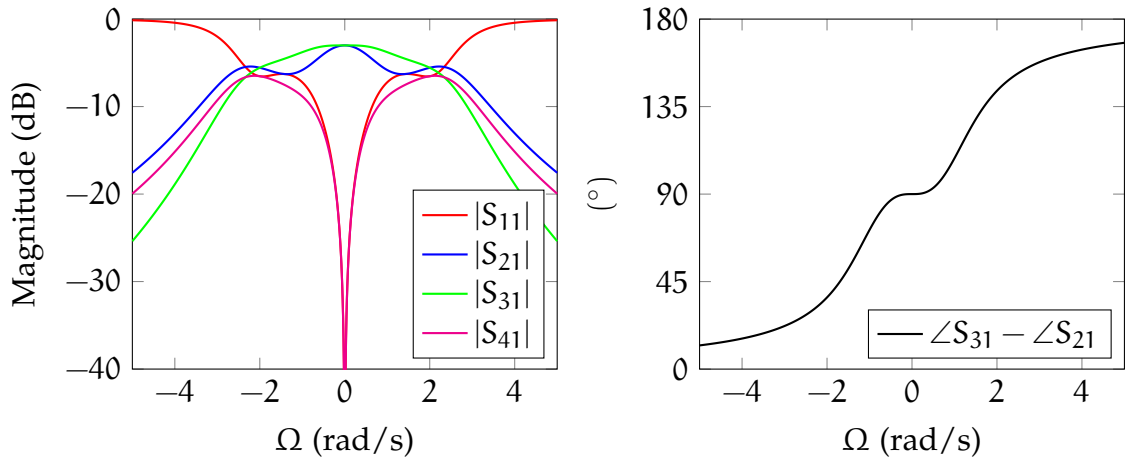

(a) Magnitude response

(b) Output phase shift

Figure 3.8: Frequency response of the conventional 2×2 quadrature hybrid based on coupled resonators

In the band-pass domain Q_e can be approximated to the inverse of the FBW [20]. Thus in the low-pass domain the value of Q_e is unitary. The coupling matrix for the structure is

$$\mathbf{M} = \begin{array}{c|cccc|cccc} & P_1 & P_2 & P_3 & P_4 & 1 & 2 & 3 & 4 \\ \hline P_1 & 0 & 0 & 0 & 0 & 1 & 0 & 0 & 0 \\ P_2 & 0 & 0 & 0 & 0 & 0 & 1 & 0 & 0 \\ P_3 & 0 & 0 & 0 & 0 & 0 & 0 & 1 & 0 \\ P_4 & 0 & 0 & 0 & 0 & 0 & 0 & 0 & 1 \\ \hline 1 & 1 & 0 & 0 & 0 & 0 & \sqrt{2} & 0 & 1 \\ 2 & 0 & 1 & 0 & 0 & \sqrt{2} & 0 & 1 & 0 \\ 3 & 0 & 0 & 1 & 0 & 0 & 1 & 0 & \sqrt{2} \\ 4 & 0 & 0 & 0 & 1 & 1 & 0 & \sqrt{2} & 0 \end{array} \tag{3.31}$$

The coupling matrix of the circuit of Fig. 3.7 can be defined by blocks, hence the matrix of the couplings between external ports is 0 as there is no coupling between them. The matrix between external ports and internal resonators is the identity $\mathbf{I}_4$ as shown in Fig. 3.7, while the one for internal resonators is set by eq.s (3.30). The response

of the coupling matrix of eq. (3.31) is shown in Fig. 3.8a while the output phase difference is shown in Fig. 3.8b as function of the low-pass frequency variable Ω. From both figures it is possible to notice that at the centre frequency ($\Omega = 0$) there exists a perfect direct relation between the model based on resonators and the one based on transmission lines: the output power split is equally distributed among ports 2 and 3, the RL and isolation are 0 and the output phase shift is exactly 90°. This is a consequence of the synthesis procedure that produces an equivalence between the elements of the coupling matrix and the impedances of the model based on transmission lines. Note that the configuration with resonators introduces a filtering characteristic as $|S_{11}|$ tends towards the level of 0 dB in the out band while the other parameters shows a sort of *skirt* rejection characteristic at the same frequencies. Naturally the assumption made during the synthesis was made only at the centre frequency and polynomials of the transfer function not defined for a broader bandwidth. However it is important to remember that in the band-pass domain the Q_e controls the bandwidth of the component, hence the frequencies where there exists an almost constant equal power splitting can be varied in accordance to the physical limitations of the coupling structure. Also, the selectivity of the 2 transmission parameters S_{21} and S_{31} is not the same as it appears to be higher for the latter. Finally it is observed a transition around the frequency points $\Omega = \pm 2$ where the characteristic is not monotonic.

This example shows that inclusion of filtering characteristic into an hybrid coupler made by means of resonator is possible. However additional study is necessary to improve the electrical response and eventually to provide a prescribed IL level over a bandwidth.

3.3 EXTENSION TO MULTIPLE BRANCHES

The synthesis of the coupling matrix of the hybrid based on resonators through the equivalence technique can be extended to the case of multiple branches [105]. The idea is to exploit the wider bandwidth provided by the BGC together with the filtering selectivity given by the resonators. The equivalence method can be used

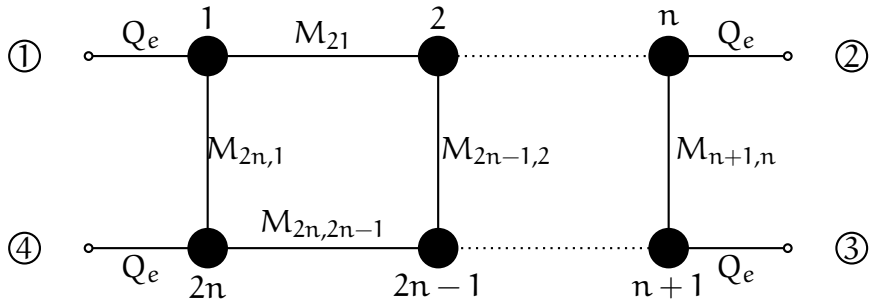

Figure 3.9: General schematic of BGC based on resonators

again to calculate the coupling matrix of the BGC based on resonators of Fig. 3.9. In the figure n is the number of branches, thus there are a total of $2n$ resonators. The rest the structure of Fig. 3.9 is very similar to the one for 2 branches. The labels of the couplings between internal resonators and Q_e are indicated in Fig. 3.9. The procedure begins first with the calculation of shunt and straight through line impedances a_i and b_i with the synthesis described in [92] and in appendix A. The formulas for the coupling matrix are:

$$M^{(i)}_{\text{shunt}} = \frac{1}{Q_e a_i} \qquad i = 1, \ldots, n \tag{3.32a}$$

$$M^{(j)}_{\text{straight}} = \frac{1}{Q_e b_j} \qquad j = 1, \ldots, n-1 \tag{3.32b}$$

$$Q_e \approx \frac{1}{w} \tag{3.32c}$$

Note that here n indicates the number of branches while a_i and b_j are normalised characteristic impedances. Thus the total number of resonators in this circuit is $\dot{n} = 2n$.

Table 3.2: Elements of the 5-branch Tchebycheff hybrid coupler based on resonators. Synthesis parameters are $n = 5$, $K = 22$, $R = 1$, $\theta_c = 35°$ and $Q_e = 1$.

Element i	a_i	b_i	$M^{(i)}_{shunt}$	$M^{(i)}_{straight}$
1	8.4162	0.8401	0.1188	1.1903
2	1.8102	0.5930	0.5524	1.6863
3	0.9288	0.5930	1.0767	1.6863
4	1.8102	0.8401	0.5524	1.1903
5	8.4162		0.1188	

As an example, following this method, a new BGC based on resonators is calculated with the following specifications: $n = 5$, $K = 22$, symmetric with $R = 1$ and exhibiting a Tchebycheff response with cut-off $\theta_c = 35°$. First the impedances of the model based transmission lines are obtained, later the coupling elements, shunt and straight lines, are calculated with eq.s (3.32). The results are summarised in Tab. 3.2. Based on these results the response is shown in Fig. 3.10. The scattering parameters of the 5-branch BGC based on transmission lines are shown in Fig. 3.10a, while the output phase difference in Fig. 3.10b. From the impedances the coupling coefficients are calculated directly as shown in the Tab. 3.2 with the magnitude of scattering parameters shown in Fig. 3.10c and the output phase difference in Fig. 3.10d. Many differences can be noticed between the magnitude of scattering parameters of the transmission line version and the one based on coupled resonators. The theory of the equivalence technique is valid only at centre frequency, hence only at $\Omega = 0$ it is possible to observe an equal power distribution and quadrature output phase shift. The rest of the response shows peaks and ripples that degrade the filtering response. Also, the output power division and phase shift are not constant over a bandwidth.

To overcome this problems an optimisation of the elements of the coupling matrix has been done in order to improve the electrical response of the model based on resonators. Note that from now the coupling matrix is not shown explicitly as its relevant elements are shown in the form included in Tab. 3.2. An optimisation is performed through an optimising routine which operates an algorithmic procedure over a set of variables in order to reduce a *cost function*. The optimisation algorithm

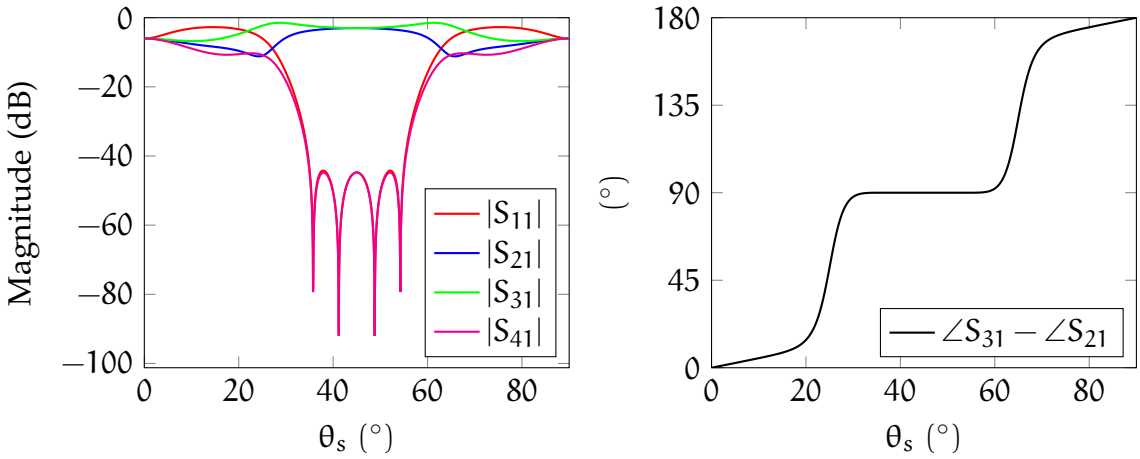

(a) Transmission lines - magnitude response

(b) Transmission lines - output phase shift

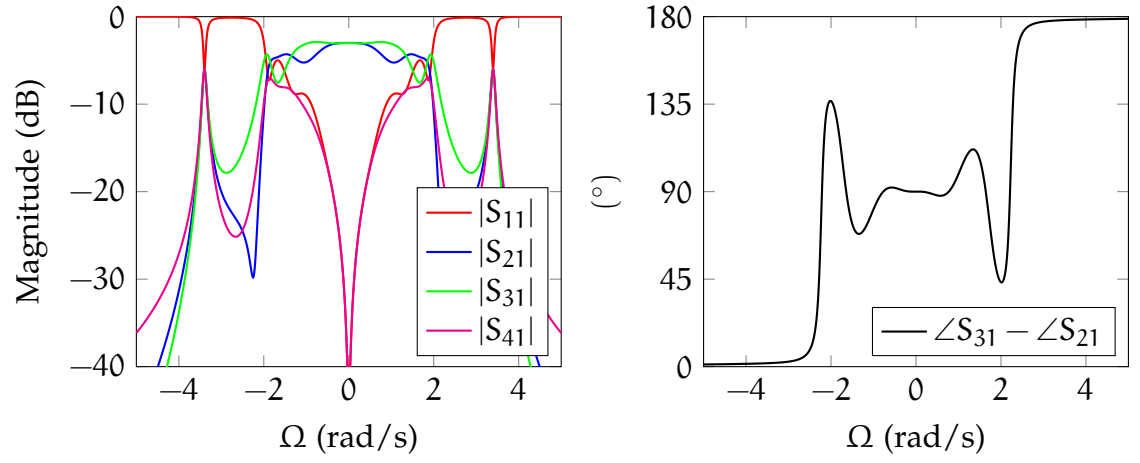

(c) Resonators - magnitude response

(d) Resonators - output phase shift

Figure 3.10: Frequency response of 5-branch BGC based on transmission lines and on resonators.

used here is the gradient-based to find the local minima while the starting variables are the coupling coefficients of straight and shunt elements shown in Tab. 3.2. The cost function developed calculates the difference of magnitude parameters between the model based on transmission lines and the one based on resonators. It can be defined as follows:

$$\begin{aligned}\mathrm{Err} = \sum_{f\in P} \Bigg\{ \left| |S_{11}^{(t)}(f)| - |S_{11}(f)| \right|^2 + \left| |S_{21}^{(t)}(f)| - |S_{21}(f)| \right|^2 + \\ + \left| |S_{31}^{(t)}(f)| - |S_{31}(f)| \right|^2 + \left| |S_{41}^{(t)}(f)| - |S_{41}(f)| \right|^2 \Bigg\} \end{aligned} \tag{3.33}$$

where P is a set of equally distributed frequencies in the operational bandwidth and $S^{(t)}$ are the theoretical scattering parameters calculated with the standard technique for transmission lines. Naturally, as there is a different type of normalised frequency between the model based on resonators and the one with transmission line, the frequency should be mapped using the eq. (3.19). The shunt and straight couplings of the example shown for 5 branches are optimised with the cost function of eq. (3.33) obtaining the following values:

$$M_{\mathrm{shunt,opt}}^{(i)} = \{0.0142; 0.3403; 0.8134; 0.3403; 0.0142\} \tag{3.34a}$$

$$M_{\mathrm{straight,opt}}^{(i)} = \{0.9811; 1.0208; 1.0208; 0.9811\} \tag{3.34b}$$

The optimised response is shown in Fig. 3.11. The optimisation is able to define an operational bandwidth where the coupler based on resonators exhibits almost constant properties. In the band $|\Omega| \leqslant 1$ the magnitude of S_{31} is in the range between $-2.6\,\mathrm{dB}$ and $-3.25\,\mathrm{dB}$. The return loss and isolation shows a ripple behaviour below $-20\,\mathrm{dB}$ while the output phase difference is 90° with ripples that are inside $\pm 0.6°$. However, it is also important to notice that in the magnitude there are still two peaks outside the band. The degree of freedom for the optimiser can be increased by increasing the number of branches of the coupler.

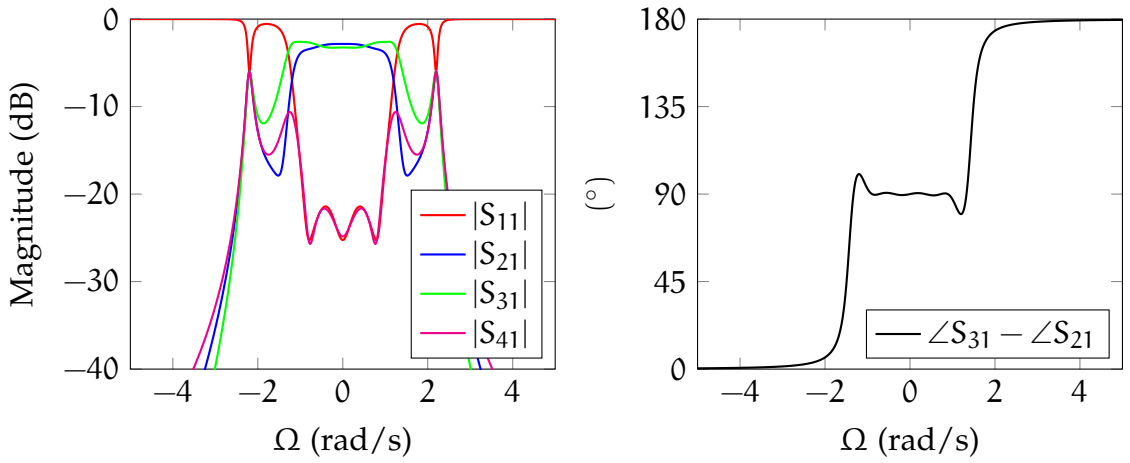

(a) Optimised Magnitude response

(b) Optimised output phase shift

Figure 3.11: Optimised frequency response of 5-branch BGC based on resonators.

Table 3.3: Elements of the 7-branch Tchebycheff hybrid coupler based on resonators. Synthesis parameters are $n = 7$, $K = 50$, $R = 1$, $\theta_c = 35°$ and $Q_e = 1$.

Element i	a_i	b_i	$M^{(i)}_{shunt}$	$M^{(i)}_{straight}$	$M^{(i)}_{shunt,opt}$	$M^{(i)}_{straight,opt}$
1	28.8474	0.9361	0.0347	1.0683	−0.0696	0.8756
2	5.6115	0.7241	0.1782	1.3811	−0.0292	0.7128
3	1.6896	0.5209	0.5918	1.9199	0.3509	1.0783
4	0.9973	0.5209	1.0027	1.9199	1.1956	1.0783
5	1.6896	0.7241	0.5918	1.3811	0.3509	0.7128
6	5.6115	0.9361	0.1782	1.0683	−0.0292	0.8756
7	28.8474		0.0347		−0.0696	

The same 2-step technique can be applied to the example of 7-branch coupler of Fig. 3.5. As before, the initial values of the shunt and straight couplings are calculated with formulas of eq.s (3.32) and then optimised with the cost function of eq. (3.33). The table of impedances and coupling coefficients is updated in order to accommodate two additional columns for the optimised values as shown in Tab. 3.3. The starting point, calculated through eq.s (3.32), of the resonant hybrid is shown for the magnitude in Fig. 3.12b and for the output phase shift in Fig. 3.12c. The schematic is shown in Fig. 3.12a with indicated the coupling of the straight lines as M^i_{st} and the ones of shunt couplings as M^i_{sh}, where i is the number of the element. This example demonstrates a more complicated is the response of with an higher number of branches. Again, the perfect match of the equivalence technique is granted

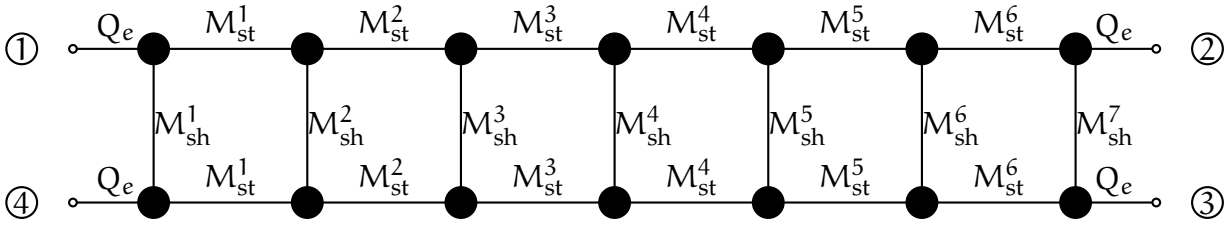

(a) Schematic

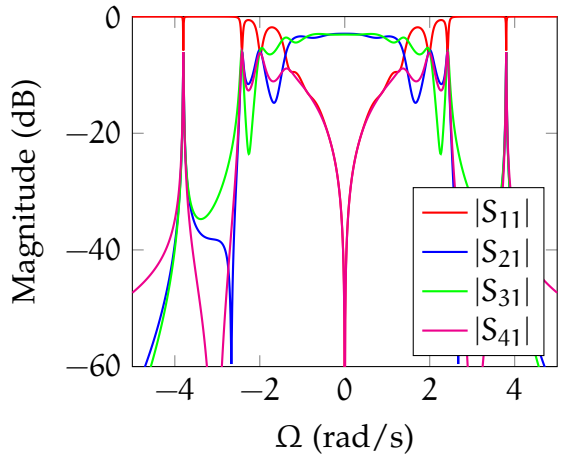

(b) Starting point magnitude response

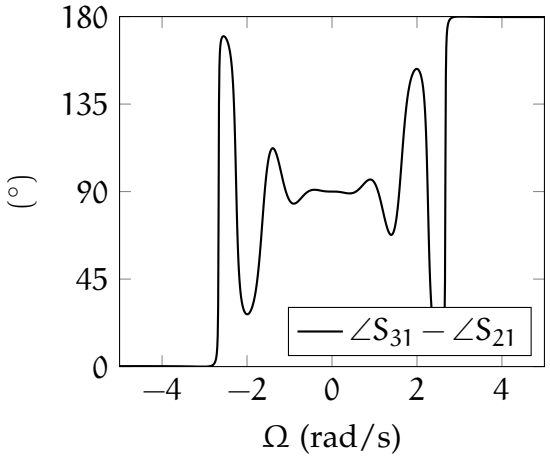

(c) Starting point output phase shift

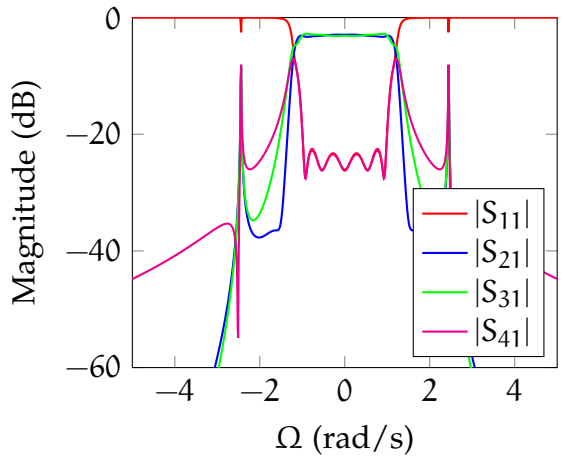

(d) Optimised magnitude response

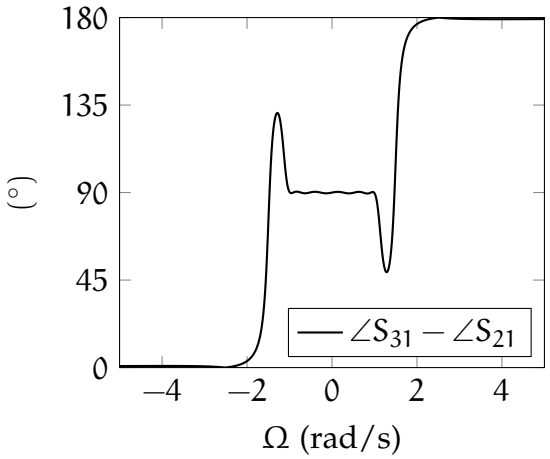

(e) Optimised output phase shift

Figure 3.12: Starting point and optimised frequency response of 7-branch BGC based on resonators. Initial synthesis parameters are $n = 7$, $K = 50$, $R = 1$, $\theta_c = 35°$ and $Q_e = 1$.

only at centre frequency. The optimisation shown in Fig. 3.12d for the magnitude, and in Fig. 3.12e for the output phase represent a significant improvement with regard the starting point. Inside the operation bandwidth of the optimised version it is possible to recognise an almost equal power splitting as the $|S_{31}|$ is in the range between -2.75 dB and -3.17 dB. The return loss shows 5 poles in the in-band with a RL and isolation better than 22 dB. Also the output phase characteristic shows good performances as the drift from the nominal level of 90° is of $\pm 0.5°$. Also for this case, two peaks are visible in the out-band of the magnitude response. The negative values shown in the column of the shunt coefficients of Tab. 3.3 are responsible for the appearance of TZs.

The procedure shown so far for the synthesis of BGC based on resonators is not able to provide a filtering response able to give a fully Tchebycheff (or Butterworth) transfer function. The optimisation of the coupling matrix improves the electrical responses, however the relation governing the RL, the number of visible poles and the out-band peaks is not known. It is important to underline that with the method proposed, there are no assumptions made on the characteristic required and no polynomials have been used for the derivation of the transfer function. It is also clear that there is not a direct relation between the number of visible poles of the magnitude response and the degree (number of resonators) of the network, as it is with conventional filters. Thus, a more complex synthesis technique needs to be investigated. This is stated in the next section.

3.4 POLYNOMIALS BASED SYNTHESIS

This section is focused on the definition of a new set of characteristic polynomials in order to force the transfer function of the filter to comply with the requirements of bandwidth, selectivity and RL. It will be shown that it is not possible to define a-

priori a set of polynomials because of the limitations of general synthesis techniques for multi-port circuits. In the following section a more detailed explanation on why the problems encountered here will be addressed.

Once the polynomials are defined, the procedure described in appendix B is applied in order to get the coefficients of the coupling matrix. The following iterative procedure [40, 58] is used to find the characteristic polynomials taking into account the particular symmetries of the circuit. The scattering parameters can be expressed as a ratio between a numerator and a common denominator:

$$S_{11} = \frac{F(s)}{E(s)} \tag{3.35a}$$

$$S_{21} = \frac{P(s)}{\epsilon_1 E(s)} \tag{3.35b}$$

$$S_{31} = \frac{Q(s)}{\epsilon_2 E(s)} \tag{3.35c}$$

$$S_{41} = \frac{X(s)}{E(s)} \tag{3.35d}$$

Among the main characteristics of the 90° hybrid coupler are:

1. perfect isolation at port 4,
2. output phase shift of 90°.

Thus, the following simplifications can be applied to the polynomials of eq. (3.35):

$$X(s) = 0 \tag{3.36a}$$

$$Q(s) = j\sqrt{\alpha}P(s) \tag{3.36b}$$

where the term α controls the output power splitting ratio. Combining the simplifications of eq.s (3.36) into the scattering polynomials of eq. (3.35), the loss-less condition is defined as

$$F(s)F^*(-s) + \frac{P(s)P^*(-s)}{\epsilon_1^2} + \alpha\frac{P(s)P^*(-s)}{\epsilon_2^2} = E(s)E^*(-s) \tag{3.37}$$

Table 3.4: Coefficients of the new set of rational scattering polynomials

Degree of s	E(s)	F(s)	P(s)	Q(s)
2	1	1		
1	4.0967	0		
0	8.8914	0.5	j	1

The value of the ripple constants are directly derived from eq. (3.37) and they have the form [58]:

$$\epsilon_1 = \sqrt{\frac{1+\alpha}{10^{-L_r/10}-1}} \cdot \left|\frac{P(s)}{F(s)}\right|_{s=\pm j} \tag{3.38}$$

$$\epsilon_2 = \sqrt{\frac{1+\alpha}{\alpha(10^{-L_r/10}-1)}} \cdot \left|\frac{P(s)}{F(s)}\right|_{s=\pm j} \tag{3.39}$$

Eq. (3.37) is similar to the Feldtkeller equation for filters. In fact the polynomial $P(s)$ is determined directly from the position (if any) of the transmission zeros of the response and in eq. (3.37) only 2 unknown polynomials, $F(s)$ and $E(s)$, are present and to be determined. Thus, it is possible to use the same iteration technique for filters in order to determine the element $F(s)$ [40]. As usual, once all the polynomials have been calculated, the common denominator $E(s)$ is found by selecting its roots that lie on the left-hand side of the complex plane (Hurwitz polynomial).

Here the example is given of the synthesis of the polynomials for a 2×2 hybrid with a Tchebycheff response, 25 dB RL, 2 reflection zeros and equal output power splitting. As the result of the synthesis, the coefficients of the polynomials are listed in Tab. 3.4. The other coefficients are obtained from eq.s (3.37), (3.38) and (3.39) resulting:

$$\alpha = 1 \tag{3.40a}$$

$$\epsilon_1 = 0.1593 \tag{3.40b}$$

$$\epsilon_2 = 0.1593 \tag{3.40c}$$

The scattering polynomials of Tab. 3.4 are shown in Fig. 3.13. The magnitude is represented in Fig. 3.13a and it shows a perfect equal ripple at -25 dB as well as

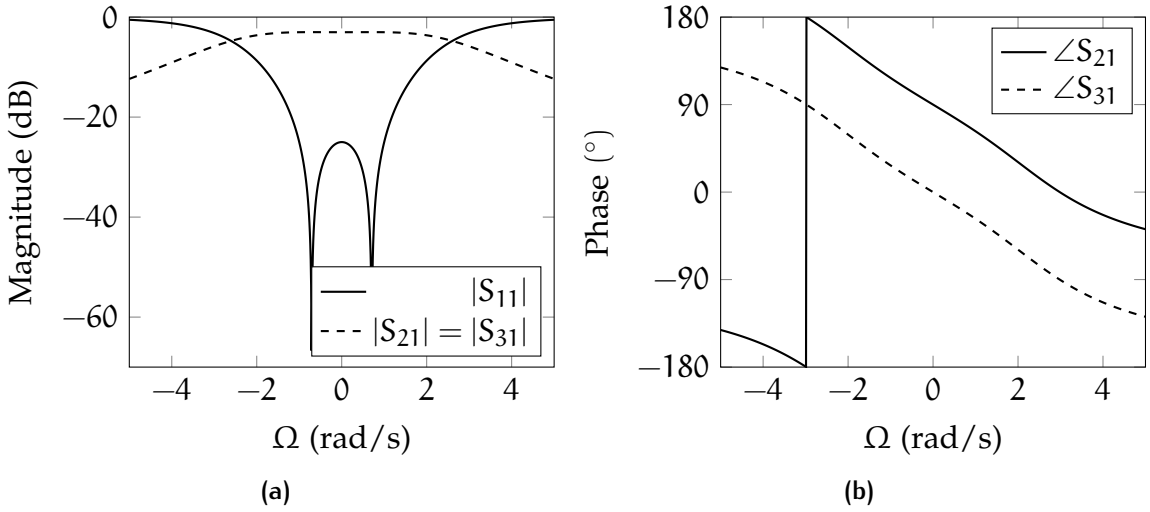

Figure 3.13: Scattering parameters from polynomial synthesis

a perfect equal power splitting among ports 2 and 3. The output phase of ports 2 and 3 is shown in Fig. 3.13b where a 90° shift is maintained constant across all the frequencies. So far only the scattering parameters for a signal entering from port 1 have been calculated. Due to the symmetries of the circuit it is easy to define the 4×4 scattering matrix entirely. Let define the reflected, the through and the coupled waves respectively with the symbols ρ, τ and γ. The final device is symmetric and exhibits the same responses independently with respect the input port:

$$\mathbf{S} = \begin{bmatrix} \rho & \tau & \gamma & 0 \\ \tau & \rho & 0 & \gamma \\ \gamma & 0 & \rho & \tau \\ 0 & \gamma & \tau & \rho \end{bmatrix} \tag{3.41}$$

Matrix (3.41) is built in order to keep the symmetries and the fundamental *unitary* condition

$$\mathbf{S}\mathbf{S}^* = \mathbf{I_p} \tag{3.42}$$

where $\mathbf{I_p}$ is the $p \times p$ unitary matrix. It is quite obvious the relation between the elements of matrix (3.41) and the constituting parameters of eq.s (3.35) and (3.36)

$$\rho = S_{11}(s) = \frac{F(s)}{E(s)} \tag{3.43a}$$

$$\tau = S_{21}(s) = \frac{P(s)/\epsilon_1}{E(s)} \tag{3.43b}$$

$$\gamma = S_{31}(s) = j\sqrt{\alpha}\frac{P(s)/\epsilon_2}{E(s)} \tag{3.43c}$$

The coupling matrix is directly calculated from the expression of eq. (3.41) through the synthesis technique for multi-port circuits described in [43]. Hence, the first step is to calculate the rational polynomials (numerators and common denominator) of the admittance matrix. Unfortunately, there do not exist closed formulas to derive the coefficients of admittance polynomials from the ones of Tab. 3.4 for this circuit. Thus, the admittance matrix is found, in first instance, as a set of continues curves with the well known relation

$$\mathbf{Y} = (\mathbf{I_p} - \mathbf{S})(\mathbf{I_p} + \mathbf{S})^{-1}$$

Then, the Cauchy method is used in order to get the coefficients of the polynomials [50]. Due to the symmetries of the circuit, it is possible to demonstrate the validity of the following relations

$$[\mathbf{Y}]_{22} = [\mathbf{Y}]_{33} = [\mathbf{Y}]_{44} = [\mathbf{Y}]_{11} \tag{3.44a}$$

$$[\mathbf{Y}]_{23} = [\mathbf{Y}]_{14} \tag{3.44b}$$

$$[\mathbf{Y}]_{24} = [\mathbf{Y}]_{13} \tag{3.44c}$$

$$[\mathbf{Y}]_{34} = [\mathbf{Y}]_{12} \tag{3.44d}$$

The computed polynomials are expressed in Tab. 3.5 with common denominator $y_d(s)$ and the numerators of the most relevant elements of the admittance matrix (the

Table 3.5: Coefficients of the polynomials for the admittance matrix

Degree of s	$y_d(s)$	$Y_{11n}(s)$	$Y_{21n}(s)$	$Y_{31n}(s)$	$Y_{41n}(s)$
6	1				
5	4.0248	2.1311			
4	18.2356	7.6811	−j3.2449	−3.1536	
3	34.8829	30.2821	−j12.7094	−12.7299	
2	76.8292	43.8445	−j42.4119	−41.5554	j20.2034
1	44.8283	86.8289	−j59.1722	−57.5828	j38.2476
0	97.9201	4.1459	−j128.4211	−8.5620	j91.0106

others are obtained directly due to the symmetries of the network). In this table all the coefficients are normalized to the highest degree of the common denominator since it is preferred to have them as monotonic polynomials. It is interesting to note that the degree of the common denominator $y_d(s)$ is 3 times the degree of the polynomials of the scattering parameters. Moreover, the degree of y_d corresponds to the number of resonators in the resonant circuit, meaning that there will be 6 resonators in order to implement a network with the given specifications. Another consideration is that the coefficients of Tab. 3.5 are, for each parameters, either pure real or pure imaginary. The direct synthesis described in [43] states that it is better to calculate the coupling coefficients of an equivalent transversal network and then to get the final topology through a set of matrix similarities. The main reason is that closed simple formulation, relates the elements of the coupling matrix with the coefficients of the admittance matrix are provided [44]. Among them, the elements of the diagonal matrix of the internal couplings of the network ($\mathbf{M_n}$), are the roots of $y_d(s)$. It is possible to show that the roots of $y_d(s)$ have both a real and an imaginary part. This fact is critical because, in order to use this theoretical technique, the frequency of the poles of the function are supposed to be all imaginary. In Fig. 3.14 the poles/zeros diagrams of the polynomials listed in Tab. 3.5 are shown. All the elements come in complex conjugate pairs and all have a real part. This fact is a major problem because it shows that the elements of the transversal network are complex, and consequently not feasible in practice. A correct behaviour would be with the zeros of the admittance matrix lying

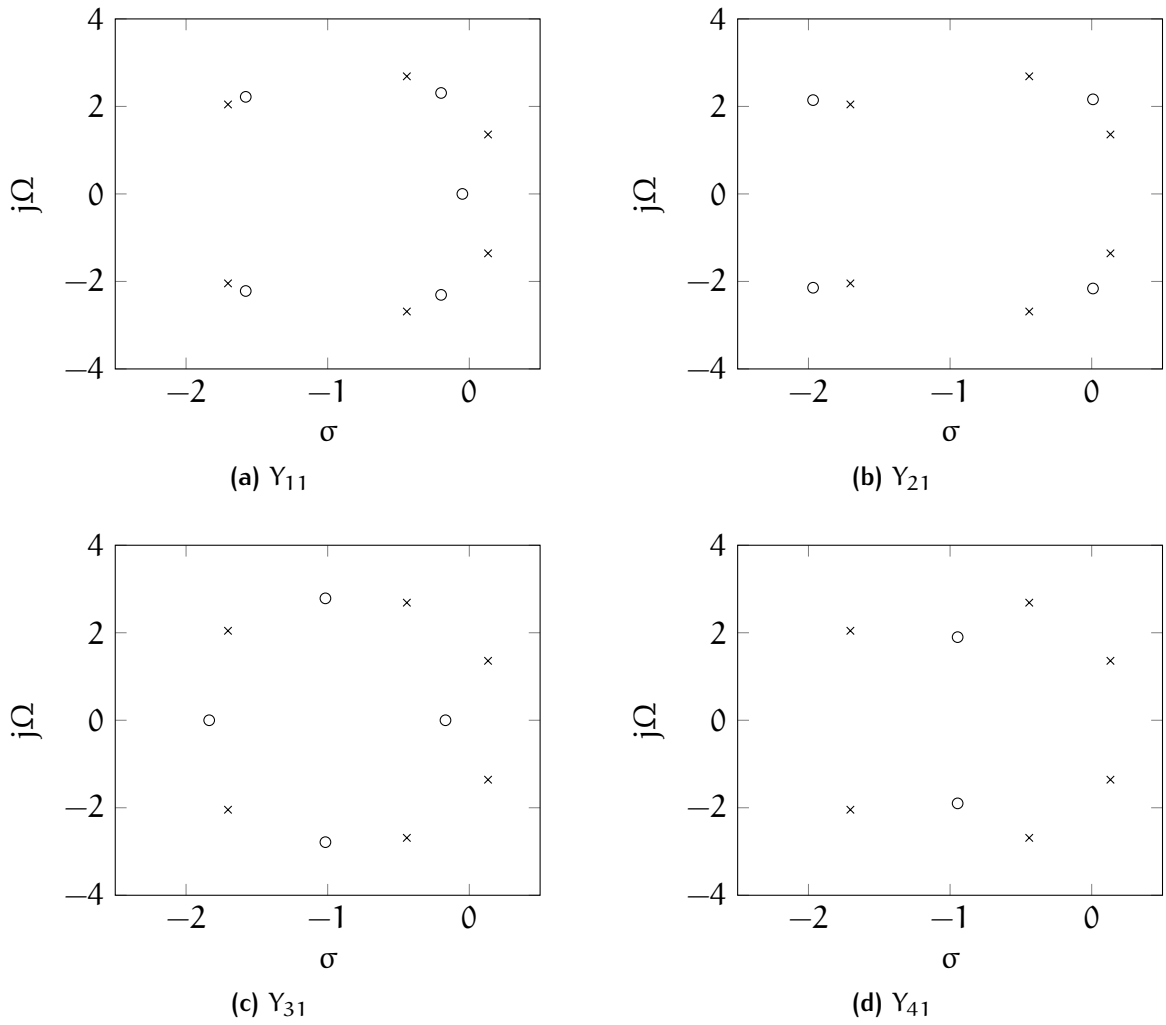

(a) Y_{11} **(b)** Y_{21}

(c) Y_{31} **(d)** Y_{41}

Figure 3.14: Poles (x) and zeros (o) diagram of the elements of the admittance matrix

in complex conjugate pairs on the axis of $\sigma = 0$. Obviously, this also compromises the coupling between internal and external nodes since they are related each other with the residues associated to the poles of the function, hence this would also produce complex coefficients in the coupling matrix $\mathbf{M_{pn}}$. One approximated solution could be to suppress the real part of the poles and the imaginary part of the residues, with a general optimization of the coupling matrix at the end. However, the problem of the real component of the poles has already seen in the synthesis of diplexers when the two pass-band are very close [44]. In that case the strong interaction between the two channels introduces the unwanted real part in the poles, leading to a further optimization of the final coupling matrix. For the case of the diplexers, the approximation was possible since the real part was significantly lower with respect the imaginary part, and not all the poles had it. This fact can be understood since the interaction between the two channels of the diplexer was relatively low. Only for very narrow guard band the problem does begin to affect the validity of the theory [43]. For the hybrid coupler it is possible to conclude that the interaction of the two output signals, that share the same bandwidth, is so strong that a not negligible real part is present in each pole. Hence, the approximation of eliminating the real part from the poles would not work in this case because the computed result, and consequently the starting point of an optimisation, would be very far for a gradient-based algorithm.

The problem seen here is a demonstration of one of the limitations of the general synthesis procedure described in section 2.4. The hybrid coupler is different from the diplexer because the transfer function for the transmission ports (ie. port 2 and 3) is the same. For this reason an a-priori definition of the polynomials without considering the topology and characteristics of the 2×2 hybrid based on resonators is not possible.

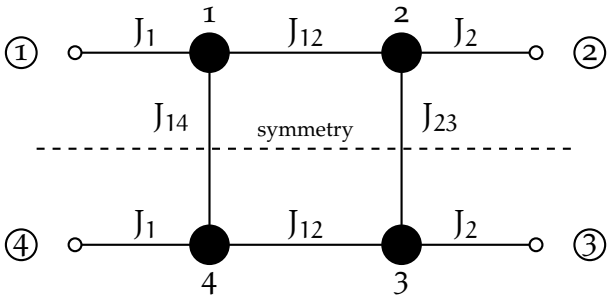

(a) Quadruplet of resonators and ports

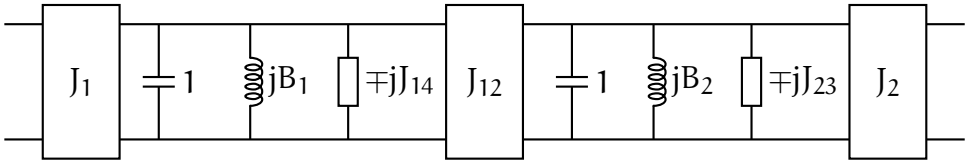

(b) Schematic of the even/odd network

Figure 3.15: Analysis of quadruplet of resonators and ports

3.5 ANALYSIS OF 4-RESONATOR HYBRID

The definition of the polynomials of the transfer function in the previous section shows that it is not possible to make the assumption of perfect isolation and equal transfer function made in eq.s (3.36). Moreover, the topology of the network and the numbers of resonators were not defined at the beginning, demonstrating that a deeper understanding of the intrinsic behaviour of the network is needed. Thus, in this section the characteristics of the response that a quadruplet of resonators with 4 ports can produce will be studied in detail. Here, an analytical analysis will show the constraints on the characteristic polynomials, while a novel topological method will provide a fast way to predict the frequency response of these multi-port circuit [106].

3.5.1 Analytical analysis

The fundamental quadruplet of resonators of the hybrid coupler with filtering is shown in Fig. 3.15a with port numbers indicated. In this figure the symmetry plane of the structure through a dashed line is also shown. Hence, it is very convenient to

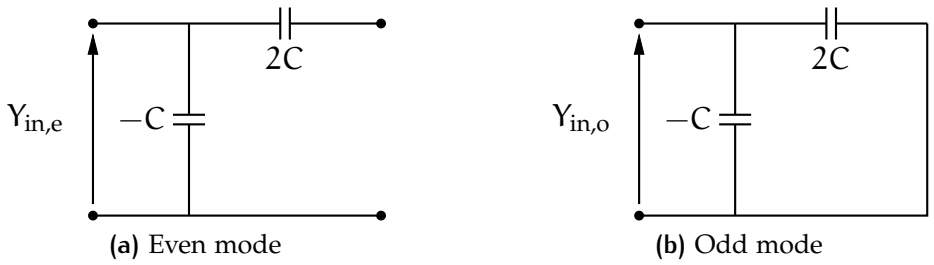

(a) Even mode **(b)** Odd mode

Figure 3.16: Even/odd mode shunt inverter

study the response of this network with the even/odd mode superposition approach [72]. The electromagnetic couplings can be modelled through an admittance inverter J with the subscripts indicating the pair of resonators at the two ends of the inverter. The model is narrow band and the inverters are considered ideal. In this way the scattering response of the 4-port device is obtained from two simple 2-port networks (even and odd network) through the eq.s (3.14). The network to study is shown in Fig. 3.15b: the first inverter J_1 is represented with the typical admittance inverter of inversion parameter J_1, while the resonator in the low-pass domain is represented by a parallel of a unitary capacitor and a FIR B to take into account the asymmetries of the response [34]. The symmetry plane of Fig. 3.15a cuts the shunt inverters in the middle with, alternatively a magnetic or an electric wall: the inverter can be represented by means of a π network with three capacitors shown in Fig. 2.8b with inversion coefficient $J = \omega C$. The symmetry plane is placed in the middle of the π network of capacitors so the series admittance element is split in 2. For the even mode place an open circuit at the symmetry plane as shown in Fig. 3.16a. The input admittance is given by the contribution of the shunt element only because the other has an open circuit at the end, so no current is flowing, giving

$$Y_{in,e} = j\omega(-C) = -jJ \tag{3.45}$$

where the inversion parameter $J = \omega C$ has been substituted. When the odd mode is considered a shorted circuit is placed as shown in Fig. 3.16b, the input admittance is the parallel of the two capacitors:

$$Y_{in,o} = j\omega(-C + 2C) = jJ \tag{3.46}$$

The shunt inverter is represented in Fig. 3.15b with a parallel admittance of value $\mp jJ_{14}$ or $\mp jJ_{23}$ with the sign depending on the mode considered in accordance with eq.s (3.45) and (3.46). The study is carried out by calculation of the $ABCD$ matrices for both even and odd networks. For the even mode the inputs (ports 1 and 4) are excited with the same signal, thus a magnetic wall is placed on the symmetry plane and the circuit is split with an open circuit [107]:

$$\begin{bmatrix} A_e & B_e \\ C_e & D_e \end{bmatrix} = \begin{bmatrix} 0 & \frac{j}{J_1} \\ jJ_1 & 0 \end{bmatrix} \times \begin{bmatrix} 1 & 0 \\ s + jB_1 - jJ_{14} & 0 \end{bmatrix} \times \\ \times \begin{bmatrix} 0 & \frac{j}{J_{12}} \\ jJ_{12} & 0 \end{bmatrix} \times \begin{bmatrix} 1 & 0 \\ s + jB_2 - jJ_{23} & 0 \end{bmatrix} \times \begin{bmatrix} 0 & \frac{j}{J_2} \\ jJ_2 & 0 \end{bmatrix} \tag{3.47}$$

The odd network is obtained when the input signals are antisymmetric and an electric wall is placed between the two halves of the circuit. This can be done by closing the two parts with a short circuit, thus becoming:

$$\begin{bmatrix} A_o & B_o \\ C_o & D_o \end{bmatrix} = \begin{bmatrix} 0 & \frac{j}{J_1} \\ jJ_1 & 0 \end{bmatrix} \times \begin{bmatrix} 1 & 0 \\ s + jB_1 + jJ_{14} & 0 \end{bmatrix} \times \\ \times \begin{bmatrix} 0 & \frac{j}{J_{12}} \\ jJ_{12} & 0 \end{bmatrix} \times \begin{bmatrix} 1 & 0 \\ s + jB_2 + jJ_{23} & 0 \end{bmatrix} \times \begin{bmatrix} 0 & \frac{j}{J_2} \\ jJ_2 & 0 \end{bmatrix} \tag{3.48}$$

The final scattering parameters will be obtained solving the eq.s (3.12) and (3.13) for the even and odd mode, and finally to use these relation in eq.s (3.14). All the scatter-

ing parameters are rational polynomials in the complex low-pass variable $s = \sigma + j\Omega$. The elements of matrix of eq. (3.47) are calculated and expressed as a function of s as:

$$A_e = -j\frac{J_2}{J_1 J_{12}}(s + jB_1 - jJ_{14}) \tag{3.49a}$$

$$B_e = -j\frac{s^2 + js(B_1 + B_2 - J_{14} - J_{23}) + (B_1 - J_{14})(B_2 - J_{23}) + J_{12}^2}{J_1 J_2 J_{12}} \tag{3.49b}$$

$$C_e = -j\frac{J_1 J_2}{J_{12}} \tag{3.49c}$$

$$D_e = -j\frac{J_1}{J_2 J_{12}}(s + jB_2 - jJ_{23}) \tag{3.49d}$$

The same process is performed for the odd mode of eq. (3.48):

$$A_o = -j\frac{J_2}{J_1 J_{12}}(s + jB_1 + jJ_{14}) \tag{3.50a}$$

$$B_o = -j\frac{s^2 + js(B_1 + B_2 + J_{14} + J_{23}) + (B_1 + J_{14})(B_2 + J_{23}) + J_{12}^2}{J_1 J_2 J_{12}} \tag{3.50b}$$

$$C_o = -j\frac{J_1 J_2}{J_{12}} \tag{3.50c}$$

$$D_o = -j\frac{J_1}{J_2 J_{12}}(s + jB_2 + jJ_{23}) \tag{3.50d}$$

For both the modes, terms $B_{e,o}$ are polynomials of second degree, $A_{e,o}$ and $D_{e,o}$ are of first degree and $C_{e,o}$ are constants. As the highest degree of the $ABCD$ parameters is 2, then the denominators of $S_{11}^{e,o}$ and $S_{21}^{e,o}$ are also of same degree:

$$\begin{aligned}
A_e + B_e + C_e + D_e &= a_e s^2 + b_e s + c_e \\
a_e &= -j\frac{1}{J_1 J_2 J_{12}} \\
b_e &= -j\left[\frac{j(B_1 + B_2 - J_{14} - J_{23})}{J_1 J_2 J_{12}} + \frac{J_1}{J_2 J_{12}} + \frac{J_2}{J_1 J_{12}}\right] \\
c_e &= -j\frac{J_{12}^2 + j(B_1 - J_{14})(B_2 - J_{23})}{J_1 J_2 J_{12}} - j\frac{J_1 J_2}{J_{12}} + \\
&\quad + \frac{J_2(B_1 - J_{14})}{J_1 J_{12}} + \frac{J_1(B_2 - J_{23})}{J_2 J_{12}}
\end{aligned} \tag{3.51}$$

and, for the odd mode:

$$\begin{aligned}
A_o + B_o + C_o + D_o &= a_o s^2 + b_o s + c_o \\
a_o &= -j\frac{1}{J_1 J_2 J_{12}} \\
b_o &= -j\left[\frac{j(B_1 + B_2 + J_{14} + J_{23})}{J_1 J_2 J_{12}} + \frac{J_1}{J_2 J_{12}} + \frac{J_2}{J_1 J_{12}}\right] \\
c_o &= -j\frac{J_{12}^2 + j(B_1 + J_{14})(B_2 + J_{23})}{J_1 J_2 J_{12}} - j\frac{J_1 J_2}{J_{12}} + \\
&\quad + \frac{J_2(B_1 + J_{14})}{J_1 J_{12}} + \frac{J_1(B_2 + J_{23})}{J_2 J_{12}}
\end{aligned} \tag{3.52}$$

These equations are general and show that, without assumptions on the relations of parameters (additional symmetries) in Fig. 3.15a, the degree of the denominators of the final scattering is 4. This is because of the sum of two fractional expressions with different denominators for the calculation of the scattering polynomial of eq.s (3.14). For instance, eq.s (3.51) and (3.51) constitute the denominators of the even and odd part to be calculated in (3.14). They are both of degree 2 and are different. Thus, it derives that to compute the scattering parameters as defined in eq. (3.14), the sum of all the even and odd parameters are made through elements that do not share a common denominator.

In order to obtain a 90° hybrid coupler the following conditions are to be satisfied [106]:

$$B_1 = B_2 \tag{3.53a}$$

$$J_1 = J_2 \tag{3.53b}$$

$$J_{14} = J_{23} \tag{3.53c}$$

This is because the structure of the a quadrature 2-branch hybrid preserves the symmetries with regards any input and output, as it was for the coupler of Fig. 3.1. The set of conditions of eq.s (3.53) simplifies all the ABCD parameters and consequently the relations of the common denominator of scattering polynomials. Again, eq. (3.53)

is substituted in eq.s (3.49) and (3.50). The highest degree of the polynomials of the ABCD terms is 2, hence the degree of the denominators in eq.s (3.12) and (3.13) is of the second order with the following even coefficients:

$$\begin{aligned} A_e + B_e + C_e + D_e &= a_e s^2 + b_e s + c_e \\ a_e &= -j\frac{1}{J_1^2 J_{12}} \\ b_e &= -j\left[\frac{2}{J_{12}} + \frac{2j(B_1 - J_{14})}{J_1^2 J_{12}}\right] \\ c_e &= -j\frac{J_{12}^2 - (B_1 - J_{14})^2}{J_1^2 J_{12}} - j\frac{J_1^2 + 2j(B_1 - J_{14})}{J_{12}} \end{aligned} \tag{3.54}$$

and odd ones:

$$\begin{aligned} A_o + B_o + C_o + D_o &= a_o s^2 + b_o s + c_o \\ a_o &= -j\frac{1}{J_1^2 J_{12}} \\ b_o &= -j\left[\frac{2}{J_{12}} + \frac{2j(B_1 + J_{14})}{J_1^2 J_{12}}\right] \\ c_o &= -j\frac{J_{12}^2 - (B_1 + J_{14})^2}{J_1^2 J_{12}} - j\frac{J_1^2 + 2j(B_1 + J_{14})}{J_{12}} \end{aligned} \tag{3.55}$$

Here the coefficients are all different and the overall highest degree of the scattering parameter denominators is still 4 as discussed above. The relations obtained in eq.s (3.54) and (3.55) are substituted in eq.s (3.12) and (3.13) and finally into eq. (3.14). The scattering polynomials are expressed in the following rational notation:

$$S_{11} = \frac{N_{11}^{(4)}}{D^{(4)}} \tag{3.56a}$$

$$S_{21} = \frac{N_{21}^{(2)}}{D^{(4)}} \tag{3.56b}$$

$$S_{31} = \frac{N_{31}^{(1)}}{D^{(4)}} \tag{3.56c}$$

$$S_{41} = \frac{N_{41}^{(2)}}{D^{(4)}} \tag{3.56d}$$

where D is the common denominator and N_{ij} are the polynomials numerators. Between parenthesis is the degree of each polynomial. All the numerators are different and the degrees of the transmission parameters S_{21} and S_{31} differs. The isolation is not perfectly zero but it is governed by a rational expression of a denominator of degree 4 and a numerator of second order. In this scenario it is clear that it is not possible to apply any Tchebycheff transfer function as there are 5 independent polynomials (4 numerators and 1 common denominator) that must comply with the unitary condition and of course eq. (3.56). The complexity resides in finding a feasible transfer function with the polynomials expressed in equation eq.s (3.56), and in solving a system of equations to get the unique solutions in terms of circuital parameters. This makes the analytical approach not practical for the 90° hybrid. All the considerations have been made for the relatively simple 2×2 hybrid with two branches, but it is clear that increasing the number of branches an analytical synthesis could lead to even more complex constraints on the polynomials.

3.5.2 Topological approach

As the synthesis of the coupling matrix of the 90° hybrid was originally based on equivalence with the correspondent circuit of transmission lines, the analysis was initially carried out with the traditional even/odd modes method [72]. Indeed, the isolated port is 4, while the two outputs are ports 2 and 3. This is a known fact for the version based on transmission lines, but it has a relevant impact in the transformation to the coupled resonators circuit. Consider Fig. 3.17a: a signal is incident on port 1, with the consequence of leaving port 4 isolated [72]. Port 2 is excited via resonators 1-2 with coupling M_{12} while port 3 is excited via resonators 1-2-3 and couplings M_{12} and M_{23}. All coupling coefficients are positive. Thus, at the central frequency, there is always a phase shift of 90° due to the additional coupling between the two output ports. An immediate consequence is that S_{21} and S_{31} are two transfer functions

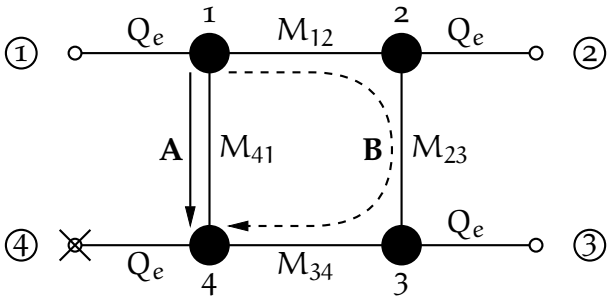

(a) Schematic with interference paths

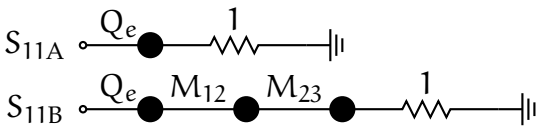

(b) Equivalent circuits of paths A and B

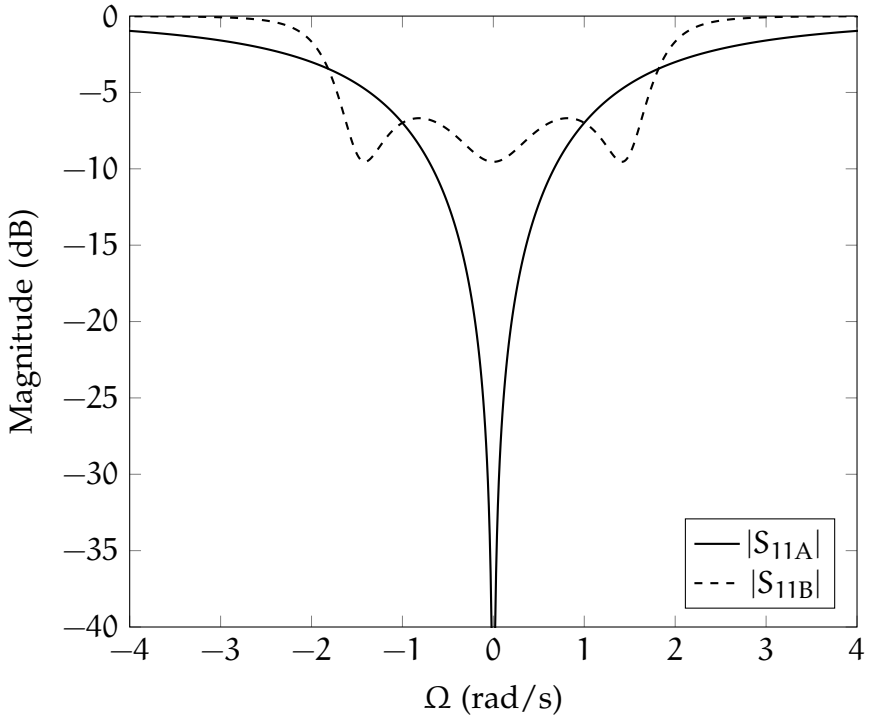

(c) Frequency response of paths A and B

Figure 3.17: Estimated interference at port 4 of the 90°, 4-resonator hybrid coupler.

having different number of resonators. Hence, it is not possible to have same filtering responses. Fig. 3.17a depicts a cross at the isolated port as well as two interfering signals A and B with a continuous and dashed line. The two contributions create the interference at resonator 4, indeed at the central frequency this resonator can be virtually removed from the circuit. Under this condition, path A is formed by resonator 1 while path B by resonators 1-2-3 with both sharing the first resonator, as shown in Fig. 3.17b. Here, paths A and B (not considering ports 2 and 3) are represented as two filters loaded with a normalized impedance with the absence of signal in resonator 4 caused by the destruction of the two out of phase signals. If output ports 2 and 3 are neglected, their responses are shown in Fig. 3.17c. It is evident that there is a presence of a common pole on both characteristics in the operational bandwidth ($|\Omega| < 1$) while two extra poles are present at $\Omega = \pm 1.4$ (out of band). Since path A is formed only by resonator 1, and it exhibits a pole at the central frequency, the same pole is also present in the path B (dashed line of Fig. 3.17c). In total, path B is formed by 3 resonators that generate 3 poles in Fig. 3.17. As one of them is shared with path A it is concluded that the pole at central frequency is determined by resonator 1 while the others from resonators 2 and 3. The consequence is that while resonators 2 and 3 generate the peaks in the out-band of Fig. 3.8a, resonator 1 is responsible for the bandwidth of the circuit. The two interferences A and B in resonator 4 assure an acceptable level of isolation only in a relatively narrow bandwidth around the central frequency. The sum of the interferences generate peaks that are unavoidable and intrinsic for this kind of topology. The response found with this topological technique is consistence with the high-order polynomials of eq. (3.56).

This topological discussion has been used mainly to make to understand the properties of the response of the 90° hybrid based on resonators after that an analytical approach shown the complexities of the polynomials. It is important to mention that also the optimiser failed to produce a filtering response comparable to the one of a standard Tchebycheff filter because of the presence of 2 peaks in the out band. With

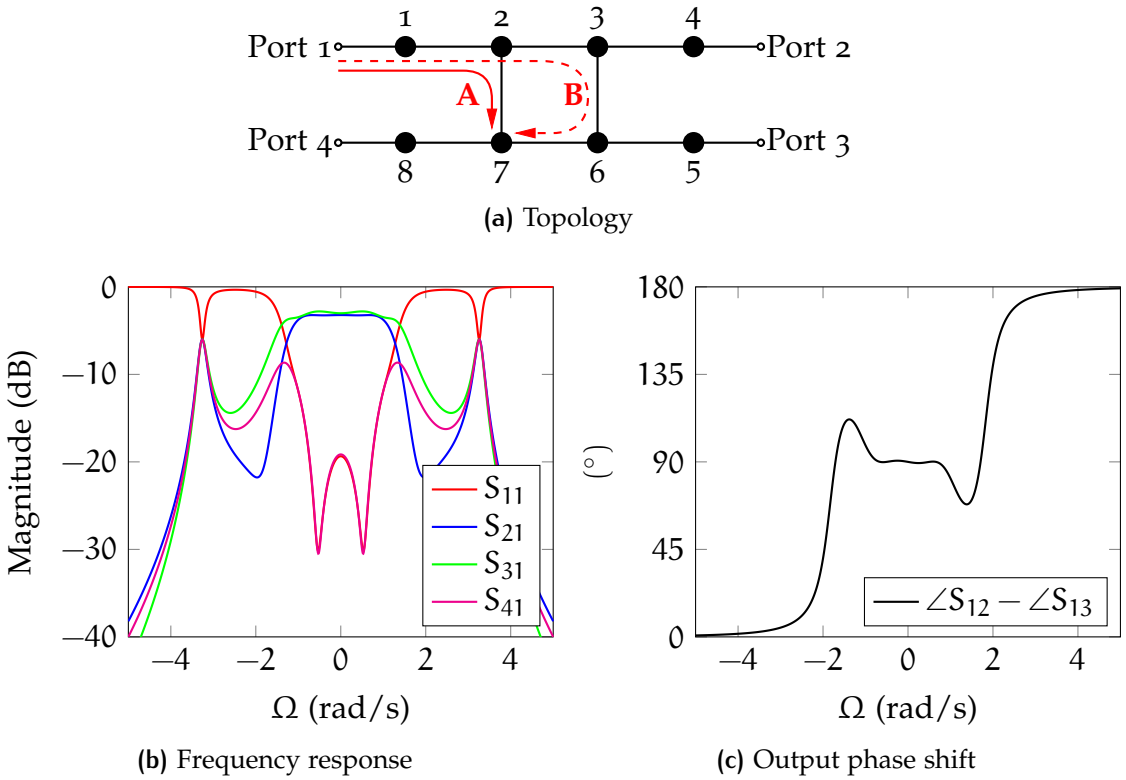

(a) Topology

(b) Frequency response

(c) Output phase shift

Figure 3.18: Eight resonators, 3 dB quadrature hybrid

the topological approach it is not only possible to understand the behaviour of this network, but it can also be used at design level in order to control bandwidth and position of the peaks by means of number of commons resonators in the interference paths.

3.6 IMPLEMENTATION OF 8-RESONATOR HYBRID

The topological approach introduced in the previous section is used here to predict the frequency response of an hybrid coupler based on 8 resonators providing the usual 90° output phase shift. Basically the quadruplet is extended with 1 additional resonator before each port. A schematic can be found in Fig. 3.18a. This configuration increases the degree of the transfer function while the absence of a shunt coupling between resonator 1, 8 and symmetrically between 4 and 5 makes the study easier to

carry out. With this example a practical demonstration of the topological approach introduced earlier will be given. Naturally, it can be proved that if the network is loaded with more resonators, keeping symmetries and the structure of the fundamental quadruplet in the centre, the same analysis is still valid. Fig. 3.18a shows also in red the interference paths generated when the input is applied to port 1. In the previous section it has been stated that the common resonators of paths A and B are the ones controlling the operational bandwidths, while the others are producing peaks in the out-band. With the same criteria it is possible to note here that in resonator 7 paths A and B interfere with a relative difference in phase of 180°. This is because path A reaches resonator 7 through resonators 1-2 while path B has 1-2-3-6 hence the difference of 2 resonant cavities is responsible for the out of phase. To simplify the study as the contribution of resonators 4 and 5 are also neglected here as it was previously. Following this analysis it is reasonable to expect 2 poles in the in-band characteristic while two other poles are outside. Thus a coupling matrix is optimised with the cost function of eq. (3.33) and taking into account the topology of Fig. 3.18a. The result matrix of internal coupling coefficients is

$$\mathbf{M_n} = \begin{bmatrix} 0 & 1.1967 & 0 & 0 & 0 & 0 & 0 & 0 \\ 1.1967 & 0 & 1.6594 & 0 & 0 & 0 & 1.2018 & 0 \\ 0 & 1.6594 & 0 & 1.1967 & 0 & 1.2018 & 0 & 0 \\ 0 & 0 & 1.1967 & 0 & 0 & 0 & 0 & 0 \\ 0 & 0 & 0 & 0 & 0 & 1.1967 & 0 & 0 \\ 0 & 0 & 1.2018 & 0 & 1.1967 & 0 & 1.6594 & 0 \\ 0 & 1.2018 & 0 & 0 & 0 & 1.6594 & 0 & 1.1967 \\ 0 & 0 & 0 & 0 & 0 & 0 & 1.1967 & 0 \end{bmatrix} \tag{3.57}$$

while the matrix of the coefficients with internal resonators and external ports is

$$\mathbf{M_{pn}} = \begin{bmatrix} 1 & 0 & 0 & 0 & 0 & 0 & 0 & 0 \\ 0 & 0 & 0 & 1 & 0 & 0 & 0 & 0 \\ 0 & 0 & 0 & 0 & 1 & 0 & 0 & 0 \\ 0 & 0 & 0 & 0 & 0 & 0 & 0 & 1 \end{bmatrix} \tag{3.58}$$

The matrix of couplings between ports is all zero. Fig. 3.18b shows the magnitude response while Fig. 3.18c is the output phase shift. Basically Fig. 3.18b confirms what said before as 2 poles are clearly visible inside the band $|\Omega| < 1$ while 2 peaks are outside. Also the phase shift is exactly 90° at centre frequency and almost constant over the bandwidth.

An experimental verification is also presented in standard WR90 waveguide with inductive irises. Specifications are $f_0 = 10\,\text{GHz}$, bandwidth of 200 MHz and RL better than 20 dB. The top view schematic of the coupler is shown in Fig. 3.19a. The initial dimensions of the iris apertures are calculated one by one in order to extract the coupling coefficient as introduced in section 2.6 on page 43. Fig. 3.19b, 3.19c and 3.19d are the extraction of coupling coefficients for several dimension of the physical apertures. The FBW is 2% and consequently [20] the external quality factor is approximately $Q_e \approx 50$. The structure also includes 4 bends in order to allow space for the flanges. The dimension of the mean bend radius has been optimised using Fest3D in order to provide minimum reflection at f_0. In order to prepare the design for the physical implementation radii of 1.5 mm are included to all internal corners while the thickness of walls and irises is 2 mm. Thus the entire structure has been optimised including a target RL of 25 dB in order to have more tolerance margins. The initial and final optimised dimensions are listed in Tab 3.6. From the table it is possible to note that the some of the optimised values differ from the initial ones. This is because some of the resonators require bigger apertures to take into account additional loading effects

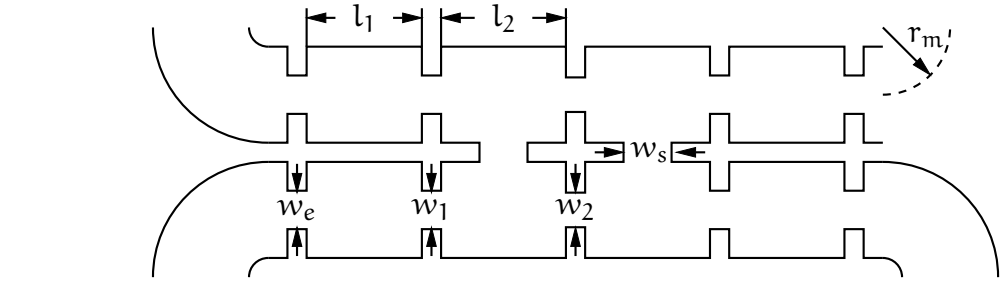

(a) Schematic top view

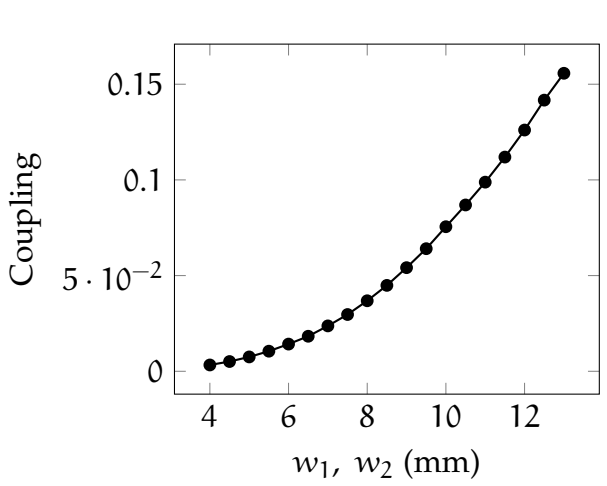

(b) Direct iris

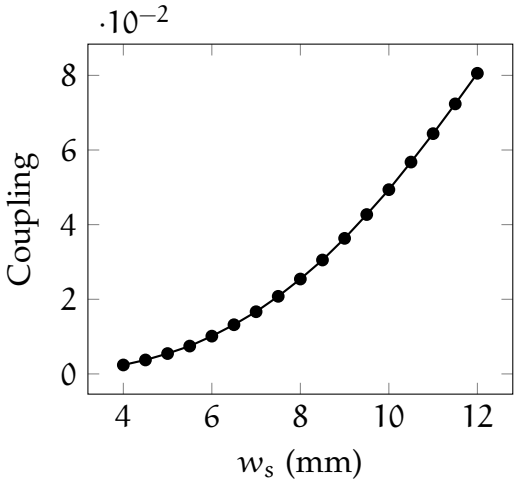

(c) Shunt iris

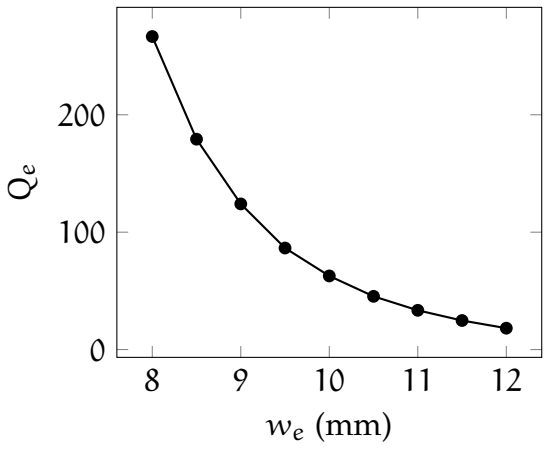

(d) External iris

Figure 3.19: Eight resonators quadrature hybrid dimensions and denormalised coupling coefficients calculated for $f_0 = 10\,\text{GHz}$ and $B = 200\,\text{MHz}$

Table 3.6: Dimensions of 8-resonator quadrature hybrid

	Initial (mm)	Optimised (mm)
l_1	19.9	15.8367
l_2	19.9	16.2353
w_1	7	8.2570
w_2	8	8.8278
w_s	8	9.6025
w_e	10.5	11.6652
r_m	16.255	16.255
Thickness	2	2
Radii	1.5	1.5

of the final structure. Also, the final model includes radii and an improved RL that required a further optimisation with respect the initial design.

The device has been cut in 2 parts, a main body and a lid to cover it. Fig. 3.20a shows the main part of the final 3D model that has been manufactured with a milling Computerized Numerical Control (CNC) machine. The advantage of making the body in one single piece instead of 2 identical halves is because it avoids the problems related to misalignment of the parts and it is practical for this design where cut in the E-plane could be difficult. Clearly this model is meant to be a proof of the concept introduced before and specific requirements to reduce losses are not considered. The prototype has been built with aluminium without silver-plating. In order to improve the contact between the lid and body there are several screws with groove to increase the contact pressure. Fig. 3.20b shows the final device assembled. Note that in this figure there are additional holes that were designed to allow tuning. All cavities, couplings and bends have been provided with tuning threads and screws. It will be shown that the measurements are in accordance with the simulation to an extent that no tuning is required and tuning screws used only to cover holes. The magnitude response and output phase shift are shown, respectively, in Fig. 3.20c and 3.20d. Solid lines are the measured data while dashed lines of the same colour are the ones obtained with CST full wave simulator. The measurements confirm very well the simulations for bandwidth, centre frequency, RL, power splitting, in-band Reflection Zero (RZ)s and

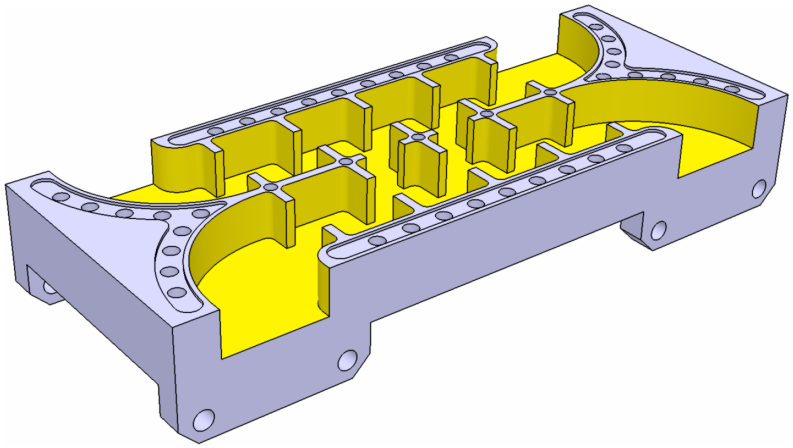

(a) Main body

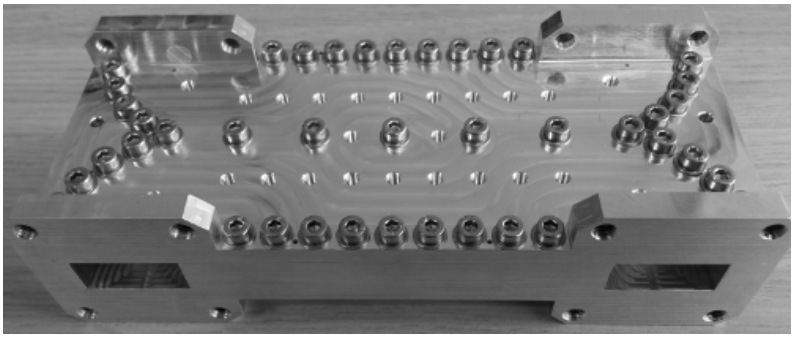

(b) Final device

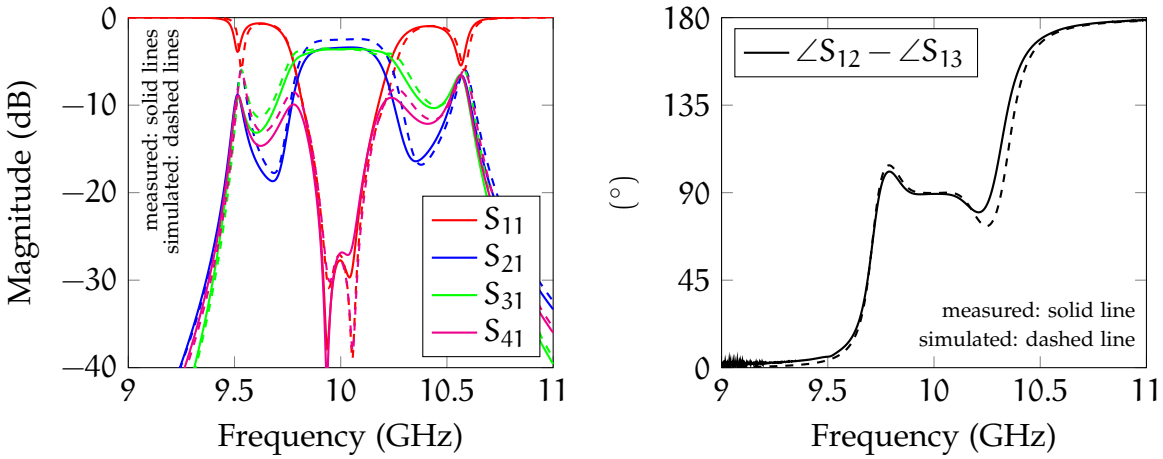

(c) Magnitude response

(d) Output phase shift

Figure 3.20: Measurements of 8-resonator quadrature hybrid. Experimental data are with solid line while simulations are shown with dashed lines.

out-band peaks. The phase difference between the 2 outputs is also in accordance with expectations and the deviation with respect the nominal 90° is less than 1.5°. As anticipated, the experimental data is very close if compared to the simulations that no tuning is required.

3.7 BUTLER MATRIX BASED ON QUADRATURE RESONANT HYBRIDS

The 90° hybrid coupler is the fundamental unit of the Butler matrix as shown in Fig. 2.1. Here the hybrid based on the quadruplet of resonators of Fig. 3.7 is used to form a multi-port Butler matrix. The schematic of a 4×4 Butler matrix based on 4 quadrature hybrids and 16 resonators is shown in Fig. 3.21a. Input ports are 1 to 4 while outputs are 5 to 8. As this circuit is based entirely on resonators, the coupling coefficients are written close to each line. Each quadruplet of resonators is exactly the same hybrid as Fig. 3.7 and the coupling coefficients of the straight through and shunt lines are indicated respectively with ϑ and φ. The external quality factors Q_e and connections between the hybrids are indicated with ε and ϖ. These couplings are calculated with the equivalence technique for the conventional hybrid and later they are connected together in order to form the Butler matrix. With reference of Fig. 3.21a the parameters are the following:

$$\varepsilon = 1 \tag{3.59a}$$

$$\vartheta = \sqrt{2} \tag{3.59b}$$

$$\varphi = 1 \tag{3.59c}$$

$$\varpi = 1 \tag{3.59d}$$

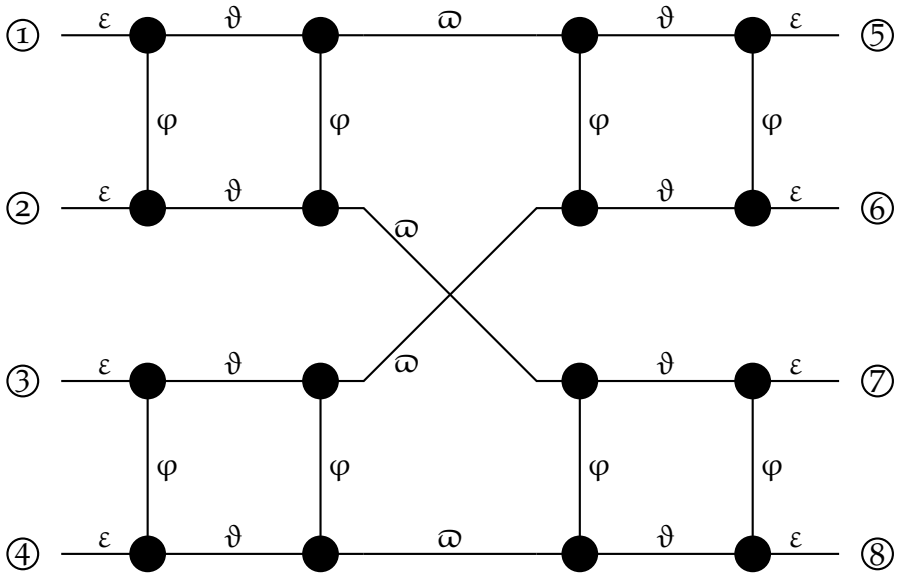

(a) Topology of the network

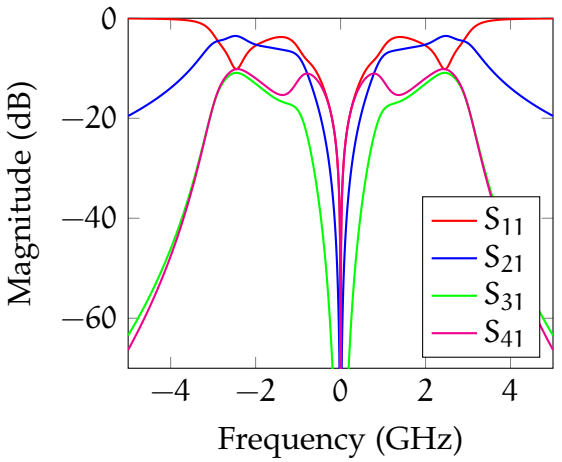

(b) Isolated parameters

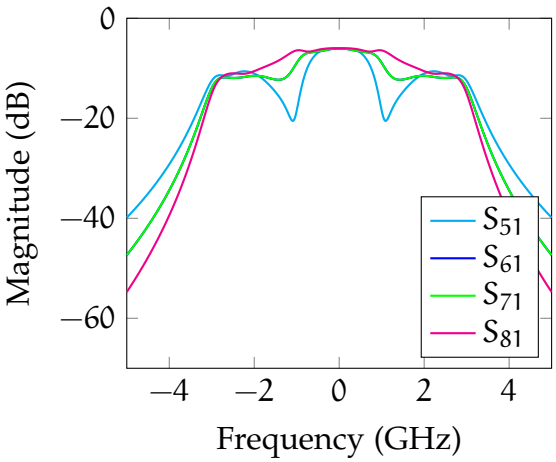

(c) Transmission parameters

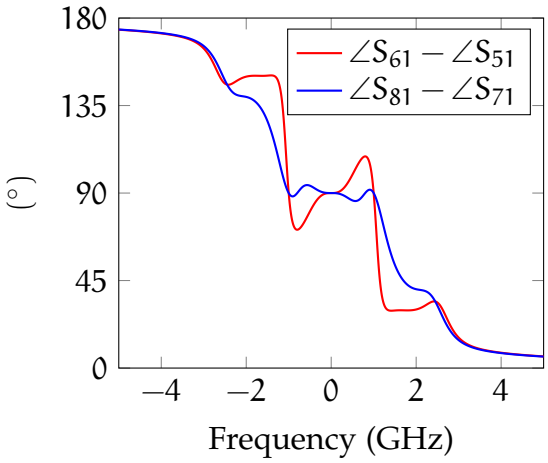

(d) Output phase shift

Figure 3.21: Butler matrix based on quadrature resonators hybrids

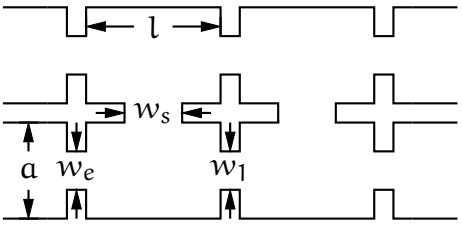

Figure 3.22: Top view schematic of the resonant hybrid coupler implemented in standard WR90 waveguide and inductive irises with dimensions

With an input signal reference applied to port 1, the magnitude of the isolated parameters is shown in Fig. 3.21b while the transmission parameters are shown in Fig. 3.21b. As expected, there is a perfect input to output power splitting at centre frequency that corresponds to $-6\,\mathrm{dB}$ while a perfect 90° output phase shift as shown in Fig. 3.21d. However this configuration is affected by the peaks in the out-band to a greater extent with respect to the case of the 2×2 hybrid. This can be explained because with the combination of multiple hybrids is built of a sort of chain of couplers that work well at centre frequency, but in the out-band all include peaks that deteriorate the transfer function. Naturally it could be possible to include hybrids with more branches in order to improve the response, however higher complexity in terms of elements cannot remove totally the peaks. This is because the intrinsic behaviour of the quadrature coupler based on resonators.

To prove the concept, a 3D implementation of the circuit of Fig. 3.21a is provided here in standard WR90 waveguide. The specifications of the 90° hybrid that constitutes the fundamental unit of the Butler matrix are: $f_0 = 10\,\mathrm{GHz}$ and FBW of 5% [104]. With reference of Fig. 3.22 the final optimised dimensions are $l = 14.46\,\mathrm{mm}$, $w_e = 11.77\,\mathrm{mm}$, $w_1 = 9.2\,\mathrm{mm}$ and $w_s = 10.84\,\mathrm{mm}$ [104]. All the hybrids are the same, hence the only missing element now is to provide their connection and cross-coupling like in Fig. 3.21a. Clearly the cross-coupling might be an issue for the design in rectangular waveguide, thus the structure is unfolded in order to obtain a easier to make solution as shown in Fig. 3.23a. This structure has a configuration of a cross with the 2 pairs of inputs and outputs on the opposite side. For example, in Fig. 3.23a input 1 and 2 are visible while the others are exactly on the opposite side of the device. The

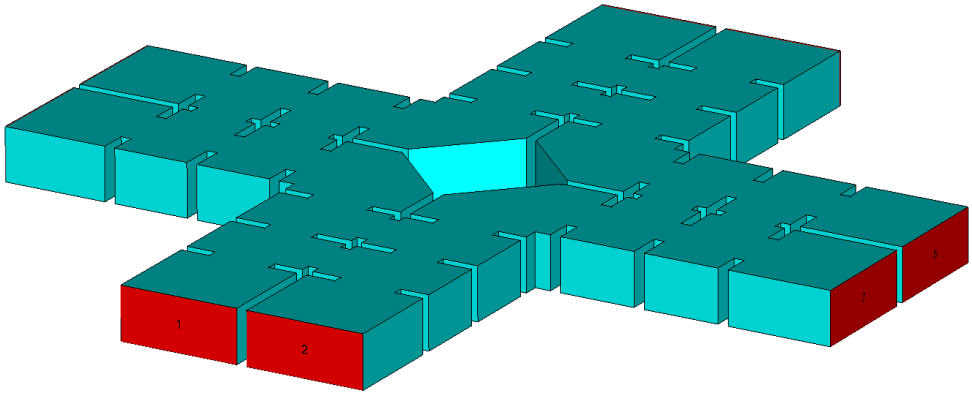

(a) 3D model of 4×4 Butler matrix based on quadrature hybrids

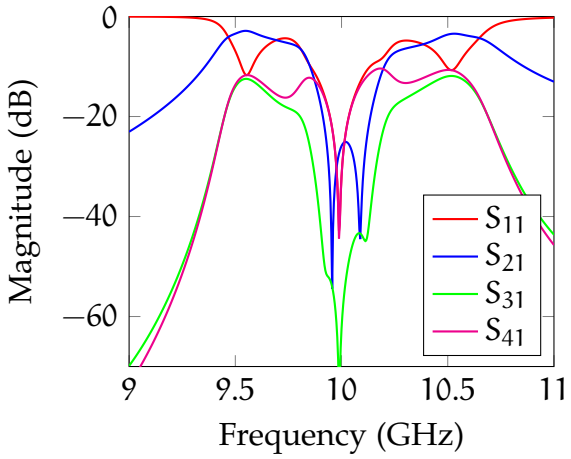

(b) Isolated parameters

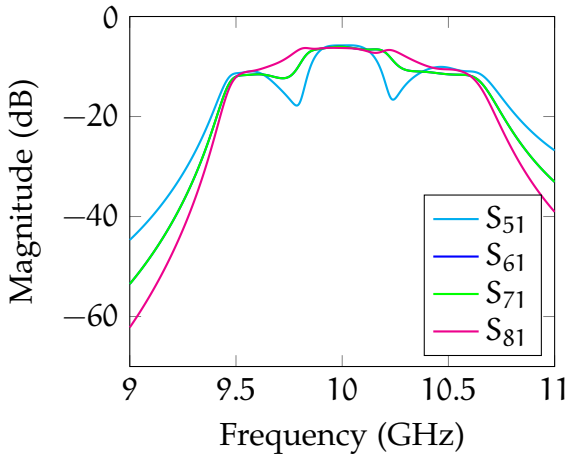

(c) Transmission parameters

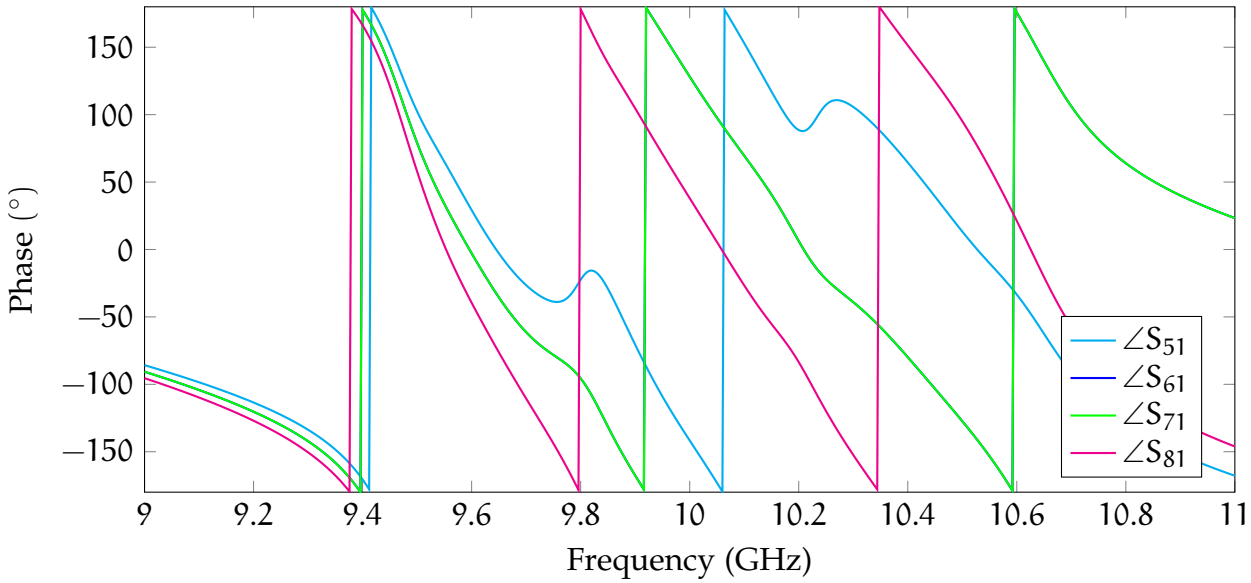

(d) Transmission output phase

Figure 3.23: Implementation of Butler matrix based on quadrature resonators hybrids

same applies to the other pairs of output ports. In this implementation the connection between couplers are made with mitered bends with length of the orthogonal walls of 8.0547 mm in order to provide reflection at centre frequency optimised at −100 dB. The isolation parameters are shown in Fig. 3.23b while the transmission ones are shown in Fig. 3.23c. If these results are compared to those obtained with the coupling matrix it is possible to confirm the relatively narrow bandwidth where the input to output power splitting is 6 dB and the perfect equivalence with transmission line models at f_0. However, the peaks in the out-band with different selectivity characteristic among the scattering parameters are also present. The phase response of the transmission parameters is finally shown in Fig. 3.23d. Over all the frequency span simulated the $\angle S_{61}$ is the same of $\angle S_{71}$ while at f_0 the difference with the others parameters $\angle S_{51}$ and $\angle S_{81}$ is of $\pm 90°$, in accordance with the expectations.

3.8 FINAL CONSIDERATIONS

The 90° hybrid coupler has been introduced because it is the fundamental building block in a Butler matrix. The hybrid coupler, but with an all-resonator circuit, in order to include also a filter transfer function to create a multi functionality device was described. Even in the simplest case, the synthesis problem is not straightforward as there does not exist an easy set of polynomials which defines the transfer function. Thus, a direct method based on the equivalence technique has been developed for the case of 2 branches, later extended to multiple branches with an additional step of optimisation of the coupling matrix. This method is exact at centre frequency while not having a totally predictable behaviour out of the band. Hence, to better understand the circuit a topological analysis has been also presented to provide a fast tool in determining the number of poles in the bandwidth and peaks. Naturally this method can be used at synthesis level in order to control the electrical response

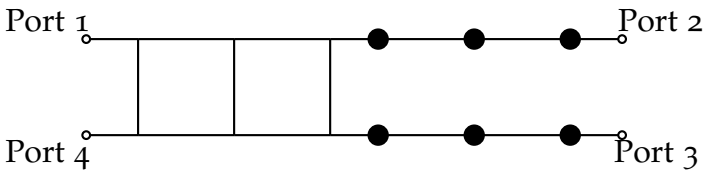

(a) BGC with separate filter interfaces

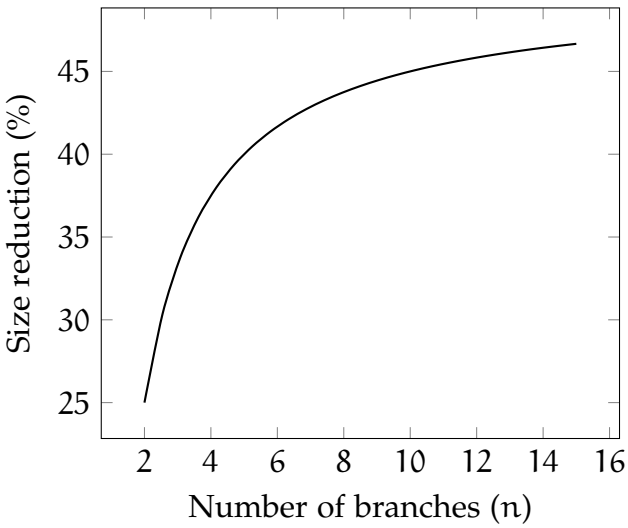

(b) Percentage of size reduction of the resonators array compared to the BGC with filtering

Figure 3.24: Size reduction of quadrature resonant coupler

of these devices. Finally it is possible to conclude that a quadrature hybrid coupler based on resonators can be used to provide also filtering if it is acceptable to have the additional peaks shown above.

Among the advantages of the hybrid coupler with filtering is the size reduction, thus a comparison has been made between the two BGC with filter functions. The first device is the traditional BGC based on transmission lines of Fig. 3.4. In order to add filtering, two band-pass filters are cascaded to the output ports. In Fig. 3.24a is an example of 3 branches BGC with filtering cascaded at both outputs. The Fig. 3.24a is an example of a third order BGC with filtering: the generic circuit is composed of a BGC of n branches with a BPF of n resonators cascaded to each output. It should be noted that no assumption is made on the type of waveguide, resonators and couplings, as in this study only the theoretical dimensions of the BGC and resonant cavity are considered. The BPF is modelled as a sequence of half-wavelength coupled resonators.

The comparison is with the branch guide coupler based on coupled resonators of Fig. 3.9. The length of the standard BGC is, in theory, $(n-1)\cdot\lambda_g/4$. In fact, there are $n-1$ direct lines each one measuring quarter-wavelength. At each output port a bandpass filter with n resonators is cascaded. The nominal length of each resonator is half-wavelength so that the length of the filter is $n\lambda_g/2$. Thus, the total length of the BGC with filtering is:

$$l_{BGC} = (n-1)\frac{\lambda_g}{4} + n\frac{\lambda_g}{2} = \lambda_g\frac{3n-1}{4} \tag{3.60}$$

The total length of the resonators array is n times the length of each cavity. By the moment that the longitudinal dimension of the couplings and the external interfaces are not considered, it is possible to think at the total length of the resonators array as:

$$l_{array} = n\frac{\lambda_g}{2} \tag{3.61}$$

From the last two equations the estimated size reduction of the resonators array can be derived. Fig. 3.24b shows the percentage of size saving of the resonators array compared to a BGC of n branches and n resonators bandpass filters in cascade. The graph shows that the multi-resonator configuration is 30% shorter compared to the BGC of 3 branches and more than 40% when the branches are more than 5. Even though the graph of Fig. 3.24b comes from a pure theoretical estimation of the total length of the device, it is very important because gives a clear view of the advantage in terms of size reduction of the multi-function hybrid coupler with filtering included.

The problem is solved using 180° hybrid coupler in place of the 90° to form an $N \times N$ Butler matrix with filtering included. An analytical synthesis technique is presented in the following chapter.

4 BUTLER MATRIX WITH INHERENT FILTER FUNCTIONS

In the previous chapter it has been shown that it is possible to include a filter transfer function into a quadrature hybrid coupler based on resonators, although the electrical performance is poor if compared to a conventional filter and hybrid separately. In this chapter it will introduced the 180° hybrid coupler and its equivalent version based on resonators. This solution provides better results for the power splitting, phase distribution and filter transfer function with regard the quadrature quadruplet of resonators. Moreover, the perfect isolation provided by the 180° hybrid is the fundamental prerequisite to make the synthesis of Tchebycheff or Butterworth filter functions. Thus, this hybrid based on resonators will be used in order to allow the synthesis of $2^k \times 2^k$ Butler matrices.

4.1 ELECTRICAL BEHAVIOUR OF THE RAT-RACE COUPLER

The typical ring configuration of a 180° hybrid coupler [30] is shown in Fig. 4.1a. From now on, the ports numbering of the 180° coupler will follow the definition shown in Fig. 4.1a. This circuit is also called *rat race* hybrid coupler. It is based by 3 quarter-wave transmission lines and 1 that is three-quarter wave. The normalised

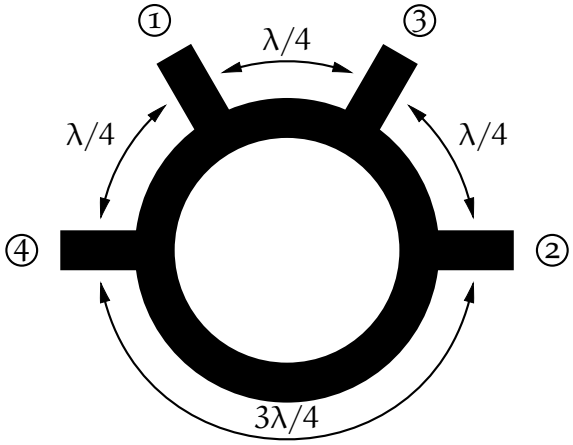

(a) Ring schematic

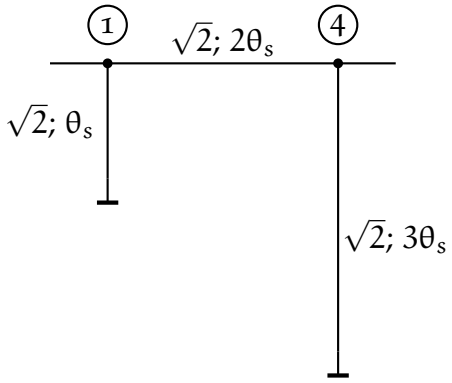

(b) Even/odd mode circuit

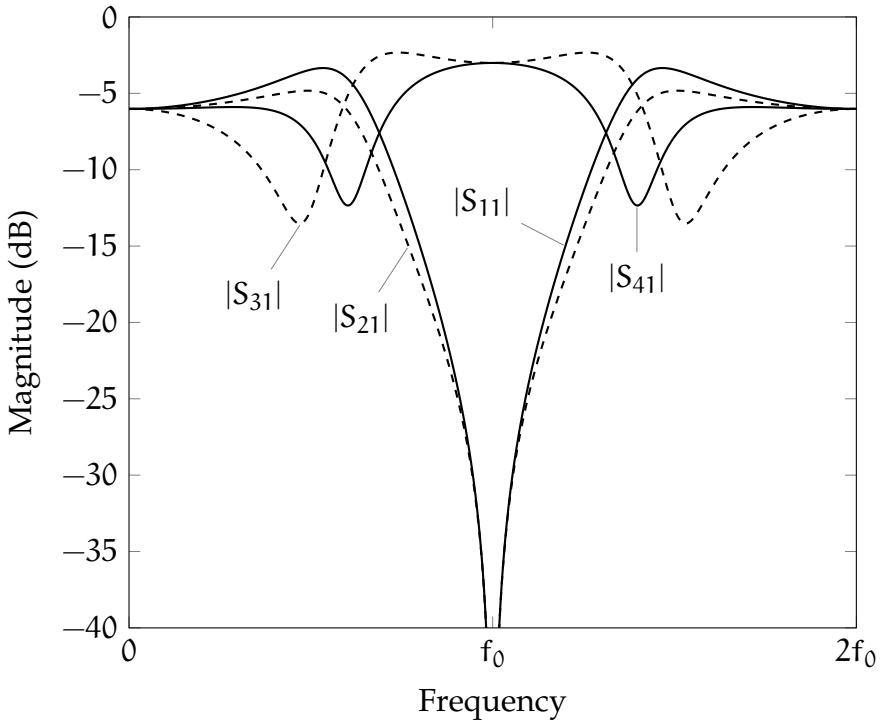

(c) Frequency response

Figure 4.1: Rat-race 180° hybrid coupler

characteristic impedance for all the lines is $\sqrt{2}$ [30]. The scattering matrix at centre frequency is

$$\mathbf{S} = \frac{-j}{\sqrt{2}} \begin{bmatrix} 0 & 0 & 1 & 1 \\ 0 & 0 & 1 & -1 \\ 1 & 1 & 0 & 0 \\ 1 & -1 & 0 & 0 \end{bmatrix} \tag{4.1}$$

The transmission line of length $3/4\lambda$ is the one that provides the out of phase contribution to the scattering response and for the perfect isolation on opposite ports. The scattering parameters are shown in Fig. 4.1c. With a source applied to port 1 the power is equally split between ports 3 and 4 while port 2 is isolated. This perfect behaviour is valid for a FBW of 10% to 20% [30]. At frequencies 0 and $2f_0$ the response converges to $-6\,\text{dB}$. The output phase difference depends on which port the excitation is applied:

IN PHASE output response is obtained when input is applied to ports 1 or 3 because the outputs are the adjacent elements at same distance of $\lambda/4$;

OUT OF PHASE output response when inputs are ports 2 or 4. This is because the two adjacent ports are separated one with a transmission line of length $\lambda/4$ while the other with length $3/4\lambda$.

The scattering parameters are obtained in a similar fashion as it was for the 90° hybrid coupler. In this case a symmetry plane can be included to cut the ring of Fig. 4.1a in 2 halves between ports 1-3 and 2-4. In this way there are a straight through line between two stubs of electrical length θ_s and $3\theta_s$, recalling that $\theta_s = \lambda/8$. A model of the even/odd mode network is shown in Fig. 4.1b where the terminations are either open or short circuits. Fig. 4.1b also shows the normalised characteristic impedances and electrical length of each line. Apart for this the calculation of the scattering parameters is the same as the ABCD matrix of eq. (3.18). It is worth to

mention that the relations for inputs applied to ports 1 and 3 are identical using the even/odd mode method, while for ports 2 and 4 it is necessary to consider first the stub of length $3\theta_s$ and later the one of length θ_s because the 2 different symmetries of the circuit [30].

4.2 180° HYBRID WITH FILTERING

The network of the 180° hybrid of Fig. 4.1a can be implemented by a quadruplet of resonators as the one of Fig. 3.15a in order to include filtering transfer functions [108, 109]. The characteristic polynomials for the 180° hybrid can be obtained in a similar fashion for the 90° coupler as shown in section 3.5. For the case of the 180° hybrid the following conditions are made [107]

$$B_1 = B_2 \tag{4.2a}$$

$$J_1 = J_2 \tag{4.2b}$$

$$J_{14} = -J_{23} \tag{4.2c}$$

These conditions are substituted into the eq.s (3.49) and (3.50) in order express the polynomial of the common denominator. It is interesting to note that conditions of eq.s (4.2) produce the following denominator for the even mode:

$$\begin{aligned} A_e + B_e + C_e + D_e &= a_e s^2 + b_e s + c_e \\ a_e &= -j\frac{1}{J_1^2 J_{12}} \\ b_e &= -j\left[\frac{2}{J_{12}} + \frac{2jB_1}{J_1^2 J_{12}}\right] \\ c_e &= -j\frac{J_{12}}{J_1^2} + \frac{2B_1}{J_{12}} + j\frac{(B_1^2 - J_{14}^2)}{J_1^2 J_{12}} - j\frac{J_1^2}{J_{12}} \end{aligned} \tag{4.3}$$

The odd mode is again found in a similar fashion:

$$\begin{aligned} A_o + B_o + C_o + D_o &= a_o s^2 + b_o s + c_o \\ a_o &= -j\frac{1}{J_1^2 J_{12}} \\ b_o &= -j\left[\frac{2}{J_{12}} + \frac{2jB_1}{J_1^2 J_{12}}\right] \\ c_o &= -j\frac{J_{12}}{J_1^2} + \frac{2B_1}{J_{12}} + j\frac{(B_1^2 - J_{14}^2)}{J_1^2 J_{12}} - j\frac{J_1^2}{J_{12}} \end{aligned} \tag{4.4}$$

The independent variable is $s = \sigma + j\Omega$. The denominator for the even and odd modes in this case of 180° hybrid are the same because the same the coefficients are obtained in eq.s (4.3) and (4.4). This fact has a major impact on the expression of the overall scattering parameters, because same denominator means that the degree of numerators of eq.s (3.14) are

$$S_{11} = \frac{N_{11}^{(2)}}{D^{(2)}} \tag{4.5a}$$

$$S_{31} = \frac{N_{21}^{(0)}}{D^{(2)}} \tag{4.5b}$$

$$S_{21} = 0 \tag{4.5c}$$

$$S_{41} = \frac{N_{41}^{(0)}}{D^{(2)}} = S_{31} \tag{4.5d}$$

where

$$N_{11} = s^2 + 2jsB_1 - B_1^2 + J_{14}^2 + J_{12}^2 - J_1^4 \tag{4.6a}$$

$$N_{31} = N_{41} = 2jJ_1^2 J_{12} \tag{4.6b}$$

$$D = s^2 + 2s(jB_1 + J_1^2) + 2jJ_{12}^2 B_1 - B_1^2 + J_{14}^2 + J_{12}^2 + J_1^4 \tag{4.6c}$$

Note that in the previous relation the further symmetry $J_{14} = J_{12}$ can be introduced [109]. For the case of 90° hybrid it was shown that all the scattering polynomials where different and of different order. Moreover no perfect isolation was mathematically

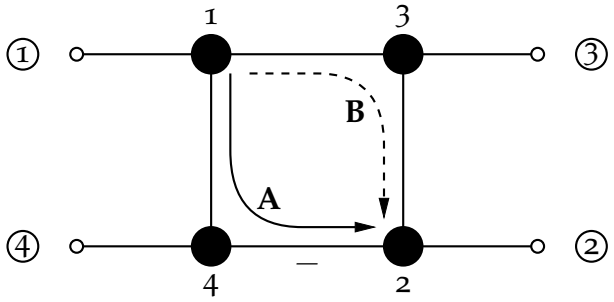

Figure 4.2: Schematic of a 180° hybrid coupler based on coupled resonators

possible. Here the elements of eq.s (4.6) are of the second order for the S_{11} and a constant for the numerator of the S_{31}. There are 3 polynomial to determine so they can be matched to the form of Tchebycheff transfer function defined with polynomials $E(s)$, $F(s)$ and $P(s)$. The synthesis consists in calculating the parameters of eq.s (4.6) by imposing a system of equations with the second order Tchebycheff polynomials [107, 110].

4.3 VIRTUAL OPEN CIRCUIT

An alternative synthesis method of the 180° hybrid coupler exploiting the perfect isolation or *virtual open circuit* is presented here. Fig. 4.2 shows the schematic of the circuit. According to symmetries of eq.s (4.2) and the one of [109], the coupling matrix defined by blocks is

$$\mathbf{M_p} = 0 \tag{4.7a}$$

$$\mathbf{M_{pn}} = K_e \mathbf{I}_4 \tag{4.7b}$$

$$\mathbf{M_n} = \begin{bmatrix} 0 & 0 & K_u & K_u \\ 0 & 0 & K_u & -K_u \\ K_u & K_u & 0 & 0 \\ K_u & -K_u & 0 & 0 \end{bmatrix} \tag{4.7c}$$

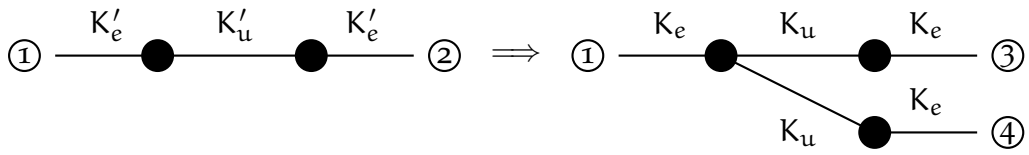

Figure 4.3: The traditional 2-pole filter on the left is transformed into a 3-port network with resonators for the principle of the virtual open circuit

Fig. 4.2 shows a minus on coupling between resonators 2 and 4 to say that it is the one that has same magnitude but opposite sign. From the definition of the coupling matrix it is possible to see that the same coefficient K_e is applied to all couplings between internal and external resonators and that also K_u is for all the internal coupling. The position of the minus sign is relevant only for the phase characteristic and it does not alter the magnitude.

If a signal source is applied to port 1 of Fig. 4.2, the signal is split to ports 3 and 4 through resonators 3 and 4, however part of the signal goes to resonator 2. From port 1 there are two paths for the signal to reach resonator 2, are shown with a solid (A) and dashed (B) line in Fig. 4.2. The signal on path A reaches resonator 2 with a phase due to the contribution of couplings between resonators 1-4 and 4-2. As each coupling is assumed as a perfect immittance inverter providing a phase shift of $\mp 90°$, the phase of path A in resonator 2 is zero. Considering the other path, the phase of a signal from resonator 1 to 2 via B is $-180°$. All the internal couplings have same magnitude as do the external ones. Thus the two signals from paths A and B in resonator 2 have same magnitude but are out of phase. This creates a perfect interference at all frequencies. The S_{21} is the isolation, and is perfect at all frequencies because of the symmetries of this network. The perfect interference of signals from paths A and B in resonator 2 makes it possible not to consider it for the calculation of the transmission scattering parameters S_{41} and S_{31}. Thus resonator 2 can be virtually removed from the circuit. With the simplification of the virtual open circuit, it is possible to consider a simpler network with just 3 ports and resonators. In this way S_{31} and S_{41} are like 2 independent 2-pole filters. Fig. 4.3 shows the transformation from a simple 2-pole in-line filter to the couplings of the 180° hybrid where one resonator has been removed

as effect of the virtual open circuit. The filter on left of Fig. 4.3 has the couplings between resonators and external ports indicated as K'_e while the internal coupling is K'_u. The couplings of the transformation on the right part of Fig. 4.3 are the ones indicated in eq. (4.7b) and (4.7c). The circuit on the right side of the figure has the characteristics S_{31} and S_{41} that are totally independent and uncorrelated, hence the conservation of energy is still valid:

$$|S_{11}|^2 + |S_{31}|^2 + |S_{41}|^2 = 1 \tag{4.8}$$

The hybrid splits equally the input power among the outputs and also the transfer function of the two transmission parameters is the same, hence $S_{31} = S_{41}$. It is possible to introduce a parameter that identifies the transmission, say β and one for the reflection, say α. The eq. (4.8) can conveniently written as

$$|\alpha|^2 + 2|\beta|^2 = 1 \tag{4.9}$$

The α and β refer to the reflection and transmission polynomials of the circuit on the right part of Fig. 4.3. In the same way it is possible to define the reflection α_{BPF} and transmission β_{BPF} parameters of the 2-pole filter of the left side of Fig. 4.3. Naturally the law of energy balance is still valid:

$$|\alpha_{BPF}|^2 + |\beta_{BPF}|^2 = 1 \tag{4.10}$$

The transfer function for the hybrid coupler is the one of a 2-pole filter, hence it the eq. (4.9) and (4.10) are imposed in order to find the relation between the parameters of the two networks:

$$|\alpha|^2 = |\alpha_{BPF}|^2 \tag{4.11}$$

$$|\beta|^2 = \frac{1}{2}|\beta_{BPF}|^2 \tag{4.12}$$

This is a consequence of the conservation of energy and it states that the virtual open circuit can produce a response that has same reflection and transmission with power splitting with respect to a conventional BPF. The coupling coefficients of the 2-pole filter are the K'_e and K'_u that are directly obtained from the low-pass g parameters

$$K'_e = \frac{1}{\sqrt{g_0 g_1}} \tag{4.13a}$$

$$K'_u = \frac{1}{\sqrt{g_1 g_2}} \tag{4.13b}$$

Because of the law of conservation of energy and the perfect isolation provided by the virtual open circuit, the direct relation between the coupling coefficients of the hybrid and the ones of the BPF are related as [109]:

$$K_e = K'_e \tag{4.14a}$$

$$K_u = \frac{1}{\sqrt{2}} K'_u \tag{4.14b}$$

The coefficient $1/\sqrt{2}$ provides the 3 dB output power splitting of the hybrid. The magnitude of the two transmission functions are the same. It is important to stress that the network with 3 resonators in the right part of Fig. 4.3 is useful to demonstrate the simplification of the synthesis provided by the concept of the virtual open circuit. Naturally, the coupling coefficients K_e and K_u calculated from the corresponding BPF are constituting the hybrid of Fig. 4.2 and are the components of the coupling matrix of eq. (4.7b) and (4.7c).

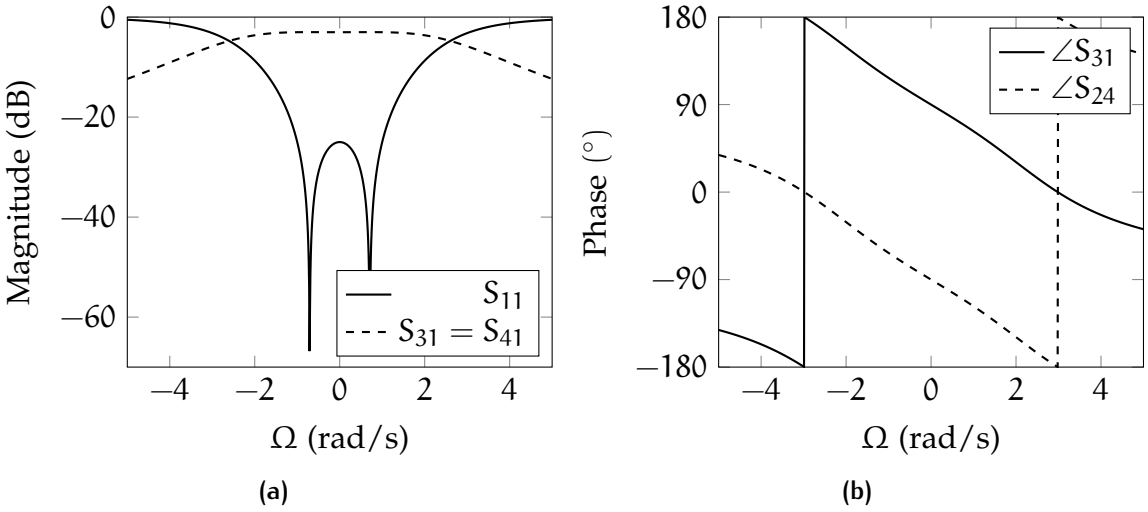

Figure 4.4: Response of the 180° Hybrid coupler based on resonators

As an example, a 180° hybrid coupler based on resonators implementing a Tchebycheff transfer function with a RL of 25 dB is given as example. Initially the g parameters constant are calculated through the eq.s (2.7), giving

$$g_0 = 1 \tag{4.15a}$$

$$g_1 = 0.4882 \tag{4.15b}$$

$$g_2 = 0.436216 \tag{4.15c}$$

$$r = 1.11917 \tag{4.15d}$$

The coupling coefficients of the corresponding in-line filter are calculated with eq. (4.13)

$$K'_e = 1.4312 \tag{4.16a}$$

$$K'_u = 2.1669 \tag{4.16b}$$

Finally, the coefficients of the coupling matrix of the 180° hybrid of eq. (4.1) are obtained with eq.s (4.14) as

$$K_e = 1.4312 \tag{4.17a}$$

$$K_u = 1.5323 \tag{4.17b}$$

The magnitude response is shown in Fig. 4.4a with $|S_{31}| = |S_{41}|$. Two phase characteristics that are in opposition are shown in Fig. 4.4b. The isolation is not included in the figure because it is 0 for all frequencies. The magnitude exhibits a 2-pole Tchebycheff filter function with the two transmissions that equally split the input power among the outputs. The results obtained here derive from the calculation of the low-pass g parameters, used in the example to produce a Tchebycheff response. However it is possible to use the same g parameters to obtain a Butterworth transfer function in the same way. The main advantage of the method based on the virtual open circuit with respect the calculation of the coefficients based on the characteristic polynomials of eq.s (4.5) resides in the use of closed formulas to calculate the couplings. Moreover, the even/odd method used to analytically calculate the polynomials simplifies the complexity only for devices with 2-input and 2-output. The virtual open circuit method instead, separates the transmission parameters over independent paths (ie. from port 1 to 3 and from 1 to 4), thus considering them as single filters except for a coefficient used to keep the power balance.

This technique of independent paths will be used in the following in order to make the synthesis of $N \times N$ with $N = 2^k$ Butler matrices based on resonators.

4.4 ANALYTICAL SYNTHESIS OF BUTLER MATRIX FORMED BY 180° HYBRIDS

The aim of this study is to do the synthesis of N × N Butler matrices with filtering included. The basic idea is to exploit the property of virtual open circuit provided by 180° hybrid couplers of Fig. 4.2. As it was shown in the previous section, the virtual open circuit is an effective method to design the coupling coefficients of the hybrid in a similar way as if it was for an in-line filter. Doing so all the complexities and limitations of the general synthesis technique for multi-port devices are avoided. This is an ad-hoc solution for Butler matrices based on resonators with equal power splitting and the same transfer function for each transmission parameter. In the following it will be shown how to combine several 180° hybrids together in order to produce a Butler matrix with filtering based only on resonators and electromagnetic couplings. It will be also provided a systematic and analytical synthesis technique for the coupling matrix.

Attempts to introduce filtering functions into the 2 × 2 hybrid was already presented in [101, 102, 108, 109, 111–114] and a circuital diagram of a 4 × 4 matrix with the coupling coefficients calculated via optimisation techniques has been introduced [112]. The 4-resonator hybrid is also extensively exploited to create more complex subsystems in [107], however optimisation of the inverters are mandatory in order to obtain desired symmetries and frequency response. Also, no general understanding of the polynomials for these multi-port circuits is provided. Other structures implementing input/output power division and filtering through coupled resonators structures are discussed in [58, 59, 115, 116], however they do not provide an analytical synthesis of the coupling matrix. A different type of solution for networks with 1-input to multiple outputs has been presented for microstrip [100]. The advantage of the proposed technology over the existing baseline of ONET and a cascade of N BPFs will be a

considerable size reduction. In the next sections it will be shown that the size saving of the new Butler matrix based on resonators is around 30% in volume.

4.4.1 Transfer function requirements

The electrical properties of the 4-resonator 180° coupler of Fig. 4.2 are exploited in order to make the synthesis of a general $N \times N$ Butler matrix with $N = 2^k$. The transfer function matrix, defined over the operational bandwidth, of the hybrid is the typical one of a rat-race coupler:

$$\mathbf{T}_{180^\circ} = \mathbf{T}_1 = \frac{1}{\sqrt{2}} \begin{bmatrix} 1 & 1 \\ 1 & -1 \end{bmatrix} \tag{4.18}$$

Here input signals are applied to ports 1 and 2 of Fig. 4.2, and outputs are at ports 3 and 4. By recursive combination of eq. (4.18), a Butler matrix can be obtained in a similar fashion to that described in [14] using only 180° hybrid couplers, with the total transfer matrix defined by the Kronecker product as:

$$\mathbf{T}_k = \mathbf{T}_1 \otimes \mathbf{T}_{k-1} = \frac{1}{\sqrt{2}} \begin{bmatrix} \mathbf{T}_{k-1} & \mathbf{T}_{k-1} \\ \mathbf{T}_{k-1} & -\mathbf{T}_{k-1} \end{bmatrix} \tag{4.19}$$

This is also known as the Hadamard matrix. Naturally, the Hadamard matrix is orthogonal, indeed becoming very attractive for the architecture of Fig. 2.17. It could be possible to assign to the INET a Butler matrix with transfer function like the one of (4.19) and to the ONET the same network but mirrored. The mirroring of the input/output of the ONET corresponds to the transposition of the transfer function matrix, hence due to the orthogonality of the Hadamard matrix it is shown how this kind of network is suitable for the use in MPAs, in the operational bandwidth. The

cascade of networks are governed in general by eq. (4.19), hence the transfer function of the MPA defined over the bandwidth is

$$\begin{bmatrix} y_1 \\ y_2 \\ \vdots \\ y_N \end{bmatrix} = [\mathbf{T}_k] \cdot G[\mathbf{I}_N] \cdot [\mathbf{T}_k]^T \begin{bmatrix} x_1 \\ x_2 \\ \vdots \\ x_N \end{bmatrix} = G \begin{bmatrix} x_1 \\ x_2 \\ \vdots \\ x_N \end{bmatrix} \tag{4.20}$$

The (4.20) states that using a combination of 180° hybrid coupler, the transfer function of the entire MPA results in a multiplication of the amplitude of the input signals of a factor G.

4.4.2 Set of polynomials

The network has 2N ports (ie. inputs $1,\dots,N$ and outputs $N+1,\dots,2N$), it is reciprocal, lossless, is described by its $\mathbf{S}$ scattering matrix and has the generic transfer function matrix $\mathbf{T}_k$ defined in eq. (4.19). The reflection (α), transmission (β) and isolation (γ) parameters are directly related with the $\mathbf{S}$ elements with the following simplified notation:

$$\alpha_r = S_{r,r} \quad \text{for } r \leqslant N \tag{4.21a}$$

$$\beta_i = S_{r,i+N} \quad \text{for } i \leqslant N \tag{4.21b}$$

$$\gamma_j = S_{rj} \quad \text{for } 1 < j \leqslant N, \wedge r \neq j \tag{4.21c}$$

where α_r is the reflection characteristic seen at port r, β_i is the transfer function between ports r and $N+i$ and γ_j is the isolation between ports r and j (with $j < N$). In eq. (4.21) the input signals are assumed to be applied at one port in the range 1 to N, though the same concept is valid if the source is applied at ports $N+1$ to 2N due

to the reciprocity of the network. For a generic lossless network the unitary condition is expressed by the well known formula:

$$\mathbf{S} \cdot \mathbf{S}^* = \mathbf{I} \tag{4.22}$$

where $\mathbf{S}^*$ is the complex conjugate of matrix $\mathbf{S}$ and $\mathbf{I}$ is the identity matrix. The set of definitions eq. (4.21) can be substituted in eq. (4.22) producing the following relation in terms of parameters α_r, β_i and γ_j valid for $r \leqslant N$:

$$|\alpha_r|^2 + \sum_{i=1}^{N} |\beta_i|^2 + \sum_{\substack{j=1 \\ j \neq r}}^{N} |\gamma_j|^2 = 1 \tag{4.23}$$

The traditional cascading of a Butler matrix and a bank of bandpass filters as it was shown in Fig. 2.17a is taken as the reference model with scattering matrix $\mathbf{S}_{ref}$. It can also be studied as a reciprocal lossless network with a scattering matrix derived by the combination of the ONET and filters:

$$\mathbf{S}_{ref} = \mathbf{S}_{ONET} \cdot \mathrm{diag}\{\mathbf{S}_{BPF}\} \tag{4.24}$$

that must comply with the condition eq. (4.22). In this study the non-linearities of the ONET are not taken into account and the network is just considered as an equal power divider except for the output phase contribution with perfect isolation between pair of input ports. With this in mind, the unitary condition eq. (4.24) is applied to eq. (4.22) resulting in:

$$\sum_{h=1}^{N} \frac{1}{N} \left(|\alpha_{BPF,h}|^2 + |\beta_{BPF,h}|^2 \right) = 1 \tag{4.25}$$

where the return loss and transmission of the generic bandpass filter on the output port h are indicated with parameters $\alpha_{BPF,h}$ and $\beta_{BPF,h}$ respectively. As the Butler matrix performs an equal power splitting, there is a term $1/N$ in the eq. (4.25). The

assumptions made in the previous sections stated that all the inputs/outputs of the distribution network were mutually isolated and same bandpass filter transfer function were applied to all the ports. They are expressed in the notation introduced here with the following set of equations:

$$\sum_{i=1}^{N} |\beta_i|^2 = N|\beta|^2 \tag{4.26a}$$

$$\sum_{\substack{j=1 \\ j\neq r}}^{N} |\gamma_j|^2 = 0 \tag{4.26b}$$

$$\sum_{h=1}^{N} \frac{1}{N}|\alpha_{BPF,h}|^2 = |\alpha_{BPF}|^2 \tag{4.26c}$$

$$\sum_{h=1}^{N} \frac{1}{N}|\beta_{BPF,h}|^2 = |\beta_{BPF}|^2 \tag{4.26d}$$

A direct consequence of eq. (4.26) is that all the insertion loss characteristics are the same, indeed $\alpha_r = \alpha$. The unitary condition is exploited in order to equate relations eq. (4.23) and eq. (4.25) with the set of conditions expressed in eq. (4.26):

$$|\alpha|^2 + N|\beta|^2 = |\alpha_{BPF}|^2 + |\beta_{BPF}|^2 = 1 \tag{4.27}$$

The two parts of eq. (4.27) demonstrate the direct relation between the characteristics of the transfer functions of the circuit under investigation and the ones of a generic band-pass filter:

$$|\alpha|^2 = |\alpha_{BPF}|^2 \tag{4.28}$$

$$|\beta|^2 = \frac{|\beta_{BPF}|^2}{N} \tag{4.29}$$

This highly simplifies the complexity of the synthesis of polynomials of the multi-port network with regard the difficulties mentioned at the beginning of the section. The concept of virtual open circuit used to make two independent paths in the 180° of

Fig. 4.2 is generalized here to the case of N ports. This is a fundamental assumption to specify independent paths, each of them producing a filter transfer function. Hence, the synthesis of the generic set of functions α and β starts from the one of a 2-port bandpass filter with known α_{BPF} and β_{BPF}.

4.4.3 Topology

The 180° hybrid of Fig. 4.2 is identified to be the suitable candidate as fundamental building block of the Butler matrix with filtering because of the properties of perfect isolation, equal power division and transfer function matrix compliant with the application requirements. Each independent path, needed to perform the transfer functions α and β, is obtained through a sequence of hybrid couplers of the type of Fig. 4.2. As each hybrid equally splits the power at the 2 output-transmission ports, for a single path the following number of hybrids are necessary:

$$k = \log_2 N \tag{4.30}$$

The contribution of each of them to one single path is of exactly 2 resonators, indeed, the total transfer function achievable with the current technique produces a minimum number of poles ρ given as:

$$\rho = 2k \tag{4.31}$$

Moreover, each unit (ie. 180° hybrid coupler) accepts 2 input signals, hence a number of $N/2$ units, in order to receive all the input signals are necessary. Indeed, the entire

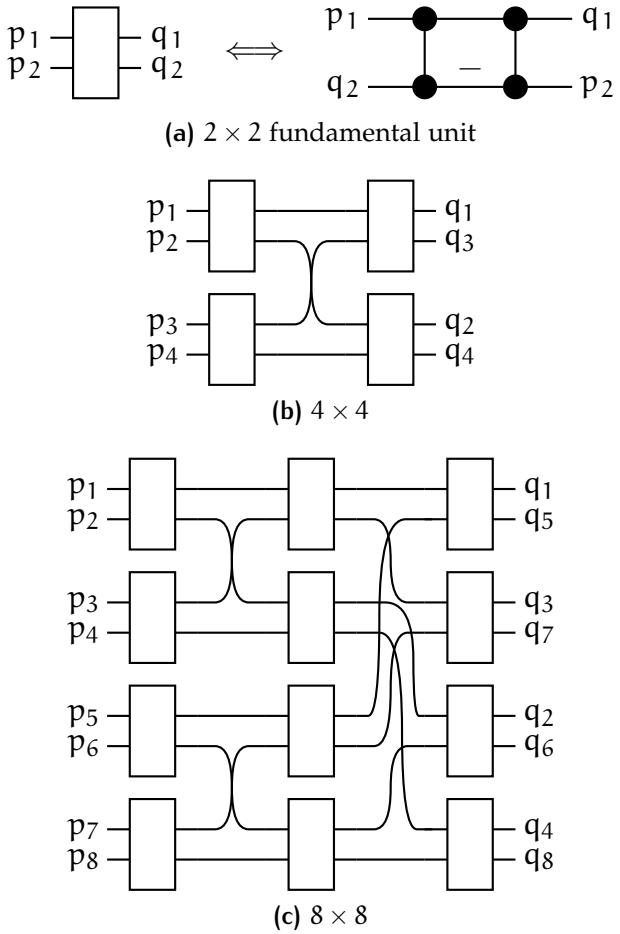

Figure 4.5: Configurations of the hybrid couplers as introduced in [14] but with the lines representing electromagnetic couplings

network can be thought as a matrix of units of $N/2$ rows and k columns with a total number u of hybrids and n resonators given by the following relations:

$$u = \frac{N}{2}k = \frac{N}{2}\log_2 N \tag{4.32}$$

$$n = 4u = 2N\log_2 N \tag{4.33}$$

Every hybrid coupler constituting the network should be connected to others hybrid or to the external ports in order to comply with the prescribed output power and phase distribution. The structures shown in Fig. 4.5 solves this problem for different numbers of inputs [14]. In this figure the input ports are indicated with $p_1, \ldots, p_N$ and the output with $q_1, \ldots, q_N$. The basic building block of the circuit is the 180° hybrid

of Fig. 4.2. Each unit is represented with the two input ports on the left of the block, while on the right are the outputs: these are shown in Fig. 4.2, with ports 1, 2 for the inputs and 3, 4 for the outputs. The entire circuit described here is based on resonant cavities coupled by electromagnetic couplings, thus each line of Fig. 4.5 represents a coupling between pairs of resonators which are embedded in the units shown as rectangular blocks. The figure includes the configurations of a 2×2 (Fig. 4.5a), 4×4 (Fig. 4.5b) and an 8×8 (Fig. 4.5c) Butler matrices that implement the Hadamard transfer function matrix eq. (4.19). It should be noted that the numbering of the output ports q_i has been derived in the figure in order to have the phase distribution identical to the transfer function matrix of eq. (4.19). However, it can be proved that if a sequential numbering, for instance from top to bottom, is applied to the networks of Fig. 4.5, the resulting matrix is still orthogonal. Starting from the schematics depicted in Fig. 4.5, it is also possible to generalize to $N \times N$ networks recursively.

In some practical cases it might be more appropriate to change, for example, the relation between the input/output ports of some units of Fig. 4.5 with the ones of the 180° hybrid of Fig. 4.2. The reason for this change depends on particular constraints that can arise at the design stage of the hybrids, leading to impractical or even impossible implementations of the electromagnetic couplings between the resonators of different unit-hybrids. The output power division of the whole Butler matrix is not affected, with the change applying only to the distribution of the output phases. This, in general, is not a limit as long as the transfer function matrix is capable of recombining the signals. This statement confers a greater degree of freedom to the topology configuration of the network because it does not bound the response to the only pure Hadamard transfer matrix, but gives the designer the ability to change the physical connections of the hybrids without losing the properties of the circuit.

4.4.4 Formulation of the coupling matrix

The synthesis technique for the formulation of the coupling matrix is summarised here with the following step-by-step procedure:

1. Review of the RF specifications. The number of input/output ports N depends on the number of signals that are supposed to be applied to the network while the bandwidth B and the return loss RL are functions of the rejection required after the bank of power amplifiers;

2. Calculate of total number of poles ρ through eq. (4.30) and eq. (4.31), number of unit-hybrids u with eq. (4.32) and total resonators n with eq. (4.33);

3. The polynomials of the transfer function of this network are directly related to the ones of bandpass filters with the relations eq. (4.28) and eq. (4.29). This calculation is performed initially with the normalized low-pass parameters on a filter of $2k$ resonators and $2k+1$ ideal inverters. For maximally flat or equal ripple transfer functions the low-pass g parameters are calculated with the well known formulas [20]. The coupling coefficients of the band-pass filter are directly obtained from g parameters with the formula:

$$M_{h+1,BPF} = \frac{1}{\sqrt{g_h g_{h+1}}} \tag{4.34}$$

with $h \in \{0, \ldots, 2k\}$. In order to simplify the following computations, entity $M_{h,BPF}$ is not considered here as a matrix but just as a vector where each element represents the coupling coefficient between a pair of adjacent resonators. Alternately to the formulations of the g parameters, more advance techniques to generate the $M_{h,BPF}$ can be eventually used as described in [34].

4. The first resonators of every 180° hybrid coupler on the first column of unit-hybrids of the circuit are all coupled with the external inputs. The same is for

the second resonators of all the hybrids on the last columns that are coupled with the external outputs. The value for these coefficients correspond to the first and the last element of vector $M_{h,BPF}$.

5. Each independent path has the coupling coefficients equal to the ones calculated with the eq. (4.34). The power splitting factor and the phase distribution are governed by the configuration of the hybrids. The hybrid's coupling coefficient K_{u_i} are all the same except one that is opposite phase (ie. Fig. 4.2). Their magnitudes are defined as:

$$K_{u_i} = \frac{1}{\sqrt{2}} M_{2i,BPF} \tag{4.35}$$

where the subscript u_i is used to indicate all the identical hybrids on columns i . The coupling coefficients between pair of hybrids, indicated as $K_{u_i,u_{i+1}}$ are directly obtained (cf. eq.s (4.7b) and (4.7c)) as:

$$K_{u_i,u_{i+1}} = M_{2i+1,BPF} \tag{4.36}$$

6. The coupling matrices $\mathbf{M_{pn}}$ and $\mathbf{M_n}$ are populated with the values of vectors eq. (4.35) and eq. (4.36) in order to reflect the chosen topology connections. Typically, the $\mathbf{M_{pn}}$ has the values of first and last elements of eq. (4.34) for the coupling coefficients between the terminal resonators and external interfaces. The final coupling matrix of the overall network is defined by blocks with the form eq. (2.41).

7. The obtained coupling matrix should be de-normalized to the centre frequency f_0 and bandwidth B and expressed in term of the external quality factors Q_{em}

between the external port e and the internal resonator m and the coupling coefficient k_{ij} between two internal resonators i and j as follows [34]:

$$Q_{em} = \frac{f_0}{B} \frac{1}{[\mathbf{M_{pn}}]^2_{em}} \tag{4.37a}$$

$$k_{ij} = \frac{B}{f_0} [\mathbf{M_n}]_{ij} \tag{4.37b}$$

Note that the achievable operational bandwidth B depends on the technology of the resonator/coupling used in the physical implementation.

4.5 EXAMPLE OF 4×4 BUTLER MATRIX WITH FILTERING

The procedure to synthesis the coupling matrix of a 4×4 Butler matrix with filtering is illustrated in this section. In this example all the calculation will be made in the low-pass domain in order to produce the scattering response in terms of transmission β and reflection α. The specifications are of a Butler matrix implementing input to output equal power and phase distribution and a Tchebycheff transfer function with 25 dB of RL. Fig. 4.6 is a representation of the structure of the Butler matrix and, on top, the fundamental in-line 4-pole filter. In this figure all the lines are electromagnetic couplings, black circles are resonators and the rectangles are the 180° hybrids of Fig. 4.2 and 4.5a. The hybrids are also included with the indication of the column through label u_i where the subscript is the column number. For the Butler matrix input ports are $p_1, \ldots, p_4$ while the outputs are $q_1, \ldots, q_4$. Input and output ports of the corresponding in-line filter are 1 and 2 and on top of each coupling is the coefficient M_h. The M_h in Fig. 4.6 is an abbreviation of term $M_{h,BPF}$ used in the previous section.

The network has $N = 4$ inputs/outputs, it requires $k = 2$ hybrids for every independent path as for eq. (4.30), and it will produce $\rho = 4$ poles (cf. eq. (4.31)) through a total number of $n = 16$ resonators as given by eq. (4.33). The definition of char-

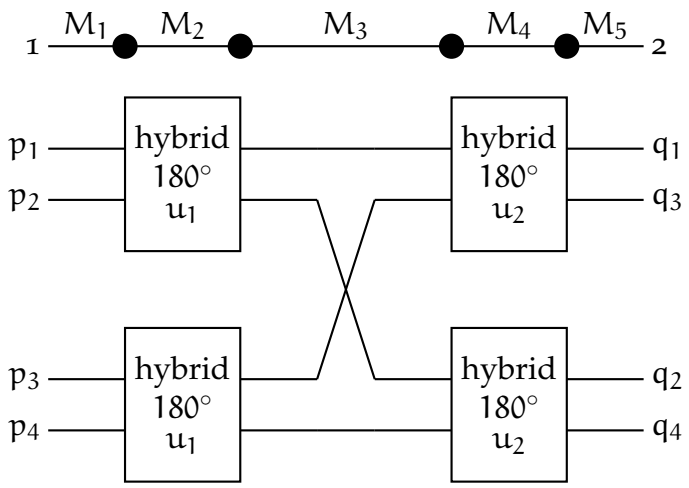

Figure 4.6: Example of 4×4 Butler matrix with filtering. On top is the equivalent in-line filter with coupling coefficient. On bottom topology of the 4×4 Butler matrix with hybrids based on resonators and electromagnetic couplings

Table 4.1: Coefficients of the equivalent 4-pole Tchebycheff filter with 25 dB return loss

h	g_h	$M_{h,BPF}$
0	1	
1	0.753308	1.15216
2	1.2252	1.0409
3	1.37121	0.771517
4	0.673096	1.0409
5	1.11917	1.15216

acteristic polynomials of eq.s (4.28) and (4.29) states that, apart for a scaling factor, they are the same to the ones of a conventional 2-port filter. The equivalent filter is represented in the top part of Fig. 4.6. The first step of the synthesis is to calculate the couplings M_i through the techniques introduced in section 2.3.1. Tab 4.1 shows the g parameters and the coupling coefficients of the equivalent filter included in the top of Fig. 4.6. This is a fundamental step because the coupling coefficients of the Butler matrix are directly derived with eq.s (4.35) and (4.36). Firstly the matrix $\mathbf{M_{pn}}$ is created. The couplings between external input ports and internal resonators are all set to M_1 as shown in Fig. 4.6. With respect to each hybrid on the first column u_1, the first input is coupled to resonator 1 of the hybrid with the second input is to resonator 2 as shown in Fig. 4.2. The outputs couplings are between resonators 3 and 4 of hybrids on the last columns (column u_2 of Fig. 4.6) and they are all equal

to M_5 of the equivalent in-line filter. Secondly, the coupling matrix $\mathbf{M_n}$ is created. The internal couplings are the ones between the resonators of each hybrid and the couplings connecting pair of hybrids. Each hybrid has the same topology of Fig. 4.2 and the couplings are related to the equivalent in-line filter through eq. (4.35). Again, all the hybrids on the same column are all identical. For the first column of hybrids the internal coupling coefficients are:

$$K_{u_1} = \frac{1}{\sqrt{2}} M_2 = 0.7360 \tag{4.38}$$

The in-line filter is symmetric and then $K_{u_1} = K_{u_2}$ because $M_2 = M_4$. Naturally, all the couplings of the quadruplet of resonators constituting the hybrid have the same magnitude, with one of them that has negative sign as shown in Fig. 4.2 and 4.5a. The coupling between pairs of internal resonators are related by coefficient M_3 as of eq. (4.36). Each of these couplings are connecting one output resonator of hybrid on column u_1 to an input resonator to the hybrids of column u_2 as shown in Fig. 4.6. They are all the same and equal to

$$K_{u_1,u_2} = M_3 = 0.771517 \tag{4.39}$$

Whatever numbering of resonators has been chosen, the elements of matrix $\mathbf{M_n}$ should follow the rules of topology shown in Fig. 4.5 and the eq.s (4.35) and (4.36).

The magnitude response of the 4×4 Butler matrix is shown in Fig. 4.7. The graphic is expressed in terms of reflection parameter α and transmission β with no indication of isolation γ as it is 0 at all frequencies. The return loss is 25 dB and the transfer function exhibits 4 poles as expected. The transmission characteristic β shows an equal power splitting of 6 dB of one input signal among the outputs. The transfer

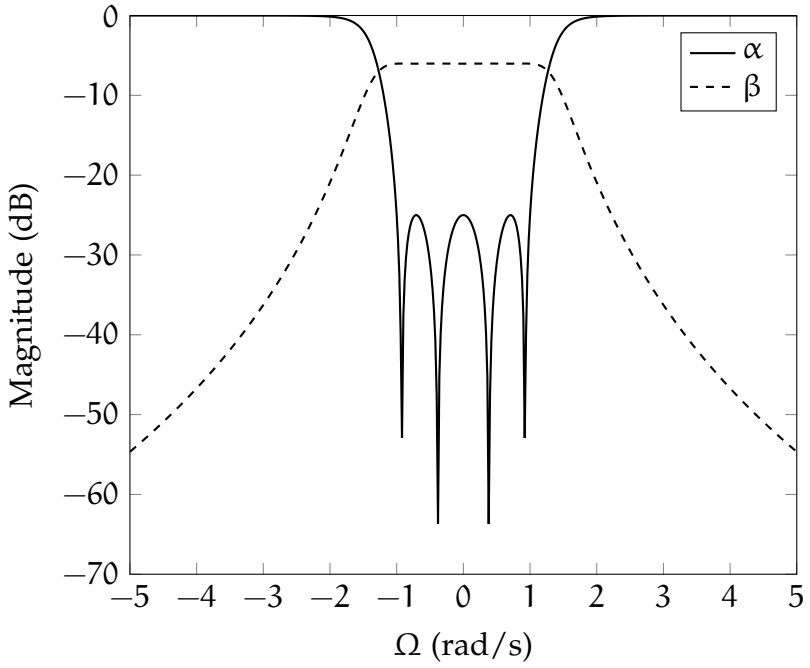

Figure 4.7: Response of 4×4 Butler matrix with filtering

function at central frequency is also governed by the Hadamard matrix $\mathbf{T}_k$ with $k = 2$ as

$$\mathbf{T}_2 = \begin{bmatrix} 1 & 1 & 1 & 1 \\ 1 & -1 & 1 & -1 \\ 1 & 1 & -1 & -1 \\ 1 & -1 & -1 & 1 \end{bmatrix} \tag{4.40}$$

In the following chapter the 3D realisation, manufacturing and measurement of this Butler matrix with filtering will be shown.

4.6 EXTENSION OF THE FILTERING CHARACTERISTIC

The procedure and equations introduced in section 4.4 define the minimum performance and transfer function for the Butler matrix with filtering for prescribed specifications. However, in many telecommunication systems it might be necessary to

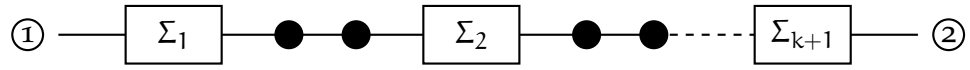

Figure 4.8: Base filter formed by sub-networks to enhance the transfer function

improve the frequency selectivity by either increasing the number of resonators of a filter or by introducing TZs. The number of poles ρ defined in eq. (4.31) is dependent by the number N of input/output and not by the designer. Hence in this section the procedure to add more complex filtering characteristic in the Butler matrix is described. The general definition of transfer function of eq.s (4.28) and (4.29) do not put necessarily restrictions on which response is achievable, although the system relies on the virtual open circuit provided by the 180° hybrids. The solution proposed here is to incorporate complex transfer functions interleaving the hybrids by *sub-networks* to enhance the filtering selectivity. Two examples will be provided, the first for a Butler matrix with symmetric filtering response and the second one implementing a TZ at finite frequency.

4.6.1 Sub-networks

The synthesis procedure for the minimal Butler matrix with filtering has been introduced in section 4.4 and it is based on the synthesis of a reference filter through standard techniques and later combining the coupling matrix. The reference filter is formed by a number of poles equal to those of each independent signal path goes through the circuit. For each path k hybrids are required in order to provide the power splitting and phase distribution, hence the number of poles are 2k in total. As the hybrid are the fundamental building block of the network, they are required to be indivisible units. The idea here is to add resonators and/or cross couplings between pairs of hybrids or between input/output hybrids and external ports through a series of sub-networks $\Sigma_i(\rho_i;\zeta_i)$. Each sub-network Σ_i is introducing an additional number of poles ρ_i and complex/imaginary TZs ζ_i. Fig. 4.8 is a schematic of the reference

filter, where a number of sub-networks Σ_i are shown between pairs of resonators and at the input and output stage of the circuit. The two resonators between each block represent the 2 poles introduced by each hybrid of the Butler matrix. It is known that each path has k hybrids and consequently there are up to $k+1$ sub-networks. Each sub-network can be a resonant circuit or just a simple coupling when there is no need for elements in a particular position. It is possible to see the circuits of Fig. 4.5 is a particular case of Fig. 4.8, where each sub-network is an ordinary coupling. The characteristic of symmetry of the hybrids must be preserved in order to add arbitrary sections as in Fig. 4.5 without altering the properties stated in eq.s (4.26). Thus the topology of the base filter requires the pairs of resonators to be unaltered while the other sections can be included with resonators and cross-couplings.

The synthesis of the Butler matrix with extended filtering follows an analogous procedure of the one of section 4.4:

1. the coupling matrix of the base filter is firstly calculated with traditional techniques with a topology of the type of Fig. 4.8. Note that the restriction is on the symmetry of the unit hybrids, hence the self-couplings (or detuning of the single resonators) are allowed.

2. Every signal path should see the same sequence of resonators and coupling as that of the reference filter.

3. The elements of sub-networks Σ_1 and Σ_{k+1} apply, respectively between all the input/output ports and input/output of the first/last column of hybrids.

4. The element of the generic sub-network Σ_i apply to all the connections between outputs of hybrids on column u_{i-1} and inputs of hybrids on column u_i.

5. The couplings of the hybrids on the same column follow the same rule of eq. (4.35), with reference the coupling between pairs of resonator on same column of Fig. 4.8.

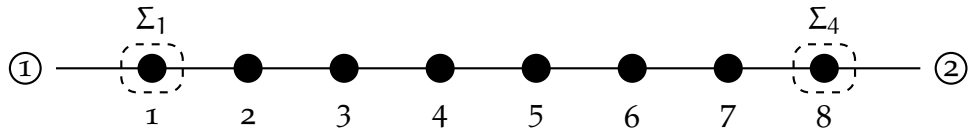

Figure 4.9: Example of in-line symmetric reference filter with 2 sub-networks formed by a single resonator

Globally, the total number of poles ρ_{tot}, total number of zeros ζ_{tot} and total number of resonators n_{tot} are given as:

$$\rho_{tot} = \sum_{i=1}^{k+1} \rho_i + 2\log_2 N \tag{4.41}$$

$$\zeta_{tot} = \sum_{i=1}^{k+1} \zeta_i \tag{4.42}$$

$$n_{tot} = \sum_{i=1}^{k+1} n_i + 2N\log_2 N \tag{4.43}$$

where n_i are the number of resonators of sub-network Σ_i.

4.6.2 Example with symmetric response

In this example an 8×8 Butler matrix with Tchebycheff transfer function of 20 dB RL will be discussed. Here the conventional response exhibiting 6 poles as stated by eq. (4.31) is enhanced by symmetrically adding 1 resonator at the beginning and on the end of each filter path. Fig. 4.9 is a schematic of the reference filter with 1 resonator added at the beginning and at the end. In the figure the sub-networks Σ_1 and Σ_4 are shown. These are simply formed by a single resonator each. The other sub-networks are not present in the circuit and the internal hybrids are directly connected through a simple coupling. The final network configuration will be the one of Fig. 4.5c with one additional resonator included after each input port and before each output. The synthesis of the reference filter of Fig. 4.9 reduces to the calculation of a simple in-line prototype with the g constants and the coupling coefficients shown in Tab. 4.2.

Table 4.2: Coefficients of the reference 8-pole Tchebycheff filter with 20 dB return loss

h	g_h	$M_{h,BPF}$
0	1	
1	1.0189	0.990683
2	1.45177	0.822214
3	1.96825	0.591576
4	1.65697	0.553736
5	2.02518	0.545897
6	1.61038	0.553736
7	1.77439	0.591576
8	0.833644	0.822214
9	1.22222	0.990683

The first column of hybrids is identified by resonators 2-3, the second by 4-5 and the third by 6-7. Thus the coupling between the first and second column of hybrids, and between the second and the third are 3-4 and 5-6 respectively. Thus the coupling coefficient in the normalised low-pass domain are again directly derived by Tab. 4.2 as: $M_{1,BPF} = 0.9907$ (external coupling), $M_{2,BPF} = 0.8222$ (extra resonator), $K_{u_1} = 0.4183$, $K_{u_2} = 0.3860$, $K_{u_3} = 0.4183$, $K_{u_1,u_2} = 0.5537$ and $K_{u_2,u_3} = 0.5537$. The magnitude response is shown in Fig. 4.10. Again only the reflection α and transmission β are shown in the figure as they are all the same for all inputs/outputs and transmission parameters. The power splitting is equal to -9 dB as it is an 8×8 Butler matrix. There are 8 poles in the transfer function, 6 of them produced by the standard network and 2 by the external additional resonators introduced. Note that here 2 sub-networks have been introduced in order to symmetrically add 1 resonator at input and output. However it was also possible to include them either at the beginning or at the end without altering the response or the synthesis procedure, but having an impact only on the physical implementation of the Butler Matrix.

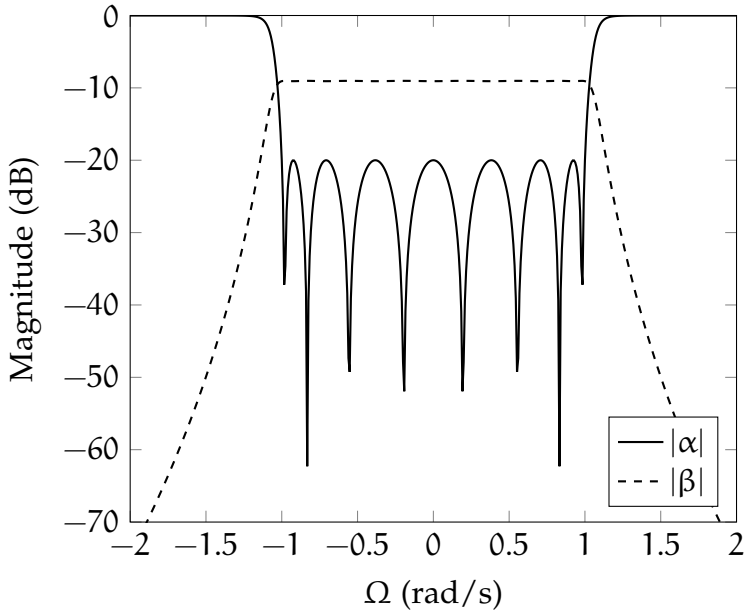

Figure 4.10: Magnitude response of reflection (α) and transmission (β) of an 8×8 Butler matrix with $\nu = 1$ extra resonator at each port

4.6.3 Example with transmission zeros

The example of extension of the filtering characteristic 4×4 Butler matrix with the inclusion of a TZ is given in this section. The reference filter used here introduces a zero at $s = j1.4$ with 25 dB of RL on a Tchebycheff 6-pole filter. The topology of the reference filter with transmission zero is shown in Fig. 4.11a together with its frequency response in Fig. 4.11b. The topology is an extension of the traditional 4-pole filter because of the addition of the sub-network Σ_2 between the internal hybrids, which includes $\rho_2 = 2$ additional poles and $\zeta_2 = 1$ zero. The configuration of the hybrids will not be modified because both resonators of Σ_2 are coupled with resonator 2 thus the virtual open circuit of the first column of hybrids u_1 is unaltered. In this example there no external sections Σ_1 nor Σ_3.

Initially the coupling matrix of the reference filter is calculated with conventional techniques, like [34] or the procedure in appendix B for $p = 2$ ports and $n = 6$ resonators. Tab. 4.3 shows the coefficients of the scattering polynomials of the filter of

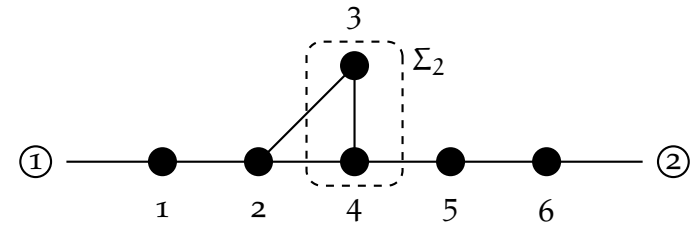

(a) Reference filter topology

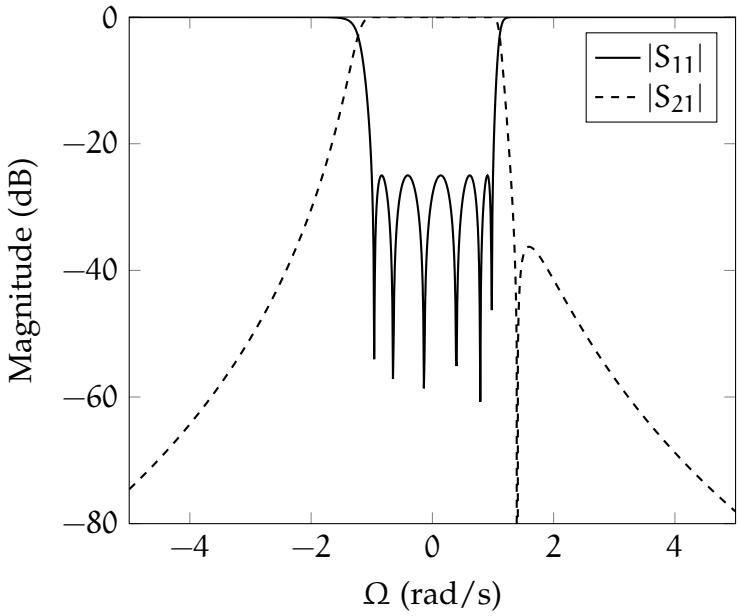

(b) Frequency response

Figure 4.11: Reference filter with transmission zero

Table 4.3: Coefficients of the polynomials of the Thebycheff 25 dB filter with one zero at $s = j1.4$. Scattering parameters $E(s)$, $F(s)$, $P(s)$ and admittance matrix common denominator $y_d(s)$ and numerators $y_{11}(s)$ and $y_{21}(s)$

Degree of s	E(s)	F(s)	P(s)	$y_d(s)$	$y_{11}(s)$	$y_{21}(s)$
6	1	1		1		
5	$2.4248 + j0.4202$	$j0.4202$		$j0.4202$	1.2124	
4	$4.3957 + j1.0796$	1.4559		2.9258	$-j0.5398$	
3	$4.9439 + j1.9077$	$j0.5253$		$j1.2165$	2.4719	
2	$3.9031 + j2.0619$	0.5184		2.2107	$-j1.0309$	
1	$1.8937 + j1.4249$	$j0.1313$	1	$j0.7781$	0.9469	0.2331
0	$0.4357 + j0.4868$	0.0257	$j1.4$	0.2307	$-j0.2434$	$-j0.3264$

Fig. 4.11 with the constant ripple of $\epsilon = 2.1446$. The residues are calculated from the admittance parameters and later the transversal coupling matrix is found to be

$$\mathbf{M}_{p,r} = 0 \tag{4.44a}$$

$$\mathbf{M}_{pn,r} = \begin{bmatrix} 0.3801 & -0.5264 & 0.5110 & -0.4681 & 0.4479 & -0.3316 \\ 0.3801 & 0.5264 & 0.5110 & 0.4681 & 0.4479 & 0.3316 \end{bmatrix} \tag{4.44b}$$

$$\mathbf{M}_{n,r} = \begin{bmatrix} 1.3343 & 0 & 0 & 0 & 0 & 0 \\ 0 & 1.0176 & 0 & 0 & 0 & 0 \\ 0 & 0 & 0.2006 & 0 & 0 & 0 \\ 0 & 0 & 0 & -0.6049 & 0 & 0 \\ 0 & 0 & 0 & 0 & -1.1462 & 0 \\ 0 & 0 & 0 & 0 & 0 & -1.2216 \end{bmatrix} \tag{4.44c}$$

Then, a set of matrix similarities are applied in order to find the final coupling matrix [117]:

$$\mathbf{M}_{p,r} = 0 \tag{4.45a}$$

$$\mathbf{M}_{pn,r} = \begin{bmatrix} 1.1011 & 0 & 0 & 0 & 0 & 0 \\ 0 & 0 & 0 & 0 & 0 & 1.1011 \end{bmatrix} \tag{4.45b}$$

$$\mathbf{M}_{n,r} = \begin{bmatrix} 0.025 & 0.9358 & 0 & 0 & 0 & 0 \\ 0.9358 & 0.0311 & 0.5475 & 0.3405 & 0 & 0 \\ 0 & 0.5475 & -0.5825 & 0.5084 & 0 & 0 \\ 0 & 0.3405 & 0.5084 & 0.0499 & 0.6448 & 0 \\ 0 & 0 & 0 & 0.6448 & 0.0311 & 0.9358 \\ 0 & 0 & 0 & 0 & 0.9358 & 0.025 \end{bmatrix} \tag{4.45c}$$

In the last equations the subscripts of the matrices are have been included with the letter r to indicate that they refer to the reference filter and not to the Butler matrix.

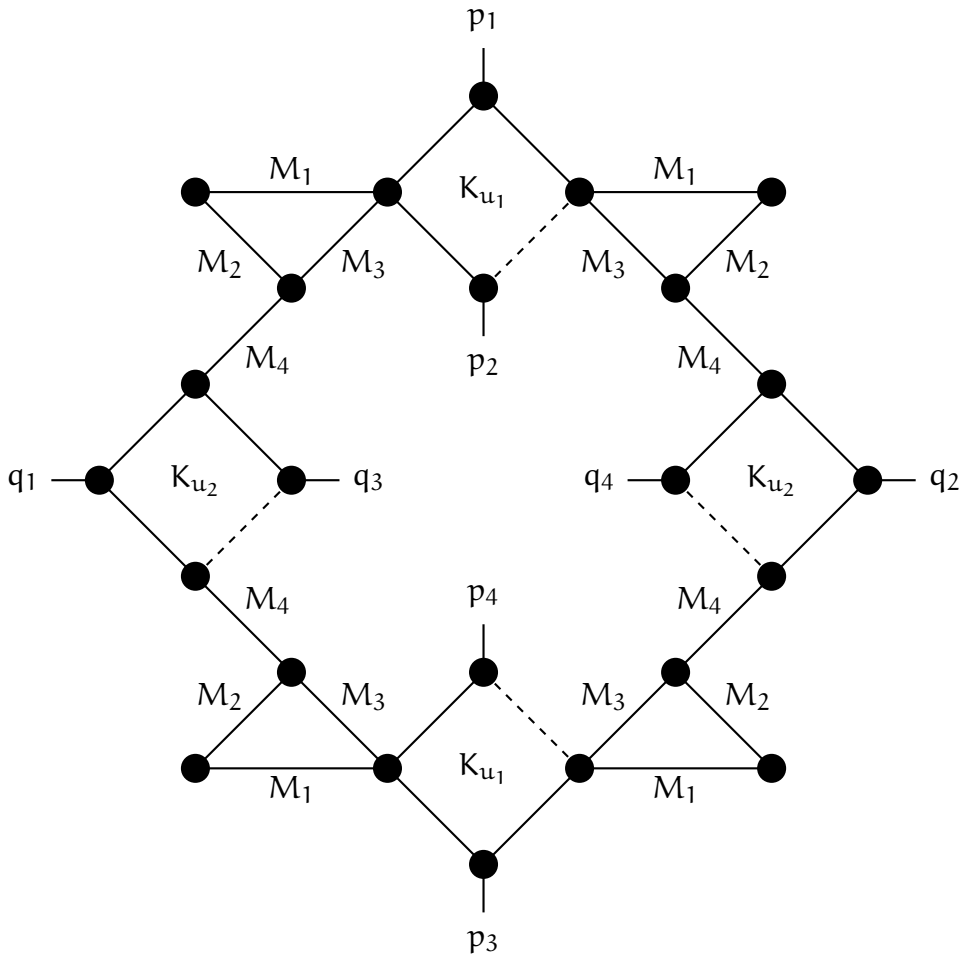

(a) Topology. From each input to output it is possible to recognise the filter configuration of Fig. 4.11a on page 145

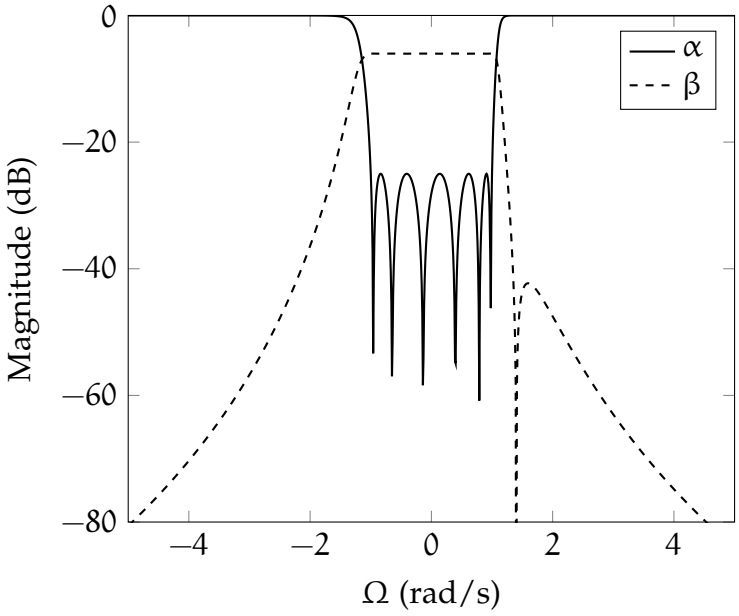

(b) Frequency response

Figure 4.12: Butler matrix 4×4 implementing a TZ

The topology of the 4×4 Butler matrix $n_{tot} = 24$ resonators is shown in Fig. 4.12a. It follows the traditional configuration of Fig. 4.5b with the addition of sub-network Σ_2 between pairs of hybrids internally. The coupling coefficients are directly calculated from eq. (4.45c). The hybrids have the same configuration of eq. (4.7c) for the internal quadruplet of resonators and of eq. (4.7b) for the external couplings. Here the external couplings are the same as $[\mathbf{M_{pn,r}}]_{1,1} = 1.1011$ while the internal are

$$K_{u_1} = \frac{1}{\sqrt{2}}[\mathbf{M_{n,r}}]_{1,2} = 0.6617 \tag{4.46}$$

Fig. 4.12a includes the negative couplings of the hybrids through dashed lines. Due to the symmetry of the reference filter, the second column of hybrids has the same couplings. In between the internal hybrids is included the sub-network Σ_2 with the couplings indicated in Fig. 4.12a as:

$$M_1 = [\mathbf{M_{n,r}}]_{2,3} = 0.5475 \tag{4.47}$$

$$M_2 = [\mathbf{M_{n,r}}]_{3,4} = 0.5084 \tag{4.48}$$

$$M_3 = [\mathbf{M_{n,r}}]_{2,4} = 0.3405 \tag{4.49}$$

$$M_4 = [\mathbf{M_{n,r}}]_{4,5} = 0.6448 \tag{4.50}$$

In this example it is also interesting to note that all coefficients on the diagonal of eq. (4.45c) are non-zero, hence all the resonators of the 4×4 Butler matrix have a frequency shift. This fact does not compromise the property of virtual open circuit of the single quadruplet-hybrid because the self-coupling $[\mathbf{M_{n,r}}]_{1,1}$ and $[\mathbf{M_{n,r}}]_{2,2}$ are systematically applied, respectively, to resonators 1, 3 and 2, 4 so as they do not alter the perfect balance of interference signal paths inside the hybrid. Naturally, also the 2 resonators of Σ_2 have their self-coupling unaltered and equal to elements $[\mathbf{M_{n,r}}]_{3,3}$ and $[\mathbf{M_{n,r}}]_{4,4}$. Fig. 4.12b shows the magnitude of the reflection α and transmission β characteristics. As expected, the magnitude of the transfer function is identical to the one of the reference filter of Fig. 4.11b with in addition the equal power split of -6 dB

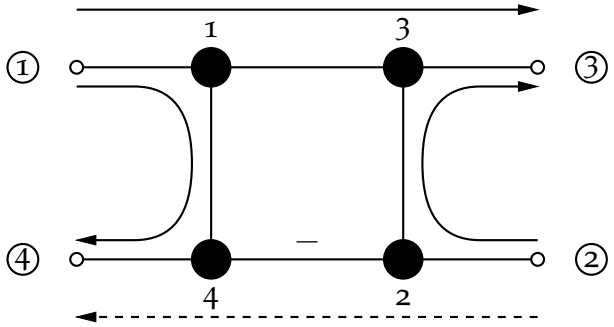

Figure 4.13: Schematic of 180° hybrid with simultaneous excitations at ports 1 and 2. Solid lines are signal in phase while dashed line is the signal with out of phase

due to the transmission to the 4 output ports. All the transmission parameters exhibit a TZ at $s = j1.4$, a RL of 25 dB and 6 poles.

4.7 MULTI-PORT EXCITATION OF N × N BUTLER MATRIX

The scattering parameters are obtained by measuring the ratio of the incident/reflecting waves at two ports while the others are terminated on matched loads. The output phase distribution is not considered when multiple inputs are applied simultaneously at more ports. The Butler matrix with filtering is made here with several 180° hybrids, each of them producing out of phase contributions that might destroy part of the input signals. Hence, it is mandatory to keep all the fields orthogonal inside the cavities of every hybrid [118].

The arrows of Fig. 4.13 show the phase relation between the two output signals. If the signal, for example, is applied to port 1 only, it is equally split between ports 3 and 4 and the signals that have the same phase at the two outputs. This is because every coupling can be modelled as an immittance inverter, which gives a phase shift of $\mp 90°$ depending on its sign. Indeed, the phase of S_{31} is the same of the phase of S_{41} as stated also in Fig. 4.13. However, between resonator 2 and 4 a negative coupling creates the out-of-phase distribution of parameters S_{32} and S_{42}. The generic scattering parameter S_{ij} is a representation of the power flowing from port j to i when

all the other ports are matched. In the current application the interest is to have at the same time two input sources at ports 1 and 2. The assumption made here is that the input signals are coming either from a common source (ie. an HPA) or from different equipment generating two identical signals. With this in mind it is clear from Fig. 4.13 that at port 3 there is the sum of two in-phase signals whilst at port 4 the two are of opposite phase at all frequencies, producing no output at that port and destroying the splitting characteristic of the device.

The problem resides in the intrinsic phase distribution of the 180° hybrid power divider and is independent on this particular implementation based on resonant cavities [30]. A possible way to overcome the problem is to introduce a phase shifter of 90° in order to have orthogonal signals in cavities 3 and 4 at all times. With Butler matrices with $N > 2$ the orthogonality should be guaranteed for each input hybrid, hence the 90° phase shift is to be included at the second port of each hybrids on column u_1. The phenomena is intrinsic to the nature of the 180° hybrid and, once corrected, does not affect the overall response of the MPA. This is a prerequisite for input signals that can also be operated at system level as it does not affect the configuration of the network proposed.

5 PROTOTYPES AND EXPERIMENTAL RESULTS

In this chapter the design, manufacturing and testing of a 2×2 and a 4×4 Butler matrix with filtering in standard rectangular waveguide will be presented. The synthesis of the coupling matrices will be obtained through the procedure given in chapter 4. The RF measurements to experimentally confirm the theoretical synthesis technique for the novel 4×4 Butler matrix that incorporates filter transfer functions. Moreover, the synthesis and design of the conventional 2×2 hybrid of 180° is included in order to have a confirmation of the proposed synthesis technique with respect a well-known reference device. The implementation has been carried out at X-band for the 2×2 hybrid and at Ku-band for the 4×4 Butler matrix.

5.1 ELECTROMAGNETIC MODEL

5.1.1 Selection of the type of resonator

The implementation of the hybrid and Butler matrix in standard rectangular waveguide is proposed. This technology has been chosen mainly for simplicity of manufacturing, reduced loss and high power handling. Also, the waveguide technology is well suited for X and Ku-band. The resonators are standard half-wavelength cavities coupled with inductive apertures.

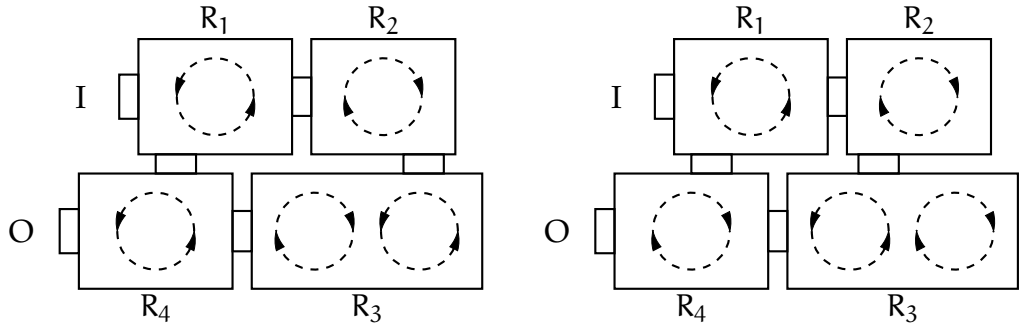

(a) Negative **(b)** Positive

Figure 5.1: TE_{102} cavity to create positive/negative couplings. Top view shown with direction of magnetic fields in the resonant cavities indicated with arrows

5.1.2 Negative coupling introduced by planar H-plane cavity

The fundamental unit for the Butler matrix is the quadruplet of resonator of Fig. 4.2 in which all couplings are the same except one that has opposite sign. In waveguide technology the implementation of such a negative element might require the inclusion in the structure of probes or loops in order to create the desired effect, affecting the power capabilities [34, 119]. Alternatively, a method exploiting the different phase of the EM fields with TE_{102} cavities may be used [120]. Fig. 5.1 shows an example of this cavity that implement either a negative or positive cross coupling between resonators 1 and 4. The input and output ports are indicated with I and O while the resonators number with R_i. In this example the cavities are all half wavelength, or one wavelength, with inductive couplings. This is a top view of a 4-pole filter with the direction of the magnetic field indicated. The figure also shows that cavities 1, 2 and 4 are using the TE_{101} mode while cavity 3 the TE_{102}. Single mode means that the fundamental resonant mode, for a rectangular waveguide for example, is the TE_{101} while in the high order mode is the TE_{102}. For the latter 2 local maxima of the electric fields are obtained. This is the case of cavity 3 of Fig. 5.1. It is well known that the phase of the fields in two adjacent resonant cavities mutually coupled is opposite [29]. This is because the half-wavelength resonator can be modelled as a pair of an inductor and a capacitor followed by a transformer of ratio $1 : -1$ in order to characterise

the 180° electrical length of the resonator. In Fig. 5.1 the reference direction of the magnetic field is anti-clockwise for both cases in cavity R_1. The field in cavity R_2 is clockwise. When it comes to resonator R_3 the EM field has 2 local maxima because of the, theoretical, double length of the cavity. Fig. 5.1a shows the implementation of negative coupling between resonators R_1 and R_4 because the directions of the fields in the two cavities is the same. The dual case is shown in Fig. 5.1b because a different position of the coupling element between R_2 and R_3 is responsible for the positive coupling between R_1 and R_4.

The method described here shows that it is possible to use a combination of TE_{101} and TE_{102} cavities in order to create negative couplings without the need of capacitive probes or loops that might reduce the power handling levels. Also, from a manufacturing point of view it is more convenient to have all the couplings the same technology. The price to pay is to use a cavity that is theoretically twice longer than the others. This solution for the design of the fundamental hybrid will be adopted.

5.1.3 Design

In any of the $N \times N$ Butler matrices to implement, the quadruplet of Fig. 4.2 is the fundamental building block for any implementation. In this chapter a 2×2 hybrid and a 4×4 Butler matrix are manufactured in standard rectangular waveguide. The design of the hybrid exploits the concept of negative coupling produced by having 3 single mode resonant cavities and one TE_{102} resonator as explained in the previous section. A similar solution was adopted also in [107, 113]. Fig. 5.2 is the top view of the implementation of the hybrid with the direction of the magnetic fields indicated in all the cavities. It implements the topology of Fig. 4.2 where ports P_1-P_2 and P_3-P_4 are mutually isolated. With reference of a anticlockwise direction of the magnetic field in resonator 1 (R_1), the field is clockwise for both cavities R_3 and R_4. The same phase between output ports P_3 and P_4 is in accordance with the theory presented in the

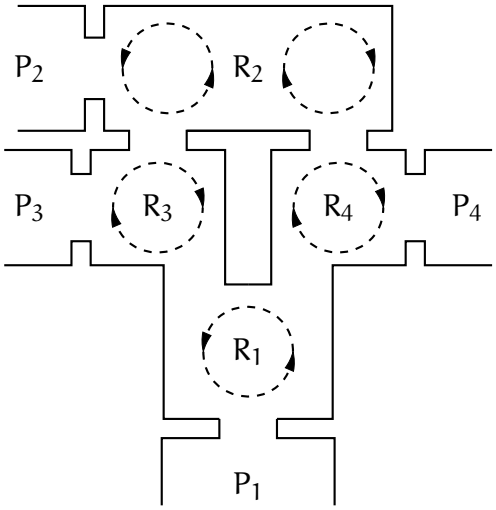

Figure 5.2: Hybrid fields configuration

previous chapter. Cavities R_3 and R_4 are coupled to the two local maxima of resonator R_2. This cavity is a TE_{102} as it's length is in principle twice of the others. Resonator R_2 has the external port coupled with the maximum on the left part of Fig. 5.2. The R_1 is the first cavity when excited is port 1 while R_2 is the first one when input is at port 2, hence the direction of the field on the left part of the latter cavity should be the same of the one in resonator R_1, hence anticlockwise. The direction of the magnetic field in the right part of R_2 is clockwise, the same as it is in R_4. Thus, the coupling between R_2 and R_4 is negative while all the others are positive. All the couplings here are obtained through inductive apertures. The configuration of the field in such a design implements the quadruplet topology of Fig. 4.2.

The adoption of the TE_{102} cavity for resonator R_2 introduces an asymmetry with regard the isolation seen for parameters S_{21} and S_{43}. From the model of Fig. 4.2 these values should be 0 at all frequencies under the assumption that a perfect symmetry is in place. With the design of Fig. 5.2 this is no longer true and the characteristics of the isolations in the 3D implementations will not be 0. Thus it will be necessary to optimise the dimensions of cavities and aperture of the couplings in order to keep the isolation below the maximum level defined by the specifications, whilst keeping unaltered the properties of filter transfer function, power splitting and phase distribution.

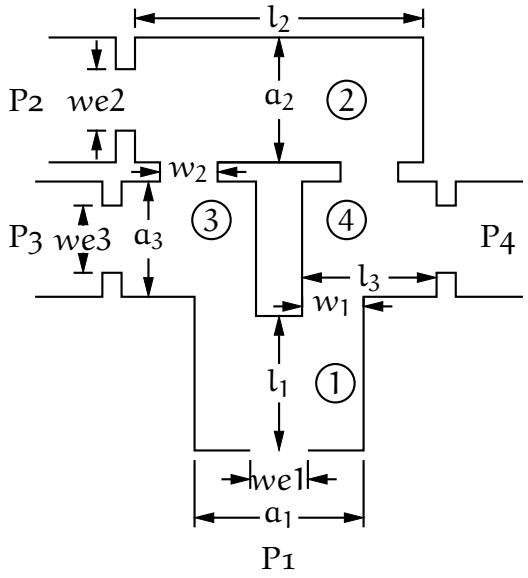

Figure 5.3: Top view schematic of 180° hybrid

5.2 HYBRID 180° WITH FILTERING

The synthesis procedure for N × N Butler matrices with filtering is firstly used to implement the basic 2 × 2 hybrid 180° power splitter. This is an example to show the validity of the theory with respect the well-known hybrid used here as a reference. The specifications are centre frequency $f_0 = 10\,\text{GHz}$, bandwidth $B = 140\,\text{MHz}$ and return loss better than 25 dB and a Tchebycheff transfer function. The isolation should result below −25 dB also. The coupler is implemented in standard WR90 rectangular waveguide.

5.2.1 Physical implementation

The design model of the device which has the structure of Fig. 5.2 is repeated here with all the dimensions and labels in Fig. 5.3. The ports and resonators numbering has not been changed. The height dimension of the waveguide is $b = 10.16\,\text{mm}$ and it is constant for all elements in Fig. 5.3. To keep symmetries, the width of resonators 3 and 4 is the same and labelled with a_3, as it is the aperture w_{e3} with the external

port and lengths l_3. The iris aperture between resonators 1, 3 and 4 is indicated with w_1 while the one between 2, 3 and 4 with w_2.

The initial coupling coefficients are extracted from the EM model through the technique given in section 2.6.2. In order to calculate the coupling by varying the w_1 dimension, only cavities 1 and 4 are considered. The other cavities are removed from the model with external couplings w_{e1} and w_{e3} set as weak couplings in order not to interfere with the contribution of w_1. The rest of the procedure is analogous to the one shown in section 2.6.2. The plot of the coupling values is shown in Fig. 5.4a. Similarly, the coupling coefficient derived by w_2 is calculated considering only cavities 2 and 4 with weak couplings w_{e2} and w_{e3}. The results for w_2 are shown in Fig. 5.4b. The diagram for the external quality factor of Fig. 5.4c has been calculated with the same technique described in section 2.6.2.

The coupling matrix takes the basic form of eq.s (4.7b) and (4.7c) and they were calculated in section 4.3 resulting in eq.s (4.17). The denormalised values are $k_u = 0.02145$ and $Q_e = 34.871$. The k_u is the absolute value of the internal couplings of the hybrid, as one of them is negative according with the topology of Fig. 4.2. From the previous values the initial dimensions of the hybrid are found and later an overall optimisation of the structure is performed. The table with initial and optimised dimensions is shown in Tab. 5.1. The initial dimensions directly come from the set of curves of Fig. 5.4, while the optimised ones also take into account the radii in the internal corners of the structure. This model has been designed in order to have a main body of the form of Fig. 5.3 with a flat lid on top to close the structure. The thickness of the irises has been set to 1 mm in order to allow a realisable aperture of the irises for the required coupling coefficient. Also, port 2 and 3 are too close to include the external flanges, so mitered bends are included in order to accommodate the flanges. In order to keep symmetry and phase to each port, the same type of bend are also added to the other ports. The length of the side of the bend has been optimised with Fest3D in order to get a RL of -80 dB at 10 GHz, resulting in 8.0535 mm length.

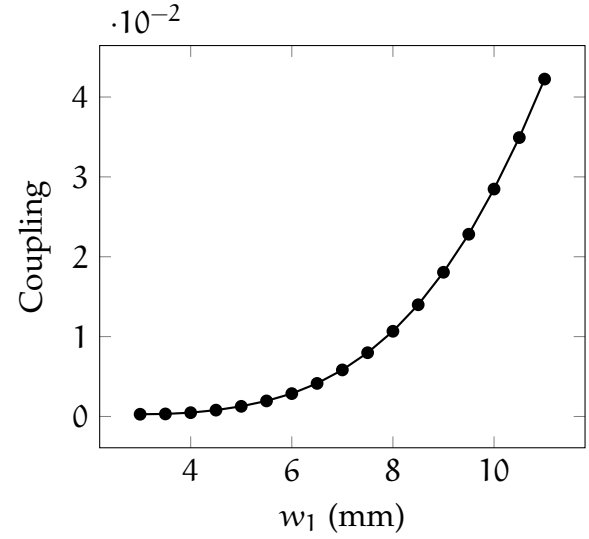

(a) w_1 iris

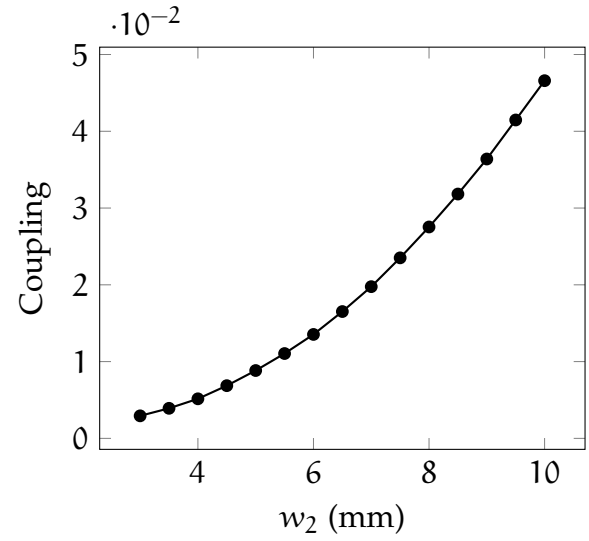

(b) w_2 iris

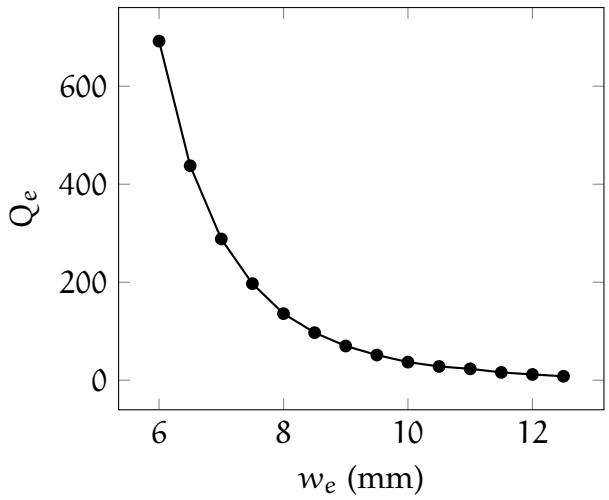

(c) w_e iris

Figure 5.4: Hybrid 180° denormalised coupling coefficients calculated for $f_0 = 10\,\text{GHz}$ and $B = 140\,\text{MHz}$

Table 5.1: Dimensions of the 180° hybrid with filtering

	Initial (mm)	Optimised (mm)
a_1	22.86	23.3214
a_2	22.86	22.86
a_3	22.86	22.86
l_1	19.9	16.2032
l_2	39.8	35.2386
l_3	19.9	16.4116
w_1	9.5	9.6519
w_2	7.5	8.3276
w_{e1}	10	10.2655
w_{e2}	10	11.7542
w_{e3}	10	10.3462
Thickness	1	1
Radii	1.5	1.5

The asymmetry introduced by cavity 2 affects the value of non-perfect isolation of S_{21} and S_{43}. Moreover it introduces a phase shift of transmission parameters $\angle S_{32}$ and $\angle S_{42}$ with respect the ones produced entering from port 1 such as $\angle S_{31}$ and $\angle S_{41}$. While $\angle S_{31}$ and $\angle S_{32}$ should have the same phase, $\angle S_{41}$ and $\angle S_{42}$ should produce a shift of 180°. These values are affected by the asymmetry of cavity 2 with respect the others, hence the phase mismatch is corrected by increasing the length of external port P_1 by $\delta = 0.8\,\text{mm}$ to have the perfect phase at centre frequency. Fig. 5.5 shows the main body of the 180° hybrid coupler with filtering, manufactured in Aluminium through a CNC milling. Port labels and cavity numbers are also included in the figure. In order to improve the contact between the main part shown in Fig. 5.5 and the lid, a number of screws has been put with grooving to increase the pressure between the two surfaces.

5.2.2 Measurements

A series of RF measurements have been conducted using a Vector Network Analyser (VNA) for the magnitude and phase response. The calibration has been performed

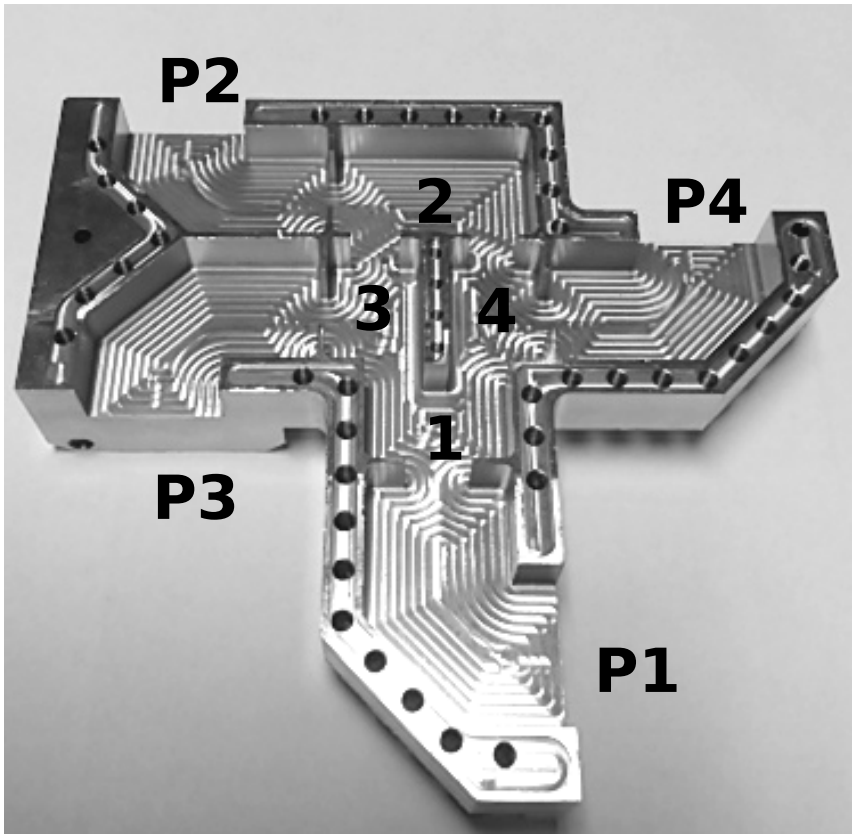

Figure 5.5: Prototype of 180° hybrid with filtering

with a standard WR90 kit to cover a frequency span from 9.5 GHz to 10.5 GHz with over 801 points. The measurements have been taken through a 2-port VNA with the other ports closed with precise (calibration) waveguide loads. The experiment can only measure 2 ports at time, hence it has been repeated in order to measure all the scattering parameters.

Fig. 5.6 shows the magnitude response of the hybrid. In all characteristics it is possible to distinguish a 2-pole Tchebycheff transfer function. Measurements, shown with solid lines, have been compared with simulation data shown with dashed lines. The RL is better than 22 dB in the worst case and the isolation is better than 25.8 dB. The tolerances of the manufacturing process are about $\pm 20\,\mu m$ and as result it is possible to see a shift down in frequency of the characteristics. The power splitting ratio is 3 dB in accordance to specifications. No tuning has been performed on this device.

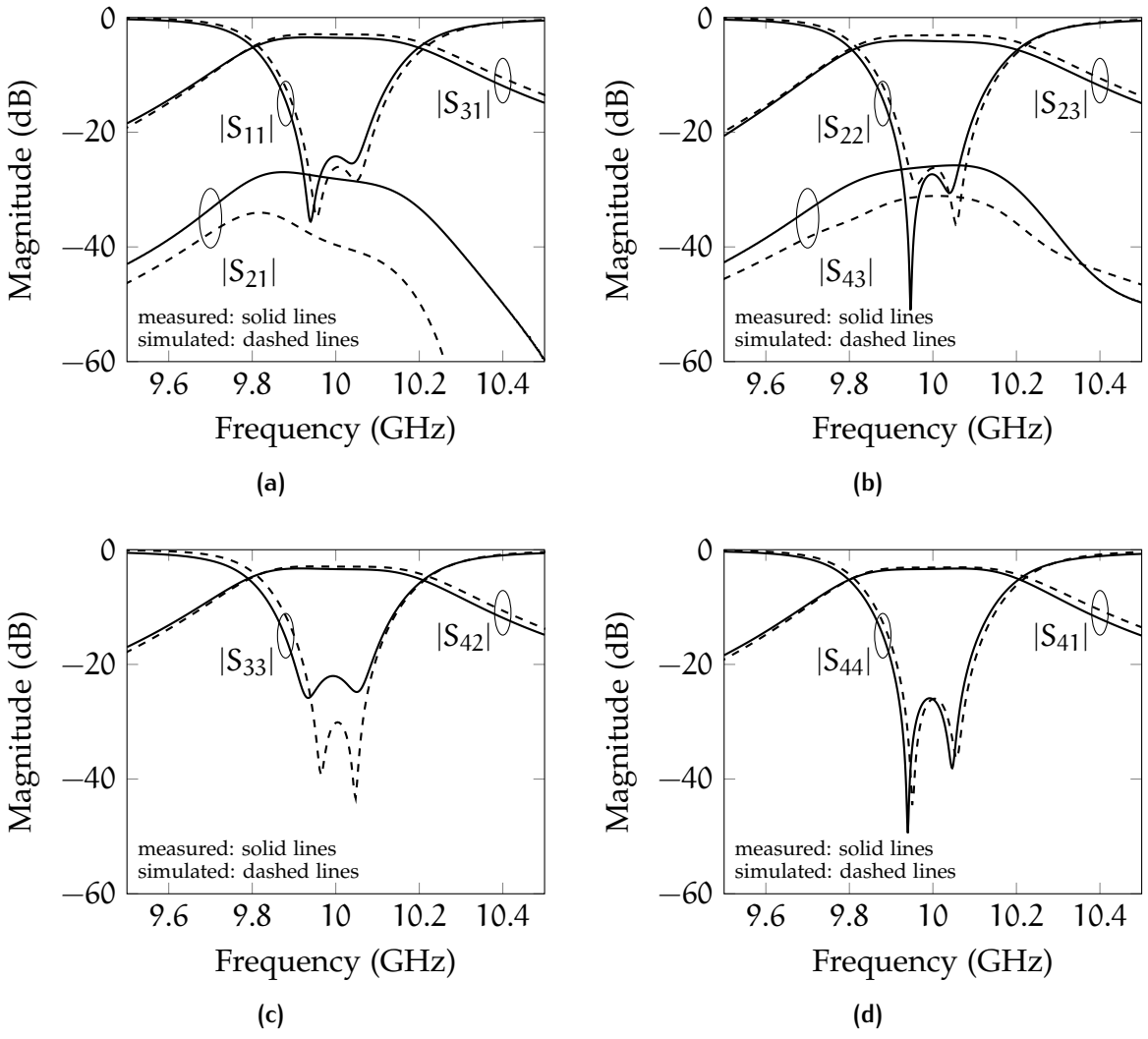

Figure 5.6: Magnitude measurements of 180° hybrid

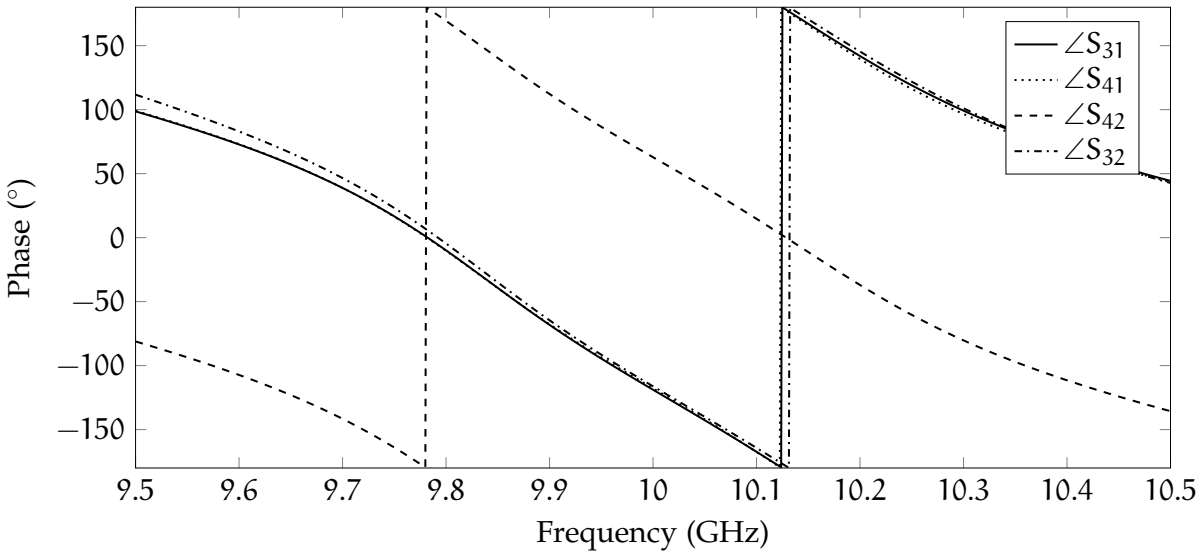

(a) Phase

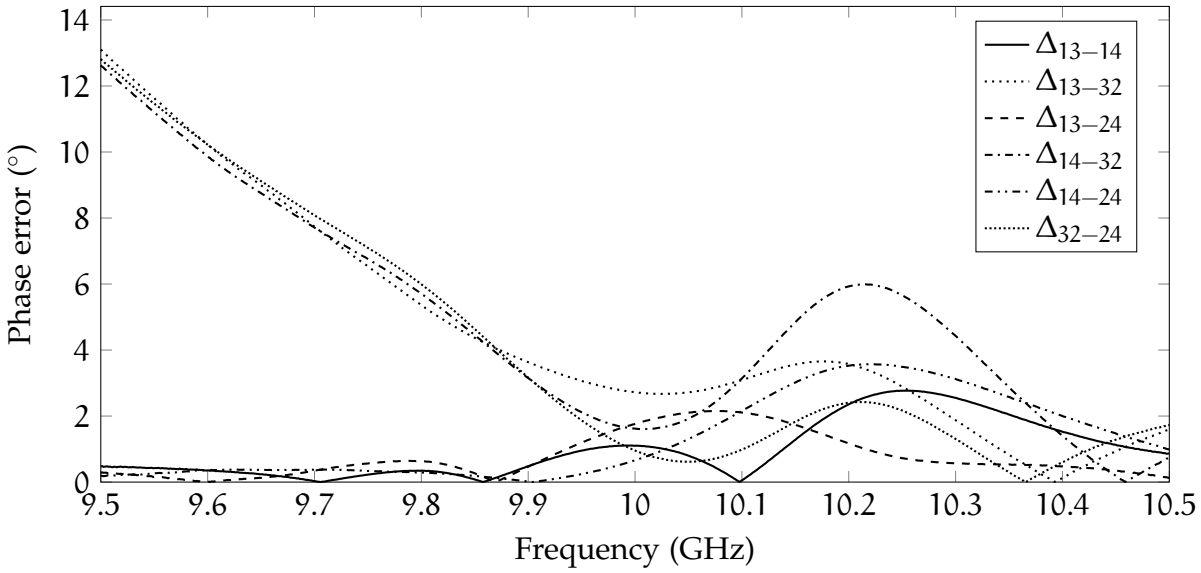

(b) Phase error

Figure 5.7: Phase measurements of 180° hybrid

The phase frequency response is shown in Fig. 5.7a. In the figure, only the phase of the transmission parameters has been shown. The distribution is in accordance with the transfer function matrix of eq. (4.18) because all the characteristics are in phase, except $\angle S_{42}$ that is out of phase. This demonstrates that the hybrid provides the power splitting, inherent filter transfer function and correct input to output phase distribution. However, it is also important to evaluate the phase error associated to this device. Fig. 5.7b shows the phase error of pairs of transmission transfer functions with respect the nominal value. Here, the error is not necessarily related to the absolute value of the phase transfer function. The phase error for these kind of hybrids is measured as the deviation of the difference of 2 transmission phase characteristics with respect the nominal value. The phase difference of 2 characteristics that are in phase should be 0° while it has to be 180° for the out-phase ones. Clearly the phase error is also a function of frequency. Fig. 5.7b shows the errors with the notation Δ_{ab-cd} in order to express the deviation between the $\angle S_{ab}$ and $\angle S_{cd}$. The phase difference is calculated in the same as was shown in Fig. 3.3. The phase distribution error has to be evaluated inside the operational bandwidth of the device, as outside the filter transfer function tends to reflect the incoming frequencies and phase becomes less relevant. The maximum deviation shown in Fig. 5.7b in the device bandwidth is 3.2° for the difference between $\angle S_{13}$ and $\angle S_{32}$.

5.2.3 Multipactor analysis

A multipactor analysis on the hybrid of Fig. 5.5 has been performed [118]. The object is to evaluate the multipactor discharge thresholds when multiple signals are applied simultaneously to the input ports. Also, multiple input signals means that they interact in the cavity in a different way with respect a traditional 2-port network. In this section the EM field distribution inside the device will be firstly described

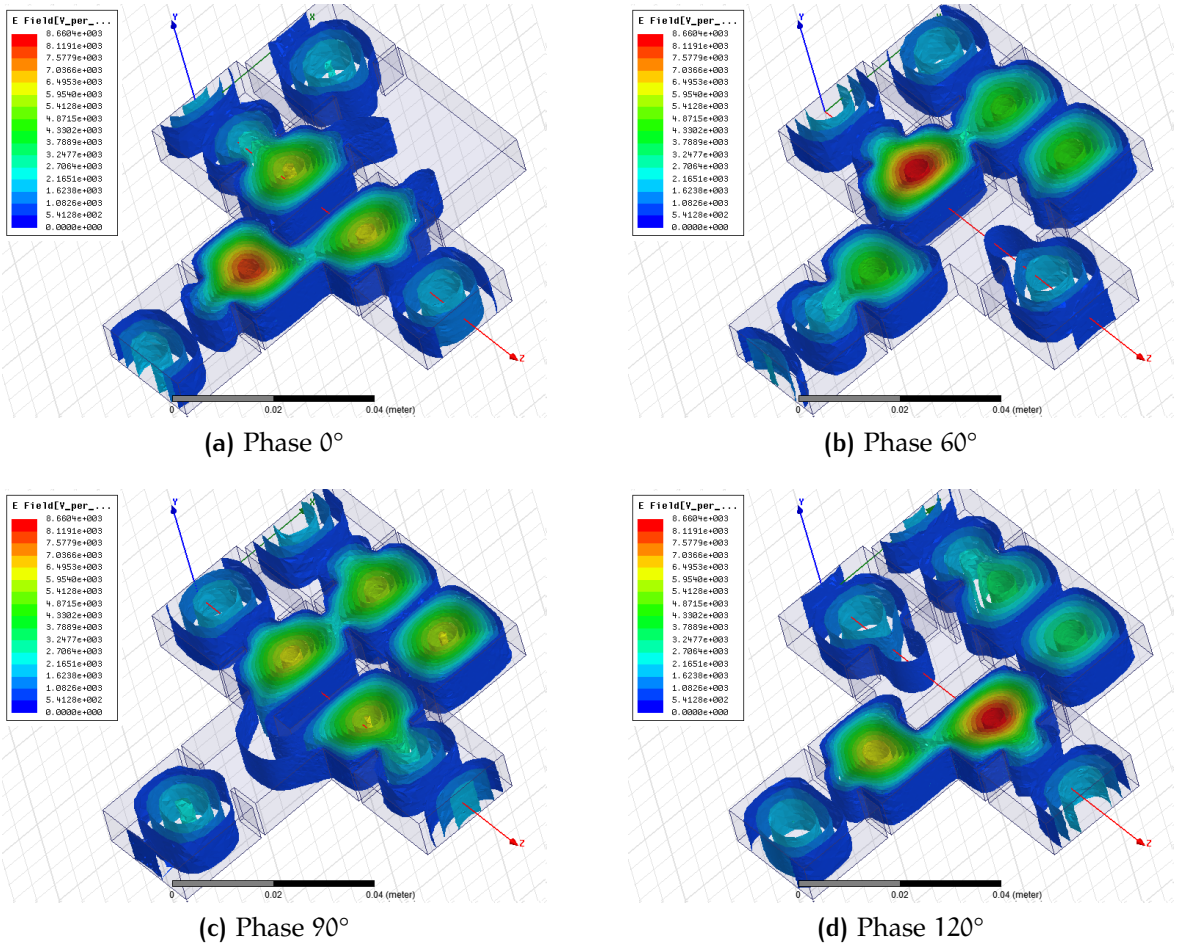

(a) Phase 0° **(b)** Phase 60°

(c) Phase 90° **(d)** Phase 120°

Figure 5.8: Hybrid electric fields with multi-port quadrature input excitations

when multiple inputs are applied, later the multipactor simulation will be evaluated at centre frequency and at the band edges.

Multiple inputs fields distribution

The input ports are 1 and 2 while the outputs are 3 and 4 as stated before. The hybrid operates when input signals are in quadrature, hence with a relative 90° phase shift as it was shown in section 4.7. Fig. 5.8 shows the configuration of the electric fields in the 180° hybrid coupler when 2, quadrature, input signals are applied simultaneously to ports 1 and 2. The figures are the representations of the fields for different times, or phase, obtained with HFSS. A signal entering from port 1 does not

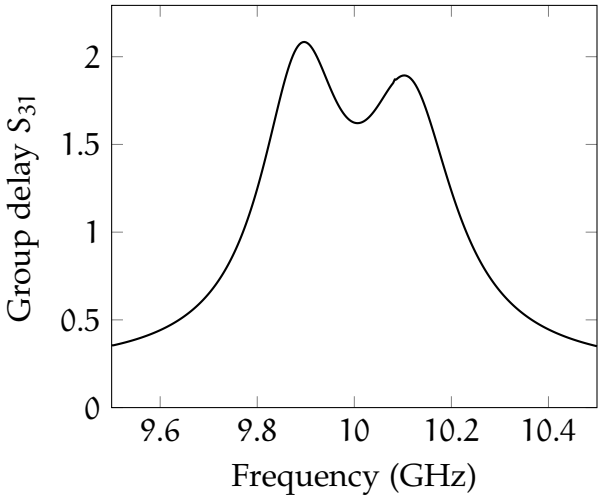

Figure 5.9: Group delay of the 180° hybrid coupler

affect the field in cavity 2, and the same happens when signal from port 2 does not have any impact on cavity 1. Thus, cavities 1 and 2 are affected by the resonance of only 1 signal contribution. However, this does not happen in cavities 3 and 4 because there is the interaction of the input signals that are in quadrature. From Fig. 5.8b and 5.8d it is possible to note the intensity of the magnitude of the electric field, concentrated in the centre of the resonator. The level of red on these cavities is higher than in cavity 1. Resonator 2 is a TE_{102} cavity and the resonance field distributes over 2 local minima. This has an impact on the maximum level of the magnitude of the electric field and is lower than in any other cavity. For this reason this study has been restricted to cavities 1, 3 and 4.

Multipactor is an effect that takes place when there is an exponential avalanche of electrons between two surfaces. The phenomena is also dependent on the frequency, angle and energy of the electric field. Thus, it is possible to predict the multipactor to happen in the areas where the field is stronger. The multipactor analysis of the device of Fig. 5.5 has been carried out using CST Particle Studio with tracking option in order to register the position of the discharges. Multipactor is also critical in resonators at the frequencies where the GD is higher, as there is a direct relation with the stored energy in the resonators [77, 121]. The GD for the S_{31} transmission parameter is shown in Fig. 5.9. The simulations will be performed at centre frequency $f_0 = 10\,\text{GHz}$

Table 5.2: Maximum voltages in the centre of cavities 1, 3 and 4

Frequency (GHz)	Cavity 1 (V)	Cavity 3 (V)	Cavity 4 (V)
10	80.8	86.8	86.05
9.9	111.9	78.69	82.01
10.1	99.5	81.9	80.34

and at $f_1 = 9.9\,\text{GHz}$ and $f_2 = 10.1\,\text{GHz}$ because in the latter 2 frequencies the GD are higher, hence the stored energy and the chance to have multipactor is also higher. For all the following simulations the material used is silver together with a Maxwellian source with an initial population of 5000 electrons over the whole structure. In order to predict the multipactor behaviour in both cavities 3 and 4, the following pair of signals is applied at ports 1 and 2:

$$s_{i1}(t) = \sqrt{P_{in}}\cos(2\pi f t) \tag{5.1}$$

$$s_{i2}(t) = \sqrt{P_{in}}\cos\left(2\pi f t + \frac{\pi}{2}\right) \tag{5.2}$$

where P_{in} is the input power at each input. Before starting the multipactor analysis at the three critical frequencies it is interesting to evaluate the maximum voltages inside the cavities. This is because the cavities that have absolute higher voltages are likely to be more affected by the multipactor [79]. With reference to the configuration of the fields in the multi-port excitation shown in Fig. 5.8, the centre of cavities 1, 3 and 4 are be expected to be affected more. However, the configuration of the electric field in cavity 2 shows a maximum level of amplitude that is lower with respect to the others by a factor 2. The maximum level of voltage inside cavities 1, 3 and 4 when signals (5.1) and (5.2) were applied with a $P_{in} = 0.5\,\text{W}$, has been evaluated in HFSS with the values tabulated in table 5.2. The calculation of the voltages was done by

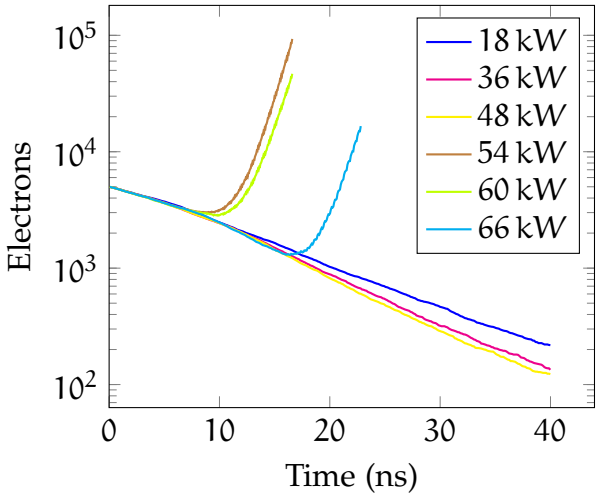

(a) Evolution of electron population for different values of P_{in}

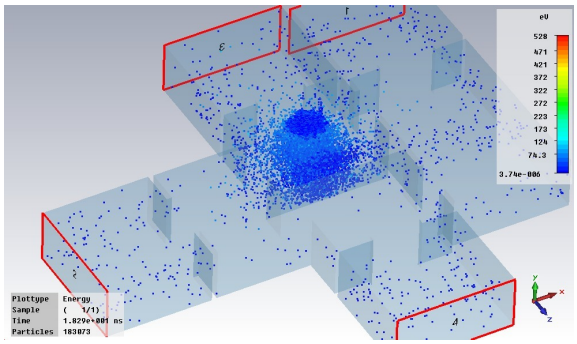

(b) Discharge at $P_{in} = 54\,kW$ in cavity 3

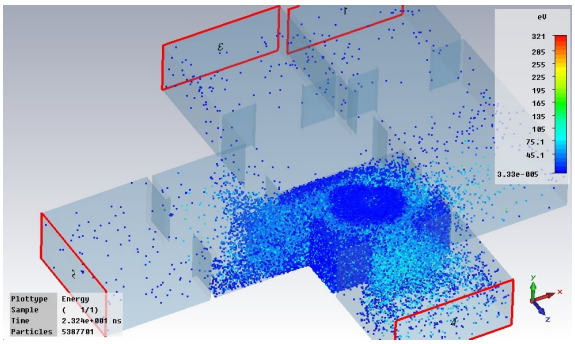

(c) Discharge at $P_{in} = 60\,kW$ in cavity 4

Figure 5.10: Multipactor analysis at 10 GHz

integrating the electric field over the line between the centres of top and bottom parts of the resonators

$$V = \int_0^b \vec{E} \cdot d\vec{s} \tag{5.3}$$

Central Frequency Analysis

The multipactor analysis has been carried out initially for the central frequency f_0. The evolution of the particles (electrons) inside the network for different level of P_{in} is shown in Fig. 5.10a. For power level less than about 50 kW there is a general absorption of the electron population and no discharges are reported. On the other hand, for power starting from 54 kW there is an exponential increase of electrons

caused by the secondary emission. Here the phenomena of multipactor occurs as the avalanche of electrons is self sustained. Fig. 5.10b is a plot of the electrons during the discharge at 54 kW. The multipactor occurs in cavity 4, one of the two with multi-carrier condition. Here the majority of the electrons are excited in the central part of the cavity, where the electric field is higher. In a similar way the multipactor occurs, with stronger effects, at higher power levels as shown in Fig. 5.10c for $P_{in} = 60\,kW$. The symmetries of the circuit create a combination of fields in cavities 3 and 4 that is very similar, so it is not possible to predict which one is more critical for multipactor.

According to the table 5.2, at the central frequency the maximum voltage in the centre of the three critical cavities shows that resonators 3 and 4 are more likely to be affected by multipactor. The voltage in cavities 3 and 4 are not exactly the same because of the non perfect symmetry of the design. However, the values are very close compared with the voltage in cavity 1. The values of maximum voltages in cavities 3 and 4 are, respectively, 7.43% and 6.5% higher than in cavity 1. This property is of great interest, as the height of all the resonators is constant and equal to $b = 10.16\,mm$, standard height WR90 waveguide.

Taking as a reference an input power $P_{in,\,ref} = 250\,W$ the margin in decibel with respect the multipactor critical power is:

$$10\log_{10}\left(\frac{P_{in,\,mul}}{P_{in,\,ref}}\right) = 10\log_{10}\left(\frac{50\,000\,W}{250\,W}\right) = 23.01\,dB \tag{5.4}$$

where the multipactor critical power has a value in between the last curve of electron absorption and electron avalanche of Fig. 5.10a. The margin is significantly higher than the typical 9 dB expressed in the standard ECSS document [86].

Analysis at Maximum of Group Delay

The analysis has also been performed where the group delay is maximum, at frequencies $f_1 = 9.9\,GHz$ and $f_2 = 10.1\,GHz$. The curves of the electron population for several input powers are shown for the two frequencies in Fig.s 5.11a and 5.11b while

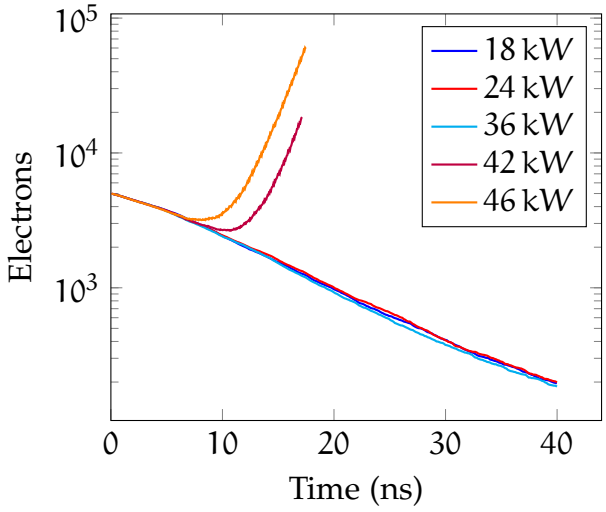

(a) Electron population at $f_1 = 9.9\,\text{GHz}$ for several P_{in}

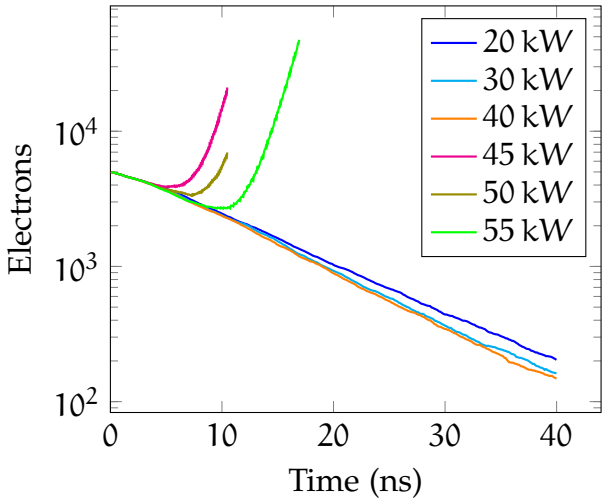

(b) Electron population at $f_2 = 10.1\,\text{GHz}$ for several P_{in}

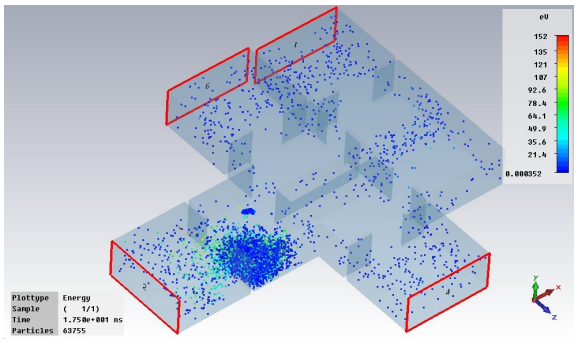

(c) Discharge at $f_1 = 9.9\,\text{GHz}$, $P_{in} = 46\,\text{kW}$ in cavity 1

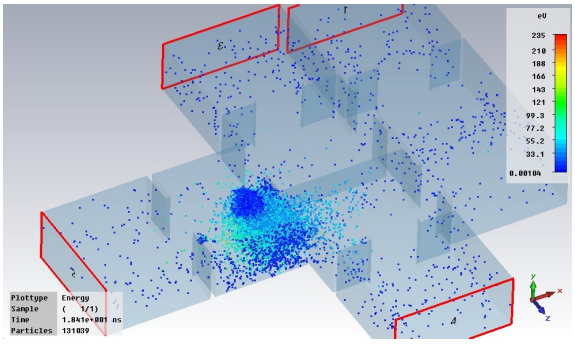

(d) Discharge at $f_2 = 10.1\,\text{GHz}$, $P_{in} = 55\,\text{kW}$ in cavity 1

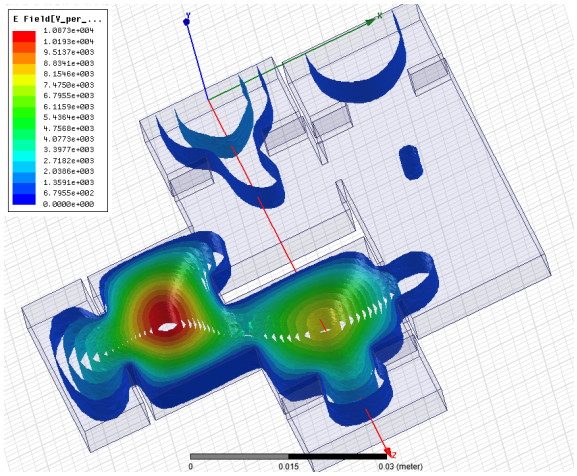

(e) Electric field distribution at $f_1 = 9.9\,\text{GHz}$

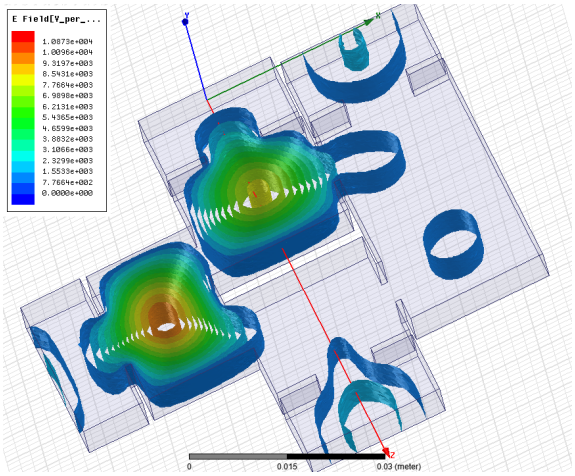

(f) Electric field distribution at $f_2 = 10.1\,\text{GHz}$

Figure 5.11: Multipactor analysis at critical frequencies f_1 and f_2.

the plots of multipactor are in Fig.s 5.11c and 5.11d. In this case the critical power is between 36 kW and 42 kW for frequency f_1 and between 40 kW and 45 kW for f_2. In contrast to the simulations conducted at the central frequency, here the critical cavity is number 1. This could be explained as at these operating frequencies the network is rejecting the input signals, so it is likely that the power is mostly stopped in the first cavity. Also, the values of voltages measured in table 5.2 are higher in cavity 1 at both f_1 and f_2. The plots of the magnitude of the electric fields at f_1 and f_2 are shown in Fig.s 5.11e and 5.11f. The red colour represents the level of the maximum value of the magnitude of the electric field and it has been normalized in both plots in order to make a comparison. The two plots are substantially in agreement with the expectations of multipactor coming from the simulations and the maximum voltage in the cavities. For both f_1 and f_2 cavity 1 has higher maximum voltage with respect the other cavities. Moreover, at f_1 at the centre of cavity 1, there was a level of 111.9 V compared with the 99.5 V for the f_2. The values of table 5.2 have been simulated with the input power of 0.5 W, but they are, once rescaled, indicative also for the level of powers conducted in other simulations. The margins respect to the nominal input power $P_{in,\,ref}$ are, for the two frequencies, 21.584 dB and 22.041 dB respectively.

The power levels necessary to create a multipactor condition in the 180° hybrid with filtering have been shown. However, it is important to state that these levels are more than 20 dB higher with respect the traditional power delivered, for example, by a TWTA of nominally 250 W. This is because of the inductive nature of the couplings and the absence of narrow gaps. Nevertheless, this study has shown which are the critical cavities of the device for different frequencies when multiple inputs are applied simultaneously.

5.3 BUTLER MATRIX 4×4 BASED ON RESONATORS

In this section, the novel implementation of a 4×4 Butler matrix with filtering in standard WR75 waveguide is shown. The device will be manufactured in 2 prototypes, one built with conventional CNC milling technique and the second one with Additive Manufacturing (AM). The aim is to provide experimental verification of the synthesis technique proposed in chapter 4, and to investigate alternative fabrication techniques.

The specifications are: bandwidth of 500 MHz, centre frequency $f_0 = 12.5$ GHz and RL better than 25 dB. The transfer function is of Tchebycheff type with no extra resonators. According to eq. (4.31) and (4.33) there will be $\rho = 4$ poles per transfer function through $n = 16$ resonators. Also, the number of 180° hybrids is $u = 4$ as stated by eq. (4.32). The calculation of the coupling matrix in the low-pass domain follows the example shown in section 4.5 on page 136. The coefficients are $K_{u_1} = 0.7360$, $K_{u_2} = 0.7360$ and the ones for the connections between pair of hybrids are $K_{u_1,u_2} = 0.77152$. The denormalized coefficients are $Q_e = 18.833$, $k_{u_1} = 0.029441$, $k_{u_2} = 0.029441$ and $k_{u_1,u_2} = 0.030861$.

The fundamental unit-hybrid is very similar to the used for the 180° hybrid of Fig. 5.3, with the second input, port 2, included on the top of cavity 2 instead of having it on the lateral side. The external coupling is placed in the centre of the cavity in order to confer better symmetry to the hybrid and to not interfere with the TE_{102} resonance mode [107]. The top view schematic of the hybrid is shown in Fig. 5.12a. In order to accommodate all the 4 hybrids, they are connected through squared mitered bends that are also acting as inductive couplings. The bends are shown in Fig. 5.12a with oblique lines external to cavities 3 and 4 of the hybrid. In order to allow connections and inclusions of the external flanges in the final design, a proper arrangement of the hybrids has to be done. In particular, the size of the TE_{102} cavity is to be considered when 2 hybrids are parallel horizontally and the other 2 are vertical. Fig. 5.12b shows the topology that implements the 3D design of the Butler matrix, shown in Fig. 5.12c.

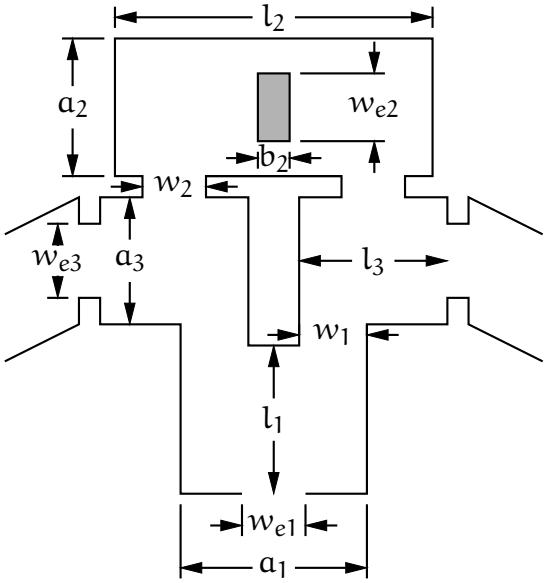

(a) Top schematic of unit hybrid

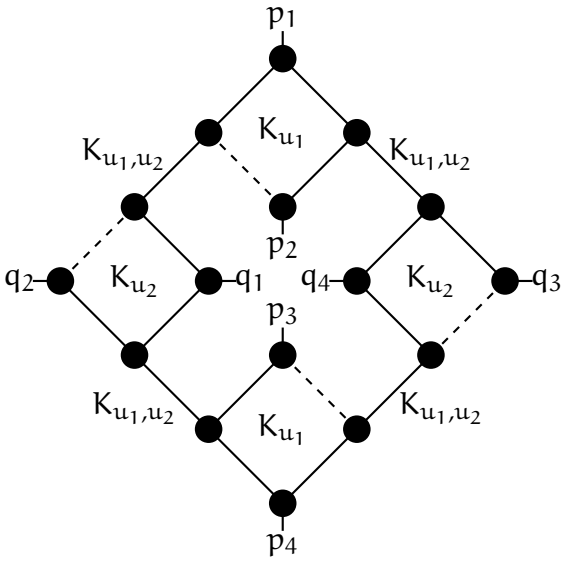

(b) Topology

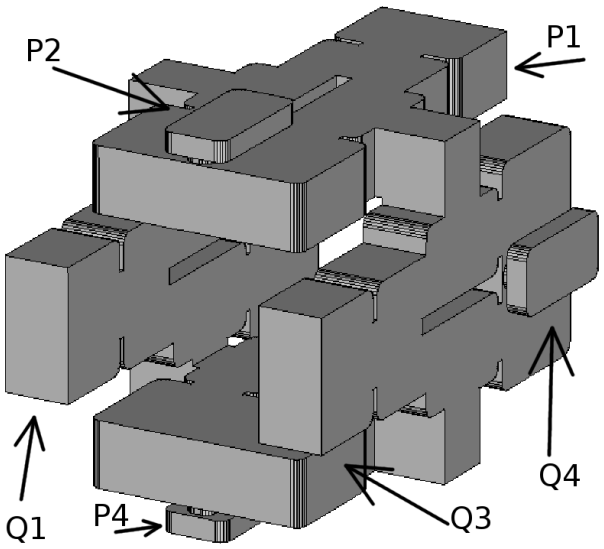

(c) 3D design

Figure 5.12: Design of the 4 × 4 Butler matrix with filtering

In Fig. 5.12b the negative couplings are shown with dashed lines. It is important to note that in this case the vertical hybrids they are oriented in a way that the position of the negative coupling is changed with respect the conventional topology introduced in Fig. 4.5. The transfer function matrix for this configuration is

$$\mathbf{T}_{4\times4} = \frac{1}{\sqrt{4}} \begin{bmatrix} 1 & -1 & 1 & 1 \\ -1 & 1 & 1 & 1 \\ 1 & 1 & 1 & -1 \\ 1 & 1 & -1 & 1 \end{bmatrix} \tag{5.5}$$

and is still orthogonal. This is also a proof of the property stated in section 4.4.3 that it is not necessary to have a perfect Hadamard transfer function to comply with rule of splitting/recombination of the INET and ONET for the MPA.

The 4 constituting hybrids are all the same and have the dimensions shown in Fig. 5.12a. The method used to calculate the dimensions is the same as shown previously, with curves for the initial approximated values shown in Fig. 5.13. These curves are calculated with Fest3D in the same way as it was for the 180° hybrid of the previous section, but this time for a standard WR75 waveguide. The model of Fig. 5.12c is simulated including radii of 1.5 mm in the internal corners. All the dimensions are later optimised in order to get the final values. Tab. 5.3 shows the dimensions of the 4×4 Butler matrix before and after the optimisation. The height dimension of the capacitive coupling on cavity 2, b_{e2}, is found by optimisation only. As it was for the 180° hybrid, the asymmetry introduced by cavity 2 introduces a mismatch in the phase response of the device. Hence a correction of $\delta = 10.45$ mm of difference between lengths of the external ports 1 and 2 of the unit-hybrid has been applied.

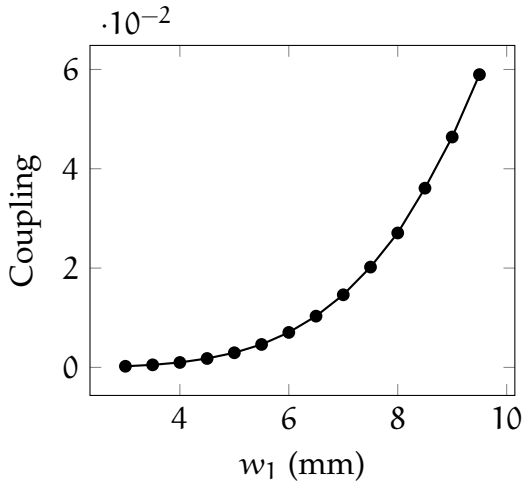

(a) w_1 iris

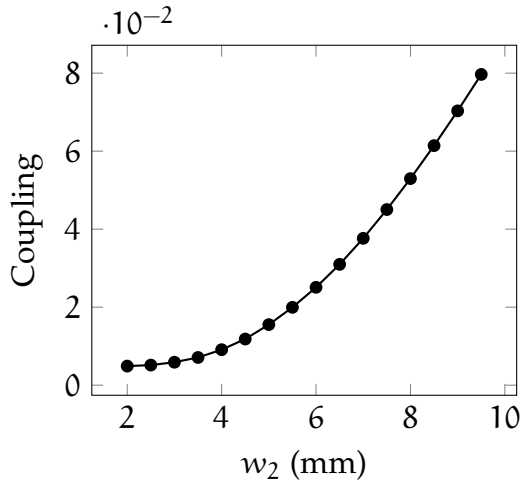

(b) w_2 iris

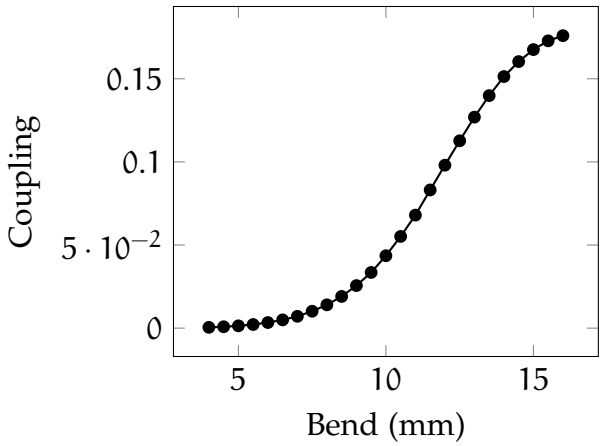

(c) Squared bend

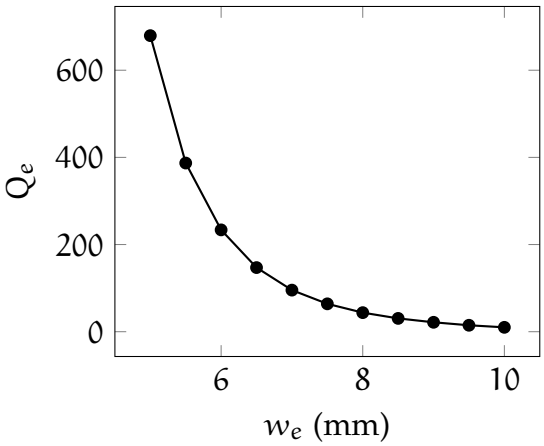

(d) External quality factor

Figure 5.13: Waveguide 4 × 4 Butler matrix denormalised coupling coefficients and physical dimensions

Table 5.3: Dimensions of 4 × 4 Butler matrix with filtering

	Initial (mm)	Optimised (mm)
a_1	19.05	19.242
a_2	19.05	18.117
a_3	19.05	19.05
l_1	15	11.906
l_2	30.1	32.046
l_3	15	12.2286
w_1	8.3	8.4468
w_2	6.5	7.9597
w_{e1}	9	9.314
w_{e2}	19.05	17.3198
w_{e3}	9.3	9.341
b_{e2}		4.0025
Thickness	1	1
Radii	1.5	1.5

5.3.1 Milling model

The first implementation of the 4 × 4 Butler matrix based on resonators of Fig. 5.12c has been manufactured with a CNC milling machine in Aluminium. Tolerances are about 20 µm of deviation with respect the nominal value. The device has been manufactured with a main body block of material where the Aluminium is removed to make the hybrids and couplings of the structure. Then, 4 lids are made to close the structure on the 4 sides of the block. Fig. 5.14 shows the model of the breadboard from different angles, and a picture of the main block of the final device. The external flanges are put on the sides and top of each hybrid. In order to improve the contact between surfaces, the maximum number of screws are used with grooving in order to increase pressure. Venting holes are also included to allow air escape in low-pressure environments. This device is symmetric and port numbering can be chosen arbitrarily with the following conditions:

- one hybrid has to be chosen to be the first one. At the beginning any hybrid is suitable for this.

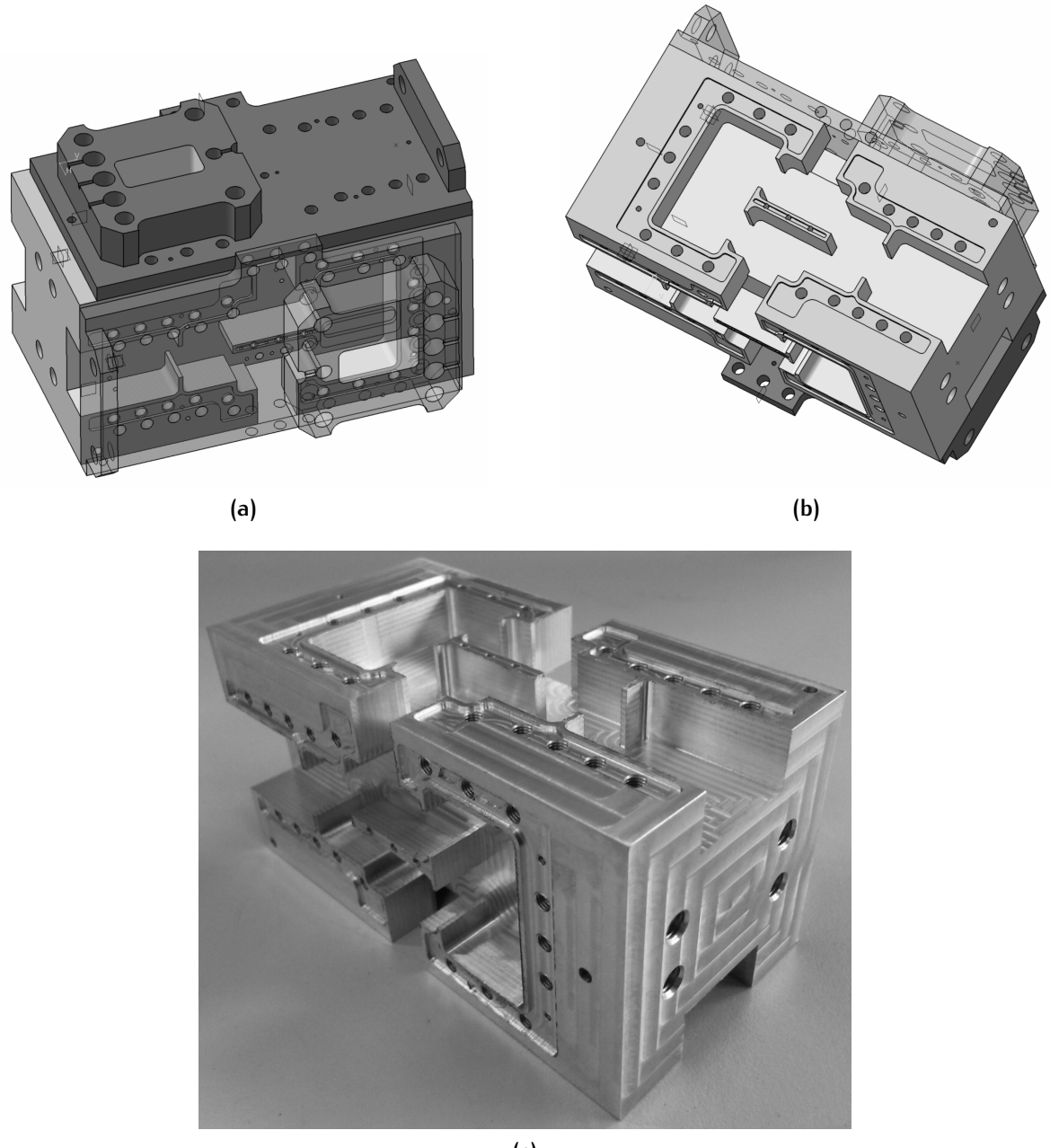

(a) (b)

(c)

Figure 5.14: Butler matrix made with milling

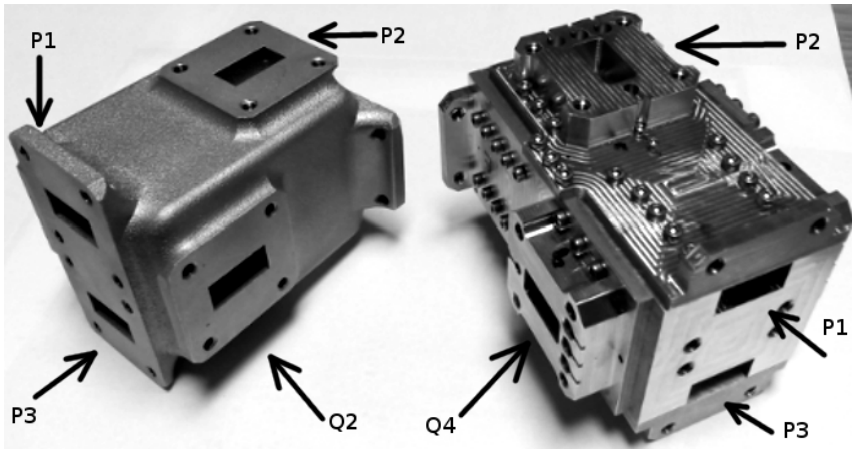

Figure 5.15: Butler matrix prototypes with port numbers

- From the first hybrid (ie. example, the top on Fig. 5.14) port number 1 is on the same plane of the waveguide while port 2 is on top of the TE_{102} cavity.
- The second input hybrid is placed symmetrically on the other side of the block, with the same port numbering.
- Output hybrids are placed, respectively, on right and left side of the first one. First output port is on the same plane of the first output hybrid while the second output port is on the top of the TE_{102} cavity.

Fig. 5.15 shows the 2 breadboards of the 4×4 Butler matrix with indicated the numbers of some of the ports. The direction of the input electric field has a direct consequence on the measured phase relation. In order to be consistent with the simulations, the flange of each port on the same plane of the hybrid is to be placed vertically, with orientation towards the external of the block, while connectors at port 2 should have an orientation right to left with respect the top-view of each hybrid.

The RF measurements have been performed with a VNA with a frequency span between 11.5 GHz and 13.5 GHz with 1601 points. The analyser used has 2 ports, thus only 2 parameters are measured at each time with the rest of the ports closed with matched terminations. A total of 28 measurements are needed to get the response of all the scattering parameters. No tuning has been performed on this device. The magnitude response of some of the parameters is shown in Fig. 5.16 and 5.17. Measured

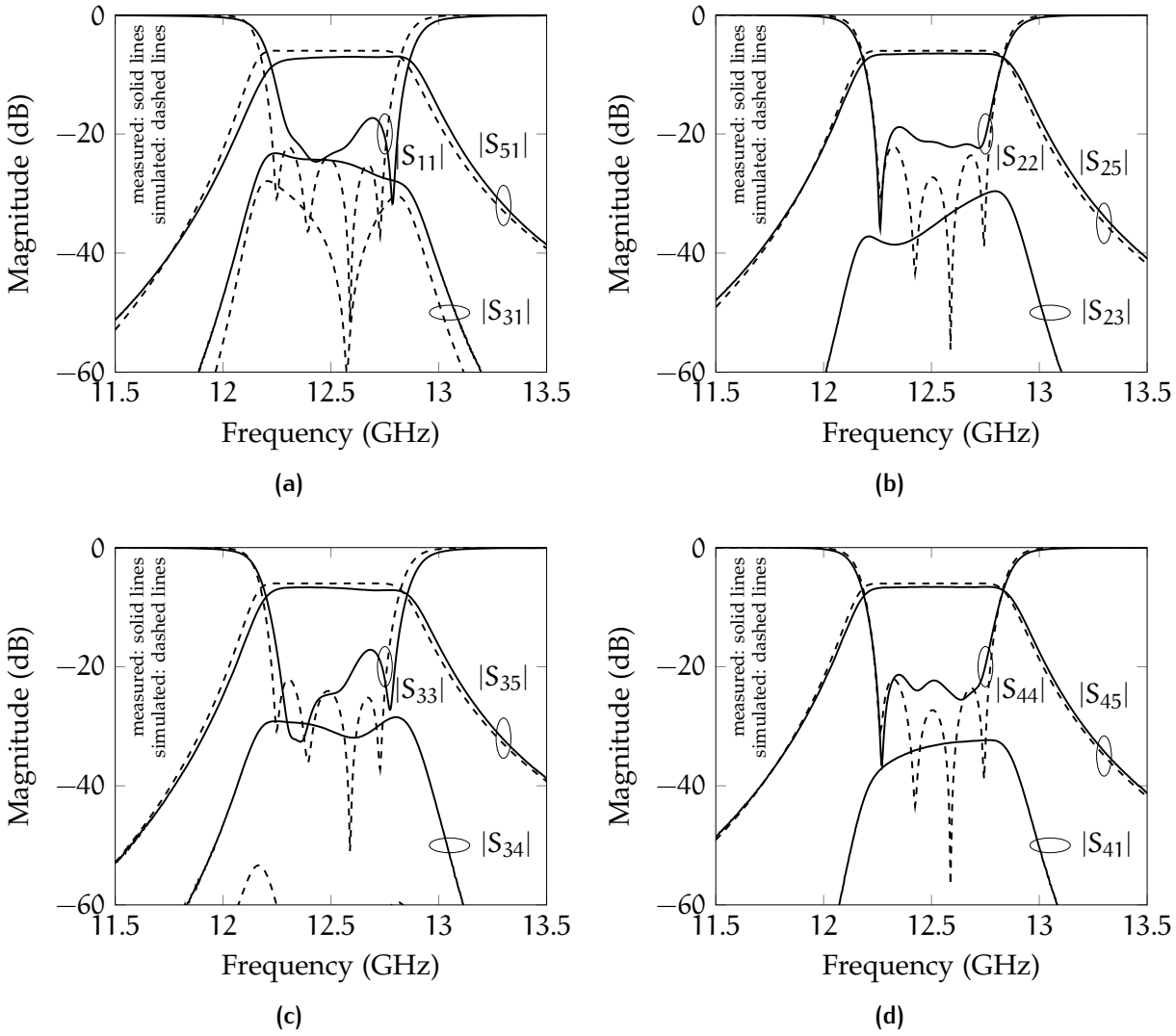

Figure 5.16: Magnitude measurements of 4×4 Butler matrix manufactured with milling

data is shown with solid line and compared with simulations, made with Fest3D and HFSS, in dashed lines. From the figures it is possible to note that there is an overall agreement of the measured data versus the simulations in terms of central frequency, bandwidth, power splitting level and filtering selectivity. The RL is different for the input ports chosen and this is a consequence of misalignments occurring during the assembly of the device. In particular, it has been registered an error of the reference coordinate position of the CNC milling machine, causing a misalignment between the lids and the main part. This aspect, together with the tolerances intrinsic of the machine, are the cause of some deviations of the scattering parameters with respect

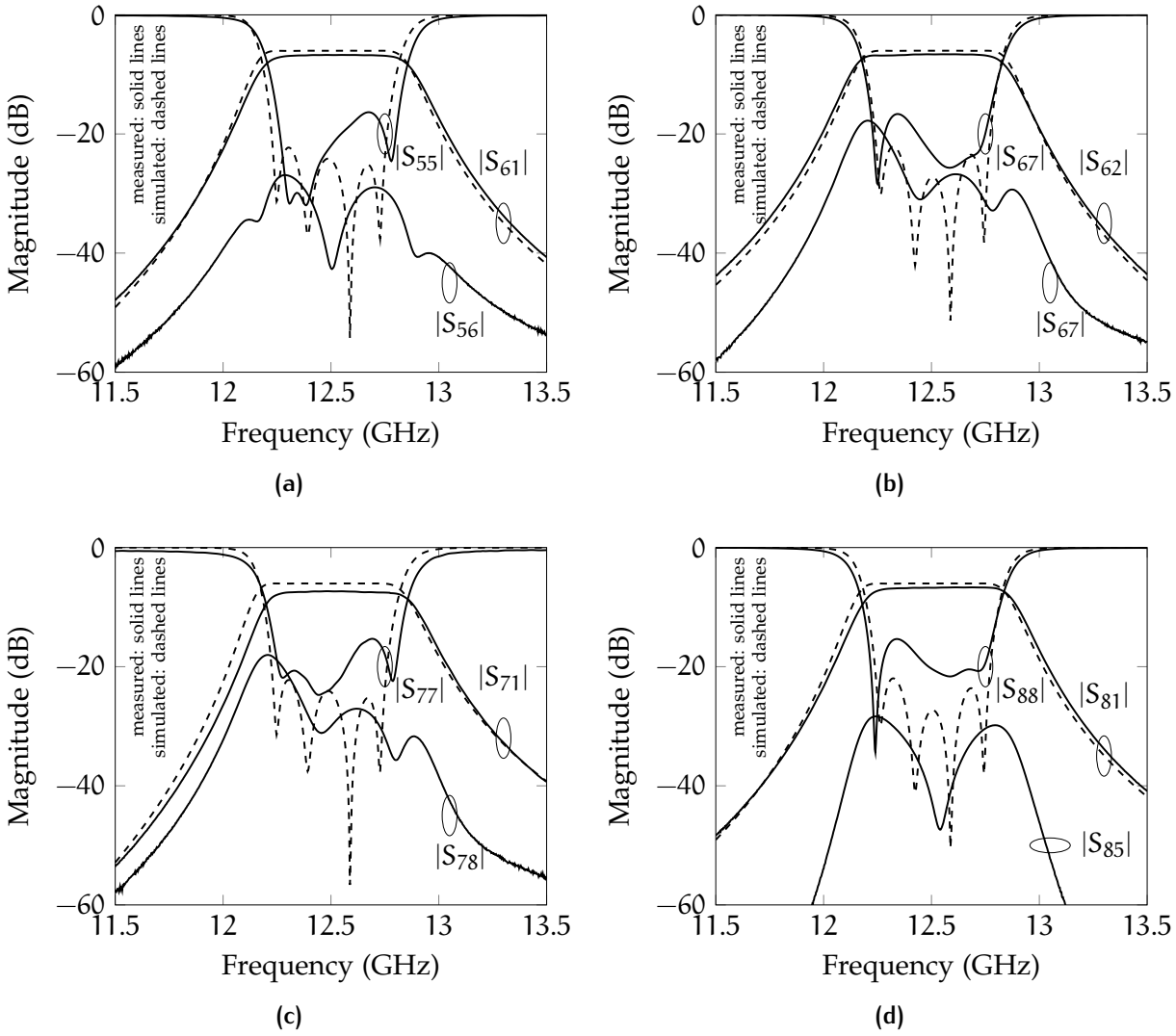

Figure 5.17: Magnitude measurements of 4×4 Butler matrix manufactured with milling

to the simulations. In particular there are differences in the maximum values of the isolations, that reach the level of -18 dB for the worst case. The RL generally exhibits 4 poles with a maximum level of -16 dB. The phase characteristics of the transmission parameters are shown in Fig. 5.18. It is seen that all the characteristics are in-phase except the $\angle S_{61}$, $\angle S_{52}$, $\angle S_{83}$ and $\angle S_{74}$ that are out of phase. This is consistent with the transfer function matrix of eq. (5.5) where the 4 negative elements correspond to the phase parameters that are out of phase in Fig. 5.18. Once the output phase distribution has been verified, the error of the phase relations are studied with respect the nominal phase difference calculated. Fig. 5.19 shows the errors with respect

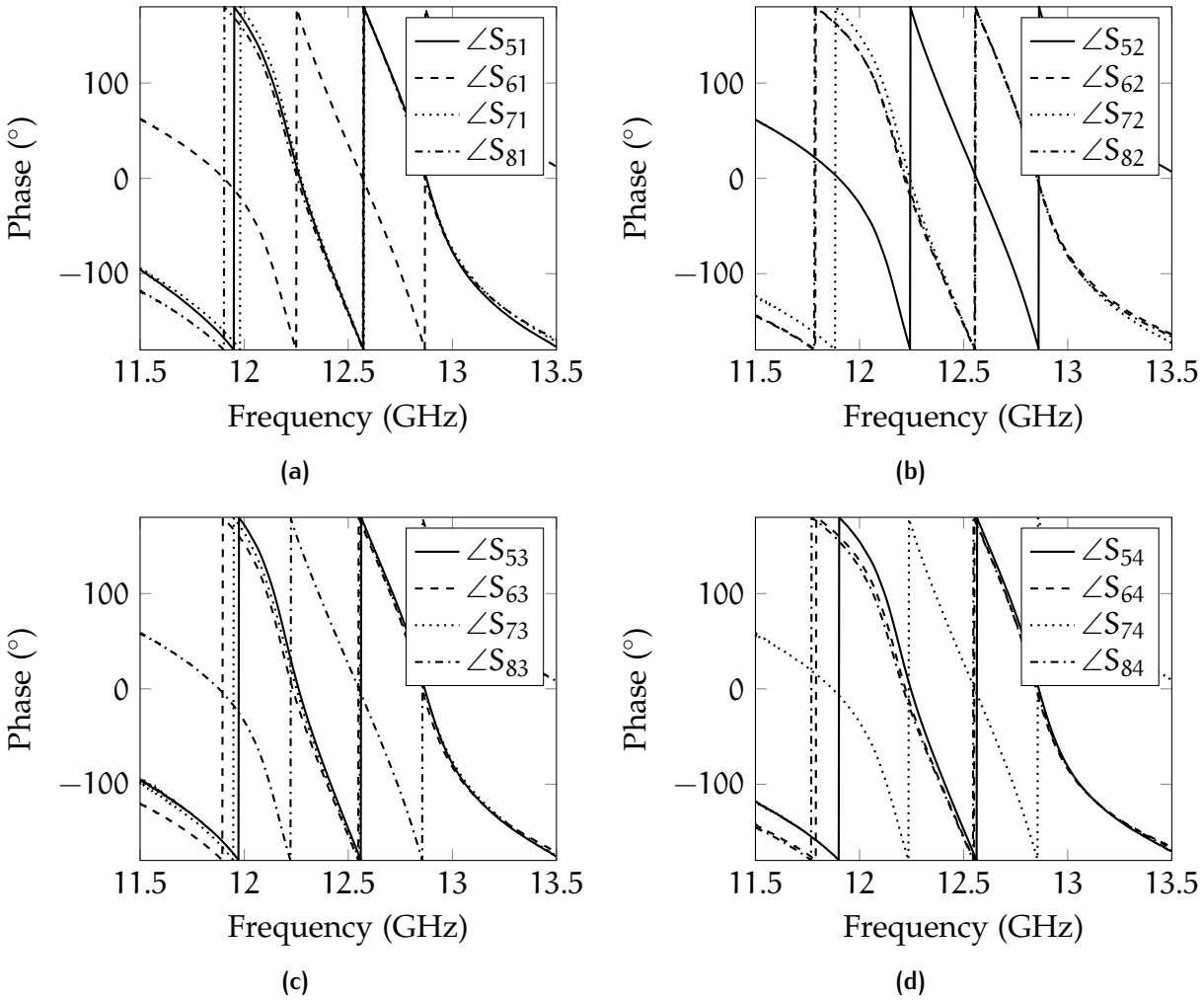

Figure 5.18: Magnitude and phase measurements of 4×4 Butler matrix manufactured with milling

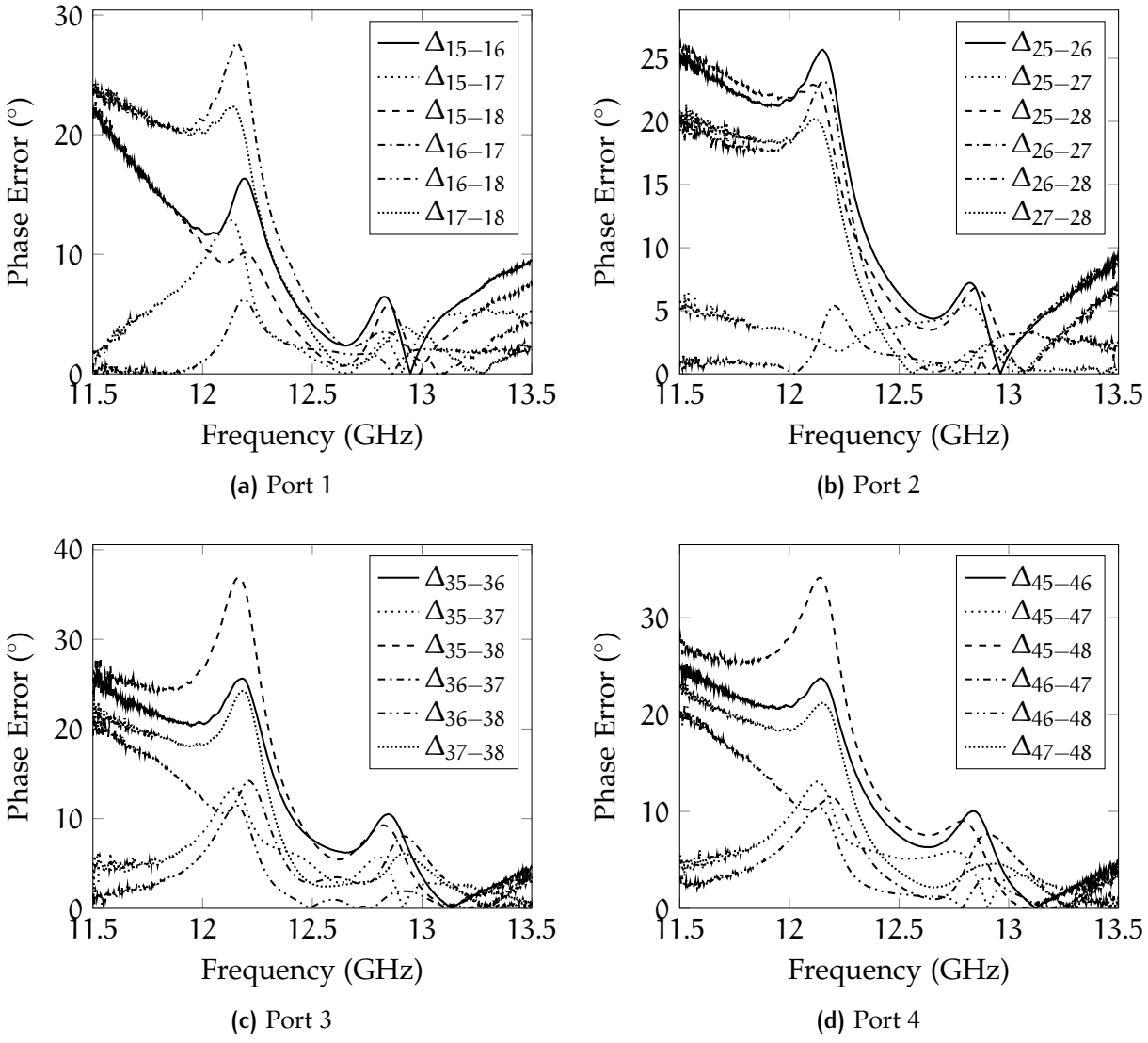

(a) Port 1

(b) Port 2

(c) Port 3

(d) Port 4

Figure 5.19: Phase error with respect the nominal value for the 4×4 Butler matrix made with milling

the theoretical value between pairs of phase characteristics. The calculation has been performed over the entire frequency span, although only the interval inside the operational bandwidth is relevant. The maximum phase error in the bandwidth is 21.2° for the difference between $\angle S_{35}$ and $\angle S_{36}$.

5.3.2 Additive manufacturing model

The 4 × 4 Butler matrix with filtering with the design shown in Fig. 5.12c has been manufactured in a monolithic block with an AM technique with Aluminium [122]. AM is defined as the direct process of joining materials to make objects from 3D model data, usually layer upon layer, as opposed to subtractive manufacturing methods (milling, spark-erosion, turning, wire-erosion, etc...). It is used to build physical models, prototypes, patterns, tooling components and production parts in plastic, metal, ceramic, glass and composite materials. In general, AM can be considered as a manufacturing method capable of reducing lead time, improve product quality and reduce costs. From the RF point of view, there are parameters like surface roughness, mechanical tolerances, dimensional limitations in the fabrication etc..., which are deemed as drawbacks for the introduction of this technology for RF passive hardware. On the other hand, this technology can enable designs of complex structures which, until now, have been only manufactured joining multiple parts fabricated separately. The process starts with the deposition of a layer of powder over which a laser, with a technique called sintering, makes the prescribed shapes of the object. Then another layer of powder is put on this and the whole process continues up to the completion of the structure.

Most of the passive RF hardware embarked on satellites are made of metals. This is due to the needs of good electrical and thermal conductivity together with the mass/envelope minimization while maintaining good mechanical performance (e.g. stiffness). At the same time the metallic parts create a shielding which avoid un-

desired RF leakage. Additionally, due to the increasing complexity of communication payloads, miniaturization for all the units is required in order to reduce total mass and allow the accommodation of a high number of units.

Some post-processing may be needed once the parts have been manufactured by AM. Typically, post-processing is needed to overcome limitations of AM and/or to achieve certain properties that the AM process cannot achieve that are required for Ka-band passive RF hardware. Depending on the AM technique used, the required post-processing will vary. Some of the processes are mandatory, while others can be applied to achieve specific requirements such as surface finishing. This has a high associated cost, therefore the number of steps should be minimized so that AM keeps being an attractive manufacturing solution. A correct selection of the AM technique will reduce the cost of the post-processing tasks. Some of these methods may include machining, abrasive blasting or polishing. In order to develop precision components made by aluminium, the following process is carried out:

1. analysis and optimization of parts,
2. design to adapt them to additive manufacturing,
3. manufacturing of the parts with metal technology,
4. post-processing of the parts (improving of surfaces).

The above steps will be performed to implement the AM Butler matrix shown in Fig. 5.20.

Due to the complexity of the model, the process of additive manufacturing has to consider the symmetries and the internal parallel surfaces. The prototype is built in aluminium AlSi10Mg. The entire structure is to be positioned on an inclined plane in order to efficiently deposit the material and to apply the laser sintering. This is due to the two lateral vertical walls and the two horizontal planes, which are all parallel. The model is then positioned over *supports* of the same material and the 3D software design adjusted accordingly. Fig. 5.20c shows the view of the model put

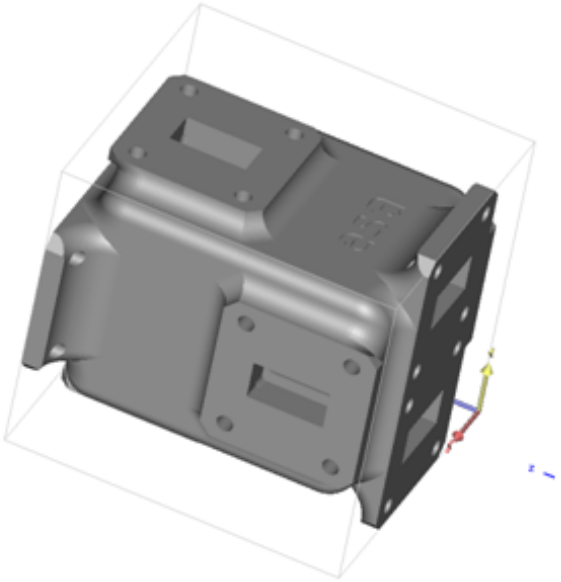

(a) Design of the 4 × 4 Butler matrix with filtering

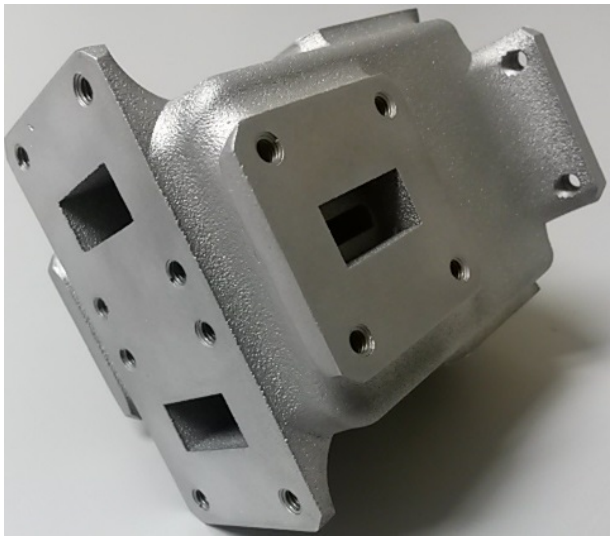

(b) Final device

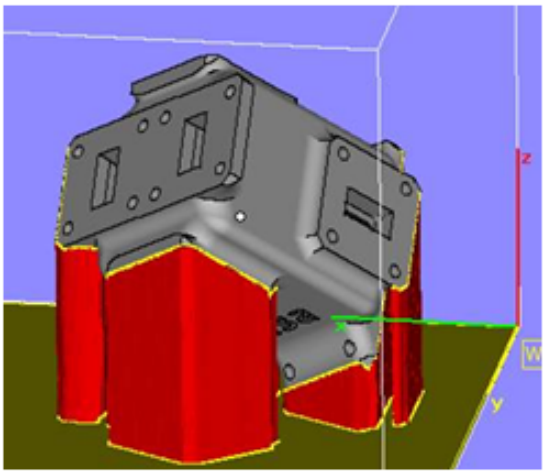

(c) Geometry placed on material supports in red

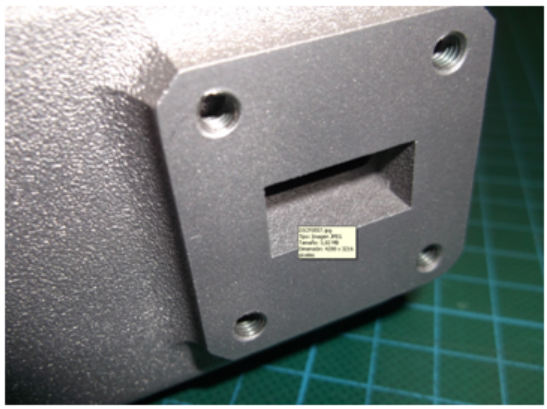

(d) Detail of the external surface interface

Figure 5.20: Butler matrix built with additive manufacturing

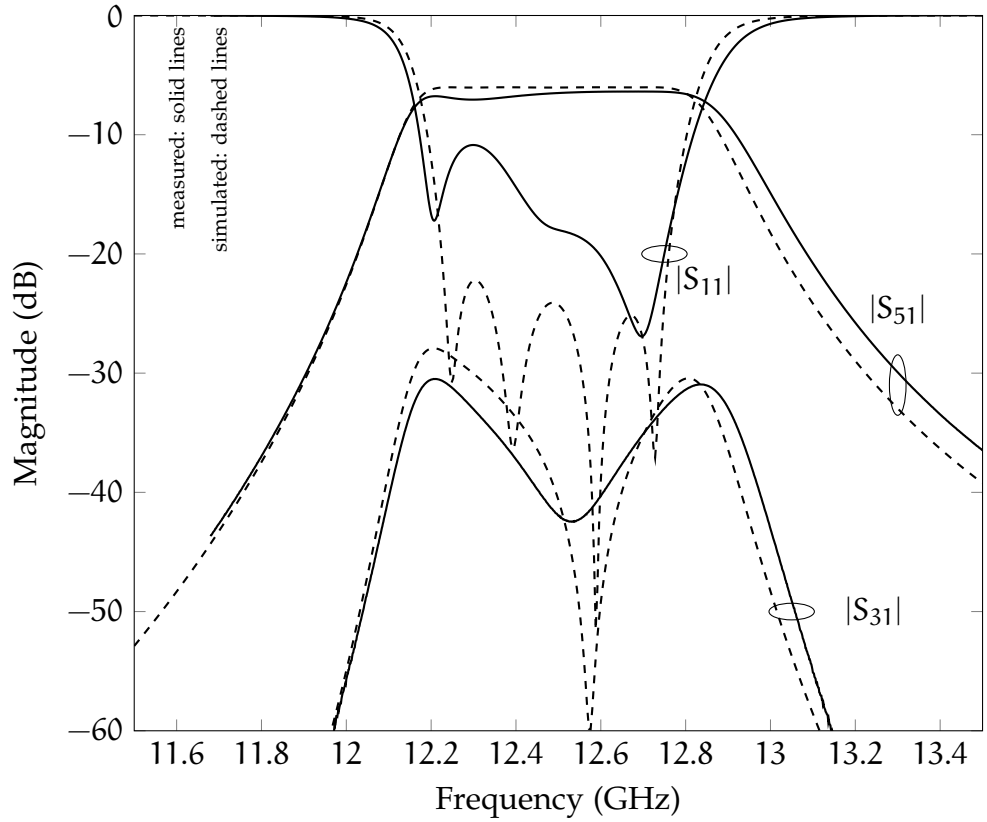

Figure 5.21: Comparison of the 4×4 Butler matrix between the simulation and measured data. Note that here the measured data are shift of 180 MHz for clarity

over same material supports, here indicated in red. The supports are all placed in correspondence to the external interfaces as shown in the figure, so as a faster laser sintering can create the structure. The piece has been made in an EOS M280 machine equipped with a 400 W laser with a layer thickness of 30 µm. The build chamber of this system is $250 \times 250 \times 300$ mm and the tolerances are in the range ± 0.05 mm. The prototype also received a thermal treatment stress relieve, corresponding to 2 hours at 300 °C. At the end of the process the supports are removed in two steps: firstly by hand to remove the majority of the material and then through automated machine tools (machining centres etc...). Fig. 5.20d shows the result of the final removal and refinement of the surface of one of the external flanges. It is crucial to have this surface as flat as possible in order to improve the contact with waveguide flanges. Fig. 5.20b shows the final device.

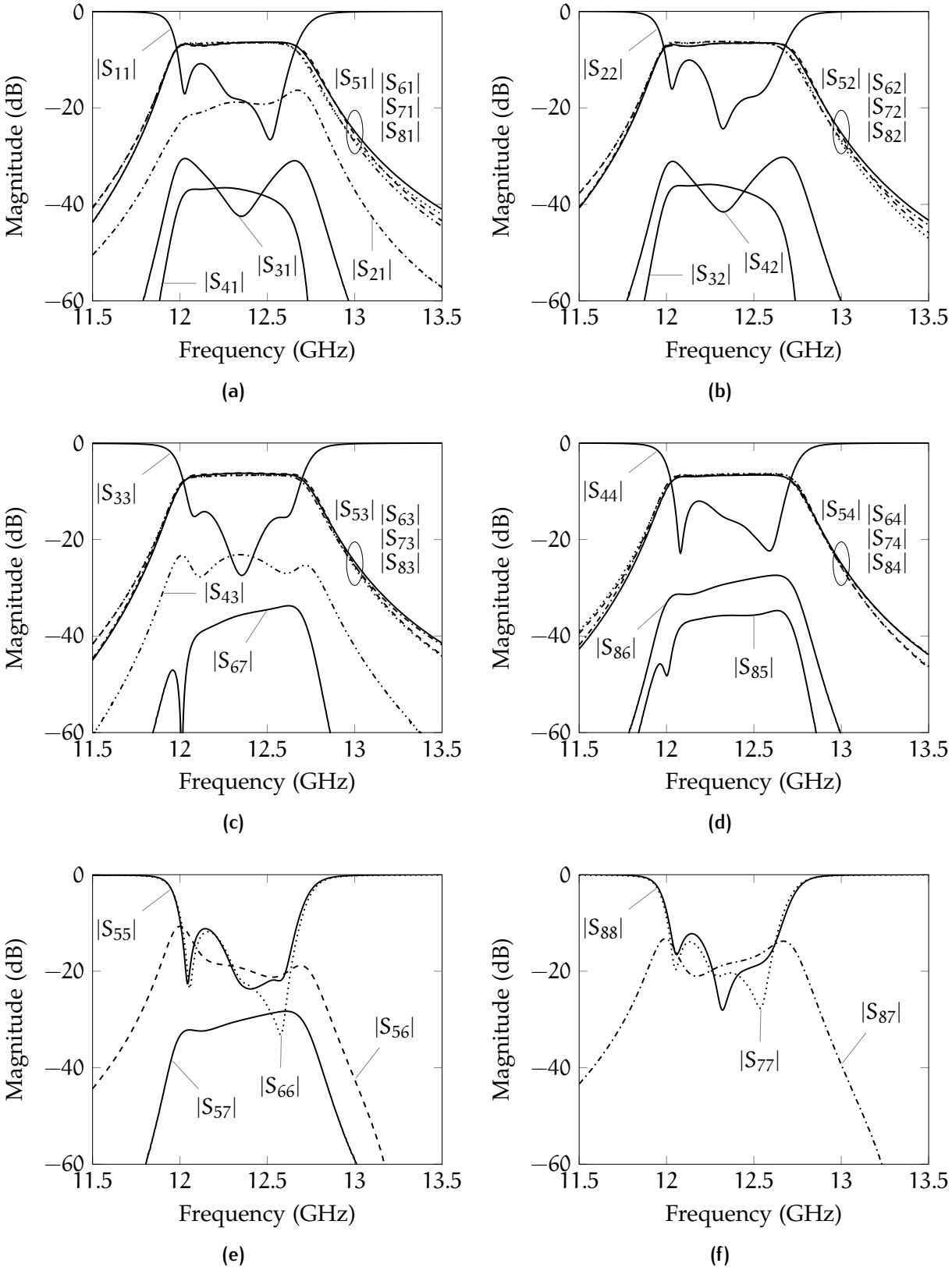

Figure 5.22: Magnitude measurements of 4×4 Butler matrix built with additive manufacturing

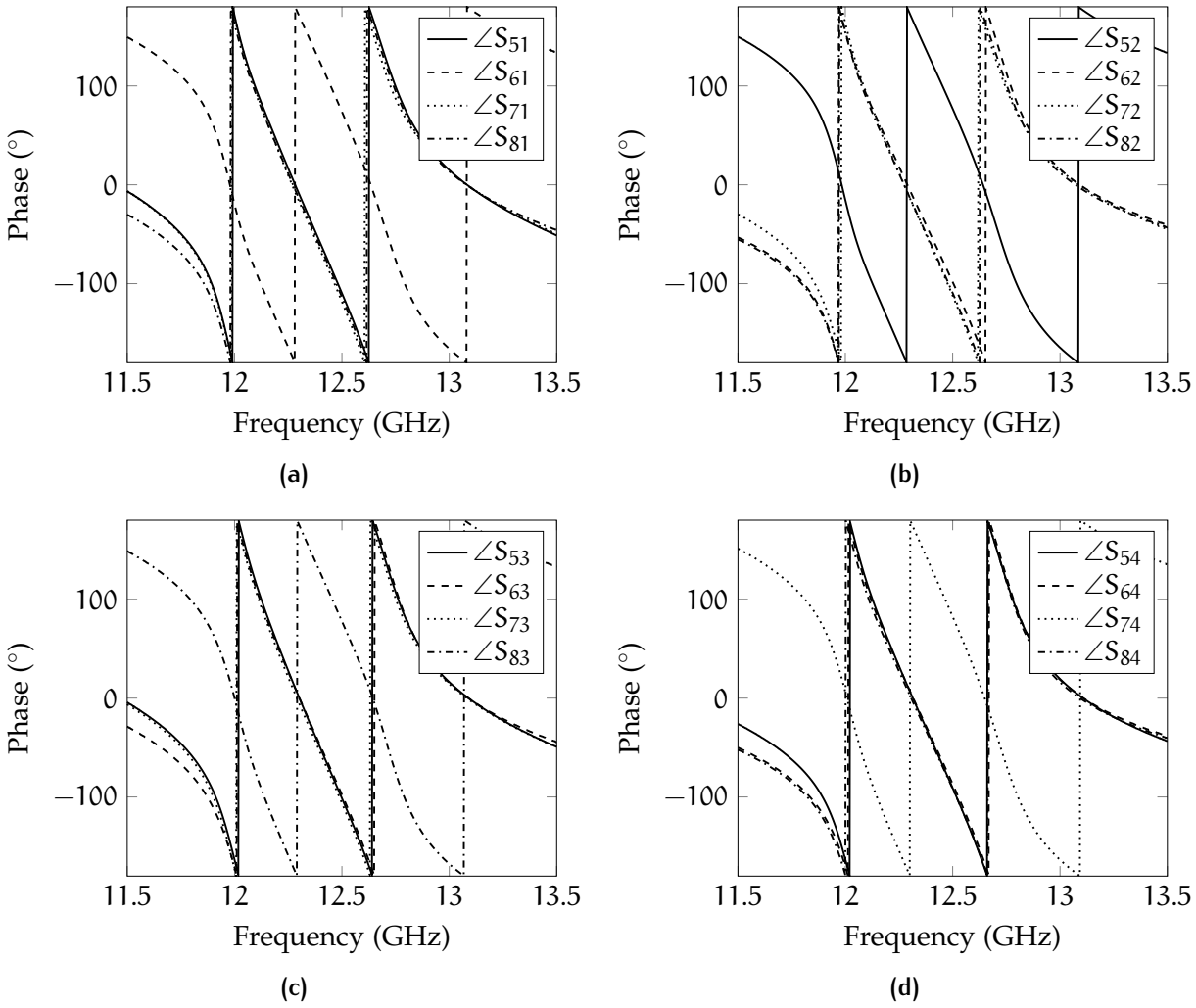

Figure 5.23: Magnitude and phase measurements of 4×4 Butler matrix built with additive manufacturing

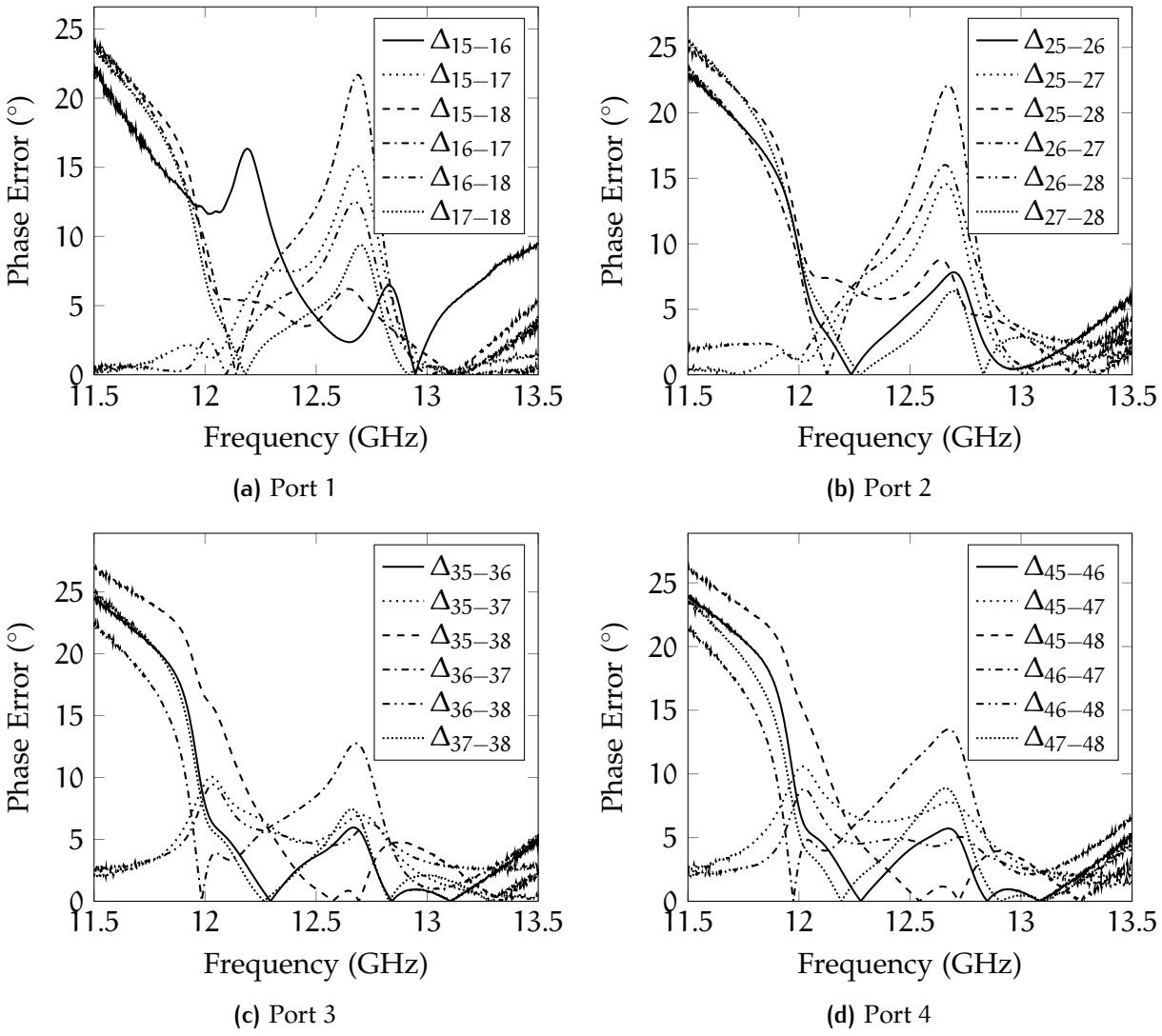

(a) Port 1

(b) Port 2

(c) Port 3

(d) Port 4

Figure 5.24: Phase error with respect the nominal value for the 4×4 Butler matrix made with additive manufacturing

The same type of measurements made for the milled model, has been conducted for this device. In general, a shift of 180 MHz down in frequency is observed on all the parameters. Hence, Fig. 5.21 is a representation of the measured data (solid lines) with respect the simulations (dashed lines), when a shift of 180 MHz up in frequency is applied to make the comparison easier. It is possible to note an agreement of the characteristics, both in terms of selectivity and power splitting. Also, the isolation parameter $|S_{31}|$ is very close to the simulated one. The IL does not exhibit clearly all the 4 poles, however it is possible to conclude that the selectivity of the transfer function is of a 4-pole Tchebycheff filter because of the close relation of the simulated and measured magnitude of the S_{51} parameter. Moreover, the maximum level of IL is of -11 dB for the worst case. The bandwidth is in line with the specifications. The measurements show that the manufacturing process has increased the internal dimensions, with the additional tolerances introduced by the AM building method. Fig. 5.22 shows the magnitude of all the scattering parameters. In this figure only the measured data is proposed without applying any frequency shift. All the transmission and return loss parameters are in line with the Fig. 5.21. The isolation is in general below -22 dB except for the S_{56} and S_{87} which are -10.7 dB for the worst case. With respect the model made by milling, here it is not always possible to observe the peaks in some isolation parameters: it is the case of S_{67} of Fig. 5.22c with respect the one for milled shown in Fig. 5.17b, but also of the S_{85} of Fig. 5.22d and Fig. 5.17d. This means that the manufacturing errors have an impact on the level and characteristic of the isolation as well. The phase relations are shown in Fig. 5.23 and it also confirms the phase distribution property of eq. (5.5) with all characteristics in phase, except for $\angle S_{61}$, $\angle S_{52}$, $\angle S_{83}$ and $\angle S_{74}$. Finally, the phase relative errors are shown in Fig. 5.24. Also for the model of Butler matrix, no tuning has been performed.

The Butler matrix made with AM has the advantage of been more lightweight with respect the milled model because it is a monolithic object with no need of screws to connect the lids with the main body. Moreover, the internal part of the main body

is hollow with the AM technique. The bandwidth has been confirmed in line with the specifications with both models and most of the isolation and transmissions parameters are also coherent with the simulations. The main issue regarding the AM is the lower accuracy with respect the milled CNC one. The centre frequency and RL of the version made with AM are not as good as the milled one. At the moment, CNC milling is the technique to be preferred to achieve more accurate designs, however, future improvements of the AM could result in an higher interest toward this technology.

5.4 SIZE REDUCTION

The major advantages of including filter transfer functions into the Butler matrix are the size and mass reduction. The comparison is made between a conventional solution where a baseline formed by an $N \times N$ Butler matrix with cascaded N BPFs of order κ (cf. Fig. 2.17a) and the proposed solution of multi-port and multi-function device based only on coupled resonators, as described in section 4.4. In the minimum condition, the whole Butler matrix with filtering can produce $\rho = 2k$ poles with a number of cavities $n = 2N \log_2 N$, according to eq. (4.31) and (4.33). Thus, the total number of cavities required by the conventional baseline to operate the filtering is κN. If the order of each filter is greater than the minimum selectivity introduced by the Butler matrix with filtering, $\kappa \geqslant 2K$, then the same transfer function can be obtained through the multi-port network based on resonators. The total number of cavities required is obtained combining eq. (4.33) into (4.30), then it is possible to verify that it is

$$n = 2kN \tag{5.6}$$

This is the minimum number of cavities required by the Butler matrix with filtering, that is the same to the number of cavities required by the conventional baseline of transmission-line Butler matrix and N band-pass filters. This is generally true if $\kappa = 2k$. However, it has been demonstrated in section 4.6 that an higher number of cavities as well as more complex transfer functions are possible. Thus, it is possible to conclude that *exactly* the same number of cavities are required by the Butler matrix with filtering in order to reproduce the same electrical characteristics of the cascading of an $N \times N$ transmission-line Butler matrix and N BPFs, of the generic form of Fig. 4.8. For this reason it is possible to conclude that the proposed technique is able to achieve the same response with the same number of cavities, hence making the transmission-line Butler matrix redundant.

As a quantitative comparison example, a conventional Butler matrix based on waveguide transmission lines has been designed with conventional inductive iris filters cascaded on the output. The goal is to quantify the volume reduction of this conventional approach with respect the resonator based Butler matrix shown in Fig. 5.12c. The internal volume of the latter device has been measured to be $66.2\,\mathrm{cm}^3$. A 4×4 Butler matrix and 4 BPFs have been designed and optimised to meet the same specification of of the Butler matrix with filtering of section 5.3 in standard WR75 waveguide. Firstly the basic waveguide hybrid has been optimised, and later it has been replicated 4 times with interconnections made by mitered bends. Other bends have been included at the output ports in order to allow placement of the external flanges. Then, a 4-cavity inductive iris band-pass filter of $f_0 = 12.5\,\mathrm{GHz}$, $B = 500\,\mathrm{MHz}$ and RL better than 25 dB has been designed, and 4 replica placed at the outputs of the Butler matrix. This conventional ONET that includes the filter transfer functions is shown in Fig. 5.25a. In this example a Butler matrix made with a conventional 90° coupler has been designed for simplicity. Fig. 5.25a also shows the Butler matrix and the 4 BPFs. The response of the Butler matrix alone is shown in Fig. 5.25b with the magnitude and in Fig. 5.25c the phase. The BPF response is shown in Fig. 5.25d. All the

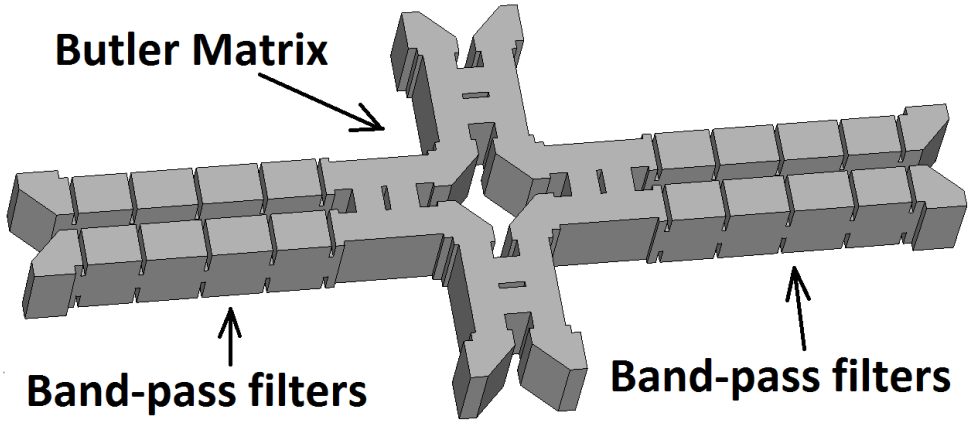

(a) Schematic of ONET with filters

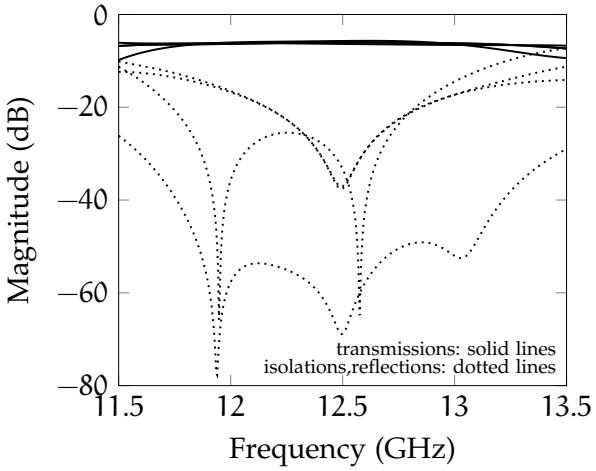

(b) Conventional Bulter matrix magnitude response

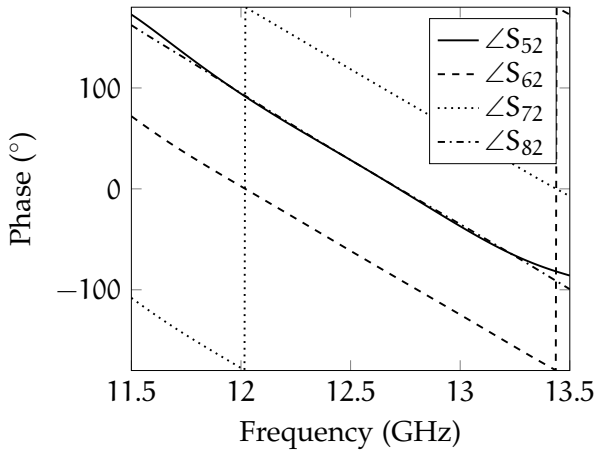

(c) Conventional Bulter matrix phase response

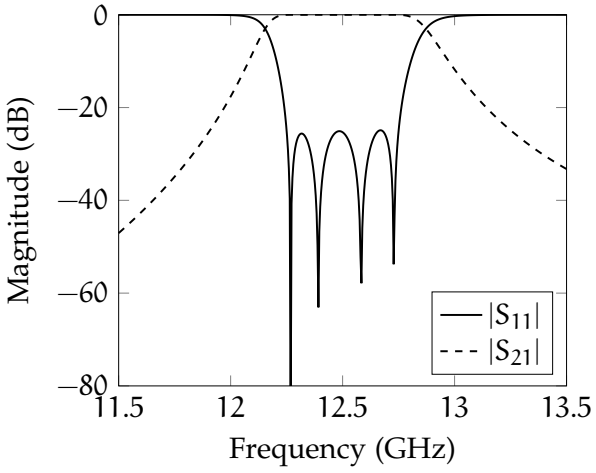

(d) Reference Band-pass filter

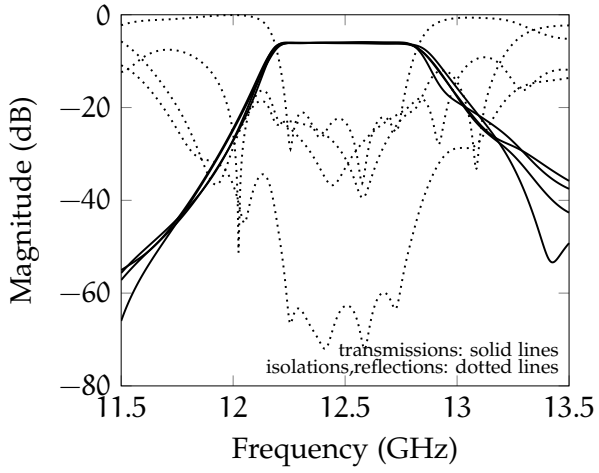

(e) Response of ONET including bank of filters

Figure 5.25: The conventional baseline is formed by a transmission-line Butler matrix cascaded by a bank of band-pass filters that are the same. Simulation made with Fest3D

filters are the same. Finally, the response of the whole ONET of Fig. 5.25a is shown in Fig. 5.25e. As there are many parameters to include in the figure, the transmissions are shown with solid lines while the reflections and isolations with dotted lines. The volume of the ONET of Fig. 5.25a is extracted and compared with the one of Butler matrix including filtering of Fig. 5.12c. It is found to be 96.7 cm^3, meaning that for this example the proposed solution is 31.5% less in volume with respect the conventional model. Clearly, this number is subject to the particular technology used to implement the device, however it gives a numerical idea of the advantages of the Butler matrix with filtering based on resonators.

6 CONCLUSIONS

This work has presented the synthesis of the coupling matrix of a novel Butler matrix that includes the filtering transfer functions through a network based on electromagnetically coupled resonators. This class of circuit is a multi-port, multi-resonators network that provides the typical power splitting ratio and input to output phase distribution of the Butler matrix, as well as the filtering transfer functions in one single device.

Traditional synthesis techniques have been found extensively in the literature and they have been developed mainly for filters (2-port devices) and for a limited class of 3-port networks. These techniques are based on the definition of the polynomials of the transfer function, and later the elements of the coupling matrix are found mathematically. However, 2 main problems have been arisen and shown to be critical: the lack of a clear and detailed theory for the definition of the characteristic polynomials for multi-port networks, and the requirement of same filter transfer functions for all the transmission parameters. It is worth recalling that the most typical passive multi-port passive components with filtering are diplexers and multiplexers, and several techniques have been developed through the years to develop resonator based methods for these. Here, a different methodology had to be investigated in order to overcome the limitations of the general techniques. The outcome is an ad-hoc solution for the Butler matrix that includes filtering. This method is based on the combination of several hybrid couplers based on resonators that are able to simplify the problem and to reduce it to well known techniques valid for 2-port circuits.

In the first instance the 90° hybrid has been investigated because it is widely used in conventional Butler matrices. The first step was to derive an equivalence technique

between the model based on transmission lines and the one based on resonators. This was already available in the literature for a simple 2-branch coupler and was extended here to multiple branches. However, the validity of the equivalence was limited to the centre frequency only, leaving great uncertainty for the rest of the response with very little margin left to the designer to define the specifications. Thus, here an additional analysis of 2×2 hybrid coupler based on resonators has been developed through a novel topological approach that is capable to quickly predict the frequency response by studying the topology of the network. This method has been proved experimentally with the implementation of a 2×2 quadrature hybrid coupler based on 8 resonators, and also mathematically with an analytical study of the limitations of these kind of networks. The 90° hybrid coupler based on resonators shows out of band peaks that have been demonstrated to be unavoidable and intrinsic to the topology of these circuits. Even with optimisation of the coupling matrix, it has been shown how these peaks are the result of the interference of the multiple paths generated in the circuit and, eventually, how to control them. It has been stated that if a 90° phase shift is necessary for the hybrid with filtering, the out-band peaks need to be taken into account. This behaviour compromises the overall responses when the hybrids are combined in order to build a more complex circuit such as the Butler matrix. The presence of the peaks in each hybrid has a disruptive consequence of the final response of the Butler matrix, hence reducing the usefulness of such solution.

A more interesting case is given by the properties of the 180° hybrid based on resonators. This network is in some way similar to the 4 resonators of the quadrature hybrid, with the difference that the values of the coupling coefficients are all the same, except 1 that has same absolute value but opposite sign. This structure is able to provide a perfect isolation of the input ports, thus creating a virtual open circuit that is the base of the synthesis technique. This virtual open circuit allows the network to be considered from one input to the outputs formed of different transmission paths, hence able to make the synthesis independently on each path. This is a major

advancement with respect the quadrature hybrid because the virtual open circuit can be preserved by cascading more hybrids. Based on this concept, a multi-port $N \times N$ Butler matrix can be made. The use of the hybrid is modular and reflects the total number of $N = 2^k$ inputs. The synthesis of the coupling matrix relies on the fact that the virtual open circuit makes independent paths from each input to each output port. It has been demonstrated that over each path it is possible to define transfer function polynomials that are proportional to the ones of a conventional 2-port filter. This characteristic is the base of a general solution that overcomes the limitations of conventional general techniques. Moreover, it has been shown that the number of poles and the introduction of transmission zeros is also possible, as an extension of the procedure proposed. The flexibility on the type of transfer function (Buttherworth, Tchebycheff or generalised Tchebycheff) adds a further degree of freedom to meet the specifications.

The synthesis technique has been used to design a 2×2 hybrid coupler 180° based on 4 resonators and a 4×4 Butler matrix with filtering in 2 versions. These are built with milling and additive manufacturing. The breadboard has been implemented in standard rectangular waveguide with inductive irises, also providing good performances in terms of multipactor power handling. The 4×4 Butler matrix has been designed following a similar design of the basic hybrid in a more complex 3D structure. The measurements conducted on the milled version shown good agreement with bandwidth, transfer function and power splitting. The advantage of the model made with additive manufacturing is that it is built from a single piece. For this model, a systematic error has been introduced so as all the characteristics are shifted down in frequency of a constant factor. Other than this a substantial agreement with respect the theoretical expectations is obtained, also considering that no tuning has been performed on any model.

The complexity of these multi-port, multi-resonator circuits is given by the high number of resonators and couplings that are to be accommodated and interconnected.

The 4×4 Butler matrix configuration shows that it is necessary to move both in the horizontal and vertical plane to properly connect the hybrids. A further extension to more inputs/outputs should be assessed for its practical implementation first. Nevertheless, the theory developed here is based on the calculation of a coupling matrix, hence generalised and independent from the technology used. Further studies may be conducted in order to find the optimum type of resonators that meet the specifications (centre frequency, bandwidth, insertion loss, power handling capabilities etc...) and their ability to be geometrically connected when the Butler matrix has an high number of ports.

A SYNTHESIS OF BRANCH-GUIDE COUPLERS

The aim of this appendix is to provide a comprehensive guide for the synthesis of symmetric and asymmetric branch-guide couplers. This is a re-arrangement of knowledge and notes found in various papers and theses. It puts together information from different sources and gets the final values of the admittances (impedances) starting from the specification in a detailed step-by-step procedure.

The main reference source is the paper of Ralph Levy [92] and the one of his student Lind [93]. The first covers in detail the general characterization of the coupler and the synthesis of symmetric structures, while the second is an extension to asymmetric devices.

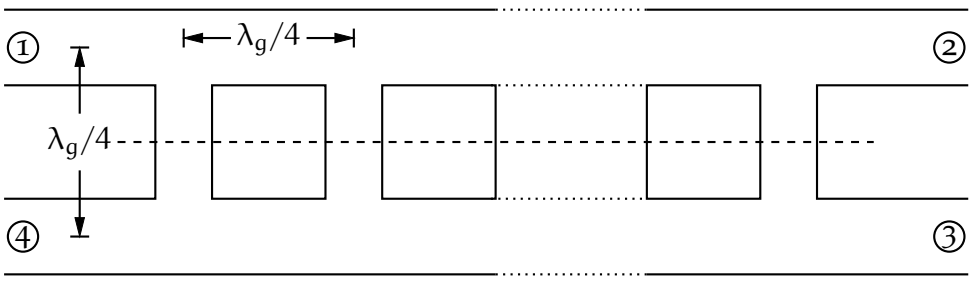

Figure A.1: Cross section of a branch-guide directional coupler.

The asymmetric nature of the problem confers the coupler a double valence: it operates as a coupler but also it acts as a impedance transformer between two transmission lines of different impedance levels. This is an important characteristic of this device and it may find several application due to this double function.

In these papers a rigorous technique for the synthesis of quarter-wavelength directional couplers is presented. It will be explained how to get the value of the ad-

mittances (impedances) of a structure composed by several branches. An example of circuit is depicted in Fig. A.1.

These two papers cover extensively the topic and present tabulated data for different specifications, however it is not completely clear how to get the final admittances (impedances) with the given specifications. Of particular interest is the Lind's PhD Thesis [123] as some important steps are not mentioned in the published papers. Information gathered from the papers and some basic knowledge on the theory of polynomials and circuit synthesis are included in this appendix to develop the explanation of the synthesis technique.

After a general description of this type of couplers, will be presented the synthesis procedure for both maximally-flat (Butterworth) and almost equal ripple (Tchebycheff) specifications. Three numerical examples have been chosen to describe in practice how to carry out the synthesis process. The first example has been taken from the Lind's thesis while the others have all the numerical results coming from a program designed by the author.

By following the theory and the examples presented here it is quite easy to produce an automated computer program. In fact, the algorithm may be directly derived from the solutions of the proposed examples.

A.1 GENERAL ANALYSIS

In general, a branch-guide coupler is a structure consisting of a number of branch lines, each of $\lambda_{g0}/4$ in length at mid-band frequency connecting two pieces of transmission line. Each branch-line is spaced at intervals of $\lambda_{g0}/4$. The device has four ports circuit as shown in Fig. A.1. The coupler is symmetrical with respect the dashed line depicted in the figure. Because of this symmetry it is suitable to study these circuits with the *even/odd* method described in [72]. The advantage of this method is that

it is possible to study the overall four-port circuit as a pair of two singles two-ports circuits independently. The circles in the figure identify the port numbers.

If an incident amplitude at the generic port i is identified with the letter A_i and the consequent reflection associated to the same port with the letter B_i, the *even* mode can be defined as

$$A_1 = \frac{1}{2} \tag{A.1a}$$

$$A_4 = \frac{1}{2} \tag{A.1b}$$

and the *odd* mode:

$$A_1 = \frac{1}{2} \tag{A.2a}$$

$$A_4 = -\frac{1}{2} \tag{A.2b}$$

When the condition (A.1) is applied a magnetic wall is present at the plane of symmetry of the circuit. In this case the voltage in the centre is maximum and the current is zero. An open circuit is associated to the condition (A.1). The dual case is represented by equations (A.2). Hence, at the symmetry plane of the structure the voltage is zero and the current maximum and a shorted circuit may be introduced.

A schematic of the consequence of the input waves (A.1) and (A.2) is shown in Fig. A.2. The even-mode circuit consists of a number of shunt open-circuited stubs of electrical length θ each separated by double-unit elements of electrical length 2θ.

Depending of the type of the fundamental mode that is propagating in the circuit, any stub is shunt for TEM modes or in series for TE/TM modes. The associated characteristic impedance or admittance of the stub depends on the type of the fundamental mode. In the following they will be addressed as *immittances* to indicate that they are impedances or admittances depending on the nature of the propagating mode.

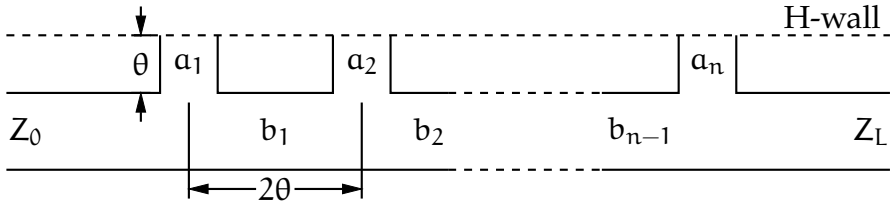

(a) Even mode.

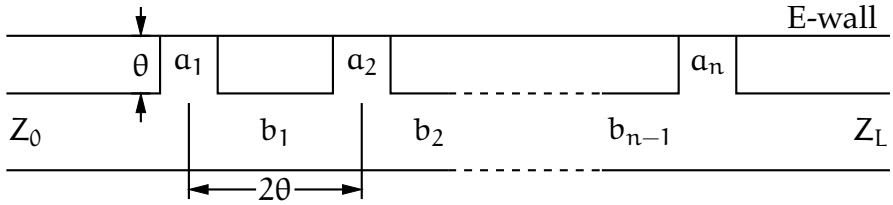

(b) Odd mode.

Figure A.2: Schematic of the networks for the even and odd modes.

The immittance of the i^{th} stub is referenced to with the letter a_i, while the one of the *double-unit* elements i^{th} with the letter b_i. In a branch-guide coupler there are n branches and $n-1$ main lines (or double-unit elements). So referring to Fig. A.2 there are n stubs and $n-1$ *double-unit* elements.

For both circuits of Fig A.2 it is possible to define a reflection coefficient Γ as wall as a transmission coefficient T. To differentiate the two modes a subscript e or o will be added to indicate that the relative coefficient is, respectively, for the even or odd mode. In order to obtain the vector amplitudes of the signals emerging from the four-port the following superposition is made:

$$B_1 = \frac{1}{2}(\Gamma_e + \Gamma_o) \tag{A.3a}$$

$$B_2 = \frac{1}{2}(T_e + T_o) \tag{A.3b}$$

$$B_3 = \frac{1}{2}(T_e - T_o) \tag{A.3c}$$

$$B_4 = \frac{1}{2}(\Gamma_e - \Gamma_o) \tag{A.3d}$$

From Fig. A.1 the scattering parameters are derived when it is assumed that the incidents amplitudes A_i are normalized to 1. Thus, the relations between the S parameters and Γ and T are the following:

$$S_{11} = \frac{B_1}{A_1} = B_1 = \frac{1}{2}(\Gamma_e + \Gamma_o) \tag{A.4a}$$

$$S_{21} = \frac{B_2}{A_1} = B_2 = \frac{1}{2}(T_e + T_o) \tag{A.4b}$$

$$S_{31} = \frac{B_3}{A_1} = B_3 = \frac{1}{2}(T_e - T_o) \tag{A.4c}$$

$$S_{41} = \frac{B_4}{A_1} = B_4 = \frac{1}{2}(\Gamma_e - \Gamma_o) \tag{A.4d}$$

There are some parameters that are useful to describe the properties of the four-port directional couplers. These are the *coupling* coefficient, the *directivity*, the *isolation* and the *voltage standing wave ratio (VSWR)*. These entities are usually expressed between the generic ports i and j of Fig. A.1, however it is common to have the excitation signal applied to port 1:

$$\text{Coupling} = -20\log_{10}|S_{31}| \tag{A.5}$$

$$\text{Directivity} = 20\log_{10}\frac{|S_{31}|}{|S_{41}|} \tag{A.6}$$

$$\text{Isolation} = -20\log_{10}|S_{41}| \tag{A.7}$$

$$\text{VSWR} = \frac{1+|S_{11}|}{1-|S_{11}|} \tag{A.8}$$

All the immittances are normalized to the input impedance/admittance. In some papers it is common to indicate with the letter R, the ratio of the input and output impedances:

$$\begin{aligned} z_0 &= \frac{Z_0}{Z_0} = 1 \\ z_L &= \frac{Z_L}{Z_0} = R \end{aligned} \tag{A.9}$$

The values of the reflection coefficient Γ and transmission coefficient T for a generic symmetric network are given in terms of $ABCD$ transfer matrix parameters by the formulas [30]:

$$\Gamma = \frac{(A - D) + (B - C)}{(A + D) + (B + C)} \tag{A.10}$$

$$T = \frac{2}{(A + D) + (B + C)} \tag{A.11}$$

while for the general asymmetric structure the reflection coefficient and the transmission are given by:

$$\Gamma = \frac{(A - D/R) + (B/R - C)}{(A + D/R) + (B/R + C)} \tag{A.12}$$

$$T = \frac{2/\sqrt{R}}{(A + D/R) + (B/R + C)} \tag{A.13}$$

For a lossless network it is

$$|\Gamma|^2 + |T|^2 = 1 \tag{A.14}$$

At this point it is useful to consider the two circuits of Fig. A.2 as two networks formed by a sequence of stubs connected by transmission lines. An useful way to characterize a stub is to operate the *Richard* transformation:

$$t = \Sigma + j\Omega \tag{A.15}$$

where

$$\Omega = \tan\theta \tag{A.16}$$

The variable θ is the electrical length of the stubs of Fig. A.2. It should be noted that the definition of (A.15) is general and it may take into account the losses of the circuit.

For this study it is of interest the *lossless* network and others evaluation about the lossy material may be integrated later by the reader simply by setting the proper value of Σ in (A.15). For the rest of this discussion $\Sigma = 0$.

It can be easily shown by fundamental network theory that the input impedances of a stub of electrical length θ and characteristic impedance Z_{ci} load with a short and open circuit are:

$$Z_i = jZ_{ci} \tan\theta \qquad \text{s.c.} \tag{A.17a}$$

$$Z_i = -j\frac{1}{Z_{ci}} \cot\theta \qquad \text{o.c.} \tag{A.17b}$$

Thus, by using the *Richard* transformation of (A.15) in the (A.17) and by normalizing them to port impedances to Z_0, the input impedances could be expressed as:

$$z_i = z_{ci} t \qquad \text{s.c.} \tag{A.18a}$$

$$z_i = -\frac{1}{t z_{ci}} \qquad \text{o.c.} \tag{A.18b}$$

The variable θ is more generally given by $\theta = \frac{2\pi}{\lambda_g} l$, where l is the length of the line, and at central frequency gives:

$$\theta_0 = \frac{2\pi}{\lambda_{g0}} \cdot \frac{\lambda_{g0}}{8} = \frac{\pi}{4} \tag{A.19}$$

The reason for using the Richard transformation is to define, in the last instance, polynomials in the t variable. Once the polynomials are obtained, the Butterworth and Tchebycheff characteristic as well as bandwidths and coupling coefficient control may be applied. A further discussion of bandwidths and coupling controls will be given in the following.

The first step in the characterisation of networks of the Fig. A.2 is to derive the ABCD matrix for the both even and odd modes separately. Note that these networks may be viewed as a concatenation of several stubs and transmission lines as stated

before. By deriving ABCD matrices of each stub and transmission line separately, the overall matrix of the circuit is given by multiplication of the terms.

If an open circuit stub of Fig. A.2 is considered as a shunt admittance a_i, its ABCD matrix is given by

$$\begin{bmatrix} 1 & 0 \\ a_i t & 1 \end{bmatrix} \tag{A.20}$$

while for the short-circuited shunt stub of same admittance the matrix is:

$$\begin{bmatrix} 1 & 0 \\ \frac{a_i}{t} & 1 \end{bmatrix} \tag{A.21}$$

The main line is a piece of transmission line of length 2θ and immitance b_i for the generic ith element. A constraint to the synthesis process is that the immitance b_i must be uniform in the main line. The ABCD matrix of the main line it is defined as [30]:

$$\begin{bmatrix} \cos 2\theta & \frac{j}{b_i} \sin 2\theta \\ j b_i \sin 2\theta & \cos 2\theta \end{bmatrix} \tag{A.22}$$

Each trigonometric function in eq. (A.22) contains the argument 2θ which means that the impedance (or admittance) b_i is constant along the direct transmission line. It is obvious that it is possible to rewrite the (A.22) as a cascade of two pieces of lines each one having immittance b_i and length θ.

Now let consider the following substitutions:

$$\sin(2\theta) = \frac{2t}{1 - t^2} \tag{A.23}$$

$$\cos(2\theta) = \frac{1 + t^2}{1 - t^2} \tag{A.24}$$

they are derived from the basic variable change:

$$t = j \tan \theta$$

The t variable had been already introduced in eq. (A.15) to characterize the input impedance of a generic stub. These substitutions play an important role in the following steps of the synthesis because they express the trigonometric functions of θ as rational functions in t variable. Furthermore it will be shown that it is possible to describe the entire device as a polynomial of variable t by operating this kind of transformation. It is also possible to demonstrate from equations (A.23) and (A.24) the following relations:

$$\cos \theta = \frac{1}{\sqrt{1 - t^2}} \tag{A.25}$$

$$\sin \theta = \frac{t}{\sqrt{1 - t^2}} \tag{A.26}$$

The proof of the definition (A.24) is given by the following:

$$\begin{aligned} \frac{1 + t^2}{1 - t^2} &= \frac{\cos^2 \theta - \sin^2 \theta}{\frac{\cos^2 \theta + \sin^2 \theta}{\cos^2 \theta}} \\ &= \cos^2 \theta - \sin^2 \theta \\ &= \cos 2\theta \end{aligned}$$

where it is well known that $\cos^2\theta + \sin^2\theta = 1$. Similarly, the proof of eq. (A.23) is given by:

$$\begin{aligned}\frac{2t}{1-t^2} &= \frac{2j\tan\theta}{\frac{\cos^2\theta+\sin^2\theta}{\cos^2\theta}} \\ &= j2\tan\theta\cos^2\theta \\ &= j2\sin\theta\cos\theta \\ &= |\sin 2\theta|\end{aligned}$$

The absolute value that comes from the last calculation may be avoided because in the present application the variable θ is bounded by physical constraints on the length of branches. In fact it cannot exceed the bounds:

$$0 < \theta < \frac{\pi}{2} \tag{A.27}$$

The other trigonometric relations (A.25) and (A.26) are obtained with the same criteria.

Recalling the definition of the transfer matrix of double length direct line, eq. (A.22) may be rewritten as a cascade of two transmission lines of same characteristic impedance and length θ. The ABCD matrix resulting from the combination of this two pieces can be represented in term of variable t by applying the substitutions (A.25) and (A.26), giving

$$\left(\frac{1}{\sqrt{1-t^2}}\begin{bmatrix}1 & \frac{t}{b_i}\\ b_i t & 1\end{bmatrix}\right)^2$$

which, after performing algebra, results in:

$$\frac{1}{1-t^2}\begin{bmatrix}1+t^2 & \frac{2}{b_i}t\\ 2b_i t & 1+t^2\end{bmatrix} \tag{A.28}$$

At this point it should be noted that the only difference between the even and odd circuits of Fig. A.2 is the termination of the shunt stubs. No change happens to the direct double-length lines. By comparing the matrices associated to the open-circuited (see eq. (A.20)) and short-circuited stubs (see eq. (A.21)), it is easy to see that they differ, respectively, by a term t and $1/t$. In addition it is possible to prove easily that if the change of variable from t to $1/t$ is substituted in the $ABCD$ matrix of the direct double-length line (A.28), the same matrix except for a change of sign is obtained. This is an important concept because it is mathematically proved that both the matrices of the stubs and direct lines are *invariant* with respect the transformation

$$t \rightarrow \frac{1}{t} \tag{A.29}$$

except for a change of sign of the matrix (A.28).

The even-mode two port circuit of Fig. A.2a has its transfer matrix that is given by the product, in the right order, of the matrices associated to the single stubs and direct double-length lines. Once the $ABCD$ matrix of the even circuit has been found, it is possible to directly obtain the matrix of the odd-mode circuit of Fig. A.2b by simply operating the variable transformation (A.29). It is convenient to express the resulting matrix of even-mode circuit as

$$\begin{bmatrix} A_e(t) & B_e(t) \\ C_e(t) & D_e(t) \end{bmatrix} \tag{A.30}$$

where $A_e(t)$, $B_e(t)$, $C_e(t)$, $D_e(t)$ are polynomials in the t variable. The subscript e indicates that the polynomial is derived by the even-mode circuit of Fig. A.2a. When

the matrix (A.30) has been calculated, to derive the one of the odd-mode circuit it is necessary to operate only the variable transformation:

$$\begin{bmatrix} A_o(t) & B_o(t) \\ C_o(t) & D_o(t) \end{bmatrix} = (-1)^{n-1} \begin{bmatrix} A_e\left(\frac{1}{t}\right) & B_e\left(\frac{1}{t}\right) \\ C_e\left(\frac{1}{t}\right) & D_e\left(\frac{1}{t}\right) \end{bmatrix} \tag{A.31}$$

The coefficient multiplying the right term of the equation derives from the change of sign of the direct double-length line when the variable transformation is performed. In a directional coupler of n branches there are $n-1$ direct lines, so when the transformation (A.29) is operated the sign "changes" $n-1$ times. As before, the o subscript means that the polynomials refer to the odd-mode network of Fig. A.2b.

The cascade of n transmission lines of same electrical length ϕ and characteristic impedance $Z_i = 1/Y_i$ are cascaded. The ABCD matrix of such a network can be obtained as the product of the matrices of each piece of line:

$$\begin{bmatrix} A & B \\ C & D \end{bmatrix} = \left(\frac{1}{\sqrt{1-t^2}}\right)^n \cdot \prod_{i=1}^{n} \begin{bmatrix} 1 & Z_i t \\ Y_i t & 1 \end{bmatrix}$$

that gives the following result:

$$\frac{1}{(1-t^2)^{n/2}} \begin{bmatrix} \check{A}(t) & \check{B}(t) \\ \check{C}(t) & \check{D}(t) \end{bmatrix} \tag{A.32}$$

The analysis of a few cases demonstrates the following statements:

- $\check{A}(t)$ and $\check{D}(t)$ are *even* polynomials in t variable
- $\check{A}(t)$ and $\check{D}(t)$ polynomials have the same degree
- the constant term in $\check{A}(t)$ and $\check{D}(t)$ is the unity
- $\check{B}(t)$ and $\check{C}(t)$ are *odd* polynomials in t
- $\check{B}(t)$ and $\check{C}(t)$ polynomials have the same degree

- the difference of degrees between $\check{A}(t)$ and $\check{C}(t)$ is 1
- the highest polynomial degree is n
- all coefficients are positive.

The description of the network as a product of terms given in eq. (A.32) is important because we will derive a similar analysis for the branch-guide network of Fig. A.2. The objective is to find a completely general form for the network of interest in order to easily adapt the characteristic parameters required by the specifications during the synthesis procedure.

Firstly, the ABCD matrix for the even mode network is derived by the multiplication in the right order of the matrices of stubs and double-length unit lines. In these devices there are n branches and $n-1$ direct lines. The formulation can be represented as follows:

$$\begin{bmatrix} A_e & B_e \\ C_e & D_e \end{bmatrix} = \prod_{i=1}^{n-1} \left\{ \frac{1}{1-t^2} \begin{bmatrix} 1 & 0 \\ a_i t & 1 \end{bmatrix} \begin{bmatrix} 1+t^2 & (2/b_i)t \\ 2b_i t & 1+t^2 \end{bmatrix} \right\} \cdot \begin{bmatrix} 1 & 0 \\ a_n t & 1 \end{bmatrix}$$

It is possible to demonstrate that it can be represented, for example, in the following general form:

$$\begin{bmatrix} A_e & B_e \\ C_e & D_e \end{bmatrix} = \frac{1}{(1-t^2)^{n-1}} \begin{bmatrix} A_{n-1}(t^2) & tB_{n-2}(t^2) \\ tC_{n-1}(t^2) & D_{n-1}(t^2) \end{bmatrix} \tag{A.33}$$

where the subscripts indicate the degree of the polynomials $A(t^2)$, $B(t^2)$, $C(t^2)$, and $D(t^2)$.

It is useful to make some points that come out from the eq. (A.33):

- $A(t^2)$, $B(t^2)$, $C(t^2)$, $D(t^2)$ are polynomials in the variable t^2
- polynomials $A_{n-1}(t^2)$ and $D_{n-1}(t^2)$ are *even* polynomials and their constant term is the unity

- $C_{n-1}(t^2)$ and $B_{n-2}(t^2)$ are *odd* polynomials.

By operating the variable transformation of eq. (A.29) it is possible to obtain the ABCD matrix of the odd mode directly from eq. (A.33):

$$\begin{bmatrix} A_o & B_o \\ C_o & D_o \end{bmatrix} = (-1)^{n-1} \frac{t^{2(n-1)}}{(1-t^2)^{n-1}} \begin{bmatrix} A_{n-1}\left(\frac{1}{t^2}\right) & \frac{1}{t}B_{n-2}\left(\frac{1}{t^2}\right) \\ \frac{1}{t}C_{n-1}\left(\frac{1}{t^2}\right) & D_{n-1}\left(\frac{1}{t^2}\right) \end{bmatrix} \tag{A.34}$$

It might be desirable to express the matrices obtained also in term of the trigonometric functions of variable θ instead of t. This double representation is useful in the next stage of the synthesis because in some cases we may prefer one of these two descriptions. By recalling the relations (A.23) and (A.24) we have:

$$\begin{bmatrix} A_e & B_e \\ C_e & D_e \end{bmatrix} = \begin{bmatrix} \bar{A}_{n-1}(-\cos 2\theta) & j\tan\theta\bar{B}_{n-2}(\cos 2\theta) \\ j\tan\theta\bar{C}_{n-1}(\cos 2\theta) & \bar{D}_{n-1}(-\cos 2\theta) \end{bmatrix} \tag{A.35}$$

for *even* mode and

$$\begin{bmatrix} A_o & B_o \\ C_o & D_o \end{bmatrix} = \begin{bmatrix} \bar{A}_{n-1}(\cos 2\theta) & j\cot\theta\bar{B}_{n-2}(-\cos 2\theta) \\ j\cot\theta\bar{C}_{n-1}(-\cos 2\theta) & \bar{D}_{n-1}(\cos 2\theta) \end{bmatrix} \tag{A.36}$$

for the *odd* mode.

All the formulation given until now are extremely important for our discussion because they are a completely general characterisation of the coupler. In the following sections the exact values of A, B, C and D will be derived for the given specifications of response type, number of branches, coupling and bandwidth.

A.2 THE APPROXIMATION PROBLEM

Once the even and odd ABCD matrices are obtained, it is possible to use the formulas (A.12) and (A.13) in order to get Γ_e, Γ_o, T_e and T_o. These quantities are then forming the output wave at each port by determining parameters of eq. (A.3). It is intuitive to understand that the B parameters consist as a ratios of rational numerator and denominator polynomials. By this way the coefficients of both numerator and denominator are related all together in a complex way. Indeed, it is quite difficult to relate these expressions to the maximally flat or equal ripple characteristics. Thus, a new function is introduced to reduce the complexity of the problem:

$$\frac{\Gamma}{T} = \frac{(A - D/R) + (B/R - C)}{2/\sqrt{R}} \tag{A.37}$$

For the case of symmetric couplers $A = D$ so eq. (A.37) reduces to

$$\frac{\Gamma}{T} = \frac{B - C}{2}$$

The new driving functions can be formulated in this way:

$$F_{\pm} = \frac{1}{2}\left(\frac{\Gamma_e}{T_e} \pm \frac{\Gamma_o}{T_o}\right) \tag{A.38}$$

Having operated this simplification it will be easier specify the functions $F_{\pm}$ as Butterworth or Tchebycheff polynomials.

From eq. (A.33) we know that A and D are even polynomial of degree $n-1$ as well as that C and B are odd polynomial of degree $n-1$ and $n-2$ respectively. The sum of two polynomials results in another polynomial whose degree is less or equal to the highest degree of the two starting polynomials. That means that the difference between A and D gives a new polynomial of degree at least $n-1$. The same applies to the second part of the numerator of eq. (A.37) because the degree of C is $n-1$. Now

the term indicating a generic polynomial of degree ξ, is introduced with the following notation:

$$P_\xi(t)$$

The equation (A.37) may be rewritten as the follows:

$$\begin{aligned}\frac{\Gamma}{T} &= \frac{(A - D/R) + (B/R - C)}{2/\sqrt{R}} \\ &= \frac{1}{2\sqrt{R}}\left[P_{n-1}(t^2)(R-1) - tP_{n-1}(t^2)\right] \\ &= \frac{P_{n-1}(t^2)}{2\sqrt{R}}\left[(R-1) - t\right]\end{aligned}$$

Thus the general form of the function Γ_e/T_e is given equivalently in one of the following two formulas, the first in t and the second equivalent in θ:

$$\frac{\Gamma_e}{T_e} = \frac{P_{n-1}(t^2)}{2\sqrt{R}}\left[(R-1) - Kt\right] \tag{A.39}$$

$$\frac{\Gamma_e}{T_e} = \frac{1}{2\sqrt{R}}\frac{P_{n-1}(x/x_c)}{P_{n-1}(1/x_c)}\left[(R-1) - jK\tan\theta\right] \tag{A.40}$$

where

K is a positive real number that has been introduced in order to control the coupling factor. This will be discussed later.

x is a variable change for the trigonometric form and is $x = \cos 2\theta$

x_c is the cut-off frequency and generally this parameter is used to control the bandwidth of the coupler. It is defined as $x_c = \cos 2\theta_c$

P_{n-1} is a generic polynomial of degree $n-1$.

From eq. (A.40) the corresponding value for the odd mode is obtained with the transformation (A.29):

$$\frac{\Gamma_o}{T_o} = \frac{1}{2\sqrt{R}} \frac{P_{n-1}(x/x_c)}{P_{n-1}(1/x_c)} [(R-1) + jK\cot\theta] \tag{A.41}$$

The driving function may be explicated as

$$\begin{aligned} F_- &= -\frac{1}{2\sqrt{R}} \frac{P_{n-1}(x/x_c)}{P_{n-1}(1/x_c)} \left(jK \frac{2}{\sin 2\theta} \right) \\ &= -\frac{1}{2\sqrt{R}} \frac{P_{n-1}(x/x_c)}{P_{n-1}(1/x_c)} \left(jK \frac{2}{\sqrt{1-x^2}} \right) \end{aligned} \tag{A.42}$$

where in the last equation the relation $\sin 2\theta = \sqrt{1-(\cos 2\theta)^2}$ has been applied.

The centre frequency of the branch-guide coupler occurs when the branches are quarter wavelength. This condition implies that at mid-band $\theta_0 = \pi/4$ and consequently $t_0 = j1$ and $x_0 = \cos 2\theta_0 = 0$. Once the polynomial P_{n-1} has been defined, the value of Γ_e/T_e is calculated by using the equations (A.39) or (A.40). At the stage it is necessary to specify the P_{n-1} in order to meet the desired frequency response. The following describes the maximally flat Butterworth and equal-ripple Tchebycheff characteristics.

A.2.1 Butterworth specification

With the maximally flat (Butterworth) response all the zeros of equations (A.39) and (A.40) are located at centre frequency $2\theta_0 = \pi/2$ as stated by eq. (A.19). Thus, the polynomial $P_{n-1}(t^2)$ that meets this requirement is the following:

$$P_{n-1}(t^2) = x^{n-1} = (\cos 2\theta)^{n-1} = \left(\frac{1+t^2}{1-t^2} \right)^{n-1} \tag{A.43}$$

where the substitution for t in eq. (A.24) has been applied. It is easy to show that at f_0 the variable $t = j$ and its square value gives $t^2 = -1$. The associated exponent defines that the number of zeros at centre frequency is exactly $n - 1$.

Thus, the formula for the Butterworth characteristic is given by:

$$\frac{\Gamma_e}{T_e} = \frac{1}{2\sqrt{R}} \frac{\left(1 + t^2\right)^{n-1}}{\left(1 - t^2\right)^{n-1}} \left[(R - 1) - Kt\right] \tag{A.44}$$

which for the symmetric case ($R = 1$) reduces to

$$\frac{\Gamma_e}{T_e} = -K \frac{t\left(1 + t^2\right)^{n-1}}{\left(1 - t^2\right)^{n-1}} \tag{A.45}$$

For the Butterworth response the K value controls the coupling at mid-band of the coupler.

Usually, no cut-off parameter is specified with the maximally flat response. So we may set the $\theta_c = 0$ that leads to $x_c = 1$. Thus, the value of the polynomial $P_{n-1}(x)$ evaluated at $1/x_c$ returns

$$P_{n-1}(1/x_c) = 1^{n-1} = 1$$

Consequently the term $P_{n-1}(1/x_c)$ is omitted in the equations (A.44) and (A.45). The driving function F is found directly from eq. (A.42)

$$F_- = -\frac{x^{n-1}}{2\sqrt{R}} \left(jK \frac{2}{\sqrt{1 - x^2}} \right) \tag{A.46}$$

A.2.2 Tchebycheff specification

In Fig. A.3 is the schematic of a generic network with the source and the load connected at each end. The generator here is represented with the equivalent of Thevenin of maximum amplitude v_0 and internal resistance R_0. Between the generator and the

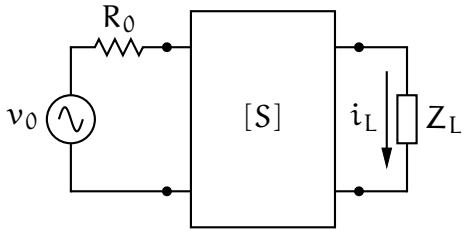

Figure A.3: General schematic for a 2 ports reactive network between source and load

load there is a reactive network which can be fully described by its S parameters. The reactive network represents the circuit that is under investigation. The ratio between the available power (P_0) and the effective power delivered on the load (P_L) is a common quantity for describing microwave components.

In the present study it is possible to define it as the following:

$$\begin{aligned}\frac{P_0}{P_L} &= 1 + |F|^2 \\ &= 1 + \frac{1}{4R}\frac{P_{n-1}^2(x/x_c)}{P_{n-1}^2(1/x_c)}\left(\frac{4K^2}{1-x^2}\right)\end{aligned} \tag{A.47}$$

The ratio is expressed in the form $1 + |F|^2$. It means that when $F = 0$ the maximum power is delivered to the load and it decreases as $|F|^2$ increases. Is should be noted that in this case the parameter K controls both the mid-band coupling and the ripple level.

The eq. (A.47) has the generic form of the insertion loss of a cascade of $n - 1$ unit element and one shorted circuit stub of electrical length 2θ. A similar circuit had been studied in the papers [124, 125]. In order to get a Tchebycheff equal ripple response in band $-x_c \leqslant x \leqslant x_c$ (and $x_c \leqslant 1$), the polynomial $P_{n-1}(x/x_c)$ must be in the form

$$P_{n-1}\left(\frac{x}{x_c}\right) = \frac{1}{2}\left(1 + \sqrt{1-x_c^2}\right)T_{n-1}\left(\frac{x}{x_c}\right) - \frac{1}{2}\left(1 - \sqrt{1-x_c^2}\right)T_{n-3}\left(\frac{x}{x_c}\right) \tag{A.48}$$

where $T_\xi(z)$ is the Tchebycheff polynomial of the first kind of degree ξ.

Once the polynomial $P_{n-1}(x/x_c)$ has been found with the eq. (A.48) it must be inserted in the general equation (A.40). To move from the trigonometric to the notation in t variable has been necessary to mvoe to the argument of eq. (A.48) to

$$\frac{x}{x_c} = \left(\frac{1+t^2}{1-t^2}\right) \cdot \left(\frac{1-t_c^2}{1+t_c^2}\right) \tag{A.49}$$

If the network has the same impedance at both ends, the function Γ_e/T_e for the equal ripple response reduces to

$$\frac{\Gamma_e}{T_e} = -jK \tan\theta P_{n-1}\left(\frac{x}{x_c}\right) \tag{A.50}$$

In the last expression the term $P_{n-1}(1/x_c)$ has been incorporated into the K parameter. This works for the particular case of symmetric network because the term $R-1$ is zero. The proposed implementation will use the general form where the constant $P_{n-1}(1/x_c)$ is normally expressed.

It is important to note that by imposing the form (A.48) to the polynomial P_{n-1} results that the driving function F of eq. (A.38) is equal ripple. However, neither the VSWR nor the isolation of the coupler remains equal ripple. This is because the parameters of eq. (A.3) are expressed in term of Γ and T rather than Γ/T. If it is true that $|\Gamma_e| \ll 1$ and $|\Gamma_o| \ll 1$, for the unity condition eq. (A.14) we can affirm that $|T_e| \approx 1$ and $|T_o| \approx 1$. If this condition is valid we can approximate

$$B_1 \approx \frac{1}{2}\left(\frac{\Gamma_e}{T_e} + \frac{\Gamma_o}{T_o}\right)$$

Thus, the functions that have been derived for the Tchebycheff specification give a nearly equal ripple response because the factors eq. (A.3) do contain the T_e and T_o variables. This approximation is not necessary for the Butterworth response because at θ_0 the values of Γ_e and Γ_o are *exactly* 0 and therefore the T_e and T_o are equal to 1.

A.3 SYNTHESIS PROCEDURE

The synthesis procedure is based on the calculation of the Γ_e/T_e for the given specifications and allows to evaluate the final immittances a_i and b_i. It is convenient to have the ratio Γ_e/T_e expressed in the variable t instead of the trigonometric functions $\cos\theta$ and $\cos\theta_c$. This expression comes mainly from the eq. (A.39) where the polynomial P_{n-1} is chosen from the equations (A.43) or (A.48) depending on the Butterworth or the Tchebycheff response.

The value $|\Gamma_e|^2$ is found by the expansion of the power balance relation of eq. (A.14) and is given in term of $|\Gamma_e/T_e|$:

$$|\Gamma_e|^2 = \frac{|\Gamma_e/T_e|^2}{1+|\Gamma_e/T_e|^2} \tag{A.51}$$

The stability of the system leads to a conceptual constraint on the type of polynomial $|\Gamma_e|$ found from the eq. (A.51). In fact, the poles of Γ_e must lie in the left-half of the complex plane. Each pole (or zero) can be expressed in the form $t_r = \sigma + j\omega$. Thus, all the poles must have the real part less or at least equal to zero:

$$\sigma \leqslant 0$$

If this were not true, it means that an hypothetical sinusoidal waveform entering the system would be subjected to exponential increasing of its magnitude clearly breaking the power balance condition of eq. (A.14).

There are two main factors in eq. (A.39), the first is the term $P_{n-1}(t^2)$ and the second is the $[(R-1)-Kt]$. The roots of the polynomial $|\Gamma_e/T_e|^2$ are all placed on the imaginary axis except for two. The two roots that do not lie on the imaginary axis come from the term $(R-1)^2 - K^2t^2$ while the others from the polynomial $P^2_{n-1}(t^2)$. In order to get the Γ_e the right roots from the numerator and denominator of eq. (A.51) must be selected. Two roots of the numerator are the ones of the polynomial $P_{n-1}(t^2)$

plus one from the second factor $(R-1)^2 - K^2t^2$. The root of the last factor is chosen according to the equations (A.12) and (A.13). It can be demonstrated that if $R > 1$ then the right-half plane root should be chosen, else if $R < 1$ the left-half plane root is selected to get the zero of the numerator. The case of a symmetric coupler is even easier because the factor degenerates into a zero located in the origin of the complex axis. The denominator of eq. (A.51) is factorized using numerical techniques and only the roots having a negative real part must be chosen. The factorization can be carried out by numerical computation since it has no closed form solution.

In a practical realization of the coupler (and of any other type of network) the value of $|\Gamma_e|$ must not exceed the unity. It can be stated that for the limit case of infinite frequency it must be

$$\lim_{t \to j\infty} |\Gamma_e| = 1 \tag{A.52}$$

If the condition (A.52) is not met a new coefficient, say κ, must be multiplied to Γ_e. From the theory of limits, it is well known that when $t \to j\infty$ the limit of a fraction of polynomials having same degree is the ratio of the coefficient whose variable has the higher power:

$$\lim_{z \to \infty} \frac{g(z)}{q(z)} = \lim_{z \to \infty} \frac{c_p z^p + c_{p-1} z^{p-1} + \cdots + c_1 z + c_0}{d_p z^p + d_{p-1} z^{p-1} + \cdots + d_1 z + d_0} = \frac{c_p}{d_p}$$

The value of κ is that coefficient in the limit (A.52) resulting, in modulus, 1:

$$\kappa = \left| \frac{d_p}{c_p} \right| \tag{A.53}$$

At this stage, the function Γ_e is obtained and from it is possible to derive the factors of the ABCD matrix for the even network. To do this it is necessary to recall the form of Γ of eq. (A.12). It is important also to stress that the terms A and D are *even* polynomial of degree $n-1$ and that the B and C factors are *odd* polynomials. It must

be noted that the degree of C is $n-1$ while the one for B is $n-2$. Having this in mind the $ABCD$ matrix is derived directly by the function Γ_e. The mathematical description of the even network is therefore given by eq. (A.33). The decomposition of the matrix that has been just found permits us to find the values of the immittances of the coupler network.

The first step in the synthesis is the extraction of a shunt stub of characteristic admittance a_1 of such a value that a double-length unit element of uniform impedance b_1 may then extracted. It is necessary to extract first a shunt open circuited stub of admittance:

$$\begin{aligned} a_1 &= \frac{\partial}{\partial t}\frac{C_e}{A_e}\bigg|_{t=1} \\ &= \frac{\partial}{\partial t}\frac{D_e}{B_e}\bigg|_{t=1} \end{aligned} \tag{A.54}$$

After the stub is removed, a double-length uniform unit element of admittance is found as

$$b_1 = \frac{C_e(1)}{A_e(1)} = \frac{D_e(1)}{A_e(1)} \tag{A.55}$$

The process continues by removing the last double unit element and by repeating these two steps until all the admittances of the coupler are obtained. It should be noted that the form of equations (A.54) and (A.55) are given in term of admittances. This is suitable for TEM networks. Of course, it is possible to derive the impedances associated to the stubs and double-unit elements by making the inversion of eqs. (A.54) and (A.55) directly.

Finally it is important to note that the relation of the K parameter expressed in section A.2.1 and A.2.2 and the mid-band coupling are related in a complex way to the number of branches n, the impedance ratio R and the cut-off θ_c. K also differs if the specifications require a maximally-flat or an equal ripple frequency response. Therefore it is very difficult to derive a mathematical closed expression for the mid-band

coupling once all parameters are specified. In practice, it is more frequent to find a proper value for K that meets the requirement for a prescribed mid-band coupling. Thus, an iterative approach is used to find the right K based on the specifications. Practical experience suggests that, when the synthesis procedure is automatized, between 2 to 4 attempts are enough to find the correct K that results in the required coupling at central frequency.

A.4 EXAMPLES

A.4.1 Three branches Butterworth asymmetric coupler

In this example a 3 branch-guide coupler with Butterworth response and asymmetric impedance load will be presented. The input specifications for this couplers are $n = 3$, $R = 2$, $K = 1$ and a Butterworth maximally flat frequency response [123].

Initially, we are looking for a driving function were all the poles are located at centre frequency, we need to use the eq. (A.44):

$$\frac{\Gamma_e}{T_e} = \frac{1}{2\sqrt{R}} \left(\frac{1+t^2}{1-t^2} \right)^2 \cdot [(R-1) - Kt] \tag{A.56}$$

where the expression for the $P_{n-1}(t^2)$ of eq. (A.43) has been inserted for the given specifications:

$$P_{n-1}(t^2) = \left(\frac{1+t^2}{1-t^2} \right)^2$$

It is convenient to express the eq. (A.56) in the form magnitude squared in order to prepare it for the following steps of calculation:

$$\left| \frac{\Gamma_e}{T_e} \right|^2 = \frac{1}{4R} \left(\frac{1+t^2}{1-t^2} \right)^4 \cdot \left[(R-1)^2 - K^2 t^2 \right] \tag{A.57}$$

Now we are ready to calculate the $|\Gamma_e|^2$ from the eq. (A.51):

$$|\Gamma_e|^2 = \frac{|\Gamma_e/T_e|^2}{1+|\Gamma_e/T_e|^2} = \frac{(1+t^2)^4[(R-1)^2-K^2t^2]}{4R(1-t^2)^4+(1+t^2)^4[(R-1)^2-K^2t^2]} = \frac{(1+t^2)^4(1-t^2)}{8(1-t^2)^4+(1+t^2)^4(1-t^2)} \tag{A.58}$$

where in the last expression the values of K and R given in the specifications have been substituted into the equation.

The expression of $|\Gamma_e|^2$ gives in the eq. (A.58) can be seen as a ratio of two polynomials, one at the numerator and the other one at the denominator. Prior to proceed with the extraction of the characteristic impedances a_i and b_i it is necessary to find the factor Γ_e. This can be done by factorizing both the numerator and denominator of eq. (A.58).

As discussed before, when the $R > 1$ the right-half t plane zero of factor $[(R-1)^2 - K^2t^2]$ must be chosen. Of course, the other factor appearing in the numerator, $(1+t^2)^4$, in eq. (A.58) has its zeros that all lie on the imaginary axis symmetrically with respect the centre. Thus, the numerator has the following factors:

$$(1+t^2)^2(1-t) = 1 - t + 2t^2 - 2t^3 + t^4 - t^5 \tag{A.59}$$

The denominator of eq. (A.58) is factored using a numerical procedure approach. It is found that its roots are the following:

$$t_r = [\pm 1.8558 \pm j1.3376;\ \pm 0.6777 \pm j0.3376;\ \pm 1] \tag{A.60}$$

A plot of the roots of both numerator and denominator of eq. (A.58) is presented in Fig. A.4. The polynomial is built from the roots of eq. (A.60) that lie in the left-half of

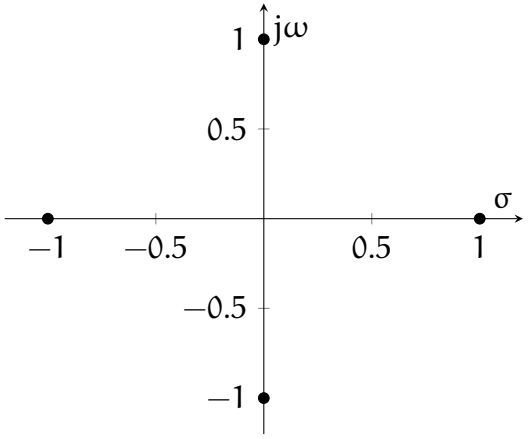

(a) Roots of numerator (zeros)

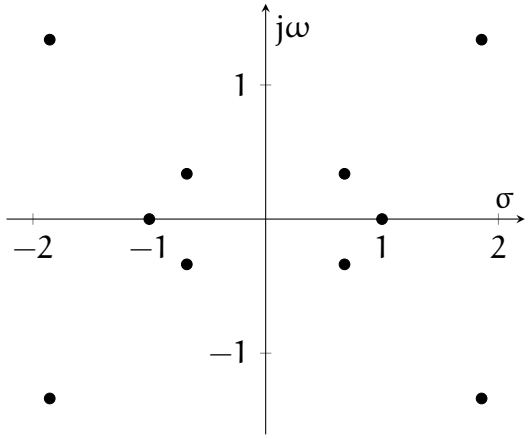

(b) Roots of denominator (poles)

Figure A.4: Roots and poles of $|\Gamma_e|^2$ of eq. (A.58) on the complex t plane.

the t plane. This means that only the roots with $\Re(t_r) < 0$ are selected and multiplied together. This result in the following polynomial:

$$t^5 + 6.0670t^4 + 15.9041t^3 + 20.0579t^2 + 12.2208t + 3 \tag{A.61}$$

One of the consequences of having chosen the poles with negative real part is that the polynomial (A.61) has its coefficients all positive. A polynomial built only from roots lying in the left-half complex plane is know as *Hurwitz* polynomial.

By recalling the limit condition that Γ_e is multiplied by a coefficient κ to comply with eq. (A.52), we get

$$\Gamma_e = \kappa \frac{-t^5 + t^4 - 2t^3 + 2t^2 - t + 1}{t^5 + 6.0670t^4 + 15.9041t^3 + 20.0579t^2 + 12.2208t + 3} \tag{A.62}$$

In this case, the coefficient is found as the modulus of the inverse of the coefficient of degree 5 as of eq. (A.53):

$$\kappa = \left| \frac{1}{-1} \right| = 1 \tag{A.63}$$

The following step is to derive the polynomials for the ABCD matrix that describes the *even* network. The transmission parameters are found by comparing equations (A.62) and (A.12). As described before, the polynomials A_e and D_e are *even* and they contain unity as a constant term. To make this comparison easier it is convenient to rewrite the (A.62) in order to put in evidence the even part and the odd part of both numerator and denominator:

$$\Gamma_e = \frac{(t^4 + 2t^2 + 1) + (-t^5 - 2t^3 - t)}{(6.0670t^4 + 20.0579t^2 + 3) + (t^5 + 15.9041t^3 + 12.2208t)}$$

This is identical in form to eq. (A.12), so the ABCD parameters are found to be:

$$A(t) = 1.7667t^4 + 5.5145t^2 + 1 \tag{A.64a}$$

$$B(t) = 6.9520t^3 + 5.6104t \tag{A.64b}$$

$$C(t) = 0.5t^5 + 4.4760t^3 + 3.3052t \tag{A.64c}$$

$$D(t) = 2.5335t^4 + 9.0289t^2 + 1 \tag{A.64d}$$

The transfer matrix for the *even* mode of the coupler in the form as was introduced in (A.33) is given as:

$$\begin{bmatrix} A_e & B_e \\ C_e & D_e \end{bmatrix} = \frac{1}{(1-t^2)^2} \begin{bmatrix} A & B \\ C & D \end{bmatrix} \tag{A.65}$$

The degree of the ABCD polynomials are in accordance with the rules stated in eq. (A.33). In particular, the (A.64a) is an even polynomial of variable t^2 of degree $n - 1 = 2$ and consequently the highest power in this polynomial is 4. Regarding the

polynomial (A.64b) it does not have the term t^5 in accordance with the rules described before.

Now that the $ABCD$ parameters are obtained from the equation of Γ_e, the *even* network is completely defined. The last step is to derive the values of the a_i and b_i immittances. The procedure used to get these values is to remove, at each iteration, one shunt stub and one double-unit transmission line. From eq (A.54) this is found to be:

$$\begin{aligned} a_1 = \frac{\partial}{\partial t}\frac{C}{A}\bigg|_{t=1} &= \frac{C'A - CA'}{A^2}\bigg|_{t=1} \\ &= \frac{19.233 \cdot 8.281 - 8.281 \cdot 18.096}{8.281^2} \\ &= 0.1373\,\mathrm{S} \end{aligned} \tag{A.66}$$

The value of a_1 is the admittance of the first stub of network of Fig. A.2a and, consequently, the admittance of the first branch-line of the final coupler. In order to get the value of the first double-unit length is necessary to *remove* the stub that has been just found. To do this, the transfer matrix of a shunt stub having negative admittance $-a_1$ is multiplied to the $ABCD$ matrix of the network. The result of this operation is the elimination of the first stub:

$$\frac{1}{(1-t^2)^2}\begin{bmatrix} 1 & 0 \\ -a_1 t & 1 \end{bmatrix}\begin{bmatrix} A & B \\ C & D \end{bmatrix} = \frac{1}{(1-t^2)^2}\begin{bmatrix} A & B \\ \bar{C} & \bar{D} \end{bmatrix} \tag{A.67}$$

where

$$\bar{C}(t) = 0.2574t^5 + 3.7187t^3 + 3.1679t \tag{A.68a}$$

$$\bar{D}(t) = 1.5787t^4 + 8.2584t^2 + 1 \tag{A.68b}$$

Table A.1: Admittances of the branch and main lines for Butterworth coupler $n = 3$, $K = 1$ and $R = 2$.

Branch line (S)	Main line (S)
0.1373	0.8627
0.1758	0.6075
0.0517	

The first double-unit length transmission line is calculated from (A.67) using the eq. (A.55):

$$b_1 = \frac{\bar{C}(1)}{A(1)} = \frac{7.147}{8.281} = 0.8627\,S \tag{A.69}$$

Now the main line is removed in a similar way as was for the shunt stub. As before, the transfer matrix of a negative length is added:

$$\frac{1}{1-t^2}\begin{bmatrix} 1+t^2 & -2.317t \\ -1.725t & 1+t^2 \end{bmatrix} \cdot \left\{ \frac{1}{(1-t^2)^2}\begin{bmatrix} A & B \\ \bar{C} & \bar{D} \end{bmatrix} \right\} = \frac{1}{(1-t^2)^3}\begin{bmatrix} A_1 & B_1 \\ C_1 & D_1 \end{bmatrix} \tag{A.70}$$

It should be noted that the terms $A_1, \cdots, D_1$ include a factor $(1-t^2)^2$ that explains the increasing power at the denominator in eq. (A.70). In order to find the transfer matrix of the circuit without the first branch and main line, the terms of the matrix (A.70) must be divided for $(1-t^2)^2$. This results in:

$$\frac{1}{1-t^2}\begin{bmatrix} 1+1.1701t^2 & 3.292t \\ 1.442t+0.257t^3 & 1+1.5787t^2 \end{bmatrix} \tag{A.71}$$

The procedure presented is repeated to find all the values of the branches and the main lines. At the end of the process the admittances found are summarized in Tab. A.1. The values calculated in Tab. A.1 are expressed as admittances as for a TEM mode. If the structure is a TE or a TM an impedance model should be used. In fact, in a medium where the a TEM mode is propagating the branches are seen in shunt

with respect the main double-unit lines. It is the contrary for the TE or TM modes where the branches are in series with the correspondent main line.

It is also interesting how this network acts as impedance transformer between the input and output impedances. The normalized admittances are 1 S for the input and $1/R = 0.5\,S$ for the output ports. The values of Tab. A.1 for the main line tends to match the input and output admittances in a similar way of a transformer matching network.

A.4.2 Four branches 3 dB Butterworth symmetric coupler

In this example a 4 branch symmetric directional coupler with Butterworth response will be described. The desired mid-band coupling is 3 dB. Thus, the parameters for these specifications are set as: $n = 4$, $K = 6$ and $R = 1$.

In this example the eq. (A.45) is to be used. To decrease the complexity of the polynomial calculation is convenient to express each rational function as the ratio of two distinct polynomial $N(t)$ and $D(t)$. Thus, the numerator and the denominator will be evaluated separately bringing a simplification, especially at the implementation stage. As before, applying the formula (A.51) it is found

$$|\Gamma_e|^2 = \frac{|\Gamma_e/T_e|^2}{1+|\Gamma_e/T_e|^2} = \frac{(1+t^2)^6[(R-1)^2-K^2t^2]}{4R(1-t^2)^6+(1+t^2)^6[(R-1)^2-K^2t^2]} = \frac{N_\Gamma^2(t)}{D_\Gamma^2(t)} \tag{A.72}$$

The coupler of interest is symmetric and this characteristic is responsible for a substantial simplification of the synthesis procedure. The roots of the numerator of $|\Gamma_e|^2$ are all located on the imaginary axis in complex conjugate pairs except for a double zero in the origin. Thus, the numerator of $|\Gamma_e|$ can be easily obtained from the $N_\Gamma^2(t)$ of eq. (A.72):

$$N_\Gamma(t) = -Kt(1+t^2)^3 = -6t^7 - 18t^5 - 18t^3 - 6t \tag{A.73}$$

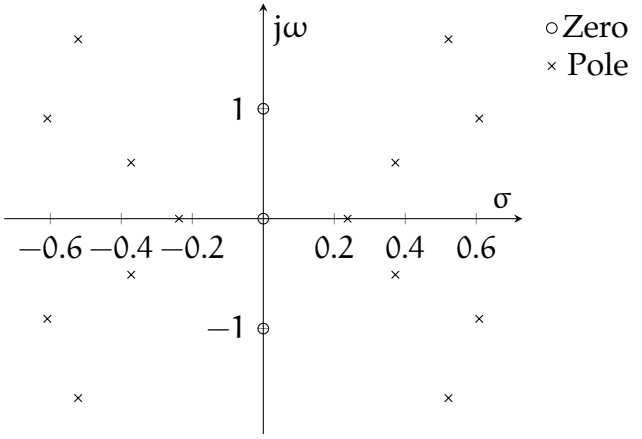

Figure A.5: Position of zeros and poles of $|\Gamma_e|^2$ for coupler A.4.2

The denominator of $|\Gamma_e|$ is found by selecting the roots of the denominator of eq. (A.72) that lie on the left-half plane of the complex t plane.

The roots of the denominator of eq. (A.72) are obtained with a numerical technique and are found to be:

$$t_r = [\pm 0.5217 \pm j1.6319;\ \pm 0.6083 \pm j0.9112;\ \pm 0.3721 \pm j0.5098;\ \pm 0.2375] \quad (A.74)$$

Fig. A.5 shows the diagram of the zeros and poles of the $|\Gamma_e|^2$ for the present coupler. The *zeros* are defined with the roots of the numerator of eq. (A.72) while the *poles* are the roots of the denominator of the fraction. By selecting the left-half roots and multiplying them back, the denominator of the $|\Gamma_e|$ if found to be:

$$D_\Gamma(t) = t^7 + 3.2417t^6 + 8.1989t^5 + 11.5241t^4 + \\ + 11.5808t^3 + 6.7440t^2 + 2.4825t + 0.3333 \quad (A.75)$$

Once the $|\Gamma_e|$ has been found, it must be checked that its limit at infinity does not exceed unity. Recalling the basic theory of the limits, at the point that both $N_\Gamma(t)$ and

$D_\Gamma(t)$ have the same degree the limit is found to be the ratio of the coefficients of maximum power:

$$\lim_{t\to j\infty} |\Gamma_e| = \lim_{t\to j\infty} \left|\frac{N_\Gamma(t)}{D_\Gamma(t)}\right| = \left|\frac{-6}{1}\right| = 6 \tag{A.76}$$

Thus, from equations (A.53) and (A.76) it is obtained:

$$\kappa = \frac{1}{6} \tag{A.77}$$

Consequently numerator may absorb the term κ thus becoming:

$$\tilde{N}(t) = \kappa N_\Gamma(t) = -t^7 - 3t^5 - 3t^3 - t \tag{A.78}$$

For the special case of symmetric coupler it can be deducted that from eq. (A.73) the value of κ is equal to the inverse value of the coupling coefficient K. However, this happens only if the coupler is symmetric and because the term $(R-1)$ disappears. This is not true in the general case and it is recommended to use the general equations (A.52) and (A.53) in order to get the right value of κ.

Now that $|\Gamma_e|$ has been found and that it is in accordance with all the conditions, it is possible to derive the $ABCD$ parameters as for the eq. (A.12). As before, it is convenient to gather both numerator and denominator of $|\Gamma_e|$ into an even and odd part:

$$\tilde{N}(t) = E_{\tilde{N}}(t) + O_{\tilde{N}}(t) \tag{A.79a}$$

$$D_\Gamma(t) = E_D(t) + O_D(t) \tag{A.79b}$$

In our example these polynomial are the following:

$$E_{\tilde{N}}(t) = 0 \tag{A.80a}$$

$$E_D(t) = 3.2417t^6 + 11.5241t^4 + 6.7440t^2 + 0.3333 \tag{A.80b}$$

$$O_{\tilde{N}}(t) = -t^7 - 3t^5 - 3t^3 - t \tag{A.80c}$$

$$O_D(t) = t^7 + 8.1989t^5 + 11.5808t^3 + 2.4825t \tag{A.80d}$$

The $ABCD$ parameters are found by solving the following system for the even part:

$$\begin{cases} A - D/R = E_{\tilde{N}} \\ A + D/R = E_D \end{cases} \tag{A.81}$$

and this second system for the odd part:

$$\begin{cases} B/R - C = O_{\tilde{N}} \\ B/R + C = O_D \end{cases} \tag{A.82}$$

The solutions of systems (A.81) and (A.82) are the polynomial of the $ABCD$ matrix that describe the circuit:

$$A(t) = 9.7252t^6 + 34.5724t^4 + 20.2321t^2 + 1 \tag{A.83a}$$

$$B(t) = 40.1932t^5 + 60.4847t^3 + 11.8949t \tag{A.83b}$$

$$C(t) = 6t^7 + 33.5966t^5 + 43.7423t^3 + 10.4474t \tag{A.83c}$$

$$D(t) = 9.7252t^6 + 34.5724t^4 + 20.2321t^2 + 1 \tag{A.83d}$$

Naturally, when solving systems (A.81) and (A.82) the rules over the degrees of polynomial stated in (A.33) apply. As expected, the term (A.83a) and (A.83d) are the same. This is a consequence of the symmetry of the circuit.

It is interesting to point out that the values of equations (A.83) are not obtained directly by solving the systems (A.81) and (A.82). In fact all the polynomials obtained

Table A.2: Admittances of the branch and main lines for Butterworth coupler $n = 4$, $K = 6$ and $R = 1$.

Branch line (S)	Main line (S)
0.1879	1.2433
0.9235	1.6257
0.9235	1.2433
0.1879	

are multiplied for constant the term of A, that is 0.1667, and that is convenient that this is removed. Thus, by dividing all the $ABCD$ polynomials by the constant term of A we obtain the final formulas stated in eqs. (A.83).

Starting from (A.83) the a_i and b_i immittances of the branches and the main lines are found with the same procedure described in the example A.4.1. The results are summarized in Tab. A.2. It can be noted that there is a symmetry among the values listed in table A.2. This is consistent with the symmetry of the circuit with respect the input and output impedances.

In order to draw the scattering parameters of the circuit that has been just synthesized, a program had been written to take as input the values of admittances of Tab. A.2 and to produce the relative responses. This program works to produce a confirmation for the values obtained with the present synthesis procedure. Its main object is to derive the $ABCD$ matrix of the coupler circuit composed by transmission lines of the given impedances. The calculation is the same described in [30] for the two-branches hybrid coupler, here extended for the general case of n branches. The results in terms of scattering parameters are presented in Fig. A.6a.

Fig. A.6a presents the magnitude values of the S parameters in dB as a function of the frequency variable θ. Recalling the general characterization of the circuit, θ can vary between 0 and $\pi/2$ and its value at centre frequency is exactly 45 degrees. The frequency response is Butterworth and this can be immediately seen by noticing that all the reflection zeros are located at centre frequency. The mid-band coupling is 3 dB and as a consequence there is equal splitter of power among the output ports 2 and 3.

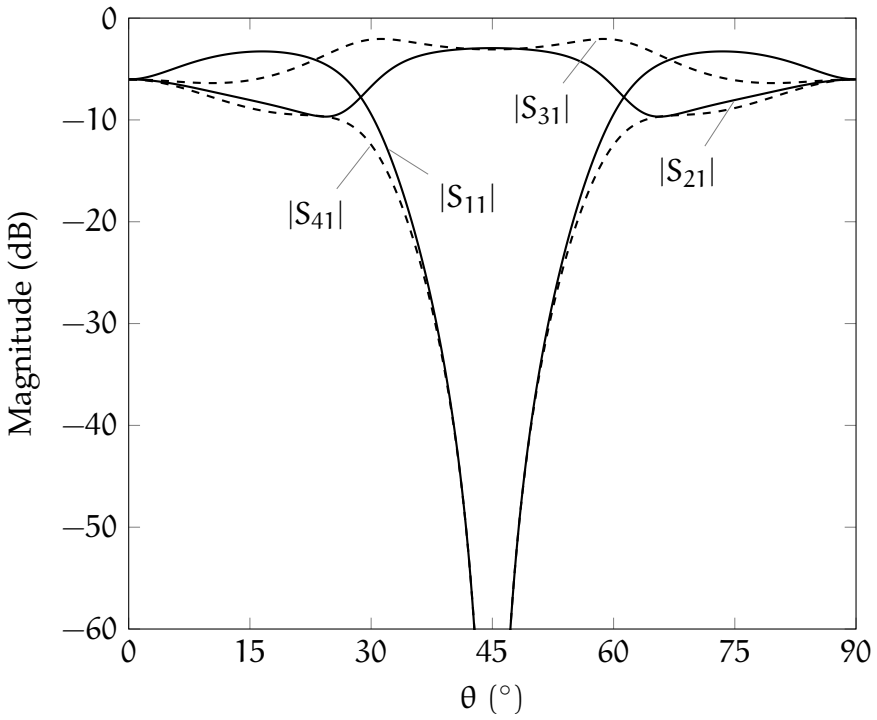

(a) Scattering parameters in magnitude

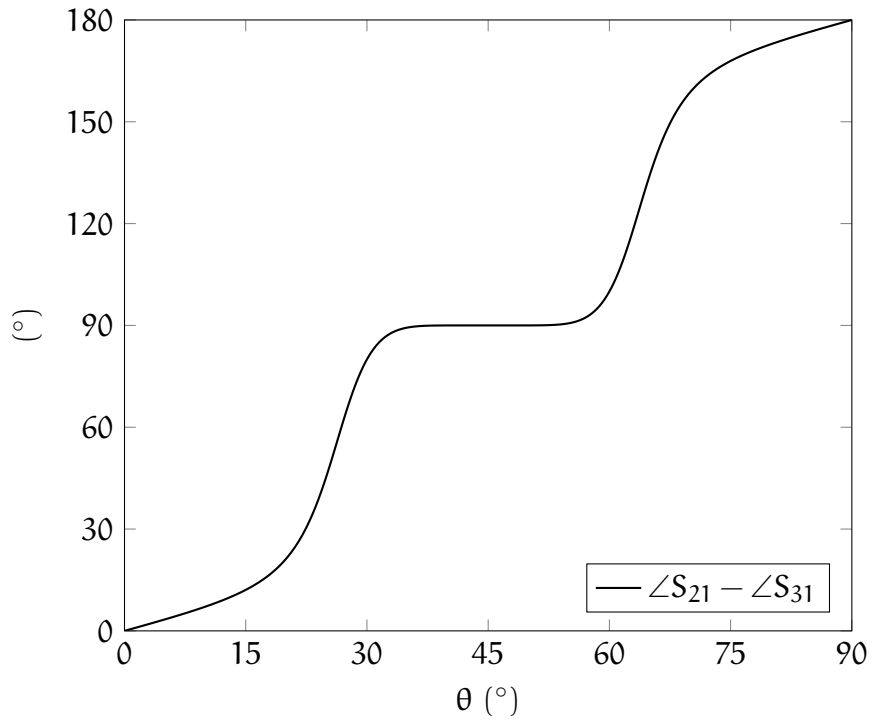

(b) Output ports phase shift

Figure A.6: Responses for the four branches Butteworth 3 dB symmetric coupler.

Table A.3: Characteristic parameters for coupler A.4.3

Parameter	Value
n	5
K	10
R	1
θ_c	40°

The frequency response is periodic with period $\theta = \pi/2$ and therefore only the first period is shown in Fig. A.6.

Another interesting parameter is the phase shift between the output ports 2 and 3. The phase shift between port 2 and 3 is shown in Fig. A.6b. Due to the fact that each transmission line of the coupler is a quarter-wavelength long, the phase shift is 90 degrees at mid-band. This is particularly important when the system requires two signals in quadrature at the outputs of the device.

The phase shift of Fig. A.6b is constant around the central frequency ($\theta = 45°$). It is possible to show that by increasing the number of branches, the interval in which the phase shift is flat and equal to 90° is wider.

The phase shift depicted in Fig. A.6b has been obtained making difference in modulus 180° of the phase of S_{21} and S_{31}.

A.4.3 Five branches 3 dB Tchebycheff symmetric coupler

In this section a 5 branch symmetric coupler with 3 dB mid-band coupling and equal ripple Tchebycheff response is going to be presented. In order to meet the specification stated earlier, the characteristic parameters are chosen in accordance to Tab. A.3.

As with the previous examples, the first step is to find the correct polynomial $P_{n-1}(t^2)$ that meets the specification. It must be in the form of eq. (A.48). In gen-

eral, a Tchebycheff polynomial of the first kind and degree k is one in variable $\cos\vartheta$ that solves the following:

$$T_k(\cos\vartheta) = \cos(k\vartheta) \tag{A.84}$$

By changing the variable $z = \cos\vartheta$ and re-arranging the formula we obtain the general definition of the Tchebycheff function:

$$T_k(z) = \cos(k \arccos(z)) \tag{A.85}$$

The dependent variable is in the range $z \in [-1, 1]$ and also the maximum value of $T_k(z)$ is in the range

$$\max_{-1 \leqslant z \leqslant 1} |T_k(z)| = 1$$

Starting from the well known trigonometric identity

$$\cos(\alpha + \beta) = \cos\alpha\cos\beta - \sin\alpha\sin\beta$$

we can derive the following two equalities:

$$\begin{aligned} \cos[(k+1)\vartheta] &= \cos(k\vartheta + \vartheta) \\ &= \cos(k\vartheta)\cos(\vartheta) - \sin(k\vartheta)\sin(\vartheta) \end{aligned} \tag{A.86a}$$

$$\begin{aligned} \cos[(k-1)\vartheta] &= \cos(k\vartheta - \vartheta) \\ &= \cos(k\vartheta)\cos(\vartheta) + \sin(k\vartheta)\sin(\vartheta) \end{aligned} \tag{A.86b}$$

by substituting the term $\sin(k\vartheta)\sin(\vartheta)$ in the last two equations it is possible to derive the following trigonometric relation:

$$\cos[(k+1)\vartheta] = 2\cos(k\vartheta)\cos(\vartheta) - \cos[(k-1)\vartheta] \tag{A.87}$$

This is useful identity because if we substitute $z = \cos\vartheta$ and the definition of Tchebycheff function (A.84) we obtain the recursive polynomial

$$T_k(z) = 2zT_{k-1}(z) - T_{k-2}(z) \tag{A.88}$$

where the initial values are easily found to be

$$T_0(z) = 1$$
$$T_1(z) = z$$

In our problem it is necessary to find a polynomial in form $N(t)/D(t)$ of the eq. (A.48). An extension of the recursive function (A.88) is derived in order to find the general equal ripple solution of the rational function $f(z)/g(z)$:

$$T_k\left[\frac{f(z)}{g(z)}\right] = 2\frac{f(z)}{g(z)}T_{k-1}\left[\frac{f(z)}{g(z)}\right] - T_{k-2}\left[\frac{f(z)}{g(z)}\right] \tag{A.89}$$

The last formula is particularly convenient if applied to our synthesis procedure because we are now able to relate the Tchebycheff general polynomial recursive definition to the equal ripple condition eq. (A.48) expressed in the variable eq. (A.49).

By solving the algebra, eq. (A.89) can be explicitly defined as the following:

$$\begin{aligned} T_k\left[\frac{f(z)}{g(z)}\right] &= \zeta_k\left[\frac{f(z)}{g(z)}\right]^k + \zeta_{k-2}\left[\frac{f(z)}{g(z)}\right]^{k-2} + \cdots + \zeta_0 \\ &= \frac{\zeta_k f^k(z) + \zeta_{k-2} f^{k-2}(z)g^2(z) + \cdots + \zeta_0 g^k(z)}{g(z)^k} \end{aligned} \tag{A.90}$$

where the terms $\zeta_0, \zeta_1, \cdots, \zeta_k$ are the coefficients of the eq. (A.88) and each subscript indicates the power of the variable to which it is associated. From eq. (A.49) we have

$$f(t) = (1 + t^2)(1 - t_c^2)$$
$$g(t) = (1 - t^2)(1 + t_c^2)$$

In this examples we can derive the values of the following parameters from the specifications of Tab.. A.3:

$$x_c = 0.1736 \tag{A.91a}$$

$$t_c = j0.8391 \tag{A.91b}$$

The characteristic polynomial resulting from equations (A.48) and (A.90) is the following:

$$P_{n-1}(t^2) = \frac{N_P(t^2)}{D_P(t^2)} = \frac{64.9344}{0.0077} \cdot \frac{t^8 + 4.1237t^6 + 6.2492t^4 + 4.1237t^2 + 1}{t^8 - 4t^6 + 6t^4 - 4t^2 + 1} \tag{A.92}$$

Again, once the characteristic polynomial has been found, it is necessary to derive the Γ_e/T_e expression from the usual eq. (A.40). The normalization constant that appears in eq. (A.40) is calculated directly from eq. (A.92) with the argument

$$\frac{1}{x_c} = \frac{1 - t_c^2}{1 + t_c^2} = 5.7588 \tag{A.93}$$

and so resulting:

$$P_{n-1}\left(\frac{1}{x_c}\right) = P_c = 10\,818 \tag{A.94}$$

Now, from eq. (A.40)

$$\begin{aligned}\left|\frac{\Gamma_e}{T_e}\right|^2 &= \frac{1}{4R}\frac{P_{n-1}^2(t^2)}{P_c^2}[(R-1)^2 - K^2t^2] \\ &= \frac{1}{4R}\frac{N_P^2(t^2)}{P_c^2 \cdot D_P^2(t^2)}[(R-1)^2 - K^2t^2]\end{aligned}$$

Thus, for the Darlington relation eq. (A.51) we have the following:

$$|\Gamma_e|^2 = \frac{N_P^2(t^2) \cdot [(R-1)^2 - K^2t^2]}{4RP_c^2D_P^2(t^2) + N_P^2(t^2)[(R-1)^2 - K^2t^2]} = \frac{N_\Gamma^2(t)}{D_\Gamma^2(t)} \tag{A.95}$$

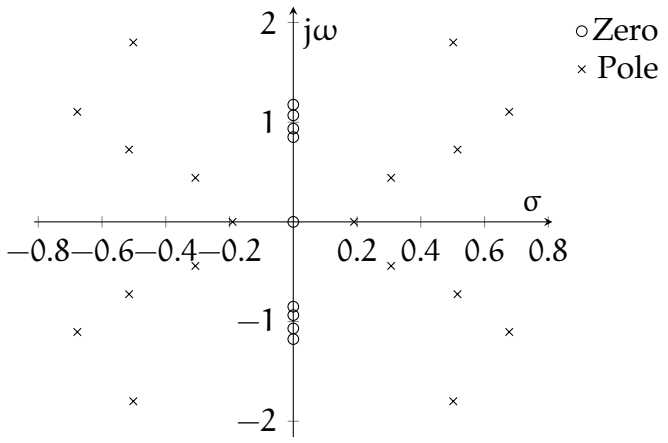

Figure A.7: Position of zeros and poles of $|\Gamma_e|^2$ for coupler A.4.3

The roots of numerator of eq. (A.95) are the following:

$$t_{rN} = [0;\ \pm j1.1758;\ \pm j1.0690;\ \pm j0.9354;\ \pm j0.8505] \tag{A.96}$$

while the roots of the denominator are:

$$t_{rD} = [\pm 0.5018 \pm j1.7997;\ \pm 0.6774 \pm j1.1041;$$
$$\pm 0.5151 \pm j0.7253;\ \pm 0.3070 \pm j0.4419;\ \pm 0.1904] \tag{A.97}$$

The diagram of the zeros and poles of eq. (A.95) is finally depicted in Fig. A.7.

Due to the symmetry of the device, only the left-half poles of Fig. A.7 must be chosen. Thus, the polynomial of the numerator and denominator of $|\Gamma_e|$ are

$$\tilde{N}(t) = \kappa N_\Gamma(t) = -t^9 - 4.1237t^7 - 6.2492t^5 - 4.1237t^3 - t \tag{A.98}$$

$$D_\Gamma(t) = t^9 + 4.1930t^8 + 12.8815t^7 + 24.2795t^6 + 33.8494t^5 +$$
$$+ 31.9267t^4 + 21.5638t^3 + 9.2152t^2 + 2.4961t + 0.2555 \tag{A.99}$$

Table A.4: Admittances of the branch and main lines for Tchebycheff coupler $n = 5$, $K = 10$, $R = 1$ and $\theta_c = 40°$.

Branch line (S)	Main line (S)
0.0997	1.1639
0.5410	1.6532
1.1348	1.6532
0.5410	1.1639
0.0997	

And finally the value of the constant that keep the limit condition eq. (A.52) is:

$$\kappa = 0.0015 \tag{A.100}$$

At this point it is possible to solve the systems (A.81) and (A.82) and to get the parameters of the ABCD matrix:

$$A(t) = 16.4123t^8 + 95.0363t^6 + 124.9693t^4 + 36.0705t^2 + 1 \tag{A.101a}$$

$$B(t) = 84.7017t^7 + 240.5299t^5 + 152.6717t^3 + 15.6267t \tag{A.101b}$$

$$C(t) = 7.8285t^9 + 66.5624t^7 + 156.9564t^5 + 100.5474t^3 + 13.6848t \tag{A.101c}$$

$$D(t) = 16.4123t^8 + 95.0363t^6 + 124.9693t^4 + 36.0705t^2 + 1 \tag{A.101d}$$

The last step is to extract the a_i and b_i immittances from the eqs. (A.101) with the same procedure explained in section A.4.1. The numerical results are listed in Tab. A.4.

The scattering parameters of this hybrid coupler are shown in Fig. A.8a. The graph shows the frequency response of the equal ripple 5 branches coupler. The first detail to be noted is that there are only 4 reflection zeros at mid-band. This is a consequence of the fact that the order of the characteristic polynomial is $n - 1$ and, consequently, the hybrid presents only 4 reflections zeros.

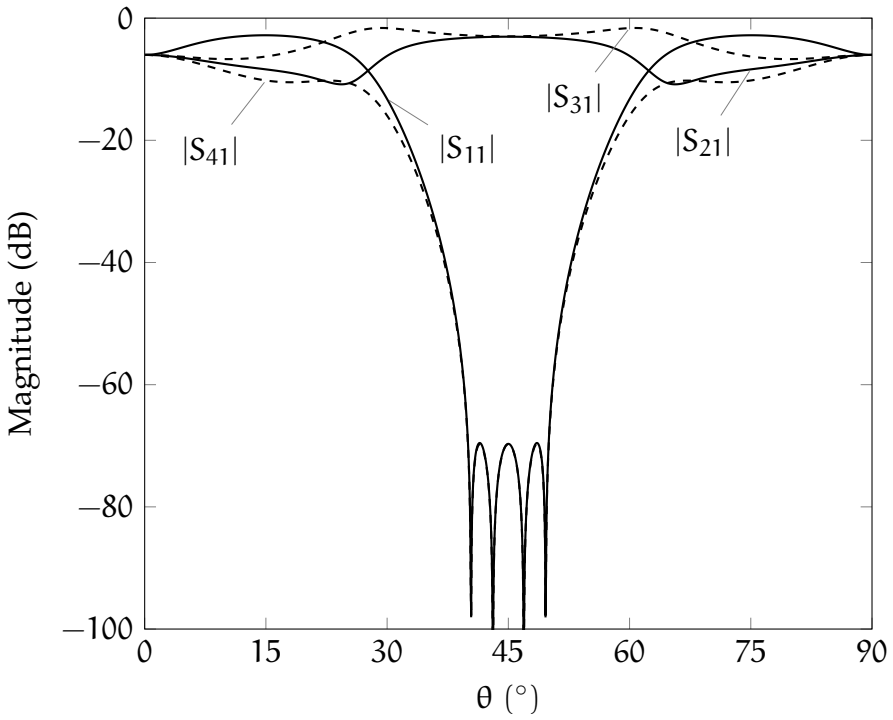

(a) Scattering parameters in magnitude

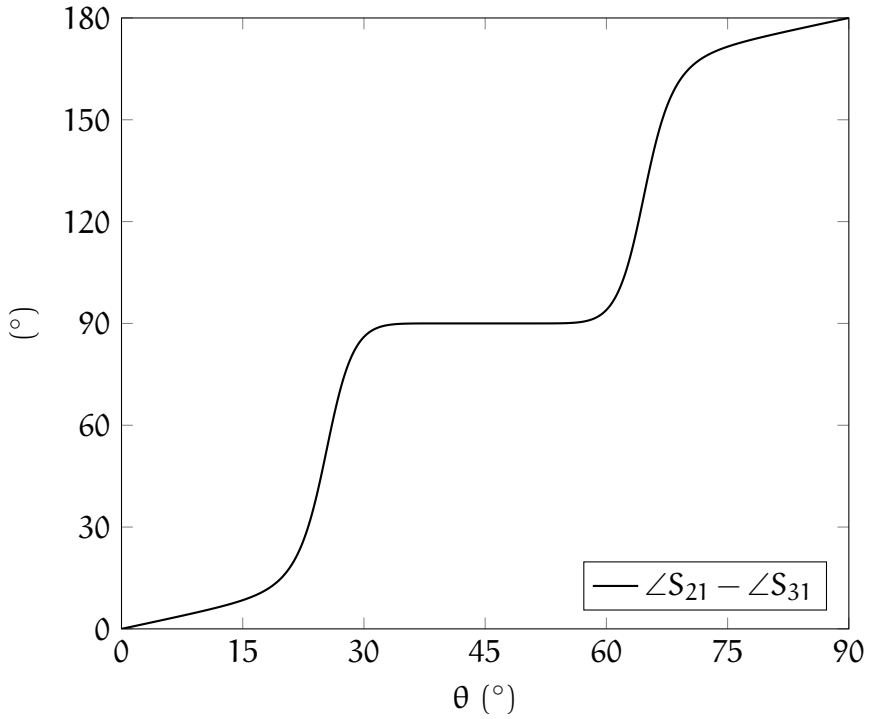

(b) Output ports phase shift

Figure A.8: Responses for the five branches Tchebycheff 3 dB symmetric coupler.

The ripples are constant and at the level of $-70\,\mathrm{dB}$. The coupling at central frequency is $3\,\mathrm{dB}$ equally distributed among the two output ports. As expected the response is strictly symmetric around θ_0.

In order to get this frequency response, proper combinations of parameters n, K, θ_c and R should be found. The final response is influenced by all these parameters. The designer should find a trade-off between the specifications, feasibility of the device and frequency response desired. For example, the number of branches n and the input-output impedance ratio R may be parameters that are fixed by the system. Indeed, the K and θ_c must be chosen to meet the requirements. The process requires optimizations where the parameters are varied until the desired specifications are met. Practical experience shows that with a few attempts it is possible to obtain results that are in accordance with the specifications. The optimization process can be carried out manually and it does not require the help of additional software or complex optimization routines. The main characteristics of the response that can be obtained are:

- the interval in which the S_{11} is below a certain value (ie. the *return loss*)
- mid-band coupling
- desired directivity
- isolation or VSWR
- interval of frequencies where the phase shift at the output ports is flat and equal to $90°$

With respect the maximally flat characteristic, here by increasing the number of branches a sharper response is obtained. This is the major change that the n operates on the S parameters. Then, if prescribed mid-band coupling, bandwidth or return loss are required, it is possible to vary the values of K and θ_c to achieve the desired response.

The phase shift modulus 180° between the output ports 2 and 3 is depicted in Fig. A.8b as a function of the driving variable θ. It shows that with this combinations of parameters, a wide interval around θ_0 results flat and equal to 90°.

B | SYNTHESIS OF MULTI-PORT RESONANT NETWORKS

In this appendix is described a technique for the synthesis of multi-port circuits formed by resonant cavities mutually coupled. The idea of the author is to collect various information from different sources into a single document. The main source used for this study is the PhD thesis of García Lamperez. Two step-by-step examples of synthesis using this technique will also be provided.

The synthesis of resonant microwave circuits is a topic extensively covered in literature. One of the most interesting example are filters: they are 2-port devices which provide frequency selectivity. Here, the focus is on the circuits with an higher number of ports. Among the networks with more than 2 ports are diplexers and multiplexers. The recent synthesis techniques for 2-port passive circuits based on resonators, use a *coupling matrix* that describe the electrical behaviour of the network. Here, a step-by-step synthesis is presented for the case of resonant circuits with more than 2 ports.

The fundamental basis of this theory is represented in the works [40, 41], where the standard technique for the synthesis of 2-port filters based on resonators is explained in detail. In [40], the polynomials for Tchebycheff filters with an arbitrary number of poles and transmission zeros is presented. The synthesis of the coupling matrix is introduced in the appendix of the same paper, and then, it is explained with greater detail in the following work [41]. For the case of filters composed by n resonators, the $n \times n$ or the extended $(n+2) \times (n+2)$ coupling matrices are the standard for the characterization of these resonant circuits [126]. However, when the number of ports is greater than 2, an alternative solution should be found. The technique explained

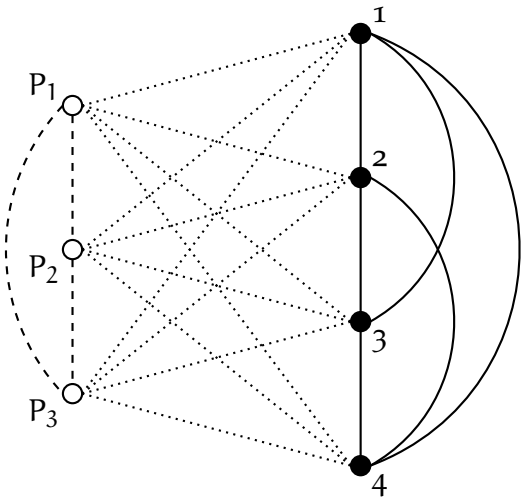

Figure B.1: Schematic of a 3 ports network with 4 resonators

in [43, Ch. 2] is an extension of Cameron's methodology for the case of multi-port networks based on coupled resonators.

In the following sections, the synthesis procedure is explained underlining the most relevant points and proposing references to some basic knowledge needed for the comprehension of the theory. Afterwords, the synthesis of a fully canonical filter and an 8-resonators diplexer are described in order to apply the concepts presented and to demonstrate their validity.

B.1 SYNTHESIS PROCEDURE

B.1.1 Characterisation of the circuit

Before starting the explanation of the synthesis procedure for multi-port circuits, it is important to formalize the generic structure that is going to be generated at the end of the process. The focus of this study is on networks exclusively formed by coupled resonators and external ports. The diagram of Fig. B.1 is a schematic representation of a generic network with $n = 4$ resonators and $p = 3$ ports. In the following, the

number of resonators will be indicated with the letter n while the number of ports with p. In the last figure, the resonators are the black points and are distinguished by the external ports that are represented with empty circles. In order to reference each circuital element of Fig. B.1, the resonators are numbered 1 to 4 and the ports are named P_1, P_2 and P_3. The last essential information that is included in Fig. B.1 are the couplings between the elements of the circuit. Here, all the possible couplings are drown as this circuit is merely a generalization of a given topology. Among them, it is possible to distinguish three types of couplings:

RESONATOR TO RESONATOR the couplings between resonators of the circuits are identified with a continuous line. They represents the electromagnetic interaction between a couple if resonators and may be both direct as well as cross-couplings;

RESONATOR TO PORT this type of couplings are identified with a dotted line and represent the interactions between a resonator and an external port;

PORT TO PORT the couplings between ports complete the generalization of the resonant network and include the information related to the interaction between the external ports of the circuit only. They are represented by the dashed line of Fig. B.1.

The characterisation of a resonant network in term of these three types of couplings is completely general and permits to fully describe the electrical properties of the circuit.

Another important aspect to underline is the fact that it is possible to include the elements of the network of Fig. B.1 into two different categories: *resonant* and *non resonant* nodes. This is a very important aspect that plays a key-role in the next steps of the synthesis. At the beginning of this section, it has been introduced the fact that this network is formed only by coupled resonators and the external ports. The fundamental unit which constitute the network is the *node* and it can be either resonant or a non-resonant one. A schematic of the nodes is proposed in Fig. B.2. These models are a parallel representation of the external ports (Fig. B.2a) and of the resonators

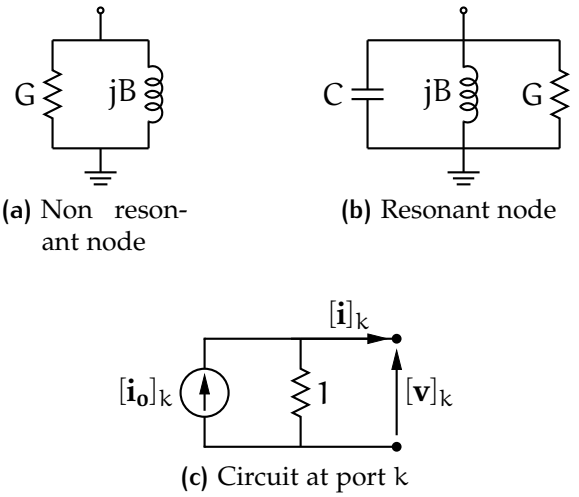

(a) Non resonant node

(b) Resonant node

(c) Circuit at port k

Figure B.2: Circuital model of the nodes of the network

(Fig. B.2b). The reason why a parallel notation has been preferred on a series one, will be clearer in the next sections. At this stage this circuit is considered as the low-pass prototype of the network. The Fig. B.2b is the typical representation of a parallel resonator, while the shunt conductance represents the lossy properties of the circuit. The non resonant node is modelled in a very similar way. It is the representation of a generic external port and the absence of the capacitor underlines the non-ability to resonate of the node. The presence of the inductor represents the mutual inductance between this element and the other nodes of the network. It is very important to put the attention on the fact that the coils in Figs.B.2 are represented by quantity jB: this implies that the elements are *frequency invariant* admittances. Through this inductance, the coupling is possible with the others ports and/or resonators. The conductance G reflects the lossy property of the node. Naturally, it is not compulsory for a node to have the conductance element: for the case of lossless network or a non-lossy element, the value of G of the corresponding node is set to 0.

Particular attention should be given to the generalization of Fig. B.2a. This model is merely an abstraction and extends the concept of a terminal port. The port is connected either on a load or a source circuit like the one shown in Fig. B.2c. We may use the model of a non-resonant node in order to understand the electromagnetic implications of the port and the other objects of the network. Here, the non-resonant

node is represented in this general configuration of a parallel of an inductor and a conductance. For example, the conductance *may* be used to identify the loss associated with an external load. In the following will be shown how to assign the proper value to the conductance of an external port, depending on what the measure is for. In Fig. B.2c the current generator connected to the generic port k, is identified with the kth element of the vector of reference currents $\mathbf{i}_0 \in \mathbb{C}^p$ with a normalized parallel conductance. Thus, the currents and voltages associated to the generic port k are, respectively, $[\mathbf{i}]_k$ and $[\mathbf{v}]_k$.

Finally, the network of Fig. B.1 has 3 ports and 4 resonators but this is only to explain the model of the circuit. In the following, the generic case of p ports and n resonators will be investigated. In this scenario the ports will be labelled as $P_1, P_2, \ldots, P_p$ and resonators with numbers $1, 2, \ldots, n$.

B.1.2 Coupling matrix formulation

One of the most convenient way to completely represent the electrical properties of a resonant circuit is through the use of a *coupling matrix*. This is a powerful tool that is employed both for studying the frequency response of a given circuit, or for the synthesis process. The models of resonant and non-resonant nodes described in the previous paragraph are the perfect candidates for a coupling matrix representation. With reference to the diagram of Fig. B.1, three different coupling matrices may be used to describe the three different types of couplings: $\mathbf{M_n}$, $\mathbf{M_p}$ and $\mathbf{M_{pn}}$. The description of each matrix is given in the following:

- $\mathbf{M_n}$ is the matrix of the internal couplings of the circuit. Each element $[\mathbf{M_n}]_{ij}$ of the matrix, with $i, j \in \{1, \ldots, n\}$, represents the coupling coefficient between 2 resonators, that may be adjacent or not. This matrix is formed by n rows and n columns of real numbers and may be indicated with the notation $\mathbf{M_n} \in \mathbb{R}^{n \times n}$. Referring to the Fig. B.1, this matrix includes the couplings coefficients repres-

ented by the continuous lines of the diagram. If the network is reciprocal, then $\mathbf{M_n}$ is symmetric. The elements on the main diagonal are the auto couplings of each resonator.

- $\mathbf{M_p}$ is the matrix of couplings between the external ports. It is of the type $\mathbf{M_p} \in \mathbb{R}^{p\times p}$. As before, if the network is reciprocal then this matrix is also symmetric and each element corresponds to the dashed line in the diagram of Fig. B.1.

- $\mathbf{M_{pn}}$ is the matrix of the coupling coefficients between the resonators and the external ports. If $p \neq n$ this is not a squared matrix and its dimensions are $\mathbf{M_{pn}} \in \mathbb{R}^{p\times n}$. It may be named as the matrix of the *external quality factors* since there is a close relation to the coupling coefficients of the external ports and resonators and the Q_e. Recalling the schematic of Fig. B.1, this matrix represents the couplings depicted with dotted lines.

It is clear that not all the elements of the matrices $\mathbf{M_n}$, $\mathbf{M_p}$ and $\mathbf{M_{pn}}$ have to be filled. Depending on the topology of the network, only the necessary nodes are mutually coupled, leaving the other elements of the matrices equal to 0.

Now that all the couplings of a resonant network, like the one shown in Fig. B.1, have been formalized into these 3 matrices, it is possible to define a *new* coupling matrix that fully characterizes the circuit. The new general coupling matrix is defined by blocks and built from the previous matrices $\mathbf{M_n}$, $\mathbf{M_p}$ and $\mathbf{M_{pn}}$:

$$\mathbf{M} \triangleq \begin{bmatrix} \mathbf{M_p} & \mathbf{M_{pn}} \\ \mathbf{M_{np}} & \mathbf{M_n} \end{bmatrix} \tag{B.1}$$

where

$$\mathbf{M_{np}} = \mathbf{M_{pn}^T}$$

is the transposed of the matrix $\mathbf{M_{pn}}$. The new matrix is of the form $\mathbf{M} \in \mathbb{R}^{(p+n)\times(p+n)}$ and it gathers all the information related to a multi-port resonant circuit. It extends the conventional representations of 2-port circuits such as the $n \times n$ and the $(n+2) \times (n+2)$ coupling matrices.

If a variable voltage signal is applied to one of the circuits of Fig. B.2, the current flowing in the dipole is expressed as

$$i(s) = v(s) \cdot (sC + jB + G) \tag{B.2}$$

where s is the complex low-pass variable defined as $s = \sigma + j\Omega$. Usually, the specifications of a resonant network are expressed in term of band-pass characteristics. In order to pass from band-pass to the low-pass domain, the following relation is applied:

$$s = j\frac{f_0}{\Delta f}\left(\frac{f}{f_0} - \frac{f_0}{f}\right) \tag{B.3}$$

where f_0 is the central frequency and Δf the operational bandwidth. The concept of eq. (B.2) can be extended to the generic network of Fig. B.1 of p ports. In this case the voltages and currents applied to the external ports may be expressed with the vectorial quantities $\boldsymbol{v}$, $\mathbf{i} \in \mathbb{C}^p$, where the generic element $[\boldsymbol{v}]_k$ and $[\mathbf{i}]_k$ are, respectively, the voltage and current applied to port k. Thus, the circuital analysis of the whole network is carried out through the definition of the *nodal admittance matrix* $\boldsymbol{A} \in \mathbb{C}^{(p+n)\times(p+n)}$:

$$\boldsymbol{A} = [s\mathbf{C} + j\boldsymbol{M} + \mathbf{G}] \tag{B.4}$$

In eq. (B.4) is possible to recognize the extended coupling matrix $\boldsymbol{M}$ defined in eq. (B.1) as well as two new entities $\mathbf{C}$ and $\mathbf{G}$. The last two matrices are the ones of capacitances

and conductances. As described before, it is likely that ports do not have a resonant behaviour, indeed matrix $\mathbf{C} \in \mathbb{R}^{(p+n)\times(p+n)}$ is defined by blocks:

$$\mathbf{C} \triangleq \begin{bmatrix} \mathbf{0_p} & \\ & \mathbf{U_n} \end{bmatrix} \tag{B.5}$$

where the matrix $\mathbf{U_n}$ is the $n \times n$ unity matrix and $\mathbf{0_p}$ is an all-zero $p \times p$ matrix. The capacitance of a resonator shows its resonant characteristic, and its value is 1 in the normalized low-pass frequency [40]. All other elements are set to zero. In a very similar fashion is defined the matrix of the conductances $\mathbf{G} \in \mathbb{R}^{(p+n)\times(p+n)}$:

$$\mathbf{G} \triangleq \begin{bmatrix} \mathbf{G_p} & \\ & \mathbf{G_n} \end{bmatrix} \tag{B.6}$$

The element $\mathbf{G_n}$ is a matrix that describes the lossy characteristic associated to each resonator. It is a function of the *unloaded quality factor* Q_u by the formula:

$$\mathbf{G_n} = \frac{f_0}{\Delta f}\frac{1}{Q_u}\mathbf{U_n} \tag{B.7}$$

where f_0 is the central frequency and Δf the operational bandwidth of the device. In the case of a lossless circuit, $Q_u \to \infty$ and, consequently, $\mathbf{G_n} = \mathbf{0_n}$. The element $\mathbf{G_p}$ is a diagonal matrix and it is related to the losses of the external ports. Here some additional attention should be spent on which quantity is calculated. In fact, ports are external elements and they might be connected either to a load or to a generator like the one of Fig. B.2c. In both cases the losses are associated to the external elements connected in parallel and are not part of the network. For this reason, depending on the context, these contributions should or should not be taken into account. In a different way respect of the internal nodes (resonators), the elements of $\mathbf{G_p}$ are the *reference* conductances of the circuit. When calculating the *S* parameters, for example, they must be considered and $\mathbf{G_p} = \mathbf{U_p}$ with $\mathbf{U_p}$ being the $p \times p$ unitary matrix. On

the contrary, when calculating the Z parameters of the network with open circuits these elements are not considered ($\mathbf{G_p} = \mathbf{0_p}$). Thus, the correct matrix is chosen as the following:

$$\mathbf{G_p} = \begin{cases} \mathbf{U_p} & \text{for S parameters} \\ \mathbf{0_p} & \text{for Z, Y parameters} \end{cases} \tag{B.8}$$

Right now only the case of internal nodes that are not resonating has been neglected. In some microwave circuits may be useful to introduce non-resonant nodes that are internal elements of the network. If this is the case, the model of Fig. B.2a will be employed for such elements. This is because of the absence of the capacitance that permits the resonance. Consequently, the matrix $\mathbf{C}$ is affected as more elements on the diagonal of eq. (B.5) are also 0. The others remains unchanged.

B.1.3 Scattering parameters

The nodal admittance matrix $\mathbf{A}$ of eq. (B.4) contains all the information needed for the circuital analysis of the network. This matrix is formed by $p + n$ rows and columns and describes the behaviour of each node when excited with a given current. In order to study the response of a network described with its general coupling matrix $\mathbf{M}$, a number of sources at the external ports are applied to generate the excitation. Mathematically, this is done by the vectors $\mathbf{v}$ and $\mathbf{i}$ introduced in Fig. B.2c. It is obvious that only the external nodes can receive an excitation by $\mathbf{v}$ and $\mathbf{i}$, since in the internal ones the currents are inducted through the couplings and mutual inductances. This fact may cause a misunderstanding because the vectors $\mathbf{v}$ and $\mathbf{i}$ are of dimensions $\mathbb{C}^p$ and the nodal matrix is of the form $\mathbf{A} \in \mathbb{C}^{(p+n)\times(p+n)}$. This problem is overcome by extending the vector of the driving currents to the form $\mathbf{i_0} \in \mathbb{C}^{p+n}$ where the last

n elements are 0. All the internal impedances are assumed to be normalized to the external ones. Thus, from Fig. B.2c this vectorial relation is valid:

$$\mathbf{i} = \mathbf{i}_0 - \boldsymbol{v} \tag{B.9}$$

The *scattering* parameters matrix is the fundamental tool used in microwave circuits where it is very difficult, or even impossible, to measure the voltages or currents flowing at each port of the network. More convenient, instead, is to measure the ratio incident and reflected amplitude waves through the scattering matrix of the form:

$$\mathbf{S} \triangleq \begin{bmatrix} S_{11} & S_{12} & \cdots & S_{1p} \\ S_{21} & S_{22} & \cdots & S_{2p} \\ \vdots & \vdots & \ddots & \vdots \\ S_{p1} & S_{p2} & \cdots & S_{pp} \end{bmatrix} \in \mathbb{C}^{p\times p} \tag{B.10}$$

The incident and reflected amplitudes are represented, respectively, with vectors $\boldsymbol{v}^+, \boldsymbol{v}^- \in \mathbb{C}^p$ and they are related each other with the relation

$$\boldsymbol{v}^- = \mathbf{S}\boldsymbol{v}^+ \tag{B.11}$$

With reference of Fig. B.2c, assuming that the external impedance is normalized to 1, it can be shown that the relation between the incident and reflected amplitudes with the voltages and currents applied to each port is defined as [30]:

$$\boldsymbol{v}^+ = \frac{1}{2}(\boldsymbol{v} + \mathbf{i}) \tag{B.12a}$$

$$\boldsymbol{v}^- = \frac{1}{2}(\boldsymbol{v} - \mathbf{i}) \tag{B.12b}$$

Thus, combining the eq.s (B.9) and (B.12) it derives that

$$\boldsymbol{v}^{+} = \frac{1}{2}\mathbf{i}_0 \tag{B.13a}$$

$$\boldsymbol{v}^{-} = \boldsymbol{v} - \frac{1}{2}\mathbf{i}_0 \tag{B.13b}$$

In our model the generator currents are represented by vectors of zeros with only the reference component set to unity. Thus, the quantity $\mathbf{i}_0 = \boldsymbol{\delta}_l$ is the usual delta of Kronecker. Consequently, the definition of each element of eq. (B.10) can be rewritten together with the combination of eq.s (B.11) and (B.13) as:

$$[\boldsymbol{S}]_{kl} = \frac{-\frac{1}{2}\delta_l + [\boldsymbol{v}]_k}{\frac{1}{2}\delta_l} = -\delta_l + 2[\boldsymbol{v}]_k \qquad k, l \in \{1, \dots, p\} \tag{B.14}$$

The last expression is then rewritten as a function of the nodal admittance matrix, whose definition was given in eq. (B.2)

$$\boldsymbol{v} = \mathbf{A}^{-1}\mathbf{i}_0$$

knowing that the term $\mathbf{i}_0 = \delta_l$ affects the expression simply by selecting the row l from the inverse of the admittance matrix:

$$[\boldsymbol{v}]_k = \mathbf{A}^{-1}|_{\text{row } k}\mathbf{i}_0 = [\boldsymbol{A}^{-1}]_{kl} \tag{B.15}$$

Finally, combining eq.s (B.14) and (B.15) it derives that:

$$[\boldsymbol{S}]_{kl} = \begin{cases} -1 + 2[\mathbf{A}^{-1}]_{kk} & \text{for } l = k \\ 2[\boldsymbol{A}^{-1}]_{kl} & \text{for } l \neq k \end{cases} \tag{B.16}$$

with $k, l \in \{1, \dots, p\}$. In a more compact way this notation is also valid:

$$\boldsymbol{S} = -\mathbf{U}_p + 2\boldsymbol{A}_p^{-1} \tag{B.17}$$

where the notation $\mathbf{A}_p^{-1}$ represents the sub-matrix of $\mathbf{A}^{-1}$ formed by the first p rows and columns. It is clear that in order to evaluate the scattering parameters the $\mathbf{A}$ matrix must be calculated. In the following section is described in detail this process.

B.1.4 Analytical synthesis of multi-port circuits

Right now, an introduction of the generalization of multi-port circuit based on coupled resonators has been presented, and in the following an analytical procedure to coupling matrix synthesis will be explained. The demonstration of the algorithm consists in two parts:

1. generation of the admittance parameters in shorted circuit,
2. partial fraction expansion of the admittance matrix.

In the previous sections a parallel model has been chosen for the nodes constituting the circuit. The explanation of this choice resides in the fact that the algorithm of synthesis is based on an admittance matrix representation. In a multi-port network the relation between the currents and voltages applied to external ports is expressed by the well known formula

$$\mathbf{i}_p = \mathbf{Y}\mathbf{v}_p \tag{B.18}$$

As was introduced before, the current and voltage are vectors of $p + n$ rows. Besides, the admittance matrix has dimensions $p \times p$ and only the first p elements of the vectors $\mathbf{v}$ and $\mathbf{i}$ are considered when dealing with this operator. Thus, it is possible to express these vectors as a part applied to external ports, and another one applied to internal resonators

$$\mathbf{i} = \begin{bmatrix} \mathbf{i}_p \\ \mathbf{i}_n \end{bmatrix} \qquad \mathbf{v} = \begin{bmatrix} \mathbf{v}_p \\ \mathbf{v}_n \end{bmatrix}$$

The last two vectors are the quantities involved in the synthesis and the object of the following procedure is to use them in order to derive the $\mathbf{Y}$ matrix of eq. (B.18).

For a lossless network, the conductance matrix is $\mathbf{G} = \mathbf{0}_p$ and the nodal admittance matrix reduced to the form $\mathbf{A} = s\mathbf{C} + j\mathbf{M}$ as from eq. (B.4). Because of $\mathbf{M}$ was defined by blocks, even the matrix $\mathbf{A}$ may be defined in a similar fashion:

$$\mathbf{A} \triangleq \begin{bmatrix} \mathbf{A}_p & \mathbf{A}_{pn} \\ \mathbf{A}_{np} & \mathbf{A}_n \end{bmatrix} \tag{B.19}$$

The complete relation between the currents and voltages applied to both internal and external nodes is given by the system

$$\begin{cases} \mathbf{i}_p = \mathbf{A}_p \mathbf{v}_p + \mathbf{A}_{pn} \mathbf{v}_n \\ \mathbf{i}_n = \mathbf{A}_{np} \mathbf{v}_p + \mathbf{A}_n \mathbf{v}_n \end{cases} \tag{B.20}$$

No generators are directly connected to the internal nodes, thus $\mathbf{i}_n = 0$. The second equation of eq. (B.20) is substituted in the first one in order to determine the expression of the $\mathbf{Y}$ matrix of the form of eq. (B.18):

$$\mathbf{Y} = \mathbf{A}_p - \mathbf{A}_{pn} \mathbf{A}_n^{-1} \mathbf{A}_{np} \tag{B.21}$$

The object of the next steps is to calculate every term of eq. (B.21) in order to find the solution of the shorted circuit admittance matrix.

Now, let consider the coupling matrix between internal nodes $\mathbf{M}_n$. This is a symmetric real matrix: its eigenvalues are $\{-\lambda_k\}_{k\in\{1,\dots,n\}}$ and eigenvectors are $\{\xi_k \in \mathbb{R}^n\}_{k\in\{1,\dots,n\}}$. For the purpose of simplification of the next calculation, here the eigenvalues are expressed with the opposite sign. In linear algebra, the *spectrum* is defined as the set of distinct eigenvalues of a matrix [127]. The *spectral decomposition* is an

operation that recasts the matrix in terms of its eigenvalues and eigenvectors. Thus, the matrix of the internal coupling may be expressed as:

$$\mathbf{M_n} = -\sum_{k=1}^{n} \lambda_k \boldsymbol{\xi}_k \boldsymbol{\xi}_k^T \tag{B.22}$$

The eigenvectors $\boldsymbol{\xi}_k$ are orthogonal, this means that

$$\boldsymbol{\xi}_k^T \boldsymbol{\xi}_l = \delta_{kl} \tag{B.23}$$

$$\sum_{k=1}^{n} \boldsymbol{\xi}_k \boldsymbol{\xi}_k^T = \mathbf{U_n} \tag{B.24}$$

where δ is the delta of Kronecker. At this point it is possible to combine the eqs. (B.24) and (B.22) in order to relate the nodal admittance matrix $\mathbf{A_n}$ with the eigenvalues and eigenvectors of the matrix $\mathbf{M_n}$:

$$\begin{aligned} \mathbf{A_n} &= s\mathbf{U_n} + j\mathbf{M_n} \\ &= s\sum_{k=1}^{n} \boldsymbol{\xi}_k \boldsymbol{\xi}_k^T - j\sum_{k=1}^{n} \lambda_k \boldsymbol{\xi}_k \boldsymbol{\xi}_k^T \\ &= \sum_{k=1}^{n} (s - j\lambda_k) \boldsymbol{\xi}_k \boldsymbol{\xi}_k^T \end{aligned} \tag{B.25}$$

From the eq. (B.25) can be derived the inverse of the matrix $\mathbf{A_n}$:

$$\mathbf{A_n^{-1}} = \sum_{k=1}^{n} \frac{\boldsymbol{\xi}_k \boldsymbol{\xi}_k^T}{s - j\lambda_k} \tag{B.26}$$

where the property of eq. (B.23) has been applied to the numerator. The denominator of this equation contains the *poles* of the function. It is also important to note that the eigenvalues of matrix $\mathbf{M_n}$ had been chosen with the negative sign in order to build

the term $s - j\lambda_k$. At this point there are all the information required to relate the $\mathbf{Y}$ matrix to the blocks of $\mathbf{M}$ with the following relations valid for a lossless network:

$$\mathbf{A_p} = j\mathbf{M_p} \tag{B.27a}$$

$$\mathbf{A_{pn}} = j\mathbf{M_{pn}} \tag{B.27b}$$

$$\mathbf{A_{np}} = j\mathbf{M_{np}} = j\mathbf{M_{pn}^T} \tag{B.27c}$$

Thus, the eq. (B.21) may be rewritten by combinations of eqs. (B.26) and (B.27) as:

$$\mathbf{Y}(s) = j\mathbf{M_p} + \mathbf{M_{pn}} \left(\sum_{k=1}^{n} \frac{\boldsymbol{\xi}_k \boldsymbol{\xi}_k^T}{s - j\lambda_k} \right) \mathbf{M_{pn}^T} \tag{B.28}$$

The last equation may be simplified with the introduction of the vector:

$$\boldsymbol{\gamma}_k \triangleq \mathbf{M_{pn}} \boldsymbol{\xi}_k \tag{B.29}$$

with $k \in \{1, \ldots, n\}$ and this new vectorial quantity has dimensions $\boldsymbol{\gamma}_k \in \mathbb{R}^p$. Indeed, the expression of the admittance matrix can be formalized with the more compact relation:

$$\mathbf{Y}(s) = j\mathbf{M_p} + \sum_{k=1}^{n} \frac{\boldsymbol{\gamma}_k \boldsymbol{\gamma}_k^T}{s - j\lambda_k} \tag{B.30}$$

With the last formula, the derivation of the admittance parameters in term of the general coupling matrix of the circuit is complete. It is very important to underline that matrix $\mathbf{Y}(s)$ has its elements expressed as a ratio between two polynomial in s variable: a numerator and a common denominator. This property is shown by the denominator of the sum of eq. (B.30) where the poles are the *real* eigenvalues of the

internal coupling matrix. The generic element of the admittance matrix is of the form $[\mathbf{Y}]_{ij}(s) = n_{ij}(s)/y_d(s)$. This leads to the following notation:

$$\mathbf{Y}(s) = \frac{1}{y_d(s)} \begin{bmatrix} n_{11}(s) & n_{12}(s) & \cdots & n_{1p}(s) \\ n_{21}(s) & n_{22}(s) & \cdots & n_{2p}(s) \\ \vdots & \vdots & \ddots & \vdots \\ n_{p1}(s) & n_{p2}(s) & \cdots & n_{pp}(s) \end{bmatrix} \tag{B.31}$$

From eq. (B.30) is also easy to show that the common denominator is given by the product of the eigenvalues λ_k, thus it may be expressed as:

$$y_d(s) = \prod_{k=1}^{n} (s - j\lambda_k) \tag{B.32}$$

The advantage of using the admittance matrix in shorted circuit, is that it is possible to exploit its *partial fraction expansion* to relate the elements of $\mathbf{M}$ to the analytical characteristics of polynomials of $\mathbf{Y}$. Let consider the ratio between polynomial $f(x)/g(x)$. Its partial fraction expansion is given by the well known formula

$$\frac{f(x)}{g(x)} = \frac{r_1}{x - x_1} + \frac{r_2}{x - x_2} + \cdots + \frac{r_m}{x - x_m} + k_0$$

where k_0 is a direct term, $x_1, x_2, \ldots, x_m$ are the m poles of the function, and $r_1, r_2, \ldots, r_m$ are the residues. This concept is directly applied to the $\mathbf{Y}$ matrix of eq. (B.31) with the following formulation:

$$\mathbf{Y}(s) = \mathbf{Y}^{(\infty)} + \sum_{k=1}^{n} \frac{\Gamma_k}{s - j\lambda_k} \tag{B.33}$$

In the definition of eq. (B.33) there are three key-elements:

- $\mathbf{Y}^{(\infty)}$ is a constant element representing the response of the admittance matrix at infinity frequency. This matrix has p rows and columns.
- λ_k is the kth pole of the common denominator $y_d(s)$

- $\mathbf{\Gamma}_k \in \mathbb{R}^{p\times p}$ is the matrix of the *residues* associated to pole λ_k.

The formulation of the elements at infinite frequency is given by the limit:

$$\mathbf{Y}^{(\infty)} = \lim_{s\to j\infty} \mathbf{Y}(s) \tag{B.34}$$

Since the the admittance matrix is formed by ratio of polynomials with a common denominator, the poles λ_k are the same for all the elements of the matrix. Thus, there is a residue of every element of matrix $\mathbf{Y}$ associated to each poles of the function. The general notation of the matrix of residues associated to kth pole is:

$$\mathbf{\Gamma}_k = \begin{bmatrix} r_{11,k} & r_{12,k} & \cdots & r_{1p,k} \\ r_{21,k} & r_{22,k} & \cdots & r_{2p,k} \\ \vdots & \vdots & \ddots & \vdots \\ r_{p1,k} & r_{p2,k} & \cdots & r_{pp,k} \end{bmatrix} \tag{B.35}$$

It is clear that, upon the definition of eq. (B.35), the particular single element of the admittance matrix is:

$$[\mathbf{Y}]_{ij}(s) = [\mathbf{Y}^{(\infty)}]_{ij} + \sum_{k=1}^{n} \frac{r_{ij,k}}{s - j\lambda_k} \tag{B.36}$$

that is the partial fraction expansion of the ratio of polynomials $n_{ij}(s)/y_d(s)$.

Given a function $f\colon \mathbb{C}\setminus\{x_0, x_1, \ldots, x_d\} \to \mathbb{C}$ (defined on an open domain D except a set of isolated points $x_0, x_1, \ldots, x_d$) and a close curve γ contained in D and containing one isolated discontinuity $x_s \in \{x_0, x_1, \ldots, x_d\}$, the *residue* of function $f(x)$ in the point $x = x_s$ is defined as:

$$\mathrm{Res}(f, x_s) \equiv \frac{1}{2\pi j} \oint_\gamma f(x)\,dx \tag{B.37}$$

The value of the residue of order n is calculated with the help of the Cauchy formula, derived from the theorem of residues:

$$\mathrm{Res}(f, x_s) = \frac{1}{(n-1)!} \lim_{x \to x_s} \left\{ \frac{\partial^{n-1}}{\partial x^{n-1}} \left[(x - x_s)^n \cdot f(x) \right] \right\} \tag{B.38}$$

In our case, the rational functions constituting the matrix $\mathbf{Y}$ have all *simple* poles. The formula eq. (B.38) for $n = 1$ (case of a simple pole) reduces to:

$$\mathrm{Res}(f, x_s) = \lim_{x \to x_s} (x - x_s) \cdot f(x) \tag{B.39}$$

In the following, the eq. (B.39) will be used to calculate the elements of matrix $\mathbf{\Gamma}_k$ of eq. (B.35).

At this point there is all the information and tools to extrapolate the values of the coupling matrix of the circuit starting from the admittance matrix $\mathbf{Y}(s)$. The first thing to consider are the similarities between the expressions of eq. (B.30) and the one of partial fraction expansion of eq. (B.33). It is immediate to observe that the following relations:

$$\mathbf{Y}^{(\infty)} = j\mathbf{M_p} \tag{B.40}$$

$$\mathbf{\Gamma}_k = \boldsymbol{\gamma}_k \boldsymbol{\gamma}_k^T \tag{B.41}$$

Before proceeding, it is valuable to make some consideration over the matrix of residues and its relation to the vector $\boldsymbol{\gamma}_k$:

- it is important to remind that the vectors $\boldsymbol{\gamma}_k \in \mathbb{R}^p$ are all formed of real numbers, indeed also the elements $r_{ij,k}$ are real.
- The product of vectors $\boldsymbol{\gamma}_k$ and $\boldsymbol{\gamma}_k^T$ causes the residues to have the form

$$r_{ij,k} = [\boldsymbol{\gamma}_k]_i \cdot [\boldsymbol{\gamma}_k]_j \tag{B.42}$$

- The elements on the main diagonal of $\mathbf{\Gamma}_k$ are non-negative. This can be easily shown since the element

$$r_{ii,k} = [\boldsymbol{\gamma}_k]_i^2 \geqslant 0 \tag{B.43}$$

- The square of the residues off the main diagonal of $\mathbf{\Gamma}$ follows this rule:

$$r_{ij,k}^2 = \left([\boldsymbol{\gamma}_k]_i \cdot [\boldsymbol{\gamma}_k]_j\right)^2 = r_{ii,k} \cdot r_{jj,k} \tag{B.44}$$

The study of the partial fraction expansion of $\mathbf{Y}$ has permitted to analytically relate its poles to the eigenvalues of $\mathbf{M_n}$, its residues to the couplings between resonators and ports (matrix $\mathbf{M_{pn}}$ and its response at infinite frequency with the couplings between external ports of the matrix $\mathbf{M_p}$. This achievement is at the base for the analytical synthesis of complex networks starting from the admittance polynomials of the desired frequency response.

B.1.5 Transversal networks

In the last section were derived the analytical formulas that relate the polynomials constituting the admittance matrix to the various blocks of the general coupling matrix of the resonant circuit. Even if the simple mathematical expressions seem to solve the great complexity of multi-port synthesis, there are some additional aspects to consider. First of all the coupling matrix strictly depends on the topology of the network and it might be difficult to find the relation between γ_k, $\mathbf{\Gamma}_k$, $\mathbf{Y}^{(\infty)}$ and the coupling coefficients of a circuits with a given structure. The main aspect to consider is that the response of a circuit mainly depends on the eigenvalues and eigenvectors of its coupling matrix. Thus, there are several different configurations, and consequently different coupling coefficients, that give identical frequency responses. In this section

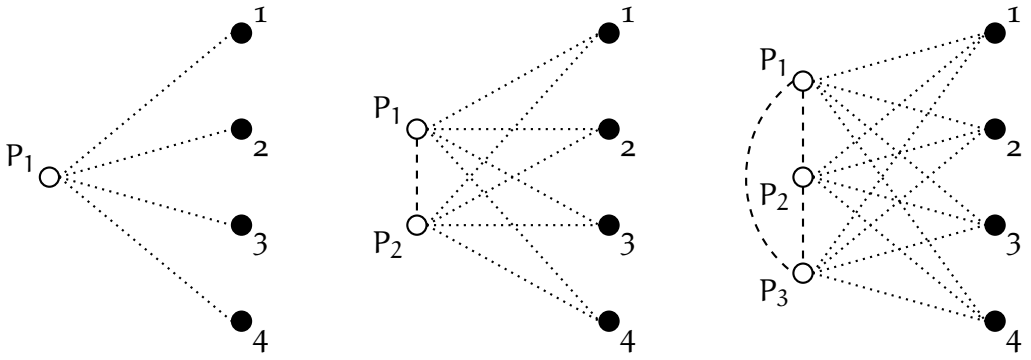

(a) $p = 1, n = 4$ **(b)** $p = 2, n = 4$ **(c)** $p = 3, n = 4$

Figure B.3: Examples of transversal networks. The empty circles represent the external ports while the black points are the internal resonators. All the possible couplings are shown.

	P_1	P_2	P_3	1	2	3	4
P_1		×	×	×	×	×	×
P_2	×		×	×	×	×	×
P_3	×	×		×	×	×	×
1	×	×	×	×			
2	×	×	×		×		
3	×	×	×			×	
4	×	×	×				×

Figure B.4: Block matrix $\mathbf{M}$ of the transversal network $p = 3, n = 4$

a possible solution to this problem will be presented through the use of a *transversal* network.

A transversal network is a circuit with these fundamental characteristics:

1. there are no couplings between resonators,
2. each resonator may be coupled with the external ports and itself,
3. the external ports can be coupled each other .

Three examples of transversal networks are shown in Fig. B.3, all having 4 resonators. In these pictures are shown all the possible couplings for this type of circuits. In the figure, a dashed line has been used to indicate the mutual coupling between pair of external ports, while a dotted line is for the couplings between resonators and

ports. As stated in the definition of transversal network, there are no couplings (and consequently no lines) between internal resonators. The general coupling matrix of a transversal network reflects its topology and is populated accordingly. In Fig. B.4 is a representation of $\mathbf{M}$ defined by blocks reflecting the structure of Fig. B.3c. In this representation it is possible to recognize the three different portions that correspond to sub-matrices $\mathbf{M_p}$, $\mathbf{M_n}$ and $\mathbf{M_{pn}}$ through the continuous line that bounds them. On the top and on the left sides of the matrix are the labels referring to the elements of the network. The labels $P_1, P_2, \ldots, P_p$ are the numbered external ports, while the simple numbers $1, 2, \ldots, n$ are the internal resonators. In Fig. B.4 a cross is depicted in the box corresponding to the couplings of Fig. B.3c. Naturally, in this representation are shown all possible couplings between elements of the circuit and, consequently, there are all the possible elements in the coupling matrix.

At this point some interesting properties of the transversal networks are investigated and it will be clear how they can help the synthesis procedure. The main consequence of the absence of mutual couplings between pairs of internal resonators, is that $\mathbf{M_n}$ is a *diagonal* matrix. This leads to these two fundamental properties:

1. the eigenvalues of such a matrix are the elements of the main diagonal,
2. there are n eigenvectors corresponding to the delta of Kronecker.

Put these concepts in mathematical notation:

$$\mathbf{M_n} = \begin{bmatrix} -\lambda_1 & & & \\ & -\lambda_2 & & \\ & & \ddots & \\ & & & -\lambda_n \end{bmatrix} \tag{B.45}$$

$$\xi_k = \delta_k \qquad k \in \{1, \ldots, n\} \tag{B.46}$$

The conditions of eq.s (B.45) (B.46) simplify the the calculations when a suitable coupling matrix that gives the frequency response of matrix $\mathbf{Y}$ is searched. It is immediate

to see from eq. (B.45) that the roots of common denominator $y_d(s)$ are the poles of the transfer function and, consequently, the elements of the main diagonal of $\mathbf{M_n}$. In eq. (B.45) the signs of the eigenvalues has been put the opposite to be in compliance with the notation of eq. (B.30).

An additional important property of the transversal networks is given by the condition of eq. (B.46) because, recalling eq. (B.29), it forces the vector to be equal to the kth column of matrix $\mathbf{M_{pn}}$:

$$\boldsymbol{\gamma}_k = [\mathbf{M_{pn}}]_{col.k} \tag{B.47}$$

The direct consequence of eq. (B.47) is on the matrix of residues that takes the form

$$\begin{aligned}\boldsymbol{\Gamma}_k &= \boldsymbol{\gamma}_k \boldsymbol{\gamma}_k^T = [\mathbf{M_{pn}}]_{col.k} \cdot [\mathbf{M_{pn}}]_{col.k}^T \\ &= \begin{bmatrix} [\mathbf{M_{pn}}]_{1k}^2 & [\mathbf{M_{pn}}]_{1k}[\mathbf{M_{pn}}]_{2k} & \cdots & [\mathbf{M_{pn}}]_{1k}[\mathbf{M_{pn}}]_{pk} \\ [\mathbf{M_{pn}}]_{2k}[\mathbf{M_{pn}}]_{1k} & [\mathbf{M_{pn}}]_{2k}^2 & \cdots & [\mathbf{M_{pn}}]_{2k}[\mathbf{M_{pn}}]_{pk} \\ \vdots & \vdots & \ddots & \vdots \\ [\mathbf{M_{pn}}]_{pk}[\mathbf{M_{pn}}]_{1k} & [\mathbf{M_{pn}}]_{pk}[\mathbf{M_{pn}}]_{2k} & \cdots & [\mathbf{M_{pn}}]_{pk}^2 \end{bmatrix}\end{aligned} \tag{B.48}$$

The last equation is of great importance because is a direct relation between the elements of the external couplings of the matrix $\mathbf{M_{pn}}$ and the residues of the poles. The last step is to find a relation between these two entities expressed in a closed formula. It is immediate to note that the elements of the main diagonal of eq. (B.48) are linked to the same residues:

$$|[\mathbf{M_{pn}}]_{ik}| = \sqrt{r_{ii,k}} \tag{B.49}$$

However, this formulation is not sufficient to solve the problem since it produces a system with more equations than unknown variables. In fact, there exists a solution

if the condition of eq. (B.44) is satisfied. Let consider the *sign* function defined $\forall x \in \mathbb{R}$ as

$$\operatorname{sgn}(x) \equiv \begin{cases} -1 & x < 0 \\ 0 & x = 0 \\ +1 & x > 0 \end{cases}$$

or in the alternative version not valid in the origin ($x \neq 0$)

$$\operatorname{sgn}(x) = \frac{x}{|x|} \tag{B.50}$$

From eq. (B.48) is derived the obvious relation

$$\operatorname{sgn}(r_{ij,k}) = \operatorname{sgn}([\mathbf{M_{pn}}]_{ik}) \cdot \operatorname{sgn}([\mathbf{M_{pn}}]_{jk}) \tag{B.51}$$

If it is assumed that the sign of $[\mathbf{M_{pn}}]_{ik}$ is positive, the last relation degenerates into

$$\operatorname{sgn}([\mathbf{M_{pn}}]_{jk}) = \operatorname{sgn}(r_{ij,k}) \tag{B.52}$$

and, consequently, it is valid the following:

$$[\mathbf{M_{pn}}]_{jk} = \operatorname{sgn}([\mathbf{M_{pn}}]_{jk}) \cdot \left|[\mathbf{M_{pn}}]_{jk}\right| \tag{B.53}$$

By substituting the eq. (B.49) into the (B.53) is obtained:

$$[\mathbf{M_{pn}}]_{jk} = \operatorname{sgn}([\mathbf{M_{pn}}]_{jk}) \sqrt{r_{jj,k}} \tag{B.54}$$

and, recalling the alternative definition of sign function of eq. (B.50) and the assumption made with eq. (B.52)

$$[\mathbf{M_{pn}}]_{jk} = \frac{r_{ij,k}}{|r_{ij,k}|}\sqrt{r_{jj,k}} \tag{B.55}$$

Finally, the condition of eq. (B.44) is applied to the relation of eq. (B.55) giving the closed formula that relates the generic element on the matrix of external couplings with the residues associated to pole k:

$$[\mathbf{M_{pn}}]_{jk} = \frac{r_{ij,k}}{\sqrt{r_{ii,k}}} \tag{B.56}$$

with $i, j \in \{1, \ldots, p\}$ and $k \in \{1, \ldots, n\}$.

B.1.6 Matrix transformations

The transversal network discussed in the previous section is a powerful abstraction used to easily derive the relations between the coupling matrix and the admittance parameters of the circuit. With the formulas presented, an analytical procedure to get the coupling coefficients can be followed starting from the admittance matrix. It is well known that the frequency response expressed in terms of S parameters, can be directly transformed into the matrix Y and, then, a corresponding transversal network may be obtained. However, a circuit where there are no couplings between resonators and, potentially, each resonator is coupled with all the ports, may not be feasible or very difficult to construct. In addition, the designer would calculate the numerical values of coupling coefficients of a network with a *given* topology and frequency response. It is clear that the combinations allowed by the transversal configuration impose unacceptable restrictions to the design. Thus, an alternative solution shall be found to overcome the problem while keeping the procedure as simple as possible.

The important property that is exploited in the following, is that two different coupling matrices with same eigenvalues, rank and determinant have same frequency response. This principle is also known as *similarity* between matrices [40]. The main idea is to operate a sequence of transformations to the coupling matrix obtained in order to modify its structure into the one of the topology of the target circuit. The coupling matrix $\mathbf{M}$ calculated with the previous methodology for the transversal networks, is transformed in a new one, say $\mathbf{M'}$, that has same frequency response but that is compliant with the final topology of the circuit. The method discussed here to transform $\mathbf{M}$, is the *Jacobi transformation* for symmetric matrices:

$$\mathbf{M'} = \mathbf{R}(i,j,\phi)\mathbf{M}\mathbf{R}^{T}(i,j,\phi) \tag{B.57}$$

The rotation operator $\mathbf{R} \in \mathbb{R}^{(p+n)\times(p+n)}$ is an orthogonal matrix defined as follows:

$$\mathbf{R}(i,j,\phi) = \begin{bmatrix} 1 & & & & & & \\ & \ddots & & & & & \\ & & \cos\phi & \cdots & -\sin\phi & & \\ & & \vdots & 1 & \vdots & & \\ & & \sin\phi & \cdots & \cos\phi & & \\ & & & & & \ddots & \\ & & & & & & 1 \end{bmatrix} \tag{B.58}$$

The rotation term $\mathbf{R}$ is formed from an unitary matrix except for the four trigonometric quantities $[\mathbf{R}]_{ii} = [\mathbf{R}]_{jj} = \cos\phi$ and $[\mathbf{R}]_{ji} = -[\mathbf{R}]_{ij} = \sin\phi$, where i and j are the *pivot* parameters $i, j \in \{1, \ldots, p+n\}$ and ϕ is the angle of rotation. This matrix has the characteristic to be orthogonal so as $\mathbf{R}^{-1} = \mathbf{R}^{T}$. Such a transformation can also be called as pivot [i, j] of angle ϕ.

The application of eq. (B.57) implies that the transformed matrix has the elements on row and columns i, j changed, while all the other elements remain the same. The following equations show how the new terms are affected:

$$[\mathbf{M}']_{ik} = \cos\phi[\mathbf{M}]_{ik} - \sin\phi[\mathbf{M}]_{jk} \tag{B.59a}$$

$$[\mathbf{M}']_{jk} = \cos\phi[\mathbf{M}]_{jk} + \sin\phi[\mathbf{M}]_{ik} \tag{B.59b}$$

$$[\mathbf{M}']_{ki} = \cos\phi[\mathbf{M}]_{ki} - \sin\phi[\mathbf{M}]_{kj} \tag{B.59c}$$

$$[\mathbf{M}']_{kj} = \cos\phi[\mathbf{M}]_{kj} + \sin\phi[\mathbf{M}]_{ki} \tag{B.59d}$$

for $k \in \{1, \ldots, p+n\} \setminus \{i, j\}$. It is interesting to note that depending where is positioned the element to be annihilated, one of the eqs. (B.59) may be more suitable than others. In particular, if the element is in row i the eq. (B.59a) is likely to be used, if it is on row j is used eq. (B.59b). By symmetry is easy to show that for the element of column i the eq. (B.59c) is used, as well as eq. (B.59d) is for the element of column j. By choosing a proper value of ϕ is also possible to annihilate the desired element $[\mathbf{M}']_{ij}$ of the rotated matrix. Indeed, the formula eq. (B.57) can be used for a series of transformation in which at each step is annihilated a particular element of the coupling matrix. This procedure will be used to transform the not practical transversal matrix to the final topology of the circuit. Depending on the position of the element to be annihilated, the proper equation from the eqs. (B.59) is chosen and the rotation angle ϕ calculated accordingly.

The eq.s (B.59) apply to all the elements of the coupling matrix except the cross points of the pivoting rows and columns. These elements are governed by the following relations:

$$[\mathbf{M}']_{ii} = \cos^2\theta[\mathbf{M}]_{ii} + \sin^2\theta[\mathbf{M}]_{jj} - 2\sin\theta\cos\theta[\mathbf{M}]_{ij} \tag{B.60a}$$

$$[\mathbf{M}']_{jj} = \sin^2\theta[\mathbf{M}]_{ii} + \cos^2\theta[\mathbf{M}]_{jj} + 2\sin\theta\cos\theta[\mathbf{M}]_{ij} \tag{B.60b}$$

$$[\mathbf{M}']_{ij} = (\cos^2\theta - \sin^2\theta)[\mathbf{M}]_{ij} + \sin\theta\cos\theta([\mathbf{M}]_{ii} - [\mathbf{M}]_{jj}) \tag{B.60c}$$

In last instance, it is important to consider the following properties when choosing the pivots parameters i, j and the rotation angle ϕ:

- the elements that are not on rows and columns i, j are not affected by the transformation. The elements on rows and columns i, j change with the equations in (B.59);
- if there are two elements on rows and columns i, j that are zero before the transformation, than they remain zero after;
- when a particular non-zero element $[\mathbf{M'}]_{ij}$ is annihilated with eq. (B.57), also the element $[\mathbf{M'}]_{ji}$ is set to zero;
- if two series of transformations are applied in different order, the resulting matrices are not equal;
- once the element $[\mathbf{M}]_{ji}$ to be annihilated has been chosen, the right equation between the (B.59) is to be selected as well as the the pivot i, j. The rotation angle ϕ is calculated from the reverse equation of (B.59) considering the proper k value.

The final coupling matrix will produce the same frequency response of the initial one of the transversal network. Indeed, the new matrix can be in line with the specifications of the topology of the network solving the feasibility problems of the transversal configuration.

B.1.7 Low-pass to band-pass transformation

Following the synthesis procedure till this point it should be clear that the computed coupling matrix $\mathbf{M}$ refers to the normalized low-pass prototype of the circuit. In order to obtain the corresponding band-pass model the coupling matrix is re-scaled. The frequency variable is also to be transformed from the low-pass band to the band-pass

edges. The key variables are the band extremes f_1 and f_2 and the central frequency f_0 that, by inversion of the eq. (B.3), permit to define the *bandwidth* (Δf) and the *fractional bandwidth* (w):

$$\Delta f = f_2 - f_1$$
$$w = \frac{f_2 - f_1}{f_0} = \frac{\Delta f}{f_0}$$

The coupling matrix $\mathbf{M}$ calculated in the previous sections is to be de-normalized in order to have it in suitable form for the 3D implementation and manufacturing of the device. It is often useful to have the de-normalized parameters such as the external quality factors Q_{em} between the external port e and the internal resonator m, the coupling coefficient k_{ij} between two internal resonators i and j and, finally, the resonant frequency $f_{ris,q}$ of each resonator q. These parameters are directly calculated from the matrix $\mathbf{M}$ with the following relations [34, 49]:

$$Q_{em} = \frac{f_0}{\Delta f} \frac{1}{[\mathbf{M_{pn}}]^2_{em}} = \frac{1}{w[\mathbf{M_{pn}}]^2_{em}} \tag{B.61a}$$

$$k_{ij} = \frac{\Delta f}{f_0}[\mathbf{M_n}]_{ij} = w[\mathbf{M_n}]_{ij} \tag{B.61b}$$

$$f_{ris,q} = f_0 \left[\sqrt{1 + \left(w\frac{[\mathbf{M_n}]_{qq}}{2} \right)^2} - \left(w\frac{[\mathbf{M_n}]_{qq}}{2} \right) \right] \tag{B.61c}$$

with $e \in \{1, \ldots, p\}$ and $m, i, j, q \in \{1, \ldots, n\}$.

B.1.8 Steps of the synthesis

All the theoretical details have been already included in the various sections right now, however it might be useful to summarize the entire process and to focus only on the relevant formulas needed for the synthesis. The starting point that is assumed here is that the designer has clear what kind of topology is going to be synthesised

and the desired frequency response in terms of S parameters. Thus, the synthesis procedure may follow these points:

1. formulation of the S parameters in term of rational polynomials between numerators and a common denominator. The independent variable of these polynomials is the normalized complex low-pass frequency $s = \sigma + j\Omega$. If band-pass specifications are given, the normalized frequency is obtained through the formula of eq. (B.3).

2. Evaluation of the topology of the network, number of resonators, ports and couplings between resonators in order to achieve a certain frequency response. In this step the physical constraints of the network should be considered in light of the type of input/output system, resonators and couplings.

3. Starting from the S parameters, the admittance matrix in shorted circuit $\mathbf{Y}$ shall be derived. Each element is expressed as a ratio of polynomials in s between a numerator and a common denominator. Closed formulas are defined for 2-port devices, while for multi-port circuits the coefficients may be obtained with the *Cauchy* method as explained in section B.2.

4. The resonant circuit is described through the coupling matrix defined by blocks of eq. (B.1). At this stage it is possible to identify on this matrix which element are zero depending on the topology of the circuit. This configuration will be the final target of the synthesis procedure. Each of these elements must be a real number.

5. Expansion in partial fractions of the $\mathbf{Y}$ matrix. In this step the constant value $\mathbf{Y}^{(\infty)}$, the poles λ_k and the matrix of residues $\mathbf{\Gamma}_k$ shall be calculated. The $\mathbf{Y}^{(\infty)}$ is obtained through the formula of eq. (B.34) while the poles λ_k are the roots of common denominator $y_d(s)$. Once the imaginary poles are obtained, the matrix of residues $\mathbf{\Gamma}_k$ is calculated with eq. (B.56) for each pole.

6. Generation of transversal matrix. It has been shown that this type of network simplify the calculations due to the convenient relations between the partial fraction expansion of $\mathbf{Y}$ and the coupling matrix $\mathbf{M}$. The matrix of the couplings between ports $\mathbf{M_p}$ is directly obtained from eq. (B.40). The matrix of the internal couplings is the diagonal of the poles of the admittance matrix (eq. (B.45)). Finally, the matrix of the external couplings $\mathbf{M_{pn}}$ is derived from the matrix of residues Γ_k with the eq. (B.56). At this point all the couplings of the transversal network are found and the general coupling matrix $\mathbf{M}$ is fully populated.

7. If the transversal network is difficult or impossible to realize, it is necessary to transform it with a series of Jacobi similarities of eq. (B.57). The designer should consider the topology of the final circuit to operate the correct sequence of transformation. This is an iterative approach where at each step the correct equation among the (B.59) and a proper rotation algorithm are to be chosen. It is fundamental to decide in advance the sequence of element to annihilate in order to define the coordinates of each pivot rotation.

8. The coupling matrix found at this stage of the procedure is defined in the normalized low-pass domain. Finally, the coupling matrix of the final circuit is directly calculated with the low-pass to band-pass transformation of eq.s (B.61).

At this point the coupling matrix has the desired frequency response as well as the right topology of the circuit. The synthesis is now completed.

B.2 CAUCHY METHOD

Although in section B.1 has been described the general synthesis for for a multi-port resonant circuit, no many information were provided to define the starting point of the synthesis. The procedure allows to directly calculate the coupling matrix of the low-

pass prototype starting from the admittance representation of the frequency response. However, it is not always straightforward to directly derive the coefficients of the $\mathbf{Y}$ matrix in rational form directly from the scattering polynomials. For the simple case of 2-port networks (filters) there exists an analytical formulation (see section B.3.1), but for more complex circuits it can be very difficult to define an approach without losing generality. The solution proposed in this section is to apply the *Cauchy method* to approximate a curve with a rational polynomial expression [50]. The procedure is based on solving a set of linear equations where the known variables are the points of the sampled curve. Then a *least square* algorithm is applied to the system in order to compute the coefficients of the polynomials that approximate the function.

The curves of the scattering parameters are directly obtained from their characteristic polynomials. Then, the admittance matrix is calculated for each frequency point with the well known relation

$$\mathbf{Y_p} = (\mathbf{U_p} - \mathbf{S_p})(\mathbf{U_p} + \mathbf{S_p})^{-1} \tag{B.62}$$

being $\mathbf{U}$ the unitary matrix. Each element of the eq. (B.62) can be approximated to rational polynomials of finite degree and common denominator. The response of the $\mathbf{Y}$ matrix is evaluated in a finite number of frequency points N that may be not equally-spaced. The generic element of the matrix is expressed with the following notation:

$$[\bar{\mathbf{Y}}]_{ij}(s) = \frac{\sum_{k=0}^{n_a} a_k s^k}{\sum_{k=0}^{n_b} b_k s^k} \approx [\mathbf{Y}]_{ij}(s) \tag{B.63}$$

where n_a and n_b are the degree of the numerator and denominator respectively. The principle of analytical continuation states that the expression (B.63) can be substituted with a system of N linear equations like the following:

$$\sum_{k=0}^{n_a} s_m^k - Y_{ij}(s_m) \sum_{k=0}^{n_b} b_k s_m^k = 0 \tag{B.64}$$

with $m \in \{1, \ldots, N\}$. The curve must be sampled in a suitable way and the minimum number of samples N depends on the degree of numerator and denominator:

$$N \geqslant n_a + n_b + 1 \tag{B.65}$$

In the case of the equality there are an exact number of equations and unknowns, otherwise the system is *overdetermined*. The system of linear equations (B.64) can be equivalently expressed with a matrix notation as in the following:

$$\left[\mathbf{V}_{n_a} - \mathbf{Y}_{ij}\mathbf{V}_{n_b}\right] \begin{bmatrix} \mathbf{a} \\ \mathbf{b} \end{bmatrix} = \mathbf{X} \begin{bmatrix} \mathbf{a} \\ \mathbf{b} \end{bmatrix} = \mathbf{0} \tag{B.66}$$

where the vectors $\mathbf{a} \in \mathbb{C}^{n_a+1}$ and $\mathbf{b} \in \mathbb{C}^{n_b+1}$ are the unknowns variables, $\mathbf{Y}_{ij} = \operatorname{diag}\{[\mathbf{Y}]_{ij}(s_m)\}$ a diagonal matrix of the sampled values of the curve and $\mathbf{V}_r$ is the Vandermonde matrix defined as

$$\mathbf{V}_r \triangleq \begin{bmatrix} 1 & s_1 & s_1^2 & \cdots & s_1^r \\ 1 & s_2 & s_2^2 & \cdots & s_2^r \\ \vdots & \vdots & \vdots & \ddots & \vdots \\ 1 & s_N & s_N^2 & \cdots & s_N^r \end{bmatrix} \in \mathbb{C}^{N\times(r+1)} \tag{B.67}$$

The system of linear equations defined in eq. (B.66) is valid to obtain the coefficients of the rational polynomials approximating one single curve. However, in our application we are interested in rational functions that share a common denominator. It is clear that is not possible to apply several systems of the kind of eq. (B.66) since they

will result in having different denominators. The solution is to create a more complex system of equations in which is forced the dependency of the denominator:

$$\mathbf{X} = \begin{bmatrix} \mathbf{V}_{n_1} & \mathbf{0} & \cdots & \mathbf{0} & -\mathbf{Y}_1\mathbf{V}_{n_b} \\ \mathbf{0} & \mathbf{V}_{n_2} & \cdots & \mathbf{0} & -\mathbf{Y}_2\mathbf{V}_{n_b} \\ \vdots & \vdots & \ddots & \vdots & \vdots \\ \mathbf{0} & \mathbf{0} & \cdots & \mathbf{V}_{n_q} & -\mathbf{Y}_q\mathbf{V}_{n_b} \end{bmatrix} \in \mathbb{C}^{(qN)\times(n_1+\cdots+n_q+n_b+q)} \tag{B.68}$$

In matrix (B.68) there are all the q curves of the admittance matrix in the diagonal form as explained before. It has been assumed that the degree of each numerator are, respectively, $n_1, n_2, \ldots, n_q$ and the degree of the denominator is n_b. For clarity, in system (B.68) has been omitted the dimensions of the zero sub-matrices that are present at any line: it is obvious that these zeros are included just to fill the empty elements of the matrix and to ensure the alignment with the other systems of equations of the other curves. Each null sub-matrix has N rows and a number of columns equal to the degree incremented by 1 of the Vandermonde matrix associated to that column. Thus the condition on the number of sampling points required for the system is

$$N \geqslant n_1 + n_2 + \cdots + n_q + q \cdot n_b + q \tag{B.69}$$

The vector of unknowns include all the coefficients associated to denominators of each curve $\mathbf{a}^{(1)}, \mathbf{a}^{(2)}, \ldots, \mathbf{a}^{(q)}$ and the denominator $\mathbf{b}$:

$$\mathbf{X} \begin{bmatrix} \mathbf{a}^{(1)} \\ \vdots \\ \mathbf{a}^{(q)} \\ \mathbf{b} \end{bmatrix} = \mathbf{0} \tag{B.70}$$

The system (B.70) is solved with the *total least square* (TLS) method. It does not matter whether it is exactly determined or overdetermined, the TLS technique permits to

find the vector of coefficients that solve the system. In order to do the calculation a *singular value decomposition* of $\mathbf{X}$ is performed in order to solve the system [45]:

$$\mathbf{X}\begin{bmatrix} a^{(1)} \\ \vdots \\ a^{(q)} \\ b \end{bmatrix} = \mathbf{U}\mathbf{\Sigma}\mathbf{V}^{H}\begin{bmatrix} a^{(1)} \\ \vdots \\ a^{(q)} \\ b \end{bmatrix} = \mathbf{0} \tag{B.71}$$

The terms $\mathbf{U}$ and $\mathbf{V}^{H}$ are unitary matrices while $\mathbf{\Sigma}$ is the matrix of the singular values of $\mathbf{X}$. The operator $(.)^{H}$ denotes the complex conjugate transpose of a matrix. The TLS method states that the solution of the system (B.71) is proportional to the last column of matrix $\mathbf{V}^{H}$:

$$\begin{bmatrix} a^{(1)} \\ \vdots \\ a^{(q)} \\ b \end{bmatrix} = [\mathbf{V}^{H}]_{n_1+\cdots+n_q+n_b+q} \tag{B.72}$$

The method for the solution of the system presented here has some disadvantages that impact on the accuracy of the coefficients of the polynomials. As it has been shown in [53], the Vandermonde matrix is ill-conditioned and other approaches might improve the approximation for certain curves. Among the many methods that might be used to solve the system of linear equations, the $\mathbf{QR}$ algorithm seems to be a good compromise between complexity, computational power required and accuracy of the results [53]. Moreover, in the definition of eq. (B.68) there are several zero elements that are avoided with this last methodology.

The Cauchy method is also a powerful tool when it is necessary to compute the characteristic polynomials of a circuit and, consequently, the associated coupling matrix. In this way it might be of interest the comparison between the coupling matrix of the theoretical circuit and the measured one, leading to a deeper understanding

of the impact of the tolerances of the fabrication process. It is worth to remind that any measurement of a real device is affected by the losses of the material. Thus, some changes to the traditional Cauchy method are likely to be applied as it is explained in [52].

B.3 EXAMPLES

B.3.1 Fully canonical filter

In this example will be presented the synthesis of a *fully canonical* filter starting from the specifications up to the building of the coupling matrix. The synthesis of a two ports circuit is the most common problem of microwave engineering and it will be solved with the general approach described in the sections before. Here, a 4 resonators with asymmetric filtering, 22 dB in-band return loss and 4 transmission zeros will be considered exactly the same of [41]. The first two transmission zeros are located, respectively, at $-j3.7431$ and $-j1.8051$ in order to produce 2 attenuation lobes in the lower side of the passband better than -30 dB. The others 2 transmission zeros are located at $+j1.5699$ and $+j6.1910$ to produce an attenuation lobe of 20 dB in the upper side of the band-pass.

The synthesis of the polynomials is carried out with the iterative algorithm explained in [40]. As usual, the S parameters are expressed as rational polynomials between numerators and a common denominator to all the elements. In the literature it is practice to express the S parameters of a filter in term of:

$$S_{11}(s) = \frac{F(s)/\epsilon_R}{E(s)} \tag{B.73a}$$

$$S_{21}(s) = \frac{P(s)/\epsilon}{E(s)} \tag{B.73b}$$

Table B.1: Coefficients of $E(s)$, $F(s)$, $P(s)$ polynomials of fully canonical filter

Degree of s	E(s)	F(s)	P(s)
4	1.0	1.0	j1.0
3	$+2.2467 - j0.0047$	$-j0.0026$	2.2128
2	$+3.6063 - j0.0031$	1.0615	j26.5826
1	$+3.2898 - j0.0489$	$-j0.0009$	1.4870
0	$+1.9877 - j0.0025$	0.1580	j65.6671

For the filters, like the one under consideration, that have all the TZs at *finite* frequencies, the constant term ϵ_R is added to the previous set of equations and acts as a normalization factor between $F(s)$, $P(s)$ and $E(s)$. It is defined as:

$$\epsilon_R = \frac{\epsilon}{\sqrt{\epsilon^2 - 1}} \tag{B.74}$$

The factor ϵ controls the in-band ripples of the return loss. The coefficients of the polynomials are summarized in Tab. B.1 with

$$\epsilon = 33.140652 \tag{B.75a}$$

$$\epsilon_R = 1.000456 \tag{B.75b}$$

Before proceeding with the synthesis, it is necessary to derive the admittance parameters from the scattering polynomials of Tab. B.1. To do this we think the filter as a 2-port network connected to a source to one side and to an output impedance, say R_L, to the other one. The *driving-point impedance* is the ratio between voltages and currents when the terminals of the network are connected to a driving force or to an energy source. It is common to define these quantities with capital letters:

$$Z(s) = \frac{V(s)}{I(s)} \tag{B.76}$$

When referring to the driving impedances, or admittances, of the network loaded either to an open or shorted circuit, the non-capital letter are used. In the following, the driving point impedance will be derived as a function of its parameters in open and shorted circuit (z and y). Consider the circuit of Fig. B.5, it represents a network

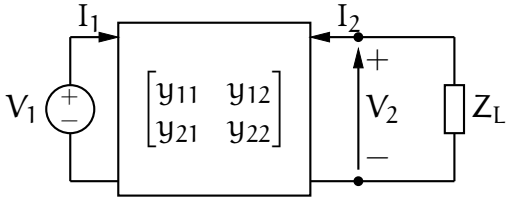

Figure B.5: Generic 2 ports circuit described by y parameters

described with its y matrix of the driving admittance parameters in shorted circuits, connected with a source and a load. On the figure is included the voltages and currents at ports with their directions. In this first stage, it is necessary to derive the expression of the input driving impedance of eq. (B.76) in terms of z or y of the network as described in [128]. These parameters are defined in this way:

$$y_{11} = \left.\frac{I_1}{V_1}\right|_{V_2=0} \tag{B.77a}$$

$$y_{12} = \left.\frac{I_2}{V_1}\right|_{V_2=0} \tag{B.77b}$$

$$y_{21} = \left.\frac{I_1}{V_2}\right|_{V_1=0} \tag{B.77c}$$

$$y_{22} = \left.\frac{I_2}{V_2}\right|_{V_1=0} \tag{B.77d}$$

In order to derive the formulation of the input driving impedance of circuit of Fig. B.5, the theorems of Norton and Thevenin are applied to this circuit when it is, respectively, connected to an open circuit and to a load. Let consider the generic network with the equivalent Norton representation. Fig. B.5 can be taken as reference by disconnecting the load at port 2 and closing it on a shorted circuit without loss of generality. By definition of y_{12} given in eq. (B.77b), the current I_2 in shorted circuit is:

$$I_{2sc} = -y_{12}V_1 \tag{B.78}$$

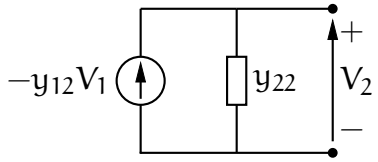

(a) Norton's equivalent of a generic network in open circuit

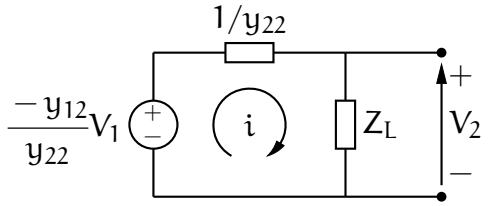

(b) Thevenin's equivalent of the circuit loaded

Figure B.6: Equivalent models of network left in open circuit and connected to an impedance

where the minus sign reflects the orientation of the current that is opposite with the respect the direction given in Fig. B.5. The Norton's equivalent admittance is found when the generator at port 1 is substituted with a shorted circuit. Naturally, the equivalent admittance seen from port 2 when port 1 is shorted circuited is y_{22} because we are still considering the network of Fig. B.5 without the load impedance. Thus, the equivalent Norton circuit of Fig. B.5 left in open circuit is given by the network shown in Fig. B.6a. In this representation the equivalent Norton of the current generator is expressed as function of the input voltage V_1 and by the transmission admittance in accordance with eq. (B.78). From network of Fig. B.6a, the voltages V_2 is the potential difference at the ends of equivalent admittance y_{22} and it's value is

$$V_2 = \frac{-y_{12}V_1}{y_{22}}$$

and consequently the voltage gain is

$$\frac{V_2}{V_1} = -\frac{y_{12}}{y_{22}} \tag{B.79}$$

Formula (B.79) is totally general and refers to any two port network described with its driving admittance parameters in shorted circuit. Now, let consider the equivalent

Thevenin representation of Fig. B.5 but using the formulations derived so far. As known, the Thevenin theorem is applied to a network in open circuit, let say, the circuit of Fig. B.5 considered in open circuit with no impedance loaded in first instance. In this case the voltage at port 2 has already been calculated and it is

$$V_{2oc} = \frac{-y_{12}V_1}{y_{22}} \tag{B.80}$$

The equivalent impedance is calculated when the input voltage generator is disconnected and substituted with a shorted circuit. By definition of eq. (B.77d) the Thevenin impedance is $1/y_{22}$. At this point it is possible to connect the load impedance to the equivalent circuit obtained in order to evaluate the necessary parameters. Fig. B.6b is representing the equivalent Thevenin of a generic network in terms of its $\mathbf{y}$ parameters. By connecting the load impedance to this circuit it is possible to derive all the parameters as function of the driving admittances in shorted circuit, as required by the problem.

Let solve the equation of loop current of circuit in Fig. B.6b. It is easy to find that

$$I_1 = \frac{\sum V}{\sum Z} = \frac{-\frac{y_{12}}{y_{22}}V_1}{1/y_{22} + Z_L}$$

so that

$$\frac{V_1}{I_1} = \frac{1/y_{22} + Z_L}{-\frac{y_{12}}{y_{22}}} \tag{B.81}$$

At this point it is useful to remind the relations between the $\mathbf{y}$ and $\mathbf{z}$:

$$y_{11} = \frac{z_{22}}{\Delta z} \tag{B.82a}$$

$$y_{12} = \frac{-z_{12}}{\Delta z} \tag{B.82b}$$

$$y_{21} = \frac{-z_{21}}{\Delta z} \tag{B.82c}$$

$$y_{22} = \frac{z_{11}}{\Delta z} \tag{B.82d}$$

$$\Delta z = z_{11}z_{22} - z_{12}z_{21} \tag{B.82e}$$

The driving impedance that is under investigation is function of both the element of $\mathbf{z}$ of the network as well as the load impedance Z_L. It follows that the transfer driving impedance is

$$z_{12} = \left.\frac{V_1}{I_2}\right|_{I_1=0} = z_{22} + Z_L \tag{B.83}$$

Combining eqs. (B.83), (B.82b) and (B.82d) into (B.81) is obtained the expression of the driving impedance of the double terminated network on a load:

$$Z_{11}(s) = \frac{z_{11}(1/y_{22} + Z_L)}{z_{22} + Z_L} = \frac{z_{11}(1/y_{22} + 1)}{z_{22} + 1} \tag{B.84}$$

where the load Z_L has been normalized to unity in the second part of the last equation. The definition of driving point impedance is then extended to incorporate the S parameters as

$$Z_{11}(s) = \frac{1 - S_{11}(s)}{1 + S_{11}(s)} = \frac{E(s) \pm F(s)}{E(s) \mp F(s)} = \frac{m_1 + n_1}{m_2 + n_2} \tag{B.85}$$

where the numerator and denominator have been separated in their even m and odd n parts. In eq. (B.85) appears the relation between the even/odd terms and the polynomials $E(s)$ and $F(s)$ constituting the response of the filter. For this reason, the elements

m_1 and n_1 are defined from the coefficients of both $E(s)$ and $F(s)$ with the following relations:

$$m_1(s) = \Re(e_0 + f_0) + j\Im(e_1 + f_1)s + \Re(e_2 + f_2)s^2 + \dots \tag{B.86}$$

$$n_1(s) = j\Im(e_0 + f_0) + \Re(e_1 + f_1)s + j\Im(e_2 + f_2)s^2 + \dots \tag{B.87}$$

The terms $e_i, f_i \wedge i \in \{1, \dots, n\}$ (where n is the order of the filter) are the coefficients of polynomials $E(s)$ and $F(s)$ respectively associated to variable with power i. It is clear that both m_1 and n_1 have purely real or purely imaginary coefficients. If the element n_1 is brought outside the bracket, the eq. (B.85) takes the form

$$Z_{11}(s) = \frac{n_1(m_1/n_1 + 1)}{n_2 + m_2} \tag{B.88}$$

that if it is compared with eq. (B.84) it is possible to derive the expression of y_{22} as

$$y_{22}(s) = \frac{n_{22}(s)}{y_d(s)} = \frac{n_1(s)}{m_1(s)} \tag{B.89}$$

The eq. (B.89) is the first one of the admittance parameters on short circuit that are needed for the derivation of the coupling matrix. The formulation of eq. (B.89) also puts in evidence the relation between the polynomials found here and the elements of the admittance matrix $\mathbf{Y}$ of eq. (B.31). It is immediate to see that

$$y_d(s) = m_1(s) \tag{B.90}$$

The common denominator has been identified to be $m_1(s)$ indeed, the transmission parameter $y_{21}(s)$ that contains the information of the TZs as was it for the $S_{21}(s)$, it derives that

$$y_{21}(s) = \frac{P(s)}{\epsilon m_1(s)} \tag{B.91}$$

Table B.2: Coefficients of $[\mathbf{Y}]_{11}(s)$, $[\mathbf{Y}]_{21}(s)$, polynomials of the fully canonical filter expressed as a ratio between a numerator and a common denominator $y_d(s)$.

Degree of s	$y_d(s)$	$n_{11}(s)$	$n_{21}(s)$
4	1.0		j0.0151
3	−j0.0036	1.1236	0.0334
2	2.3342	−j0.0016	j0.4012
1	−j0.0249	1.6453	0.0224
0	1.0730	−j0.0012	j0.9910

The formulas (B.89), (B.90) and (B.91) are true only when the degree n of the filter is *even*. Otherwise it simply needs to reverse the fraction of eq. (B.89) and correcting the followings to have the relations for the case of n *odd*:

$$y_d(s) = n_1(s) \tag{B.92a}$$

$$y_{11}(s) = y_{22}(s) = \frac{m_1(s)}{n_1(s)} \tag{B.92b}$$

$$y_{12}(s) = y_{21}(s) = \frac{P(s)}{\epsilon n_1(s)} \tag{B.92c}$$

In the case under investigation there are an even number of resonant nodes n and the eq.s (B.90), (B.91) and (B.89) are to be used. The matrix of the rational polynomials of the admittance matrix is directly found by solving the eq.s (B.86) and (B.87) with the coefficients of Tab. B.1. Here are the numerical results for the even and odd polynomials:

$$m_1(s) = 1.9995s^4 - j0.0073s^3 + 4.6674s^2 - j0.0498s + 2.1456 \tag{B.93a}$$

$$n_1(s) = 2.2467s^3 - j0.0032s^2 + 3.2898s - j0.0025 \tag{B.93b}$$

Now that the equations that relate the coefficients of the scattering parameters of the filter with its admittance characteristic in shorted circuit, it is possible to begin with the synthesis technique explained in section B.1. The coefficients of the $\mathbf{Y}$ elements are summarized in Tab. B.2 for the case of fully canonical filter. It is worth to remember that the elements of Tab. B.2 are the coefficients of the polynomials of

the common denominator $y_d(s)$ and the numerators of y_{11} and y_{21}. To be consistent with the notation given in eq. (B.31), the numerators of $y_{11}(s)$ and $y_{21}(s)$ are indicated with $n_{11}(s)$ and $n_{21}(s)$ respectively. All the values in Tab. B.2 are normalized to the coefficient of highest degree of $y_d(s)$.

The first step is to build up the coupling matrix defined by blocks of the transversal transfer network. Obviously, for a filter of the fourth order it is $p = 2$ and $n = 4$. The matrix of the internal couplings $\mathbf{M_n}$ is obtained directly from the imaginary part of the roots of polynomial $y_d(s)$, since they represent the poles of the function common to all $\mathbf{Y}$ parameters:

$$\mathbf{M_n} = \begin{bmatrix} 1.3142 & 0 & 0 & 0 \\ 0 & 0.7830 & 0 & 0 \\ 0 & 0 & -0.8041 & 0 \\ 0 & 0 & 0 & -1.2968 \end{bmatrix} \tag{B.94}$$

The (B.94) reflects the minus change of sign as introduced in (B.45). The list of the eigenvalues of the transversal network is enclosed in Tab. B.3. The matrix of the external couplings is calculated firstly by evaluating the constant terms $\mathbf{Y}^{(\infty)}$ with eq. (B.34) and then the $\mathbf{M_p}$ is promptly obtained with eq. (B.40). The result of the last two operations is

$$\mathbf{M_p} = \begin{bmatrix} 0 & 0.0151 \\ 0.0151 & 0 \end{bmatrix} \tag{B.95}$$

The last result shows one peculiarity of the fully canonical filter: the number of TZs is equal to the number of resonators (order of the filter) since a coupling between ports is necessary to create an additional path that is responsible for the "fourth" zero.

Before building the last matrix, of the external couplings $\mathbf{M_{pn}}$, the matrix of residues $\mathbf{\Gamma}_k$ associated to each pole is required. In order to perform this operation the formula of eq. (B.39) is applied to all the element of $\mathbf{Y}$. Matrix $\mathbf{\Gamma}_k$ is symmetric. The matrix of

Table B.3: Eigenvalues and residues of the fully canonical filter

k	λ_k	$r_{11,k}$	$r_{21,k}$
1	−1.3142	0.1326	0.1326
2	−0.7830	0.4272	−0.4273
3	0.8041	0.4460	0.4459
4	1.2968	0.1178	−0.1178

the coupling coefficients between the internal elements (resonators) and the external ones (ports) is carried out with the use of formula of eq. (B.56) for the transversal network. It is interesting to observe that from Tab. B.3 there are not any residues that are coincident with the poles of the $\mathbf{Y}$ function. This characteristic brings to a matrix of external couplings with no zeros elements. This is the more general case of transversal network when all the resonators are coupled with the output ports. Therefore it follows that:

$$\mathbf{M_{pn}} = \begin{bmatrix} 0.3640 & -0.6537 & 0.6677 & -0.3434 \\ 0.3642 & 0.6536 & 0.6678 & 0.3432 \end{bmatrix} \tag{B.96}$$

The procedure is now completed since the complete coupling matrix is build by blocks $\mathbf{M_n}$, $\mathbf{M_p}$ and $\mathbf{M_{pn}}$ as defined by eq. (B.1).

Once the general coupling matrix for the transversal network has been completed, it is possible to draw the scattering parameters through the relation of eq. (B.17). The plot of the S parameters is shown in Fig. B.7. The filter response has all the characteristics in accordance with the specifications both in the in-band as well as in the out-of-band. The 4 poles of the function are visible with an equal ripple response at −22 dB. Out of the band it is possible to distinguish the 4 transmission zeros and the relative lobes. In the left side of the response, the transmission parameters does not exceed the rejection of −30 dB as stated in the specifications, while in the upper side the position of the TZs produce a lobe with a maximum of −20 dB.

The response of Fig. B.7 is determined by the transversal network, whose matrix must be transformed into a practical design. In order to produce the the same filtering

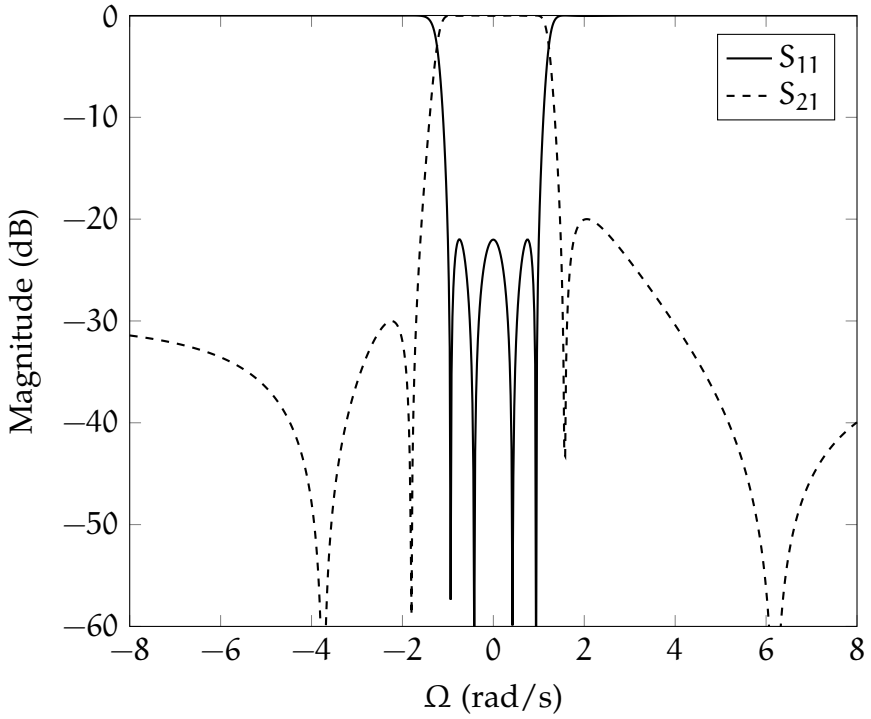

Figure B.7: Scattering parameters in magnitude of the fully canonical filter

function in a feasible structure, a topology for the network shall be found. Due to the characteristics cited before, the structure of Fig. B.8a seems to be suitable for the application. In this case is interesting to note that all these three types of couplings are present in the filter. The TZs are made possible because in this filter there are some additional *path* called cross-couplings. A conventional 2 ports filter has a path of the type: P1-1-2-3-4-P2 while with this topology the others path (say secondary paths) that are responsible of the transmission zeros. In particular, an additional coupling is between resonators 1-4 and 2-4. Resonator 1 is coupled contemporary with ports P1 and P2. All these aspects are required when transforming the coupling matrix of the transversal network into the topology studied.

In light of these considerations, the final topology of the filter is represented with the schematic shown in Fig. B.8a. At the moment the synthesis procedure produces a network giving an *equivalent* frequency response but that is far from the final topology of the filter. The schematic of this intermediate circuit has been introduced with the Fig. B.3b and its coupling matrix is represented in Fig. B.8b. The figure represents

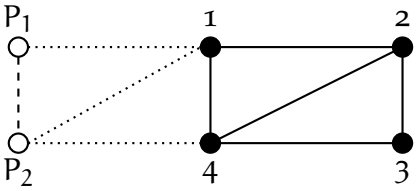

(a) Topology

	P1	P2	1	2	3	4
P1		×	×	×	×	×
P2	×		×	×	×	×
1	×	×	×			
2	×	×		×		
3	×	×			×	
4	×	×				×

(b) Transversal network

	P1	P2	1	2	3	4
P1		×	×			
P2	×		×			×
1	×	×	×	×		×
2			×	×	×	×
3				×	×	×
4		×	×	×	×	×

(c) Rotated matrix

Figure B.8: Topology of the fully canonical filter

the general coupling matrix of the transversal network. The final filter topology is depicted in Fig. B.8a and its general coupling matrix is shown in Fig. B.8c. Thus, a series of similarity transformations are applied to matrix Fig. B.8b in order to reduce the transversal matrix to the final disposition of Fig. B.8c. The sequence of similarities shall be applied so as at any following rotation the previous annihilated elements are not altered. This is the reason why is very important to choose

1. Sequence of annihilation to follow,
2. position of the pivot i and j parameters,
3. right formula among the eqs. (B.59).

Here, an iterative procedure is applied firstly to terms of the first row starting from right to left: $[\mathbf{M}]_{P_1 4}$, $[\mathbf{M}]_{P_1 3}$ and $[\mathbf{M}]_{P_1 2}$. Then, from left to right for the elements of the row 2: $[\mathbf{M}]_{P_2 2}$ and $[\mathbf{M}]_{P_2 3}$. Ultimately, the element $[\mathbf{M}]_{13}$ is annihilated taking care not to change the values of the others annulled coefficients. It is very important to underline that all the subscripts are referring to the grid of the generalized matrix. In this context for example, the coupling coefficient between resonator 2 and 4 is

represented with the element$[\mathbf{M}]_{24}$ and, consequently, the subscripts are $i = 2$ and $j = 4$. In the same manner, the element $[\mathbf{M}]_{P_24}$ for example, is the coupling coefficient between port 2 and resonator 4 that is the last element of second row in Fig. B.8c. For the first three elements the eq. (B.59d) is used with pivot centres in $[3,4]$, $[2,3]$ and $[1,2]$. The rotation angle to be applied to formula of eq. (B.57) is directly derived from eq. (B.59d) and is:

$$\phi = \arctan\left(-\frac{[\mathbf{M}]_{kj}}{[\mathbf{M}]_{ki}}\right) \tag{B.97}$$

with $k = P_1$. For the first three elements the formula (B.59d) has been used because we are moving on the same row from left to right and the element annihilated is on the column j. Thus, we are sure to move the pivot centre of 1 step towards left without affecting the previous element. For the second row, formula (B.59c) has been chosen with pivotal centres in $[2,3]$ and $[3,4]$. The rotation angle is derived to be

$$\phi = \arctan\left(\frac{[\mathbf{M}]_{ki}}{[\mathbf{M}]_{kj}}\right) \tag{B.98}$$

with $k = P_2$. For the the second row the eq. (B.59c) annihilates the elements that stand on the column i so as the pivotal centre can be chosen in order to include a couple of zeros at the first row. The principle that if two zero elements facing the rotation remain unaltered after the transformation is exploited in order to keep safe the previous annihilations. The last element to be processed is $[\mathbf{M}]_{13}$. To ensure that the previous 5 elements are not modified, it should be noted that four of them are on columns 2 and 3 and that last one is in position $(i,j) = (P_1, 4)$. Therefore, the pivot centre is chosen to be $[2,3]$ because the existing zeros on the columns 2 and 3 are unaffected for the properties of similarities and the external elements are not involved at all. In this scenario it is only possible to move on column j and thus the eq. (B.59d) is used with rotation angle of eq. (B.97). The details of the Jacobi transformation for the fully canonical filter are listed in Tab. B.4.

Table B.4: Details of the rotations to coupling matrix of the fully canonical filter

Transformation	Element	Pivot	$\phi_r = \arctan(c \cdot [\mathbf{M}]_{kl}/[\mathbf{M}]_{mn})$				
r	annihilated	$[i,j]$	k	l	m	n	c
1	$[\mathbf{M}]_{P_1 4}$	$[3,4]$	P_1	4	P_1	3	-1
2	$[\mathbf{M}]_{P_1 3}$	$[2,3]$	P_1	3	P_1	2	-1
3	$[\mathbf{M}]_{P_1 2}$	$[1,2]$	P_1	2	P_1	1	-1
4	$[\mathbf{M}]_{P_2 2}$	$[2,3]$	P_2	2	P_2	3	1
5	$[\mathbf{M}]_{P_2 3}$	$[3,4]$	P_2	3	P_2	4	1
6	$[\mathbf{M}]_{13}$	$[2,3]$	1	3	1	2	-1

At the end of the reduction process, the rotated coupling matrix is the following:

$$\mathbf{M}' = \left[\begin{array}{cc|cccc} 0 & 0.0151 & 1.0600 & 0 & 0 & 0 \\ 0.0151 & 0 & 0.0315 & 0 & 0 & 1.0595 \\ \hline 1.0600 & 0.0315 & -0.0024 & 0.8739 & 0 & -0.3259 \\ 0 & 0 & 0.8739 & 0.0483 & 0.8360 & 0.0342 \\ 0 & 0 & 0 & 0.8360 & -0.0667 & 0.8722 \\ 0 & 1.0595 & -0.3259 & 0.0342 & 0.8722 & 0.0172 \end{array}\right] \tag{B.99}$$

B.3.2 Diplexer formed by two box-sections

The synthesis of a Diplexer formed by two box-sections is carried out here using the synthesis procedure of section B.1. This example follows the specifications of [43] and the synthesis procedure for this particular case has also been described in [46].

The topology of this type of diplexer is shown in Fig. B.9a. This is a 3 port network with 8 resonators: $p = 3$, $n = 8$. The object of this section is to demonstrate that the methodology proposed in section B.1 can be applied to a circuit with more than 2 ports. The network of Fig. B.9a has the main characteristic of having the 8 resonators divided in two quadruplets also known as *box sections*. Each box section presents a direct path and a secondary path that produces a transmission zero in each band of the diplexer. The port P_3 is chosen here as the common port, while P_1 and P_2 are

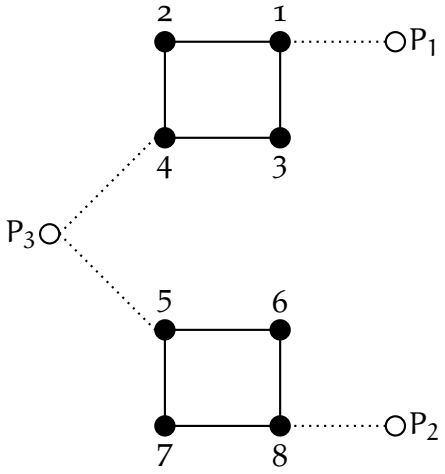

(a) Topology of the resonant network

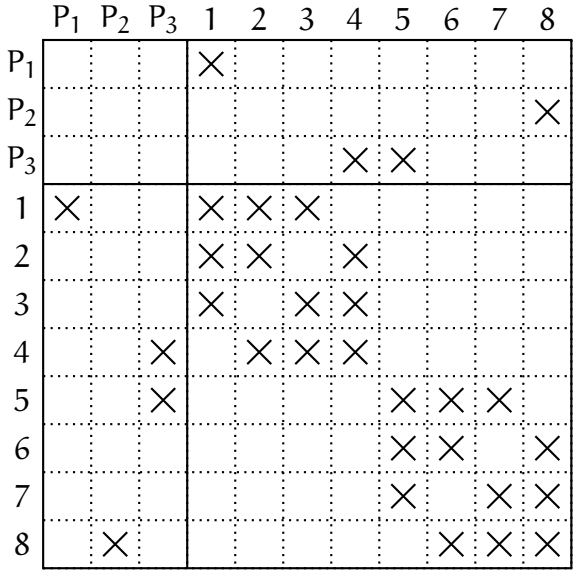

(b) Schematic of the general coupling matrix **M**

Figure B.9: Topology of the two box sections diplexer with its associated the block matrix

Table B.5: Specifications of the two box-sections diplexer

Parameter	Channel 1	Channel 2
Order	4	4
Low-pass central frequency (rad/s)	−1.3	1.3
low-pass bandwidth (rad/s)	2	2
Return loss	−20 dB	−20 dB
frequency of transmission zero (rad/s)	j0.42	−j0.42

the ports of the two channels. The numbering of the resonators has been chosen in order to be consecutive for each quadruplet, with number 1 associated to resonator connected to port P_1 and number 8 for the resonator with port P_2. The common port P_3 is directly coupled with the two quadruplets that are acting as a filter for the two different channels. Thus, port P_3 is coupled with resonator 4 for the first channel and to resonator 5 for the second. From the definition of topology given above it is possible to derive a schematic of the general coupling matrix as shown in Fig. B.9b. In this scheme the matrix $\mathbf{M}$ is represented with crosses that identify the non-zero coupling coefficients of the network. At the end of the synthesis procedure the coupling matrix $\mathbf{M}$ will be filled with the values of the coupling coefficients of the network of Fig. B.9a that give the desired response. Note from the topology of Fig. B.9a that there is a filtering response of the fourth order for each channel and that both present a transmission zero due to the secondary path of the quadruplet.

The specifications of the diplexer are summarized in Tab. B.5 and the corresponding scattering parameters will be calculated. The explanation of the derivation of the scattering parameters is a rather complex topic and it is beyond the scope of this work. If the reader is interested to investigate more in depth on this topic could refers to [129]. In this example both matrices are given as a known information.

The scattering parameters listed in Tab. B.6 with their coefficients. Each S parameter is expressed as a ratio between a numerator and the denominator $E(s)$ that is common

Table B.6: Scattering parameters of the two box-sections diplexer. Here $E(s)$ is the common denominator and S_{ij} are the numerators of S parameters.

Degree of s	$E(s)$	$S_{11}(s)$	$S_{22}(s)$	$S_{33}(s)$
8	1	1	1	1
7	4.2569	2.1285	2.1285	0
6	17.0239	$10.2284 + j2.8742$	$10.2284 - j2.8742$	7.9633
5	37.1058	$13.7325 + j6.1176$	$13.7325 - j6.1176$	−0.0017
4	61.6604	$21.3992 + j20.2589$	$21.3992 - j20.2589$	16.9042
3	59.1576	$9.7312 + j20.0167$	$9.7312 - j20.0167$	−0.0159
2	33.5219	$-0.1621 + j16.7543$	$-0.1621 - j16.7543$	8.8735
1	8.1140	$-2.2180 + j3.2371$	$-2.2180 - j3.2371$	−0.0066
0	0.9289	$-0.6282 + j0.6218$	$-0.6282 - j0.6218$	0.8388

(a)

Degree of s	$E(s)$	$S_{32}(s)$	$S_{31}(s)$	$S_{21}(s)$
8	1			
7	4.2569			
6	17.0239			
5	37.1058	0.7157	0.7157	
4	61.6604	$0.7617 - j4.1187$	$0.7617 + j4.1187$	
3	59.1576	$-7.7226 - j3.3547$	$-7.7226 + j3.3547$	
2	33.5219	$-4.3141 + j5.4862$	$-4.3141 - j5.4862$	0.2561
1	8.1140	$1.4802 + j1.8977$	$1.4802 - j1.8977$	0
0	0.9289	$0.2610 - j0.1073$	$0.2610 + j0.1073$	0.0450

(b)

Table B.7: Diplexer **Y** parameters

Degree of s	$y_d(s)$	$n_{33}(s)$	$n_{31}(s)$	$n_{32}(s)$
8	1			
7	0	2.1285		
6	11.3610	0		
5	0	16.1431	−0.3579	−0.3579
4	30.3407	0	j2.0594	−j2.0594
3	0	19.6590	3.8613	3.8613
2	10.5178	0	−j2.7431	j2.7431
1	0	0.9211	−0.7401	−0.7401
0	0.1279	0	j0.0537	−j0.0537

(a)

Degree of s	$y_d(s)$	$n_{11}(s)$	$n_{22}(s)$	$n_{21}(s)$
8	1			
7	0	1.0642	1.0642	
6	11.3610	−j1.4371	j1.4371	
5	0	9.2760	9.2760	
4	30.3407	−j10.1294	j10.1294	
3	0	14.7854	14.7854	
2	10.5178	−j8.3772	j8.3772	
1	0	2.0268	2.0268	
0	0.1279	−j0.3109	j0.3109	0

(b)

to all terms. From Tab. B.6 is possible to notice that, due to the symmetric response of the diplexer, there exist the following relations:

$$S_{11} = S_{22}^* \tag{B.100a}$$

$$S_{31} = S_{32}^* \tag{B.100b}$$

The polynomials in Tab. B.6 are used to calculate the $\mathbf{Y}$ matrix. The parameters needed for the synthesis are the admittance matrix expressed as ratio of polynomials and they are obtained with the Cauchy method explained in sec. B.2. The coefficients of the common denominator $y_d(s)$ as well as the coefficients of the numerator of the other polynomials are shown in Tab. B.7. As for the scattering parameters, the admittance matrix presents the same symmetry between channels, and it follows that

$$n_{11} = n_{22}^* \tag{B.101a}$$

$$n_{31} = n_{32}^* \tag{B.101b}$$

With the coefficients listed in Tab. B.7 all the necessary elements to begin the synthesis procedure are given. First of all, the synthesis of the transversal network of the circuit of Fig. B.9a is performed. In the first stage of the procedure, the fundamental elements of the partial fraction expansion of $\mathbf{Y}$ are investigated. The poles of the $\mathbf{Y}$ functions are the roots of the common denominator $y_d(s)$ and they constitute the eigenvalues of the coupling matrix $\mathbf{M_n}$. In the transversal network, the matrix of

internal couplings is diagonal, therefore its non-zero elements are also its eigenvalues:

$$\mathbf{M_n} = \begin{bmatrix} 2.7394 & 0 & 0 & 0 & 0 & 0 & 0 & 0 \\ 0 & 1.8582 & 0 & 0 & 0 & 0 & 0 & 0 \\ 0 & 0 & 0.6255 & 0 & 0 & 0 & 0 & 0 \\ 0 & 0 & 0 & 0.1123 & 0 & 0 & 0 & 0 \\ 0 & 0 & 0 & 0 & -0.1123 & 0 & 0 & 0 \\ 0 & 0 & 0 & 0 & 0 & -0.6255 & 0 & 0 \\ 0 & 0 & 0 & 0 & 0 & 0 & -1.8582 & 0 \\ 0 & 0 & 0 & 0 & 0 & 0 & 0 & -2.7394 \end{bmatrix} \tag{B.102}$$

The matrix of the couplings between resonators have the values in eq. (B.102). It should be noted that the poles of the function are purely imaginary and, consequently, the coefficients of $y_d(s)$ are purely real.This is an important property because it states that the elements on eq. (B.102) are all real as it should be for a coupling matrix.

The matrix of the external ports is derived from from $\mathbf{Y}^{(\infty)}$ where the formula of eq. (B.34) is applied. It is easy to note that, in this case, the degree of common denominator $y_d(s)$ is higher than any other polynomial among the numerators of $\mathbf{Y}$. Therefore, the limit is 0 for all the elements of $\mathbf{Y}^{(\infty)}$ and, as a consequence, even the matrix $\mathbf{M_p} = \mathbf{0_p}$.

The last step of the synthesis of the transversal network is the calculation of matrix of residues $\mathbf{\Gamma}_k$ for all the poles. The routine is accomplished by the eq. (B.39) and the

Table B.8: Eigenvalues and residues of the diplexer

k	λ_k	$r_{13,k}$	$r_{23,k}$	$r_{33,k}$	$r_{11,k}$	$r_{22,k}$	$r_{21,k}$
1	−2.7394	0.2310	0	0.3173	0.1681	0	0
2	−1.8582	−0.4297	0	0.4439	0.4161	0	0
3	−0.6255	0.2796	0	0.2684	0.2913	0	0
4	−0.1123	−0.0808	0	0.0346	0.1888	0	0
5	0.1123	0	−0.0808	0.0346	0	0.1888	0
6	0.6255	0	0.2796	0.2684	0	0.2913	0
7	1.8582	0	−0.4297	0.4439	0	0.4161	0
8	2.7394	0	0.2310	0.3173	0	0.1681	0

results are listed in Tab. B.8. From these values the matrix of the external couplings is calculated with eq. (B.56) and the its values are:

$$\mathbf{M_{pn}} = \begin{bmatrix} 0.4100 & -0.6451 & 0.5397 & -0.4345 & 0 & 0 & 0 & 0 \\ 0 & 0 & 0 & 0 & -0.4345 & 0.5397 & -0.6451 & 0.4100 \\ 0.5633 & 0.6662 & 0.5181 & 0.1861 & 0.1861 & 0.5181 & 0.6662 & 0.5633 \end{bmatrix} \tag{B.103}$$

With the general coupling matrix completed there is all the information needed to characterise the frequency response of the circuit. The scattering parameters of the two channels and the reflection at the common port are shown in Fig. B.10. The response is in agreement with the specifications as all the poles of both channels are visible as well as the 2 transmission zeros. In Fig. B.10 are also present a couple of additional transmission zeros that had not been expected and they are the result of the interaction between the channels.

An interesting point is the distribution of the residues in Tab. B.8. It is possible to note that there are some zero elements for residues $r_{13,k}$ and $r_{23,k}$ regardless of the $r_{33,k}$ that has all the elements positive. As mentioned before, may happen the situation in which an element of matrix $\mathbf{Y}$ has one or more *zeros* that are coincident with the poles of the function. It is obvious from eq. (B.39) that in such a situation the result of the limit is 0. But in the case under investigation, this result brings us to an interesting

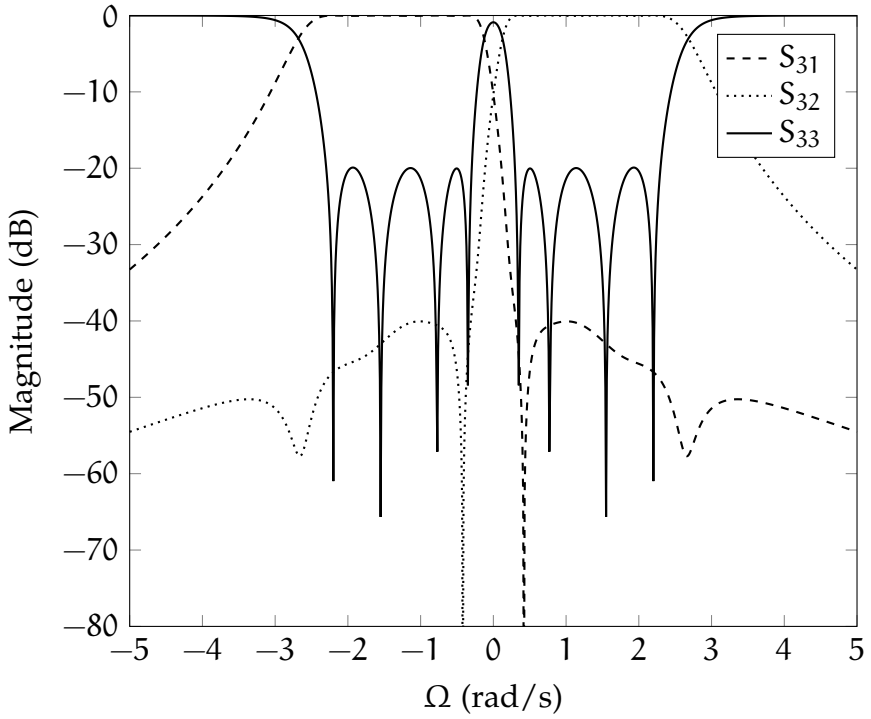

Figure B.10: Scattering parameters in magnitude of the diplexer

consequence. There is an important symmetry between the matrix of residues that is responsible for the symmetry in the matrix of eq. (B.103) where it is clear that the disposition of the couplings between port 1 and the resonators of the first quadruplet is the same to those between port 2 and the second quadruplet. This behaviour is even clearer if considering the network of the transversal coupling matrix of the diplexer shown in Fig. B.11a. This figure clearly shows this principle as well as the fact that the common port P_3 is coupled with all the resonators. Thus, it is possible to affirm that there exists a relation between the channels and the external ports that binds them. The common port is related to both quadruplet and, consequently, it is coupled with all the resonators in the transversal network. In a similar way, ports P_1 and P_2 are coupled with one of the boxes and it appears also in the transversal network. The schematic of the coupling matrix associated to the transversal network is shown in Fig. B.11b. In this figure a cross has been put in correspondence of the presence of a coupling coefficient in the transversal topology of Fig. B.11a.

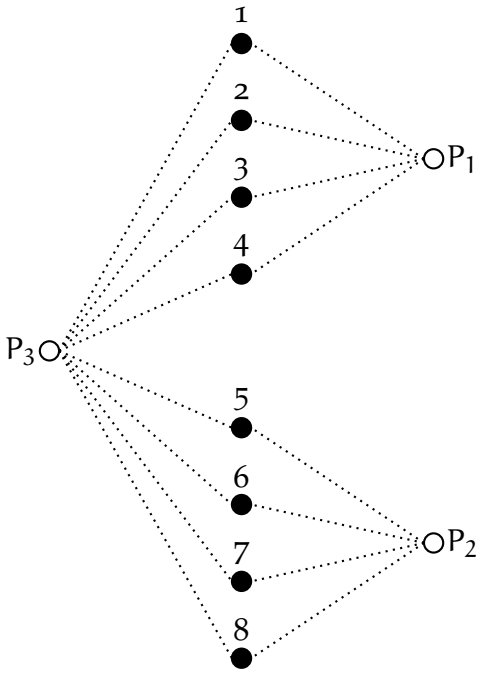

(a) Topology of the transversal network

	P_1	P_2	P_3	1	2	3	4	5	6	7	8
P_1				×	×	×	×				
P_2								×	×	×	×
P_3				×	×	×	×	×	×	×	×
1	×		×	×							
2	×		×		×						
3	×		×			×					
4	×		×				×				
5		×	×					×			
6		×	×						×		
7		×	×							×	
8		×	×								×

(b) Schematic of the general coupling matrix

Figure B.11: Topology of the transversal network two box sections diplexer

Table B.9: Details of the rotations to coupling matrix for the diplexer

Transformation	Element	Pivot	$\phi_r = \arctan(c \cdot [\mathbf{M}]_{kl}/[\mathbf{M}]_{mn})$				
r	annihilated	$[i,j]$	k	l	m	n	c
1	$[\mathbf{M}]_{P_1 4}$	$[3,4]$	P_1	4	P_1	3	-1
2	$[\mathbf{M}]_{P_1 3}$	$[2,3]$	P_1	3	P_1	2	-1
3	$[\mathbf{M}]_{P_1 2}$	$[1,2]$	P_1	2	P_1	1	-1
4	$[\mathbf{M}]_{P_3 2}$	$[2,3]$	P_3	2	P_3	3	1
5	$[\mathbf{M}]_{P_3 3}$	$[3,4]$	P_3	3	P_3	4	1
6	$[\mathbf{M}]_{P_2 5}$	$[5,6]$	P_2	5	P_2	6	1
7	$[\mathbf{M}]_{P_2 6}$	$[6,7]$	P_2	6	P_2	7	1
8	$[\mathbf{M}]_{P_2 7}$	$[7,8]$	P_2	7	P_2	8	1
9	$[\mathbf{M}]_{P_3 7}$	$[6,7]$	P_3	7	P_3	6	-1
10	$[\mathbf{M}]_{P_3 6}$	$[5,6]$	P_3	6	P_3	5	-1

The transversal network is a abstract topology that has been used to easily relate the elements of matrix of residues to the coupling coefficients between ports and resonators, other than to find directly the values of the auto-couplings of the internal nodes. This network is to be transformed into the final topology of Fig. B.9b through a series of similarities, as it has been explained in section B.1.6.

Since there are no couplings between external ports, the procedure of matrix transformation can be applied separately for the two channels. The first step is to annihilate the elements that are relative to the first quadruplet (resonators 1-2-3-4), then the same concept is applied to the second box (resonators 5-6-7-8). Operating this approach, the coupling matrix having the structure of Fig. B.11b is transformed to the final topology of diagram Fig. B.9b. For the reduction of the generalised coupling matrix is convenient to start from right to left and from up to down for each channel. Thus are annihilated the first three elements of the first row exploiting the formula (B.59d), then the two elements on row P_3 from left to right with eq. (B.59c). In a complementary manner, the elements on row P_2 and P_3 are annihilated for the second channel. In Tab. B.9 is listed the complete sequence of similarities applied to the coupling matrix of the transversal network in order to produce the topology of Fig. B.9b.

Table B.10: Untwisting rotations for the diplexer

Transformation r	Element annihilated	Pivot [i, j]	k	ϕ_r
11	$[\mathbf{M}]_{23}$	[2, 3]	1	1.2042
12	$[\mathbf{M}]_{67}$	[6, 7]	1	1.9374

However, after the rotations listed in Tab. B.9 there are 4 unwanted couplings between the internal resonators of the circuit. The reason is that with the last transformations a 2-channel diplexer is obtained instead of the *box section* configuration. The advantage of the box section is that each channel has no cross couplings inside each channel. In order to obtain this topology the elements $[\mathbf{M}]_{23}$ and $[\mathbf{M}]_{67}$ need to be annihilated too. Nevertheless, it is not possible to use the eqs. (B.59) since the absence of the cross diagonal coupling in each box section. This problem was solved in [130] where an appropriate formula has been derived to annihilate the diagonal coupling:

$$\phi_r = \frac{1}{2}\arctan\left(\frac{2[\mathbf{M}]_{ij}}{[\mathbf{M}]_{jj} - [\mathbf{M}]_{ii}}\right) + \frac{k\pi}{2} \tag{B.104}$$

where i, j are the pivotal coordinates of the element to be annihilated and k is an arbitrary number. Finally, the eq. (B.104) is applied twice to *untwist* the topology of each channel with the last 2 rotations listed in Tab. B.10.

At the end of the process of reduction of the matrix $\mathbf{M}$ of the transversal network through the sequence of similarities listed in Tabs. B.9 and B.10, the matrices of the 8-resonator diplexer with 2 box-sections are the following:

$$\mathbf{M}'_{p} = \mathbf{0}_{p} \tag{B.105a}$$

$$\mathbf{M}'_{pn} = \begin{bmatrix} 1.0316 & 0 & 0 & 0 & 0 & 0 & 0 & 0 \\ 0 & 0 & 0 & 0 & 0 & 0 & 0 & 1.0316 \\ 0 & 0 & 0 & 1.0316 & 1.0316 & 0 & 0 & 0 \end{bmatrix} \tag{B.105b}$$

$$\mathbf{M}'_{n} = \begin{bmatrix} 1.3503 & 0.4942 & 0.7596 & 0 & 0 & 0 & 0 & 0 \\ 0.4942 & 0.4359 & 0 & -0.4279 & 0 & 0 & 0 & 0 \\ 0.7596 & 0 & 1.7959 & 0.7210 & 0 & 0 & 0 & 0 \\ 0 & -0.4279 & 0.7210 & 1.7532 & 0 & 0 & 0 & 0 \\ 0 & 0 & 0 & 0 & -1.7532 & 0.7210 & -0.4279 & 0 \\ 0 & 0 & 0 & 0 & 0.7210 & -1.7959 & 0 & 0.7596 \\ 0 & 0 & 0 & 0 & -0.4279 & 0 & -0.4359 & 0.4942 \\ 0 & 0 & 0 & 0 & 0 & 0.7596 & 0.4942 & -1.3503 \end{bmatrix} \tag{B.105c}$$

B.4 CONCLUSIVE NOTES

A summary of the technique presented in the PhD Thesis of García Lamperez has been reported in this appendix and the analytic synthesis for multi-port circuits based on coupled resonators has been described. The abstraction used here allows the procedure to be applied to any network with an arbitrary number of ports and resonators. In order to describe the electrical properties of these type of networks, a new definition of coupling matrix has been introduced [43]. This new coupling matrix is defined by

blocks of sub-matrices, each one representing the different types of couplings among the elements of the network.

The algorithm is based on the knowledge of the admittance parameters in rational form, where the coefficients of the polynomials are related to the **S** parameters. For 2-port devices there exist closed formulas to derive the polynomials of the **Y**, however this is no longer true for networks with more ports. Thus, the Cauchy method has been introduced and applied to solve this problem.

The poles and residues of the $\mathbf{Y}(s)$ must be real number. If this is not the case, no practical circuits can be analytically derived from the specified **S** parameters.

To prove the validity of this theory, the synthesis procedure has been applied to two different types of resonant circuits: a fully canonical filter and a diplexer configured with two box sections. With the first example has been shown that the algorithm extends the traditional techniques valid only for 2 ports networks since it is also fully compatible for these circuits. In the design of the diplexer it has been shown that the same principle apply to a network with 3 ports without loss of generality. Thus, it is possible to conclude that, with this synthesis procedure, any network of arbitrary number of ports and resonators can be synthesised.

C | LIST OF PUBLICATIONS

[131] V. Tornielli di Crestvolant, P. Martin Iglesias and M. J. Lancaster; "Advanced Butler matrices with integrated Band-Pass filter functions" in *IEEE Transactions on Microwave Theory and Techniques*, Vol. 63, No. 10, pp. 3433-3444, October 2015.

ESA PAT 649 V. Tornielli di Crestvolant, P. Martin Iglesias and M. J. Lancaster; "Advance Distribution network with integrated band-pass filter functions". ESA Patent 649. United Kingdom patent application number 1513395.2 (Multiport Distribution Network), submitted on 30th July 2015.

[106] V. Tornielli di Crestvolant, P. Martin Iglesias and M. J. Lancaster; "Topological analysis of hybrid couplers incorporating filter functions" in *6th CNES/ESA International Workshop on Microwave Filters 2015*, March 2015.

[122] V. Tornielli di Crestvolant, P. Martin Iglesias and M. J. Lancaster; "Advances in manufacturing of 4×4 Butler matrices with inherent bandpass filter functions" in *6th CNES/ESA International Workshop on Microwave Filters 2015*, March 2015.

[118] V. Tornielli di Crestvolant, P. Martin Iglesias, M. J. Lancaster and P. Booth; "Multipaction prediction in 180° hybrid power divider based on resonant cavities" in *MULCOPIM 2014*, September 2014.

[105] V. Tornielli di Crestvolant and M. J. Lancaster; "Synthesis of a Class of Quadrature Circuits Based on Coupled-Resonators" in *IET 4th Annual Seminar on Passive RF and Microwave Components*, March 2013.

BIBLIOGRAPHY

[1] G. Maral and M. Bousquet. *Satellite Communications Systems. Systems, Techniques and Technology*. Trans. by Nelson. Fifth edition. UK: Wiley & Sons, 2009. 742 pp. ISBN: 978-0-470-71458-4.

[2] D. Roddy. *Satellite Communications*. Fourth edition. Professional Engineering. McGraw-Hill, 2006. 636 pp. ISBN: 978-0-071-46298-3.

[3] Robert W. Jones. *Handbook on Satellite Communications*. Ed. by ITU. 3rd ed. Wiley, Apr. 2002. 1112 pp. ISBN: 978-0-471-22189-0.

[4] J. Butler and R. Lowe. "Beam-forming matrix simplifies design of electrically scanned antennas". In: *Electron. Design* 9 (Apr. 1961), pp. 170–173.

[5] J. Butler. "Multiple beam antenna system employing multiple directional couplers in the leadin". U.S. pat. 3255450 (US). Inc. Sanders Associates. 7th June 1966.

[6] J. Shelton and K. S. kelleher. "Multiple beams from linear arrays". In: *Antennas and Propagation, IRE Transactions on* 9.2 (1961), pp. 154–161. ISSN: 0096-1973. DOI: 10.1109/TAP.1961.1144964.

[7] William P. Delaney. "An RF Multiple Beam-Forming Technique". In: *Military Electronics, IRE Transactions on* MIL-6.2 (Apr. 1962), pp. 179–186. ISSN: 0096-2511. DOI: 10.1109/IRET-MIL.1962.5008426.

[8] J. Allen. "A theoretical limitation on the formation of lossless multiple beams in linear arrays". In: *Antennas and Propagation, IRE Transactions on* 9.4 (1961), pp. 350–352. ISSN: 0096-1973. DOI: 10.1109/TAP.1961.1145014.

[9] H. Moody. "The systematic design of the Butler matrix". In: *Antennas and Propagation, IEEE Transactions on* 12.6 (1964), pp. 786–788. ISSN: 0018-926X. DOI: 10.1109/TAP.1964.1138319.

[10] M. Ueno. "A systematic design formulation for Butler matrix applied FFT algorithm". In: *Antennas and Propagation, IEEE Transactions on* 29.3 (1981), pp. 496–501. ISSN: 0018-926X. DOI: 10.1109/TAP.1981.1142601.

[11] M. Ueno. "Correction to "A systematic design formulation for butler matrix applied FFT algorithm"". In: *Antennas and Propagation, IEEE Transactions on* 29.5 (1981), pp. 825–825. ISSN: 0018-926X. DOI: 10.1109/TAP.1981.1142666.

[12] T. Macnamara. "Simplified design procedures for Butler matrices incorporating 90° hybrids or 180° hybrids". In: *Microwaves, Antennas and Propagation, IEE Proceedings H* 134.1 (1987), pp. 50–54. ISSN: 0950-107X.

[13] W. A. Sandrin. "The Butler matrix transponder". In: *ComSat technical review* 4.2 (1974), pp. 319–345.

[14] S. Egami and M. Kawai. "An Adaptive Multiple Beam System Concept". In: *Selected Areas in Communications, IEEE Journal on* 5.4 (May 1987), pp. 630–636. ISSN: 0733-8716. DOI: 10.1109/JSAC.1987.1146577.

[15] M. Tanaka and S. Egami. "Reconfigurable multiport amplifiers for in-orbit use". In: *Aerospace and Electronic Systems, IEEE Transactions on* 42.1 (Jan. 2006), pp. 228–236. ISSN: 0018-9251. DOI: 10.1109/TAES.2006.1603418.

[16] Zhiwen Zhu, Xinping Huang and M. Caron. "Ka-Band Multi-port Power Amplifier Calibration Experiment and Results". In: *Advances in Satellite and Space Communications (SPACOMM), 2010 Second International Conference on*. June 2010, pp. 11–14. DOI: 10.1109/SPACOMM.2010.8.

[17] Piero Angeletti and Marco Lisi. "Multiport power amplifiers for flexible satellite antennas and payloads". In: *Microwave Journal* (May 2010), pp. 96–110.

[18] A. Couchman and D. Jones. "Optimized Multiport Amplifiers for Wideband Multi-beam Satellites". In: *24th AIAA International Communications Satellite Systems Conference*. Ed. by American Institute of Aeronautics and Astronautics. San Diego, CA, USA, June 2006. DOI: 10.2514/6.2006-5373.

[19] R. Levy and Seymour B. Cohn. "A History of Microwave Filter Research, Design, and Development". In: *Microwave Theory and Techniques, IEEE Transactions on* 32.9 (Sept. 1984), pp. 1055–1067. ISSN: 0018-9480. DOI: 10.1109/TMTT.1984.1132817.

[20] G. Matthaei, E. M. T. Jones and L. Young. *Microwave Filters, Impedance-Matching Networks, and Coupling Structures*. London: Artech House Publishers, 1964. ISBN: 0-89006-099-1.

[21] S. Darlington. "A history of network synthesis and filter theory for circuits composed of resistors, inductors, and capacitors". In: *Circuits and Systems I: Fundamental Theory and Applications, IEEE Transactions on* 46.1 (Jan. 1999), pp. 4–13. ISSN: 1057-7122. DOI: 10.1109/81.739181.

[22] R. Saal and E. Ulbrich. "On the Design of Filters by Synthesis". In: *Circuit Theory, IRE Transactions on* 5.4 (Dec. 1958), pp. 284–327. ISSN: 0096-2007. DOI: 10.1109/TCT.1958.1086481.

[23] H.J. Orchard. "Some explicit formulas for the components in low-pass ladder networks". In: *Circuit Theory, IEEE Transactions on* 17.4 (Nov. 1970), pp. 612–616. ISSN: 0018-9324. DOI: 10.1109/TCT.1970.1083152.

[24] P.A. Mariotto. "On the explicit formulas for the elements in low-pass ladder filters". In: *Circuits and Systems, IEEE Transactions on* 37.11 (Nov. 1990), pp. 1429–1436. ISSN: 0098-4094. DOI: 10.1109/31.62418.

[25] R. Levy. "Generalized Rational Function Approximation in Finite Intervals Using Zolotarev Functions". In: *Microwave Theory and Techniques, IEEE Transactions on* 18.12 (Dec. 1970), pp. 1052–1064. ISSN: 0018-9480. DOI: 10.1109/TMTT.1970.1127411.

[26] R. Levy. "Characteristics and element values of equally terminated Achieser-Zolotarev quasi-low-pass filters". In: *Circuit Theory, IEEE Transactions on* 18.5 (Sept. 1971), pp. 538–544. ISSN: 0018-9324. DOI: 10.1109/TCT.1971.1083317.

[27] H.C. Bell. "Zolotarev bandpass filters". In: *Microwave Theory and Techniques, IEEE Transactions on* 49.12 (Dec. 2001), pp. 2357–2362. ISSN: 0018-9480. DOI: 10.1109/22.971621.

[28] R. Levy. "A New Class of Distributed Prototype Filters with Applications to Mixed Lumped/Distributed Component Design". In: *Microwave Theory and Techniques, IEEE Transactions on* 18.12 (Dec. 1970), pp. 1064–1071. ISSN: 0018-9480. DOI: 10.1109/TMTT.1970.1127412.

[29] S.B. Cohn. "Direct-Coupled-Resonator Filters". In: *Proceedings of the IRE* 45.2 (Feb. 1957), pp. 187–196. ISSN: 0096-8390. DOI: 10.1109/JRPROC.1957.278389.

[30] D.M. Pozar. *Microwave Engineering, 4th ed.* Wiley & Sons, 2012. ISBN: 9780470631553.

[31] R. Levy. "Theory of Direct-Coupled-Cavity Filters". In: *Microwave Theory and Techniques, IEEE Transactions on* 15.6 (June 1967), pp. 340–348. ISSN: 0018-9480. DOI: 10.1109/TMTT.1967.1126471.

[32] A.E. Atia and A.E. Williams. "Narrow-Bandpass Waveguide Filters". In: *Microwave Theory and Techniques, IEEE Transactions on* 20.4 (Apr. 1972), pp. 258–265. ISSN: 0018-9480. DOI: 10.1109/TMTT.1972.1127732.

[33] J. S. Hong and M. J. Lancaster. *Microstrip Filters for RF/Microwave Applications*. Ed. by Kai Chang Series. New York, NY: Wiley & Sons, 2001. ISBN: 0-471-38877-7.

[34] Richard J. Cameron, Chandra M. Kudsia and Raafat R. Mansour. *Microwave Filters for Communication Systems*. Hoboken, N.J. Wiley-Interscience, 2007. ISBN: 978-0-471-45022-1.

[35] Richard J. Cameron. "Advanced Filter Synthesis". In: *Microwave Magazine, IEEE* 12.6 (Oct. 2011), pp. 42–61. ISSN: 1527-3342. DOI: 10.1109/MMM.2011.942007.

[36] F. Seyfert and S. Bila. "General synthesis techniques for coupled resonator networks". In: *Microwave Magazine, IEEE* 8.5 (Oct. 2007), pp. 98–104. ISSN: 1527-3342. DOI: 10.1109/MMW.2007.4383440.

[37] R. Levy. "Filters with Single Transmission Zeros at Real or Imaginary Frequencies". In: *Microwave Theory and Techniques, IEEE Transactions on* 24.4 (Apr. 1976), pp. 172–181. ISSN: 0018-9480. DOI: 10.1109/TMTT.1976.1128811.

[38] J.B. Thomas. "Cross-coupling in coaxial cavity filters - a tutorial overview". In: *Microwave Theory and Techniques, IEEE Transactions on* 51.4 (Apr. 2003), pp. 1368–1376. ISSN: 0018-9480. DOI: 10.1109/TMTT.2003.809180.

[39] A. Atia, A. Williams and R. Newcomb. "Narrow-band multiple-coupled cavity synthesis". In: *Circuits and Systems, IEEE Transactions on* 21.5 (Sept. 1974), pp. 649–655. ISSN: 0098-4094. DOI: 10.1109/TCS.1974.1083913.

[40] R.J. Cameron. "General coupling matrix synthesis methods for Chebyshev filtering functions". In: *Microwave Theory and Techniques, IEEE Transactions on* 47.4 (Apr. 1999), pp. 433–442. ISSN: 0018-9480. DOI: 10.1109/22.754877.

[41] R.J. Cameron. "Advanced coupling matrix synthesis techniques for microwave filters". In: *Microwave Theory and Techniques, IEEE Transactions on* 51.1 (Jan. 2003), pp. 1–10. ISSN: 0018-9480. DOI: 10.1109/TMTT.2002.806937.

[42] H. Ezzeddine et al. "Optimized Synthesis of Self-Equalized Microwave Filters". In: *Microwave Theory and Techniques, IEEE Transactions on* 62.8 (Aug. 2014), pp. 1671–1677. ISSN: 0018-9480. DOI: 10.1109/TMTT.2014.2332135.

[43] A. García Lamperez. "Métodos avanzados de síntesis y optimización de filtros y multiplexores de microondas". PhD thesis. Madrid, Spain: Universidad Politécnica de Madrid, 2004. URL: http://oa.upm.es/29/.

[44] A. Garcia Lamperez and M. Salazar Palma. "Analytical synthesis of coupling matrices for N-port networks with reactance compensation". In: *Workshop Notes W14: Adv. N-port Netw. Space Appl., Eur. Microw. Conf.* Amsterdam, The Netherlands, Nov. 2012, pp. 1–34.

[45] A. Garcia-Lamperez et al. "Efficient electromagnetic optimization of microwave filters and multiplexers using rational models". In: *Microwave Theory and Techniques, IEEE Transactions on* 52.2 (2004), pp. 508–521. ISSN: 0018-9480. DOI: 10.1109/TMTT.2003.822021.

[46] A. Garcia-Lamperez, M. Salazar-Palma and Yu Zhang. "Analytical synthesis of microwave multiport networks". In: *Microwave Symposium Digest, 2004 IEEE MTT-S International*. Vol. 2. June 2004, 455–458 Vol.2. DOI: 10.1109/MWSYM.2004.1336009.

[47] A. Garcia-Lamperez, M. Salazar-Palma and T.K. Sarkar. "Compact multiplexer formed by coupled resonators with distributed coupling". In: *Antennas and Propagation Society International Symposium, 2005 IEEE*. Vol. 1A. July 2005, 89–92 Vol. 1A. DOI: 10.1109/APS.2005.1551250.

[48] F. Loras-Gonzalez et al. "A novel Ku-Band dielectric resonator triplexer based on generalized multiplexer theory". In: *Microwave Symposium Digest (MTT), 2010 IEEE MTT-S International*. May 2010, p. 1. DOI: 10.1109/MWSYM.2010.5517537.

[49] S. Tamiazzo and G. Macchiarella. "Synthesis of Duplexers With the Common Port Matched at All Frequencies". In: *Microwave Theory and Techniques, IEEE Transactions on* 62.1 (2014), pp. 46–54. ISSN: 0018-9480. DOI: 10.1109/TMTT.2013.2291545.

[50] R.S. Adve et al. "Application of the Cauchy method for extrapolating/interpolating narrowband system responses". In: *Microwave Theory and Techniques, IEEE Transactions on* 45.5 (1997), pp. 837–845. ISSN: 0018-9480. DOI: 10.1109/22.575608.

[51] A. Garcia-Lamperez, Yu Zhang and M.S. Palma. "Filter Model Generation from Scattering Parameters using the Cauchy Method". In: *Microwave Conference, 2002. 32nd European*. 2002, pp. 1–4. DOI: 10.1109/EUMA.2002.339310.

[52] G. Macchiarella and D. Traina. "A formulation of the Cauchy method suitable for the synthesis of lossless circuit models of microwave filters from lossy measurements". In: *Microwave and Wireless Components Letters, IEEE* 16.5 (2006), pp. 243–245. ISSN: 1531-1309. DOI: 10.1109/LMWC.2006.873583.

[53] D. Traina, G. Macchiarella and T.K. Sarkar. "Robust Formulations of the Cauchy Method Suitable for Microwave Duplexers Modeling". In: *Microwave Theory and Techniques, IEEE Transactions on* 55.5 (2007), pp. 974–982. ISSN: 0018-9480. DOI: 10.1109/TMTT.2007.895394.

[54] G. Macchiarella and S. Tamiazzo. "Generation of canonical forms for multiport filtering networks". In: *Microwave Symposium (IMS), 2014 IEEE MTT-S International*. June 2014, pp. 1–3. DOI: 10.1109/MWSYM.2014.6848300.

[55] J.D. Rhodes and R. Levy. "A Generalized Multiplexer Theory". In: *Microwave Theory and Techniques, IEEE Transactions on* 27.2 (Feb. 1979), pp. 99–111. ISSN: 0018-9480. DOI: 10.1109/TMTT.1979.1129570.

[56] J.D. Rhodes and R. Levy. "Design of General Manifold Multiplexers". In: *Microwave Theory and Techniques, IEEE Transactions on* 27.2 (Feb. 1979), pp. 111–123. ISSN: 0018-9480. DOI: 10.1109/TMTT.1979.1129571.

[57] Richard J. Cameron and Ming Yu. "Design of manifold-coupled multiplexers". In: *Microwave Magazine, IEEE* 8.5 (Oct. 2007), pp. 46–59. ISSN: 1527-3342. DOI: 10.1109/MMM.2007.904715.

[58] T.F. Skaik, M.J. Lancaster and F. Huang. "Synthesis of multiple output coupled resonator circuits using coupling matrix optimisation". In: *Microwaves, Antennas Propagation, IET* 5.9 (2011), pp. 1081–1088. ISSN: 1751-8725. DOI: 10.1049/iet-map.2010.0447.

[59] K. Song et al. "Synthesis and design method of bandpass-response power divider". In: *Microelectronics Journal* 45.1 (2014), pp. 71–77. ISSN: 0026-2692. DOI: http://dx.doi.org/10.1016/j.mejo.2013.10.002. URL: http://www.sciencedirect.com/science/article/pii/S0026269213002292.

[60] X. Shang et al. "Novel Multiplexer Topologies Based on All-Resonator Structures". In: *Microwave Theory and Techniques, IEEE Transactions on* 61.11 (2013), pp. 3838–3845. ISSN: 0018-9480. DOI: 10.1109/TMTT.2013.2284496.

[61] F. Seyfert et al. "Nevanlinna Pick Interpolation and Multiplexer Synthesis". In: *Workshop Notes W14: Adv. N-port Netw. Space Appl., Eur. Microw. Conf.* Amsterdam, The Netherlands, Nov. 2012, pp. 1–18.

[62] T. Georgiou. "A Topological Approach to Nevanlinna-Pick Interpolation". In: *SIAM Journal on Mathematical Analysis* 18.5 (1987), pp. 1248–1260. ISSN: 0036-1410. DOI: 10.1137/0518091. URL: http://epubs.siam.org/doi/abs/10.1137/0518091.

[63] B. Piovano et al. "Design And Breadboarding Of Wideband N × N Butler Matrices For Multiport Amplifiers". In: *Microwave Conference/Brazil, 1993., SBMO International*. Vol. 1. Aug. 1993, pp. 175–180. DOI: 10.1109/SBMO.1993.589533.

[64] A. Angelucci et al. "Multiport power amplifiers for mobile-radio systems using microstrip Butler matrices". In: *Antennas and Propagation Society International Symposium, 1994. AP-S. Digest*. Vol. 1. June 1994, 628–631 vol.1. DOI: 10.1109/APS.1994.407675.

[65] K. Wincza, S. Gruszczynski and K. Sachse. "Broadband Planar Fully Integrated 8 × 8 Butler Matrix Using Coupled-Line Directional Couplers". In: *Microwave Theory and Techniques, IEEE Transactions on* 59.10 (Oct. 2011), pp. 2441–2446. ISSN: 0018-9480. DOI: 10.1109/TMTT.2011.2164092.

[66] S. Gruszczynski and K. Wincza. "Broadband 4 × 4 Butler Matrices as a Connection of Symmetrical Multisection Coupled-Line 3-dB Directional Couplers and Phase Correction Networks". In: *Microwave Theory and Techniques, IEEE Transactions on* 57.1 (Jan. 2009), pp. 1–9. ISSN: 0018-9480. DOI: 10.1109/TMTT.2008.2009081.

[67] I. Hosoda et al. "Ka Band High Power Multi-Port Amplifier (MPA) Configured with TWTA for Winds Satellite". In: *Vacuum Electronics Conference, 2007. IVEC '07. IEEE International*. May 2007, pp. 1–2. DOI: 10.1109/IVELEC.2007.4283384.

[68] G. Tian, J.-P. Yang and W. Wu. "A Novel Compact Butler Matrix Without Phase Shifter". In: *Microwave and Wireless Components Letters, IEEE* 24.5 (May 2014), pp. 306–308. ISSN: 1531-1309. DOI: 10.1109/LMWC.2014.2306898.

[69] K. Song and Q. Xue. "Planar Probe Coaxial-Waveguide Power Combiner/Divider". In: *Microwave Theory and Techniques, IEEE Transactions on* 57.11 (Nov. 2009), pp. 2761–2767. ISSN: 0018-9480. DOI: 10.1109/TMTT.2009.2032483.

[70] Tong-Hong Lin, Sen-Kuei Hsu and Tzong-Lin Wu. "Bandwidth Enhancement of 4×4 Butler Matrix Using Broadband Forward-Wave Directional Coupler and Phase Difference Compensation". In: *Microwave Theory and Techniques, IEEE Transactions on* 61.12 (Dec. 2013), pp. 4099–4109. ISSN: 0018-9480. DOI: 10.1109/TMTT.2013.2288597.

[71] J. Hartmann et al. "Advanced Communication Satellite Technologies". In: *Workshop on Space Borne Antennae Technologies and Measurement Techniques*. Ed. by ISRO. Ahmedabad, India, Apr. 2002.

[72] J. Reed and G.J. Wheeler. "A Method of Analysis of Symmetrical Four-Port Networks". In: *Microwave Theory and Techniques, IRE Transactions on* 4.4 (Oct. 1956), pp. 246–252. ISSN: 0097-2002. DOI: 10.1109/TMTT.1956.1125071.

[73] J-S Hong. "Couplings of asynchronously tuned coupled microwave resonators". In: *Microwaves, Antennas and Propagation, IEE Proceedings* 147.5 (2000), pp. 354–358. ISSN: 1350-2417. DOI: 10.1049/ip-map:20000675.

[74] *Computer Simulation Technology*. Version 2014. CST. URL: http://www.cst.com.

[75] *Fest3D*. Version 6.8.6.1. Aurora Software and Testing SL. 2014. URL: http://www.fest3d.com.

[76] *Mician μWave Wizard*. Version 7.11. URL: http://www.mician.com.

[77] Ming Yu. "Power-handling capability for RF filters". In: *Microwave Magazine, IEEE* 8.5 (Oct. 2007), pp. 88–97. ISSN: 1527-3342. DOI: 10.1109/MMM.2007.904712.

[78] P. T. Farnsworth. "Television by electron image scanning". In: *Journal of the Franklin Institute* 218.4 (1934), pp. 411–444. ISSN: 0016-0032. DOI: http://dx.doi.org/10.1016/S0016-0032(34)90415-4. URL: http://www.sciencedirect.com/science/article/pii/S0016003234904154.

[79] J.R.M. Vaughan. "Multipactor". In: *Electron Devices, IEEE Transactions on* 35.7 (July 1988), pp. 1172–1180. ISSN: 0018-9383. DOI: 10.1109/16.3387.

[80] Wai-Cheung Tang and C. Kudsia. "Multipactor breakdown and passive intermodulation in microwave equipment for stellite applications". In: *Military Communications Conference, 1990. MILCOM '90, Conference Record, A New Era. 1990 IEEE*. Sept. 1990, 181–187 vol.1. DOI: 10.1109/MILCOM.1990.117409.

[81] J.W. You et al. "Accurate Numerical Analysis of Nonlinearities Caused by Multipactor in Microwave Devices". In: *Microwave and Wireless Components Letters, IEEE* 24.11 (Nov. 2014), pp. 730–732. ISSN: 1531-1309. DOI: 10.1109/LMWC.2014.2344758.

[82] A. J. Hatch and H. B. Williams. "The Secondary Electron Resonance Mechanism of Low-Pressure High-Frequency Gas Breakdown". In: *Journal of Applied Physics* 25 (4 1954), pp. 417–423. DOI: 10.1063/1.1721656.

[83] *Spark3D*. Version 1.5.1. Aurora Software and Testing SL. 2014. URL: http://www.fest3d.com/spark3d.php.

[84] I. Montero et al. "Anti-Multipactor Coatings for Ku Band RF Filters using Chemical Methods". In: *8th International Workshop on Multipactor, Corona and Passive Intermodulation, ESA MULCOPIM 2014*. Sept. 2014, pp. 1–8.

[85] I. Montero et al. "Ku Band RF Filters without Multipactor Discharge". In: *6th CNES/ESA International Workshop on Microwave Filters 2015, IWMF2015*. Mar. 2015, pp. 1–3.

[86] ESA/ESTEC, ed. *Space engineering-Multipaction design and test*. ECSS-E-20-01A. Noordwijk, The Netherlands, May 2003.

[87] J.S. Chang, P.A. Lawless and T. Yamamoto. "Corona discharge processes". In: *Plasma Science, IEEE Transactions on* 19.6 (Dec. 1991), pp. 1152–1166. ISSN: 0093-3813. DOI: 10.1109/27.125038.

[88] G.H. Schennum and G. Rosati. "Minimizing passive intermodulation product generation in high power satellites". In: *Aerospace Applications Conference, 1996. Proceedings., 1996 IEEE*. Vol. 3. Feb. 1996, 155–164 vol.3. DOI: 10.1109/AERO.1996.496060.

[89] H.J. Riblet. "A Mathematical Theory of Directional Couplers". In: *Proceedings of the IRE* 35.11 (Nov. 1947), pp. 1307–1313. ISSN: 0096-8390. DOI: 10.1109/JRPROC.1947.233573.

[90] R. Levy. ""Analysis of Practical Branch-Guide Directional Couplers" (Correspondence)". In: *Microwave Theory and Techniques, IEEE Transactions on* 17.5 (May 1969), pp. 289–290. ISSN: 0018-9480. DOI: 10.1109/TMTT.1969.1126957.

[91] Leo Young. "Synchronous Branch Guide Directional Couplers for Low and High Power Applications". In: *Microwave Theory and Techniques, IRE Transactions on* 10.6 (Nov. 1962), pp. 459–475. ISSN: 0097-2002. DOI: 10.1109/TMTT.1962.1125554.

[92] R. Levy and L.F. Lind. "Synthesis of Symmetrical Branch-Guide Directional Couplers". In: *Microwave Theory and Techniques, IEEE Transactions on* 19.2 (Feb. 1968), pp. 80–89. ISSN: 0018-9480. DOI: 10.1109/TMTT.1968.1126612.

[93] L.F. Lind. "Synthesis of Asymmetrical Branch-Guide Directional Coupler-Impedance Transformers (Correspondence)". In: *Microwave Theory and Techniques, IEEE Transactions on* 17.1 (Jan. 1969), pp. 45–48. ISSN: 0018-9480. DOI: 10.1109/TMTT.1969.1126879.

[94] R. Levy. "Zolotarev Branch-Guide Couplers". In: *Microwave Theory and Techniques, IEEE Transactions on* 21.2 (Feb. 1973), pp. 95–99. ISSN: 0018-9480. DOI: 10.1109/TMTT.1973.1127930.

[95] M. Muraguchi, T. Yukitake and Y. Naito. "Optimum Design of 3-Db Branch-Line Couplers Using Microstrip Lines". In: *Microwave Theory and Techniques, IEEE Transactions on* 31.8 (Aug. 1983), pp. 674–678. ISSN: 0018-9480. DOI: 10.1109/TMTT.1983.1131568.

[96] Tao Shen and K.A. Zaki. "Waveguide branch couplers for tight couplings". In: *Microwave Theory and Techniques, IEEE Transactions on* 48.12 (Dec. 2000), pp. 2432–2438. ISSN: 0018-9480. DOI: 10.1109/22.898994.

[97] J.A. Ruiz-Cruz et al. "Ridge waveguide branch-line directional couplers for wideband applications and LTCC technology". In: *Microwave Symposium Digest, 2005 IEEE MTT-S International*. June 2005, pp. 1219–1222. DOI: 10.1109/MWSYM.2005.1516896.

[98] F. Alessandri, G. Bartolucci and R. Sorrentino. "Admittance matrix formulation of waveguide discontinuity problems: computer-aided design of branch guide directional couplers". In: *Microwave Theory and Techniques, IEEE Transactions on* 36.2 (Feb. 1988), pp. 394–403. ISSN: 0018-9480. DOI: 10.1109/22.3528.

[99] R. Gomez-Garcia, J.I. Alonso and D. Amor-Martin. "Using the branch-line directional coupler in the design of microwave bandpass filters". In: *Microwave Theory and Techniques, IEEE Transactions on* 53.10 (Oct. 2005), pp. 3221–3229. ISSN: 0018-9480. DOI: 10.1109/TMTT.2005.855140.

[100] R. Gomez-Garcia, M. Sanchez-Renedo and J.-M. Munoz-Ferreras. "Microwave filtering power-distribution planar networks". In: *Microwave Symposium Digest (MTT), 2011 IEEE MTT-S International*. June 2011, pp. 1–4. DOI: 10.1109/MWSYM.2011.5972567.

[101] H. Uchida et al. "Bandpass Directional Couplers with Electromagnetically-Coupled Resonators". In: *Microwave Symposium Digest, 2006. IEEE MTT-S International*. June 2006, pp. 1563–1566. DOI: 10.1109/MWSYM.2006.249613.

[102] Wei-Lun Chang et al. "Design of Compact Branch-Line Coupler with Coupled Resonators". In: *Microwave Conference, 2007. APMC 2007. Asia-Pacific*. Dec. 2007, pp. 1–4. DOI: 10.1109/APMC.2007.4555113.

[103] Shuli Li, Shani Lu and Michael J. Lancaster. "WR-3 band butler matrix design using SU-8 photo-resist technology". In: *Passive RF and Microwave Components, 3rd Annual Seminar on*. Mar. 2012, pp. 19–26. DOI: 10.1049/ic.2012.0061.

[104] Shani Lu. "Design of microwave hybrid couplers using inter-coupled resonators". MA thesis. University of Birmingham, Apr. 2012.

[105] V. Tornielli di Crestvolant and M.J. Lancaster. "Synthesis of a class of quadrature circuits based on coupled-resonators". In: *Passive RF and Microwave Components, 4th Annual Seminar on*. Mar. 2013, pp. 1–4. DOI: 10.1049/ic.2013.0284.

[106] V. Tornielli di Crestvolant, P. Martin Iglesias and M. J. Lancaster. "Topological analysis of hybrid couplers incorporating filter functions". In: *6th CNES/ESA International Workshop on Microwave Filters 2015, IWMF2015*. Mar. 2015, pp. 1–7.

[107] U. Rosenberg et al. "Compact Multi-Port Power Combination/Distribution With Inherent Bandpass Filter Characteristics". In: *Microwave Theory and Techniques, IEEE Transactions on* 62.11 (Nov. 2014), pp. 2659–2672. ISSN: 0018-9480. DOI: 10.1109/TMTT.2014.2361345.

[108] Wan-Rou Liu et al. "Design of a 180-degree hybrid with Chebyshev filtering response using coupled resonators". In: *Microwave Symposium Digest (IMS), 2013 IEEE MTT-S International*. June 2013, pp. 1–3. DOI: 10.1109/MWSYM.2013.6697512.

[109] Chin-Kai Lin and Shyh-Jong Chung. "A Compact Filtering 180° Hybrid". In: *Microwave Theory and Techniques, IEEE Transactions on* 59.12 (2011), pp. 3030–3036. ISSN: 0018-9480. DOI: 10.1109/TMTT.2011.2169276.

[110] U. Rosenberg et al. "Corrections to "Compact Multi-Port Power Combination/Distribution With Inherent Bandpass Filter Characteristics"". In: *Microwave Theory and Techniques, IEEE Transactions on* 63.7 (July 2015), pp. 2390–2390. ISSN: 0018-9480. DOI: 10.1109/TMTT.2015.2434998.

[111] Chi-Feng Chen et al. "A compact filtering rat-race coupler using dual-mode stub-loaded resonators". In: *Microwave Symposium Digest (MTT), 2012 IEEE MTT-S International*. 2012, pp. 1–3. DOI: 10.1109/MWSYM.2012.6258380.

[112] U. Rosenberg and S. Amari. "New Power Distribution (Combination) Method with Frequency Selective Properties". In: *Workshop Notes W14: Adv. N-port Netw. Space Appl., Eur. Microw. Conf.* Amsterdam, The Netherlands, Nov. 2012, pp. 1–34.

[113] U. Rosenberg et al. "A Novel Frequency-Selective Power Combiner/Divider in Single-Layer Substrate Integrated Waveguide Technology". In: *Microwave and Wireless Components Letters, IEEE* 23.8 (Aug. 2013), pp. 406–408. ISSN: 1531-1309. DOI: 10.1109/LMWC.2013.2269039.

[114] L.-S. Wu et al. "Collaborative Design of a New Dual-Bandpass 180° Hybrid Coupler". In: *Microwave Theory and Techniques, IEEE Transactions on* 61.3 (Mar. 2013), pp. 1053–1066. ISSN: 0018-9480. DOI: 10.1109/TMTT.2013.2241782.

[115] F. Lin, Q. Chu and S. Wong. "Design of Dual-Band Filtering Quadrature Coupler Using λ/2 and λ/4 Resonators". In: *Microwave and Wireless Components Letters, IEEE* 22.11 (Nov. 2012), pp. 565–567. ISSN: 1531-1309. DOI: 10.1109/LMWC.2012.2224650.

[116] K. Song et al. "Compact in-phase power divider integrated filtering response using spiral resonator". In: *Microwaves, Antennas Propagation, IET* 8.4 (Mar. 2014), pp. 228–234. ISSN: 1751-8725. DOI: 10.1049/iet-map.2013.0201.

[117] Lancaster. *Microwave Designer*. 2015. URL: http://microwavedesigner.com/.

[118] V. Tornielli di Crestvolant et al. "Multipaction prediction in 180° hybrid power divider based on resonant cavities". In: *8th International Workshop on Multipactor, Corona and Passive Intermodulation, ESA MULCOPIM 2014*. Sept. 2014, pp. 1–8.

[119] A. Panariello, J. Petit and Ming Yu. "Advanced Multipactor Analysis and Test for a L-Band Diplexer". In: *8th International Workshop on Multipactor, Corona and Passive Intermodulation, ESA MULCOPIM 2014*. Sept. 2014, pp. 1–8.

[120] U. Rosenberg. "New 'Planar' waveguide cavity elliptic function filters". In: *Microwave Conference, 1995. 25th European*. Vol. 1. 1995, pp. 524–527. DOI: 10.1109/EUMA.1995.337014.

[121] C. Ernst, V. Postoyalko and N.G. Khan. "Relationship between group delay and stored energy in microwave filters". In: *Microwave Theory and Techniques, IEEE Transactions on* 49.1 (Jan. 2001), pp. 192–196. ISSN: 0018-9480. DOI: 10.1109/22.900007.

[122] V. Tornielli di Crestvolant, P. Martin Iglesias and M. J. Lancaster. "Advances in manufacturing of 4×4 Butler matrices with inherent bandpass filter functions". In: *6th CNES/ESA International Workshop on Microwave Filters 2015, IWMF2015*. Mar. 2015, pp. 1–4.

[123] Larry F. Lind. "Synthesis of Branch-Guide Directional Couplers and Filter Prototypes". PhD thesis. Leeds, UK: University of Leeds, Sept. 1968.

[124] H.J. Riblet. "The Application of a New Class of Equal-Ripple Functions to Some Familiar Transmission-Line Problems". In: *Microwave Theory and Techniques, IEEE Transactions on* 12.4 (July 1964), pp. 415–421. ISSN: 0018-9480. DOI: 10.1109/TMTT.1964.1125841.

[125] H.J. Carlin and W. Kohler. "Direct Synthesis of Band-Pass Transmission Line Structures". In: *Microwave Theory and Techniques, IEEE Transactions on* 13.3 (May 1965), pp. 283–297. ISSN: 0018-9480. DOI: 10.1109/TMTT.1965.1125992.

[126] J.R. Montejo-Garai. "Synthesis of N-even order symmetric filters with N transmission zeros by means of source-load cross coupling". In: *Electronics Letters* 36.3 (2000), pp. 232–233. ISSN: 0013-5194. DOI: 10.1049/el:20000242.

[127] Carl D. Meyer, ed. *Matrix analysis and applied linear algebra*. Philadelphia, PA, USA: Society for Industrial and Applied Mathematics, 2000. ISBN: 0898714540.

[128] M.E. Van Valkenburg. *Introduction to Modern Network Synthesis*. New York, NY: Wiley & Sons, 1960. ISBN: 0-471-89991-7.

[129] G. Macchiarella and S. Tamiazzo. "Novel Approach to the Synthesis of Microwave Diplexers". In: *Microwave Theory and Techniques, IEEE Transactions on* 54.12 (2006), pp. 4281–4290. ISSN: 0018-9480. DOI: 10.1109/TMTT.2006.885909.

[130] Richard J. Cameron, A.R. Harish and C.J. Radcliffe. "Synthesis of advanced microwave filters without diagonal cross-couplings". In: *Microwave Theory and Techniques, IEEE Transactions on* 50.12 (2002), pp. 2862–2872. ISSN: 0018-9480. DOI: 10.1109/TMTT.2002.805141.

[131] V. Tornielli di Crestvolant, P. Martin Iglesias and M.J. Lancaster. "Advanced Butler Matrices With Integrated Bandpass Filter Functions". In: *Microwave Theory and Techniques, IEEE Transactions on* 63.10 (Oct. 2015), pp. 3433–3444. ISSN: 0018-9480. DOI: 10.1109/TMTT.2015.2460739.